

Alma Mater Studiorum – Università di Bologna

DOTTORATO DI RICERCA IN

FISICA

Ciclo 34

Settore Concorsuale: 02/B1 – FISICA SPERIMENTALE DELLA MATERIA

Settore Scientifico Disciplinare: FIS/03 FISICA DELLA MATERIA

Fabrication and characterization of hybrid ferromagnetic-organic heterostructures for spintronics application

Presentata da: Mattia Benini

Coordinatore Dottorato

Prof. Michele Cicoli

Supervisore

Dott.ssa Ilaria Bergenti

Co-supervisore

Prof. Samuele Sanna

Esame finale anno 2022

Abstract

Recent research in the field of organic spintronics highlighted the peculiar spin-dependent properties of the interface formed by an organic semiconductor (OSC) chemisorbed over a $3d$ ferromagnetic metal, also known as *spinterface*. The hybridization between the molecular and metallic orbitals, typically π orbitals of the molecule and the d orbitals of the ferromagnet, give rise to spin dependent properties that were not expected by considering the single components of interfaces, as for example the appearance of a magnetic moment on non-magnetic molecules or changes in the magnetic behavior of the ferromagnet. From a technological viewpoint these aspects provide novel engineering schemes for spin memory and for spintronics devices, featuring unexpected interfacial magnetoresistance, spin-filtering effects and even modulated magnetic anisotropy. Applications of these concepts to devices require nevertheless to transfer the spinterface effects from an ideal interface to room temperature operating thin films.

In this view, my work presents for the first time how spinterface effects can be obtained even at room temperature on polycrystalline ferromagnetic Co thin films interfaced with organic molecules. The considered molecules were commercial and widely used in the field of organic electronics: Fullerene (C_{60}), Gallium Quinoline (GaQ_3) and Sexithiophene (T6).

An increase of coercivity, up to 100% at room temperature, has been obtained on the Co ultra-thin films by the deposition of an organic molecule. This effect is accompanied by a change of in-plane anisotropy that is molecule-dependent. Moreover the Spinterface effect is not limited to the interfacial layer, but it extends throughout the whole thickness of the ferromagnetic layer, posing new questions on the nature of the $3d$ metal-molecule interaction.

Contents

Abstract	I
Contents	III
List of Acronyms	VII
Introduction	1
Chapter 1	3
1.1 Introduction to organic spintronics	3
1.2 The ferromagnetic/molecule interface	6
1.2.1 Adsorption of molecules on ferromagnetic layers and spinterface concepts 6	
1.2.2 Effect of molecular adsorption on thin film magnetism.....	13
1.3 Exploiting the spinterface for voltage control of magnetism.....	17
Chapter 2	21
2.1 Origin of magnetic order	21
2.2 Band ferromagnetism	23
2.3 Magnetic anisotropy	25
2.3.1 Shape anisotropy.....	26
2.3.2 Magnetocrystalline anisotropy	28
2.3.3 Surface and strain anisotropy	30
2.4 Domains and the Stoner-Wohlfarth model.....	31
2.5 Magnetic anisotropy of thin films	35
2.6 Superparamagnetism, antiferromagnetism and exchange anisotropy	40
Chapter 3	45

3.1	UHV fabrication of hybrid systems	45
3.1.1	The growth chamber	45
3.1.2	Fabrication procedure	50
3.2	Microstructural characterization	52
3.2.1	Atomic Force Microscopy (AFM).....	52
3.2.2	AFM: <i>Calculation of the surfaces characteristic length scales</i>	56
3.2.3	Transmission Electron Microscope	60
3.3	Magnetic characterization techniques	61
3.3.1	Magneto-Optic Kerr Effect (MOKE)	61
3.3.2	Vibrating Sample Magnetometer (VSM)	66
3.3.3	Superconducting Quantum Interference Device (SQUID)	67
3.4	Magnetic resonance characterization	69
3.4.1	Nuclear Magnetic Resonance	69
3.4.2	Ferromagnetic NMR.....	71
3.4.3	Experimental setup	74
Chapter 4	77
4.1	AFM Characterization of the surfaces	77
4.1.1	Al ₂ O ₃ (0001) substrates and Cobalt thin films	78
4.1.2	The Al capping layer	81
4.1.3	The molecular layers	82
4.2	Cross-Section TEM analysis of Co thin films.....	86
4.3	Conclusions	89
Chapter 5	91
5.1	RT anisotropy of hybrid systems	91
5.2	Uniaxial anisotropy of Co/Al reference samples	92

5.2.1	UMA reduction and magnetic hardening of Co/C ₆₀ systems	96
5.2.2	Loss of UMA and magnetic hardening of Co/Gaq ₃ and Co/T ₆ hybrid systems	99
5.3	The Co/C ₆₀ case: evaluation of the anisotropy constant	102
5.4	The temperature dependence of molecular induced hardening effects	107
5.4.1	Decoupling the interface:Co/CoO _x /Molecule systems	110
5.5	Co/C ₆₀ : low temperature behavior.....	111
5.6	Conclusions	115
	Appendix 5A MOKE hysteresis loops treatment	117
	Normalization procedure, coercivity, bias field and squareness calculation.....	117
	Loop adjustments: quadratic contributions removal.....	118
	Appendix 5B VSM and SQUID loops treatment.....	120
	Removal of the background signal	120
	Calculation of the anisotropy constant.....	121
	Chapter 6.....	123
6.1	Bulk modification of the magnetic hardness.....	123
6.2	Interfacial contribution to the FNR spectra.....	126
6.3	Conclusions	129
	Chapter 7.....	131
	Bibliography	135

List of Acronyms

AC – Alternate current

ACF – Autocorrelation Function

ACL Autocovariance Length

AFM – Antiferromagnet (chapter 1, 2, 5)

AFM – Atomic Force Microscopy (chapter 3 and 4)

AM-AFM – Amplitude Modulation Atomic Force Microscopy

CEHc – Colossal Enhancement of Coercive field

DC – Direct Current

DOS – Density Of States

EM – Electro-Magnetic

fcc – Face Centered Cubic

FM – Ferromagnet

FNR – Ferromagnetic Nuclear (magnetic) Resonance

FWHM – Full Width at Half Maximum

GMR - Giant MagnetoResistance

hcp – Hexagonal Close Packed

HIS – Hybrid Interface State

HOMO – Highest Occupied Molecular Orbital

HV – High Voltage

LCL – Left Circularly Polarized Light

LLP – Linearly Polarized Light

LEL – Liquid Electrolyte

L-MOKE – Longitudinal Magneto Optic Kerr Effect

LUMO - Lowest Unoccupied Molecular Orbital

MAE Magnetic Anisotropy Energy
MCA - Magnetocrystalline Anisotropy
MOKE – Magneto Optic Kerr Effect
NMR Nuclear Magnetic Resonance
NN- Nearest Neighbors
OSC- Organic Semiconductors
QMB – Quartz Microbalance
rf – Radio Frequency
RHS – Right-Hand Side
RCL – Right Circularly Polarized Light
RT -Room Temperature
SC – Super Conductor
SPM – Scanning Probe Microscopy
SQUID - Superconducting Quantum Interference Device
UHV - Ultra-High-Vacuum
VSM – Vibrating Sample Magnetometer.

Introduction

Spintronics is a branch of electronics that exploits the electrons spin for information storage and processing. The prototypical device, called spin-valve, is composed of two ferromagnetic electrodes decoupled by a layer of nonmagnetic material. This system is characterized by two different states of resistance, that is dependent on the mutual orientation of the two electrodes. The use of Organic Semiconductors (OSC) as spin-transport media in this class of devices gained popularity in virtue of their weak spin relaxation mechanisms. The anomalous behavior observed in hybrid inorganic/organic spintronic devices soon indicated that the role of molecules is far more prominent than just spin transport materials. A coherent picture emerged which indicates that the ferromagnet/molecule interface, named *spinterface*, possesses peculiar electronic and magnetic properties that are different from the ones of their constituents. In particular, novel and interesting effects have been reported for the case of epitaxially or textured ferromagnetic thin films interfaced with OSC, such as magnetic easy axis reorientation and induced magnetism on nonmagnetic elements[1], [2]. In a perspective of ideation of novel spintronic devices, the modification of magnetic parameters by a 2D interface is a tantalizing prospect.

In this thesis I have fabricated and characterized with several microstructural and magnetic techniques hybrid systems formed by a *3d* ferromagnetic *polycrystalline* thin film hybridized with organic semiconductors. The goal is to observe any modification of the *3d* metal's magnetic properties induced by the presence of an interfacial layer with the molecules. The choice of Co as ferromagnet is due to its massive use as material for spintronic applications. In this regard the choice of a polycrystalline microstructure is dictated by the prospective of observing interfacial effects, crucially dependent on the surface geometry, on layers of interest for real applications.

In Chapter 1 an introduction to the topic of organic spintronics is given with a focus on the concept of spinterface and how this interface leads to modification of the magnetic properties at the atomic scale. I will also review the most recent results in this field, with regards to the modification of both magnetization and magnetic anisotropy. Chapter 2 instead is a

compendium of all the concepts of magnetism that are fundamental for understanding of the observed results. The origin of magnetic order is discussed along with all the anisotropy terms that are of relevance for thin films. In Chapter 3 I will describe the growth methods and procedures used for the fabrication of hybrid systems. Moreover all the experimental techniques used for the characterization of such systems will be discussed. The morphological and microstructural characterization of samples is discussed in Chapter 4, with a focus on the Cobalt crystallinity and on the surface quality of the various layers deposited. In Chapter 5 a thorough discussion of the magnetic characterizations of the hybrid Co/OSC system is given. In particular, it will be examined the molecule-induced effects on both the coercivity and the magnetic anisotropy, both at room temperature and down to 5 K. Chapter 6 focuses on answering how far from the interface the molecule-induced effects are propagating. In Chapter 7 all the main achievements of this thesis will be summarized along with a discussion of the possible explanations and future perspectives.

Chapter 1

General background

This chapter is a brief compendium of spin-dependent interfacial effects in molecular devices. Starting from a general description of organic spintronic devices, I present the concept of *spinterface*, that is the effect of spin-dependent hybridization at the interface between a ferromagnetic material and an organic molecule. The spinterface formation leads to a change of the intrinsic properties of both sides of the interfaces. In this regard, I focus especially on the modification of the magnetic behavior of the ferromagnet after the deposition of an organic molecule, in terms of magnetization and magnetic anisotropy. I will then describe the most recent results in the field, showing the possibility of efficiently tuning the magnetic properties of the interface at the atomic scale.

1.1 Introduction to organic spintronics

Spintronics (shorthand for spin electronics) is a branch of electronics that exploits the electrons spin for information storage and processing[3]. The prototypical device is the so-called spin-valve, which is a three-layer system, composed of two ferromagnetic (FM) layers decoupled by a non-magnetic *spacer* of width d . The device exploits the concept of Giant Magneto Resistance (GMR): the resistance of the system depends on the mutual configuration of the two electrodes. This is so since FM materials, due to exchange interaction, have spin-split bands also at Fermi level. This defines the *spin-polarization* of the material as the difference of the Density Of States (DOS) of the spin up and spin down electrons at the Fermi level:

$$P = \frac{D^\uparrow(E_F) - D^\downarrow(E_F)}{D^\uparrow(E_F) + D^\downarrow(E_F)} \quad (1.1)$$

If a current is generated in the material, it is spin-polarized as well. As a first approximation it can be considered the sum of two *independent* currents, defined by the spin state[3]. The total material resistivity is consequently regarded as the sum of two parallel resistors with resistivity ρ^\uparrow and ρ^\downarrow . It can be shown that the majority electrons (either up or down) have a lower resistance[3] compared to the minority. If the current produced by an electrode magnetized in one specific direction enters the other electrode that is magnetized in the opposite direction this latter acts as a strong resistor: the spin valve has high resistance. In the case of parallel alignment the second electrode is a weak resistor and the spin valve has low resistance. This shows that the device can be used for binary operation, assigning e.g. 0 to the high resistance state and 1 to the low resistance state. Now, the two electrodes have to be decoupled by a nonmagnetic spacer material. The main issue is the exponential decay of the spin-polarization due to spin-flipping scattering events. This decay is characterized by the so-called *spin-diffusion length* λ_{SD} that defines the maximum thickness of the spacer layer. For an inorganic metal material typical values are in the nm range[3], while for highly pure inorganic semiconductors like Germanium can reach some hundreds of nm[4]. After the breakthrough of Organic Semiconductors (OSC) in optoelectronics[5] molecules were implemented as spacer materials in hybrid FM/molecule/FM spin valves[6]. They have proven to sustain spin polarized currents up to 200 nm, even at RT[7]. The advantage of OSC over inorganic materials resides in their conduction mechanisms. These molecules are composed mostly of low Z ^{12}C atoms arranged as to form π -

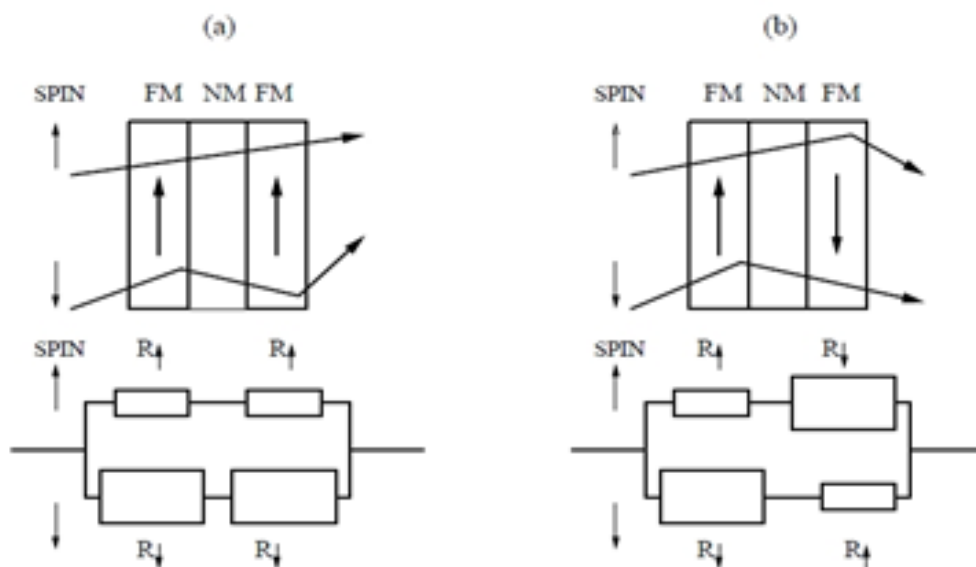


Figure 1. Sketch of a spin valve: two FM electrodes decoupled by a non-magnetic spacer (NM). (a) parallel configuration: low resistance state. (b) antiparallel configuration (high resistance state. Adapted from [3].

conjugated systems (e.g. benzene C_6H_6), indicating that they are held together by a composition of strong *localized* σ bonds and delocalized π bonds, originating by the p_z orbitals of each C atom [8], [9] (see **Figure 1. 2**). This π conjugation results in the formation of band-like structures called π bands [8], [10] reminiscent of electron bands in inorganic solids. The equivalent of the valence and conduction bands are called respectively *Highest Occupied Molecular Orbital* (HOMO) and *Lowest Unoccupied Molecular Orbital* (LUMO)

Since electrical conduction over a single molecule is due to highly delocalized π orbitals, they guarantee very low spin scattering rates (i.e. long spin diffusion lengths) [8], [9], [11]. Subsequent investigations of the magnetotransport properties of OSC in hybrid FM/OSC/FM spintronic devices revealed that the presence of a OSC spacer layer was far more important than the enhancement of the spin diffusion length [7], [12]–[14]. In particular, a molecule interacting with a ferromagnetic substrate results in a deep modification of its molecular orbitals, inducing novel electrical and magnetic properties [12]. This led to the introduction of the concept of *spininterface* [15], a term introduced for the first time in 2010 by *Stefano Sanvito* [15] for indicating the interface between the ferromagnetic material and the first molecular layers. This highly functionalized interface is an ideal building block for the creation of interfacial spin effects that have a paramount impact on the overall properties of the systems.

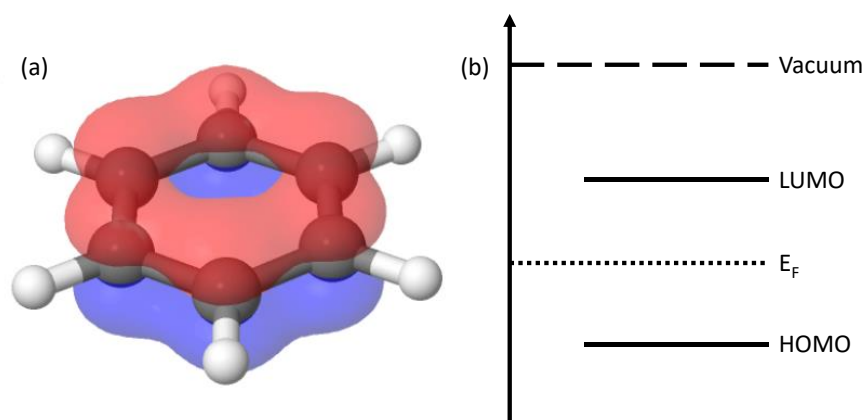


Figure 1. 2 (a) Representation of the benzene molecule C_6H_6 as example of π conjugated system. Each C atom (gray sphere) is bonded one to the other by single strongly localized σ bonds (grey cylinders) and by highly delocalized π orbitals (black and blue areas). Taken from [10]. (b) sketch of the energy levels of the molecule in its gas phase.

1.2 The ferromagnetic/molecule interface

1.2.1 Adsorption of molecules on ferromagnetic layers and spinterface concepts

The interaction of molecules deposited on surfaces is a wide and complex topic, but some important aspects can be highlighted. The adsorption of molecules on metal surfaces can be understood in the Newns-Anderson model[16], for which a key parameter is the adsorption energy ΔE , defined as the work required to separate the adsorbate (the molecule) from the adsorbent (the FM surface). The commonly accepted criterion for having chemisorption is $\Delta E \geq 1$ eV. Another important parameter that defines the interaction at interface is the bandwidth W of the metals. For $3d$ ferromagnets the narrow d bands intervening in bonds formation have a typical value of W of around 1eV[14]. If the ratio $W/\Delta E$ is much less than 1 the molecule is in the low chemisorption regime while if it is much more than 1 then it is in the strong chemisorption regime[14]. All the molecules deposited over $3d$ ferromagnets can be regarded as being in the second regime[14], [17]. Moreover, in virtue of the nature of the orbitals involved, which are $3d$ for Co and $2p$ for the molecules, it leads to formation of hybrid bonds[15]. Considering the first molecular layer chemisorbed over the FM surface, the formation of such bonds affects both systems. The Highest Occupied Molecular Orbital (HOMO) and Lowest Unoccupied Molecular Orbital (LUMO) are shifted in energy and broadened, acquiring a band-like structure[17]–[19]. Focusing on the LUMO, the broadening may be characterized by its energy level of the maximum, labelled ϵ_{eff} , and its Full Width at Half Maximum Γ , which is influenced by the FM Density Of States (DOS). Since for a ferromagnetic system due to spin-polarization there are two DOS, one for each spin state, the broadening of the molecular orbital becomes spin-dependent[17]. The overall situation is schematically depicted in **Figure 1. 3**. This picture was introduced by *Barraud et al*[18], for the interpretation of spin transport across an hybridized metal/molecule interface allowing enhancement and even sign reversal of molecular spintronic devices. Considering the interfacial DOS, it can be modelled by a Lorentzian Function, that is[12], [17]

$$D_{\text{int}}^{\uparrow(\downarrow)}(E) = (2\pi)^{-1} \frac{\Gamma^{\uparrow(\downarrow)}}{\left(E - \epsilon_{\text{eff}}^{\uparrow(\downarrow)}\right)^2 + \left(\frac{\Gamma^{\uparrow(\downarrow)}}{2}\right)^2} \quad (1. 2)$$

This equation is directly exploitable for defining the spin-polarization of the interface

$$P_{\text{INT}} = \frac{D_{\text{int}}^{\uparrow} - D_{\text{int}}^{\downarrow}}{D_{\text{int}}^{\uparrow} + D_{\text{int}}^{\downarrow}} \quad (1.3)$$

which is different from zero. If one takes $E = E_F$, $\Delta E = E_F - \epsilon_{\text{eff}}^{\uparrow(\downarrow)}$ defines the difference in energy from the LUMO^{↑(↓)} peak and the Fermi level of the FM. Two limiting cases are possible. The first one considers the energy difference much smaller than the broadening parameter, that is $\Delta E^{\uparrow(\downarrow)} \ll \Gamma^{\uparrow(\downarrow)}$. In this case the LUMO is approximately at the same level of the FM Fermi energy, and Eq (1.2) reduces to

$$D_{\text{int}}^{\uparrow(\downarrow)}(E) \approx \frac{1}{\Gamma^{\uparrow(\downarrow)}} \propto \frac{1}{D_{\text{FM}}^{\uparrow(\downarrow)}} \quad (1.4)$$

meaning that the spinterface DOS is inversely proportional to the DOS of the FM. This results in a spin-polarization of the interfacial layer that is *opposite* to the one of the FM, since

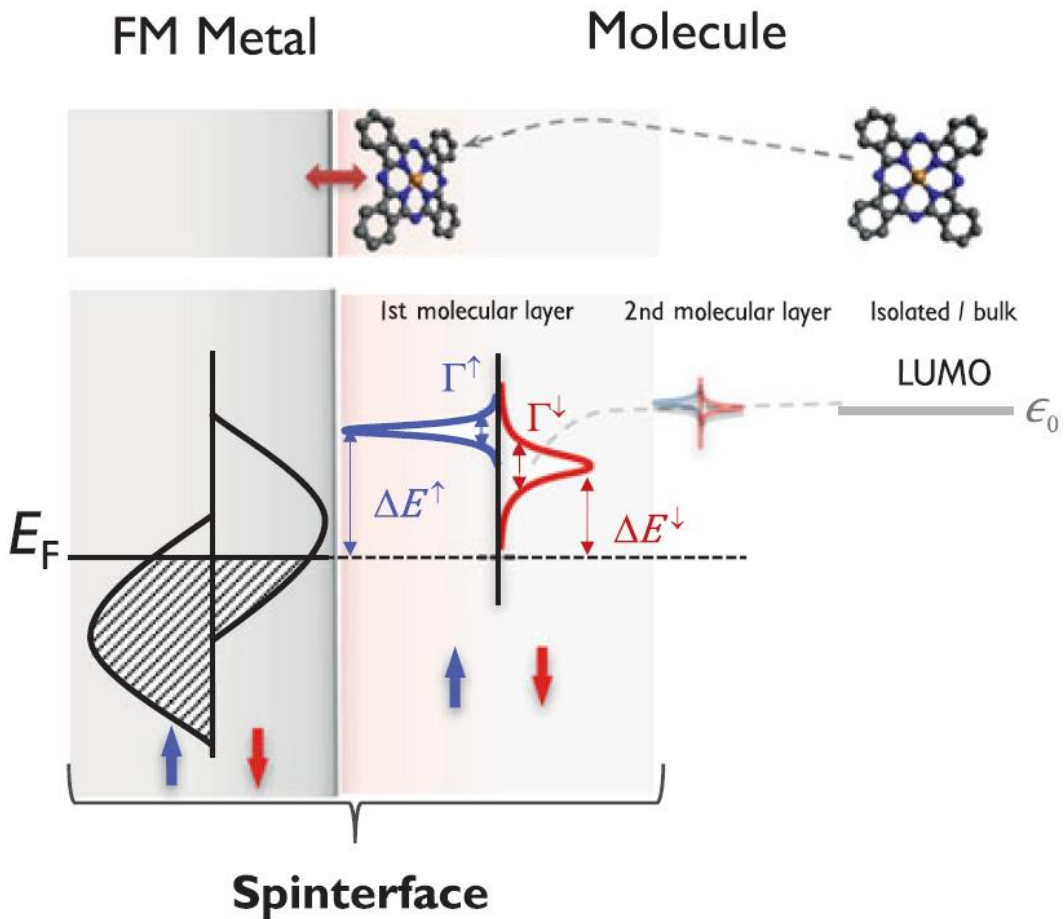


Figure 1.3 Schematics of the broadening and spin-splitting of the molecular LUMO of the first two molecular layers. ΔE is defined as the distance between ϵ_{eff} and the Fermi level of the ferromagnet. Taken from [17].

$$P_{\text{INT}} \approx \frac{\Gamma^{\uparrow} - \Gamma^{\downarrow}}{\Gamma^{\uparrow} + \Gamma^{\downarrow}} = \frac{D_{\text{FM}}^{\uparrow} - D_{\text{FM}}^{\downarrow}}{D_{\text{FM}}^{\uparrow} + D_{\text{FM}}^{\downarrow}} = -P_{\text{FM}} \quad (1.5)$$

The second case is given by the condition $\Delta E^{\uparrow(\downarrow)} \gg \Gamma^{\uparrow(\downarrow)}$, that is LUMO bands far from the Fermi energy of the metal. In this case (1. 2) becomes

$$D_{\text{int}}^{\uparrow(\downarrow)}(E) \approx \frac{\Gamma^{\uparrow(\downarrow)}}{\Delta E^{\uparrow(\downarrow)2}} \quad (1.6)$$

so the DOS of the spinterface becomes directly proportional to the one of the FM but modulated by a factor $\Delta E^{\uparrow(\downarrow)-2}$. This results in an increased or decreased value of the spinterface spin polarization. Assuming the more broadened level is closer to the FM Fermi level, the value of P_{INT} is bigger in magnitude than the one of the FM[17]. This simple model shows how the FM/Molecule interface has electronic and magnetic properties fundamentally different from the ones of the constituents. As in the case for Metal/Inorganic heterojunctions, the formation of an interface between the FM and the molecular layers results in an alignment of their Fermi levels. This alignment results in the formation of the so-called contact potential V_C . It arises since[19]

- the metal electronic wavefunction (and thus the corresponding charge density) is “pushed” inside the metal, reducing its work function;
- if the new shared Fermi level is crossing the molecule HOMO or LUMO, a charge transfer may happen between the two systems resulting in an additional electric dipole generated by the transferred charges.

From the last point, in the case E_F of the ferromagnet is crossing the LUMO, the amount of charge transferred to the metal will be spin-polarized. This not only results in a surface dipole formation, but also in a transfer of magnetic moment to the first molecular layer.

Importantly, the spinterface effect may also be extended to the second molecular layer, that may still be regarded as weakly chemisorbed or physisorbed ($\Delta E \lesssim 1$ eV). In the first case a LUMO broadened and spin-splitting will be formed, acting as an effective spin-dependent tunnelling barrier[14]. For the second case the molecular energy levels modification would be rather weak but not negligible. For a Co/Alq₃ interface it has been experimentally demonstrated that the molecules in the second layer acquire a spin-dependent lifetime[20].

It is then straightforward that the modification of the magnetic configuration can be detected in both the inorganic and organic side of the interface. On the side of the ferromagnetic layer, the variation of local electronic structure is responsible for emergent magnetism ranging from

appearance of magnetic signal in a non-magnetic element[2] or for a general change of the magnetic moment and orientation[1], [21]. On the side of the molecular layer, the DOS spin unbalance can be responsible for an induced magnetic moment on the non-magnetic molecule or can determine spin filtering effect in case of transport/tunneling phenomena across it.

The specific configuration between the Molecule and the FM surface is then critical in defining the spinterface behavior. In the following section I will resume the main results including the organic molecules I considered in my thesis, namely Fullerene C₆₀, Gallium Quinoline Gaq₃, Sexithiophene T6.

1.2.1.1 *Tris(8-hydroxyquinolinato)-Gallium (Gaq₃)*

Known also as Gallium-Quinoline, this OSC is a coordination complex molecule, in which three hydroxyquinoline ligands are held together by bonding to a Gallium atom (called coordination atom) (see **Figure 1. 4 (a)**). It is part of the family of Metal-Quinolines, the most popular being Aluminum-Quinoline for its use as active layer in organic light emitting diodes (OLED)[9], [22] and more recently in organic spin valves[7]. The energetics of Gaq₃ on Co (with *fcc*(001) surface) was experimentally and computationally characterized in the work of *Droghetti et al.*[22]. They reported a strong chemisorption of the Gaq₃ molecule (binding energy of 2.4 eV) accompanied by the formation of an interfacial electric dipole (corresponding to a contact potential of 1.5 eV).

Interestingly, as predicted by the model of *Barraud et al.*[12] novel states with band-like features are formed at the Co/Gaq₃ interface, labelled *occupied (unoccupied) Hybrid Interfacial*

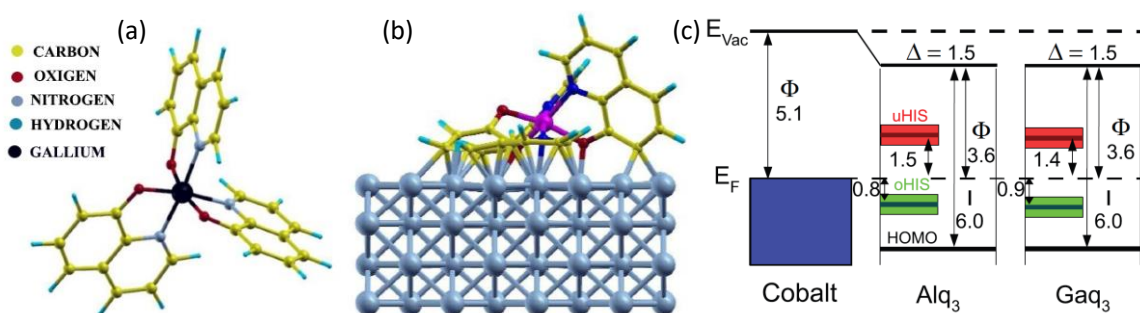


Figure 1. 4 (a) Representation of a Gaq₃ molecule. (b) sketch of the calculated adsorption geometry of the Gaq₃ molecule on *fcc* Co (001) surface. (c) energy levels of the first layer of chemisorbed Gaq₃. A contact potential Δ establishes due to an induced interfacial electric dipole, along with hybrid interface states (HIS). The same is also observed for Alq₃ on Co, showing that the energetics of the Co/Mq₃ system is very weakly dependent on the coordination atom used. Taken from [22].

States (o(u)HIS) (see **Figure 1. 4 (c)**). They are characterized by a different spin-polarization with respect to the one of Co, which is enhanced for the oHIS and reduced for the uHIS. DFT calculation of the adsorption geometry shows that the molecule ligands pointing towards the surface becomes heavily distorted, with the formation of hybrid *p-d* bonds between C, N and O and the surface Co atoms (see **Figure 1. 4 (b)**). Another important result of the study is that the spin-dependent electronic properties of the molecules are independent from the coordination atom (i.e. Al, Ga and In) , since both HOMO and LUMO levels are located over the quinoline ligands[22].

1.2.1.2 Fullerene (C_{60})

Buckminster-Fullerene C_{60} is an allotropic form of Carbon characterized by 60 atoms sp^2 hybridized and arranged as a highly symmetric truncated icosahedron. This OSC gained consideration in organic spintronics after the reported effects on the magnetic anisotropy of ultrathin Co and Fe films (discussed in detail in the next section) and the observation of induced ferromagnetism in Cu/ C_{60} multilayers[2].

The adsorption kinetics of Fullerene on Co was extensively characterized both theoretically and experimentally in a study of *Li et al.*[23]. They demonstrated that, due to the high degree of symmetry of the C_{60} molecule, the binding energies and the spin-dependent electronic features of the Co/ C_{60} interface are strongly dependent on the FM surface symmetry and on the adsorption geometry of the molecule. Nevertheless the FM/molecule interaction is always accompanied by the formation of hybrid p_z -d bonds. As can be seen from **Figure 1. 5** and the reported values in **Table 1. 1**, over surfaces with cubic symmetry, C_{60} preferentially chemisorbs with a pentagon ring pointing towards the Co, while for an hexagonal symmetry it prefers to arrange with a hexagon-pentagon edge (labelled 5:6 bond) pointing towards Co.

Interestingly, with the exception of a *bcc* Co system, there is a very limited amount of charge transfer from Co to C_{60} , ranging from 0 (pentagon geometry on *hcp*(0001) to at most 1 electron per 10 molecules (hexagon geometry on *hcp*(0001)). In contrast, each molecule acquires a negative magnetic moment, small with respect to the one possessed on average by each Co atoms ($\approx 1.7 \mu_B$ for bulk *hcp*). They also report that the C_{60} LUMO levels will be significantly spin-split only for a pentagon geometry over surfaces with cubic symmetry[23].

1.2.1.3 Sexithiophene T6

This molecule is a π -conjugated rigid oligomer composed of six linearly arranged Thiophene units, that are pentagonal rings composed of four C and one S atom. They were the first OSC

successfully used as spacer layer in a hybrid FM/OSC/FM spin valve[6] and it recently showed spinterface properties when deposited over the oxide half-metal Lanthanum Strontium Manganite ($\text{La}_{0.7}\text{Sr}_{0.3}\text{MnO}_3$ - LSMO)[24]. Despite the results a full demonstration of the adsorption mechanism of T6 on Co is still lacking. Nevertheless various theoretical studies performed over (simpler) Thiophene monomers ($\text{C}_4\text{H}_4\text{S}$) deposited on a *hcp* Co(0001) surface were done[25], [26]. As for Gaq_3 high binding energies were obtained ($\Delta E \approx 2.4$ eV)[25],

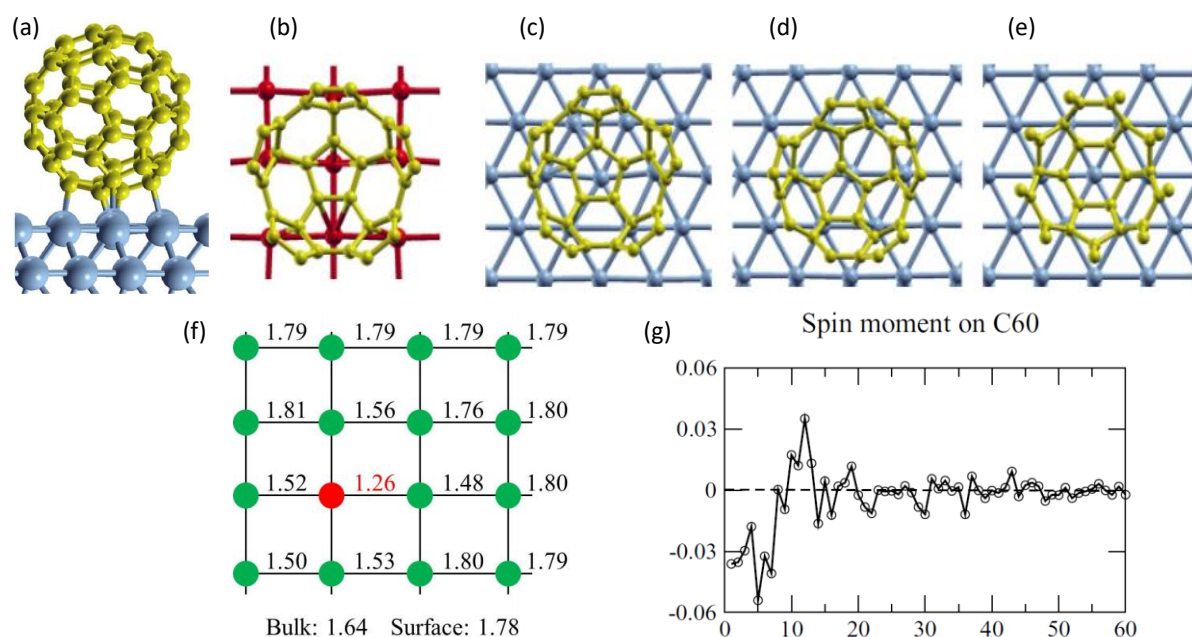


Figure 1. 5 (a) Sketch of a C_{60} molecule bonded over a Co surface, lateral view. (taken from (Bai15). Top view based on the adsorption geometry of C_{60} and Co surface plane: pentagon on *fcc* or *bcc* (001) Co (b); pentagon (c), pentagon-hexagon (labelled 5:6 bond) (d) or hexagon (e) on *hcp* Co (0001) (f). A reduction of the magnetic moment of surface *hcp* Co(0001) atoms is calculated (f) along with an induction of magnetic moment on the C_{60} molecule (g), showed as μ_B per C atom (starting from the ones at the interface with Co). Taken from [23].

Table 1. 1 Binding energy (E_B), charge transfer (in number of electrons) and induced magnetic dipole per C_{60} molecule (in μ_B) for the different adsorption geometries over *bcc*, *fcc* and *hcp* surfaces. Superscripts (b-e) are correlated to the above image index. Values taken from [23].

	Pentagon ^{*(b)}	pentagon ^{** (b)}	pentagon ^(c)	5:6 bond ^(d)	hexagon ^(e)
E_B (eV)	2.90	2.29	0.79	1.35	1.21
Δe	0.30	0.03	0.00	0.02	0.08
μ_B/C_{60}	-0.45	-0.40	-0.31	-0.23	-0.33

*on *bcc* Co(001), ** on *fcc* Co(001)

accompanied by a charge transfer of 0.3 electrons per Thiophene monomer. The bonding mechanism involves the formation of hybrid bonds between the d orbitals of Co and the p_z orbitals of both the C and S atoms of the monomer. As can be seen in **Figure 1. 6 (b)**, this chemisorption makes the orbital-resolved DOS of the molecule spin dependent, resulting in a net spin-polarization[25], [26]. Moreover, the formation of hybrid bonds affects also the local DOS of the Co atoms under the Thiophenes, with the biggest impact on the d_{z^2} , d_{xz} and d_{yz} orbitals[26]. These results imply that the molecule adsorption geometry is with the Thiophene ring parallel to the Co surface. This should be the case also for the more complex T6 oligomer, since when deposited over metallic surfaces such as Cu[27] and Ag[28], [29] it grows with the major axis parallel to the surface.

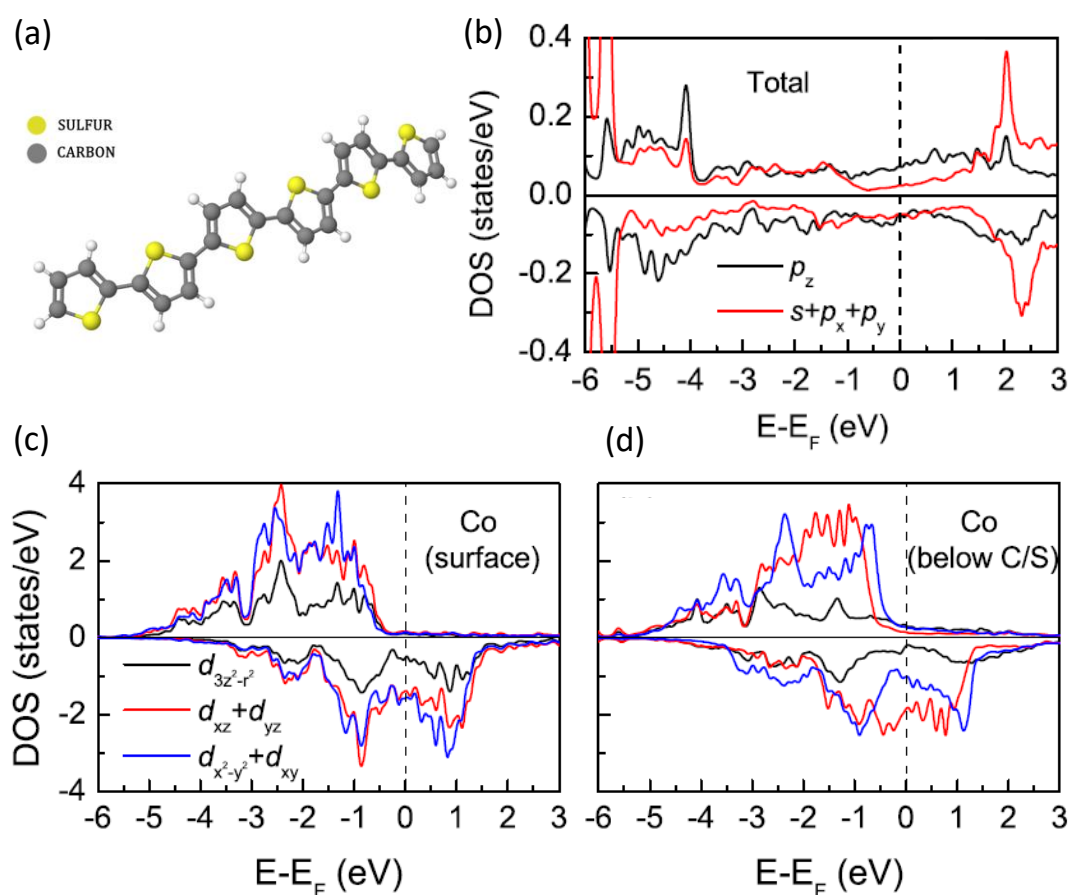


Figure 1. 6 Sketch of the Sexithiophene molecule (a). The spin-dependent DOS resolved for each p orbital (b) of a single Thiophene monomer chemisorbed on Co shows a continuum of states that are spin-dependent. The calculated spin-dependent DOS for each d orbital of a surface Co atom (c) is affected by the interaction with Thiophene (d), with the d_{z^2} , d_{xz} and d_{yz} orbitals being the most affected. (b), (c), (d) taken from [26].

1.2.2 Effect of molecular adsorption on thin film magnetism

The hybridization that emerges from the Newns–Anderson model indicates that for high enough chemisorption energies with respect to the FM bandwidth ($\Delta E \gtrsim W$) the spinterface formation should influence noticeably also the electronic and magnetic properties of the ferromagnet.

The first observation of a molecular-induced modification came in 2013, when a work by *Raman et al.*[30] reported on the magnetotransport properties of organic spin valves with a bottom 8 nm thick *fcc* (111) textured Co electrode interfaced with zinc methyl phenalenyl (ZMP). They showed that the Co electrode possessed two independent switching fields, one occurring at 40 Oe and the other at 600 Oe for $T=4.2$ K (see **Figure 1. 7**). They explained this double switching by considering the electrode as composed of two magnetic layers characterized by two different coercive fields. The smaller one is due to the bulk Co, while the other to an *independent* magnetic layer identified with the Co/ZMP interface. This hypothesis is justified by the argument that the Co interatomic exchange coupling is lowered at the surface, reducing the ratio between the interatomic exchange with Co atoms at the interface and the surface anisotropy constant, J/K_{sur} [30].

This experimental finding stimulated the work of *Callsen et al.*[31] that made a theoretical investigation of the FM/Molecule interface. They considered a molecule of 2,2- paracyclophane (PCP) chemisorbed over a Fe(001) crystalline surface, resulting in the formation of hybrid $d-\pi$ bonds. The hybridization of the Surface Fe d orbitals was shown to deeply modify the exchange

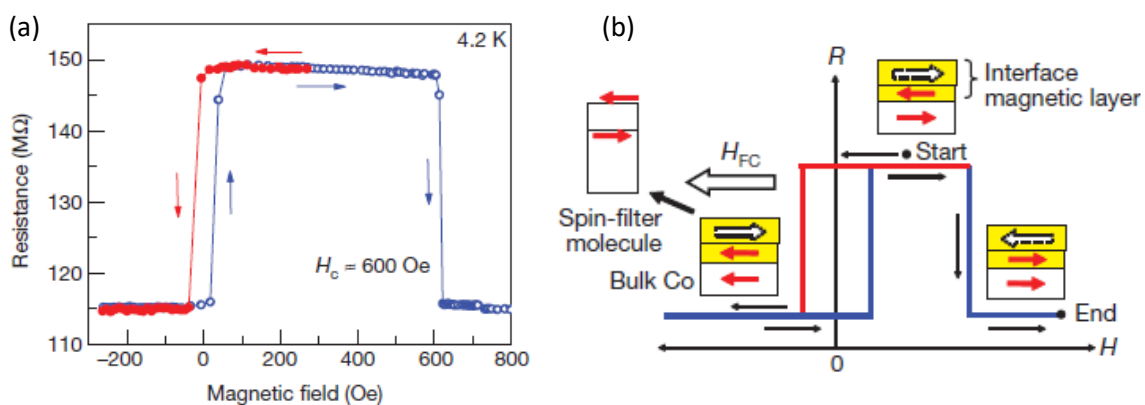


Figure 1. 7 Magnetoresistance of the spin valve Co/ZMP/Py (Permalloy) studied in [30]. (a) and relative scheme (b). The system was cooled down to 4.2 in a large applied field. Following the applied field history it is possible to see how the bottom Co electrode switches independently from the interfacial Co/ZMP layer (H_c 600 Oe). Taken from [30].

coupling *between* the Fe atoms bonded with the π orbitals of the molecule. Also the coupling between these former and the non-bonded nearest neighbors in the FM layer was affected (see **Figure 1. 8 (a), (b)**). This modification suggests that the ensemble of the molecule and the 4 iron atoms with hybridized d orbitals can be treated as a separated magnetic unit, exchange coupled with the rest of the ferromagnetic layer. Moreover, the magnetocrystalline anisotropy energy (MCA) presented by this unit is increased in magnitude (6.41 meV instead of 2.92 meV), but with the same direction of the one of the FM layer. This tuning of exchange and MCA resulted in an enhancement of the coercivity of the FM layer and a slight increase of the average magnetic moment per atom (see **Figure 1. 8(c)**). Similar calculation were performed for other nonmagnetic molecule deposited on a Fe lattice showing similar results[32].

The effects of the hybridization of Co d orbitals on the MCA were exploited by *Bairagi et al.*[1], [33] to explain their experimental observation of an easy direction reorientation from in-plane to out-of-plane for a 5.5 ML thick *hcp* Co ultra-thin film with (0001) surface orientation upon adsorption of just one monolayer of C_{60} (see **Figure 1. 9 (a)**). Moreover the new easy direction has an enhanced coercivity with respect to the one of bare Co. An analogous result

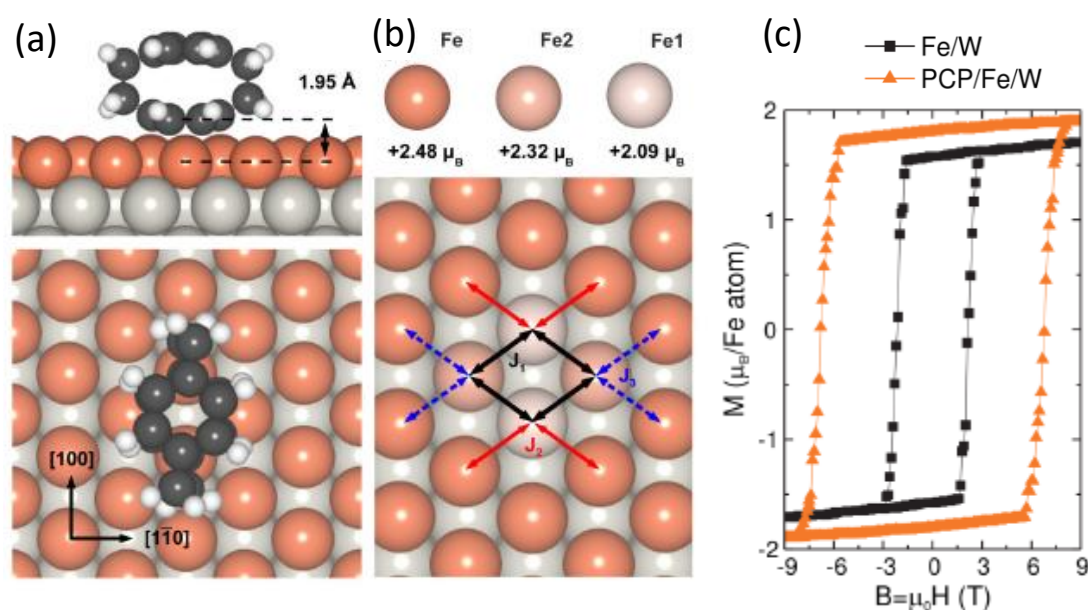


Figure 1. 8 Callsen model: (a) Adsorption of PCP on a Fe(001) crystal surface with formation of hybrid bonds with 4 Fe atoms (labelled Fe1 and Fe2). (b) The hybridization modifies the exchange constants J between each of the hybridized Fe (J_1 , black arrows) and between them and the rest of the Fe atoms of the film (J_2 , blue arrows and J_3 , blue dotted arrows). (c) calculated hysteresis loops for the bare Fe/W system (black squares) and the PCP/Fe/W system (orange triangles). Taken from [31].

was observed also for C₆₀ and Alq₃ on epitaxial Co (0001) or a mixture with *fcc* (111). The rearrangement of the magnetization easy direction is found to be caused by the different contribution to the MCA of the Co *d* orbitals hybridized with the molecules, promoting an out-of-plane easy axis. In particular (see **Figure 1. 9 (c)**) the hybridization strongly suppresses the contribution of the *d*_{z²} orbitals (favoring in-plane direction) while slightly reduces the contribution of *d*_{xy} and *d*_{x²-y²} (favoring out-of-plane direction). The change in MCA at the Co surface is about 1.5 meV. The easy axis reorientation is however very sensitive to various structural parameters as crystalline phase, stress and absorption geometry[34]. Moreover, it has to be pointed out that all the crystallographic direction they have considered are, from a magnetocrystalline point of view, already an easy direction, so the slight modifications are able to win the dipolar anisotropy by choosing a suitable Co thickness. Their calculation of C₆₀ on 2.6 ML Fe(110) surface[33] showed that the molecule increases the in-plane anisotropy. This indicates that the crystalline direction is decisive in how the organic molecule acts on the ferromagnetic layer.

In the same year *Gruber et al.*[35] experimentally observed for the first time exchange bias in hysteresis loops of a Co/MnPc (Manganese-Phtalocyanine) bilayer. This exchange bias is accompanied by the observation of an induced magnetic moment on the Mn ion and a FM coupling between the Co layer and the first molecular layer. For higher thicknesses instead the

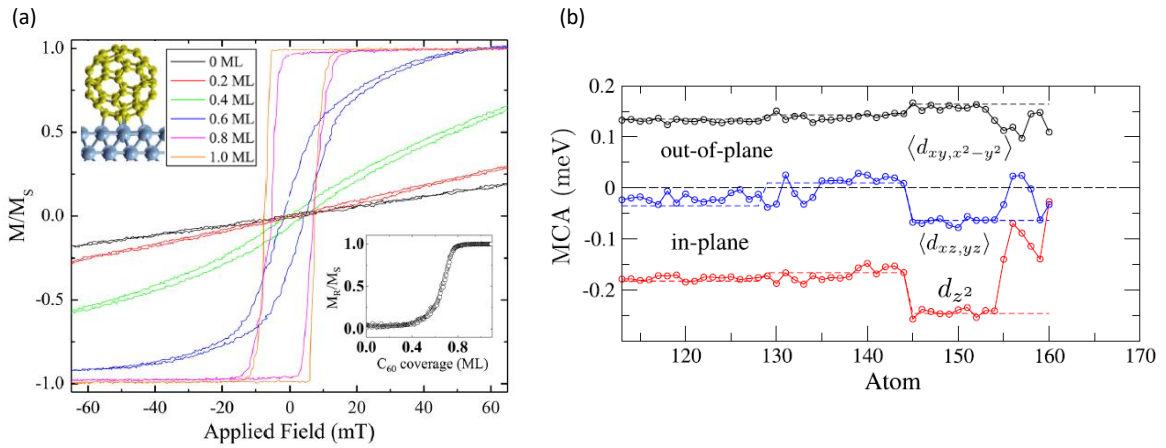


Figure 1. 9 Bairagi model: (a) experimental observation of coverage-dependent easy axis reorientation for the Co/C₆₀ system. calculated contribution to MCA of each Co *d* orbitals, for a 10 ML thick 4x4 Co(0001) slab. (b) Hybridization with C₆₀ highly suppresses the contribution of *d*_{z²} with respect to the unhybridized case (dotted lines) while slightly suppresses the contribution of *d*_{xy} and *d*_{x²-y²}, resulting in OOP direction being more favored. Adapted from [1].

coupling between each molecular layer is AFM, induced by superexchange between the stacked Mn-Pc. A subsequent investigation of *Boukari et al.*[36] on different Metallo-Phtalocyanines (M-Pc) on Co suggests that, at least for this class of molecules, the hardening effect and the onset of exchange bias can be regarded as two distinct and additive effect (see **Figure 1. 10**). The first one is originating by a modification of the Co magnetic anisotropy, while the second was due to exchange coupling between the FM Co layer and the AFM molecular layer, with the interfacial layer of M-Pc ferromagnetically aligned with the Co spins. The Phtalocyanines are thus acting as an effective AFM layer similarly to the case of inorganic FM/AFM bilayers[37].

The onset of a magnetic order in the molecular layer was reported also by *Moorsom et al.*[21] on a 5 nm thick Co layers covered with C₆₀ of various thicknesses. They reported the induction of a magnetic moment in the first layer of C₆₀ that is antiparallel to the one of C. Subsequent molecular layers also possessed an induced magnetic moment that is aligned parallel to Co. This finding is explained by charge transfer of spin-polarized electron migrating from the ferromagnet to the C₆₀ layer. Moreover an increase in coercivity with respect to the decoupled Co/C₆₀ was observed, that grows with a growing thickness of the molecular layer. The group proposed an interesting mechanism explaining both the hardening in temperature and the exchange bias onset in the same system[38]. In their model, hybridization between the Co surface orbitals and the π orbitals of C₆₀ takes place and affects the Co magnetic anisotropy[23]. The observed enhancement of coercivity at low temperatures is reconducted however to an induced magnetoelectric coupling between the Co spins and the induced electric dipole on the Fullerene after adsorption on the ferromagnetic surface. This dipole is dependent on both the surface symmetry of the Cobalt and the deposition geometry of the molecule. For C₆₀ the most

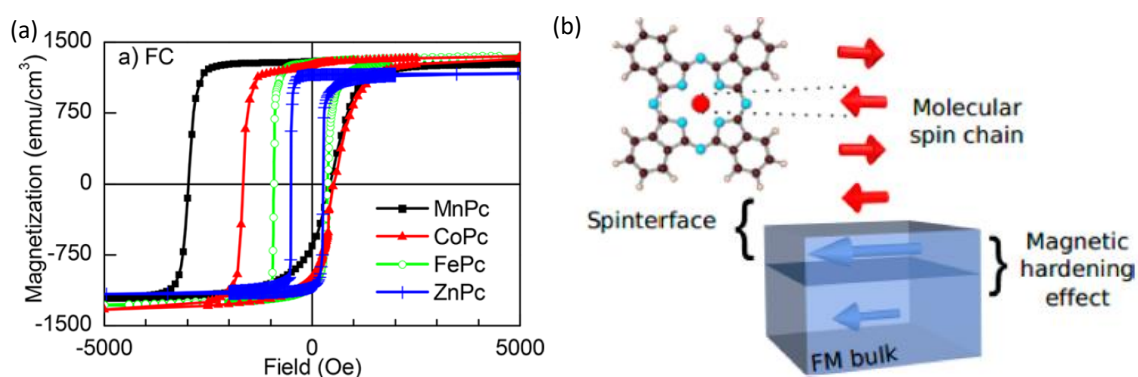


Figure 1. 10 *Boukari et al.*:(a) Hysteresis loops of Co/M-PC at 4.2 K after field cooling in a field of +2T. (b) scheme of the separation of magnetic hardening effect (due to the spinterface) and molecular spin chains inducing the exchange bias. Taken from [36].

favored, at least on *hcp* Co (0001) or *fcc* Co(111) is with a hexagon-pentagon edge pointing to one Co surface atom[21], [33], leading to -6.5 eV adsorption energy (see also **Figure 1. 11(a),(b)**). For such molecule configuration a nonzero unbalance of the spins of the Co atoms bonded to C_{60} results in a magnetoelectric coupling between the two entities. A rotation of the spins due to an external field can induce a torque on the molecule. If the energy barrier for the rotation can be overcome by the rotating Co spins, a change in adsorption configuration takes place. This makes the magnetoelectric coupling null (see **Figure 1. 11 (c)**). If, however, the energy barrier is increased by decreasing the temperature, the magnetoelectric coupling acts as an additional pinning to the spin movements, effectively increasing the FM anisotropy [38]. A maximum ideal value of 0.23 eV was estimated, much less than the energies involved in hybridization.

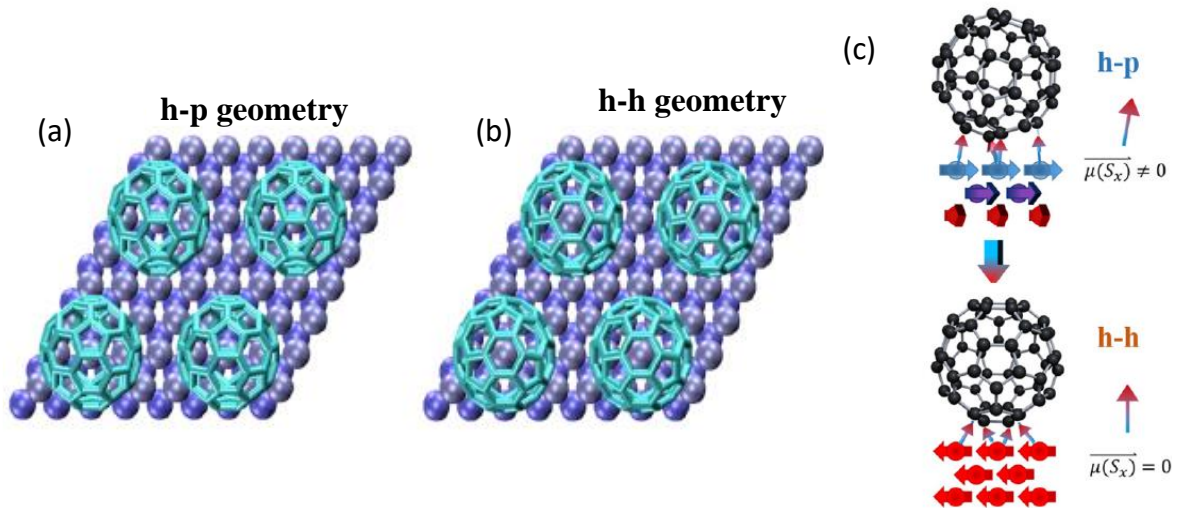


Figure 1. 11 (a),(b) representation of the two adsorption geometry considered in [38], the first with an hexagon-pentagon edge on Co, the second with a hexagon face. (c) sketch of the different Co spin configuration for the two situations, showing a non-zero in-plane component of the Co spin for h-p resulting in a magnetoelectric coupling. The symmetry of the other configuration results instead in a null in-plane component giving a zero coupling. (a),(b) taken from [21], (c) taken from [38].

1.3 Exploiting the spinterface for voltage control of magnetism

Electrical tuning of magnetism is of great fundamental and technical importance for fast, compact and ultra-low power electronic devices. Although it was previously thought that it was difficult to realize a large enough electric field effect in metals due to the short screening

length[39], the manipulation of magnetism by use of such method was demonstrated. The first observation of such effects at RT was done by *Weisheit et al.* in 2007[40] over a FePt/LEL/Pt (LEL: Liquid Electrolyte) multilayer. The LEL was used as dielectric layer. They reported a 5% variation of coercivity of a 2 nm thick epitaxial FePd layer upon application of a -1 V voltage (see **Figure 1. 12**). Subsequent studies in ultrathin Fe/MgO and CoFeB/MgO based multilayers showed (see **Figure 1.13**) a modulation of the FM magnetic anisotropy induced by the onset of an electric-field at the FM/Oxide interface[41], [42]. This effect was attributed to modification of the surface anisotropy term related to the FM/MgO interface. The hybrid bonds between the O $2p$ and Fe $3d$ alters the interfacial electronic structure of a bare Fe ultrathin film

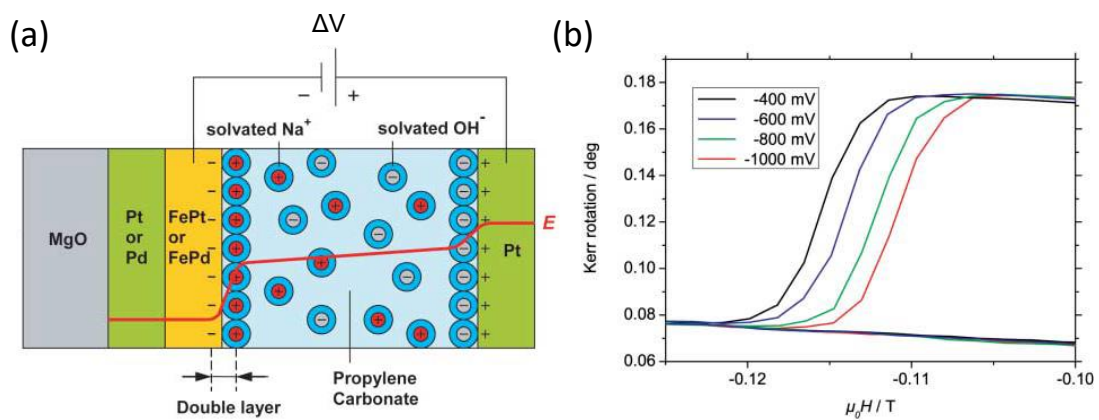


Figure 1. 12 Sketch of the device developed in [40]. (a). An increase of the coercivity is observed when applying a difference of potential to the electrodes (b). Taken from [40].

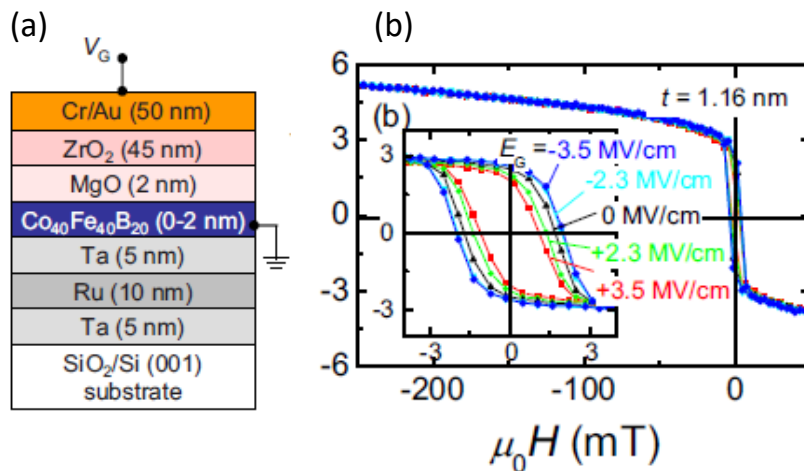


Figure 1. 13 (a) The multilayer structure characterized in [42]. The ultrathin layer of CoFeB is grounded and a gating voltage V_g is applied through the Cr/Au top contact, inducing an electric field at the CoFeB/MgO interface (a). This results (b) in a slight variation of the coercivity (measured by anomalous Hall effect) for a thickness of 1.16 nm at RT. Taken from [42].

and ultimately the surface anisotropy term through the Spin-Orbit Coupling (see Chapter 2). If an electric field is applied then the position of the Fermi level at the interface is moved, modifying also the occupation of hybrid $p-d$ bands and, in turn, their contribution to the surface MCA[43]. Other surprising voltage induced effects have been demonstrated, such as modification of the Curie temperature of a single layer Co ultrathin film[44] and magnetization switching (i.e. magnetization reversal) of a 1.3 nm thick CoFeB layer in CoFeB/MgO/CoFeB trilayers[45].

The possibility to actively tune the FM magnetic anisotropy is well-matching the interface-induced effects observed for thin Co/Molecule system. This led to the idea of creating prototypical devices akin to Field Effect Transistors (see **Figure 1. 14 (a)**). Assuming a bottom-up geometry, the FM/Molecule system is gated by a metallic electrode deposited on top of a high- k dielectric layer. Then, assuming the coercivity is dependent on the hybridization at the interface (in terms of the spin-dependent binding energy), the application of a gating voltage will induce a charge transfer/depletion at the FM/Molecule interface, resulting in measurable changes in coercivity (see **Figure 1. 14 (b)**). Some important conditions must be met, however. Firstly, the FM layer needs to be thin enough for maximizing the role of the interface with respect to the bulk. Secondly, both the OSC and the high- k dielectric layers should be thin enough for maximizing the electric field at the FM/molecule interface. Related to this is the choice of high- k dielectric materials for increasing the gating effect. Finally, the molecules should meet the criteria of hybrid bonds formation and high enough binding energies to the FM surface. From this point of view C_{60} , Gaq₃ and T6 are promising candidates given the already reported spinterface properties, as discussed in Section 1.2.

The potential of this conceptual new device can be evidenced by some quantitative estimations. The case of C_{60} on a *hcp* Co is discussed. Indeed, to completely modify the interfacial effects about 1 eV per molecule are needed (approximately the binding energy). Considering a desirable active area of at most 10^4 nm², the requirement translates to an input energy of approximately 1 fJ.

The fabrication of this new class of spintronic devices was intended to be the core part of this thesis project. However, the COVID 19 pandemic along with the emergency procedures adopted severely hampered the research activities oriented towards this goal. While no significant achievements were obtained in this direction, the overall characterization of the Co/Molecule bilayers demonstrated that they possess interesting and peculiar behaviors. The results obtained are of relevant importance for gaining a deeper understanding of the still not

fully understood mechanisms responsible for the modification of the FM magnetic properties, and they pose new question about the nature of the FM/molecule interaction.

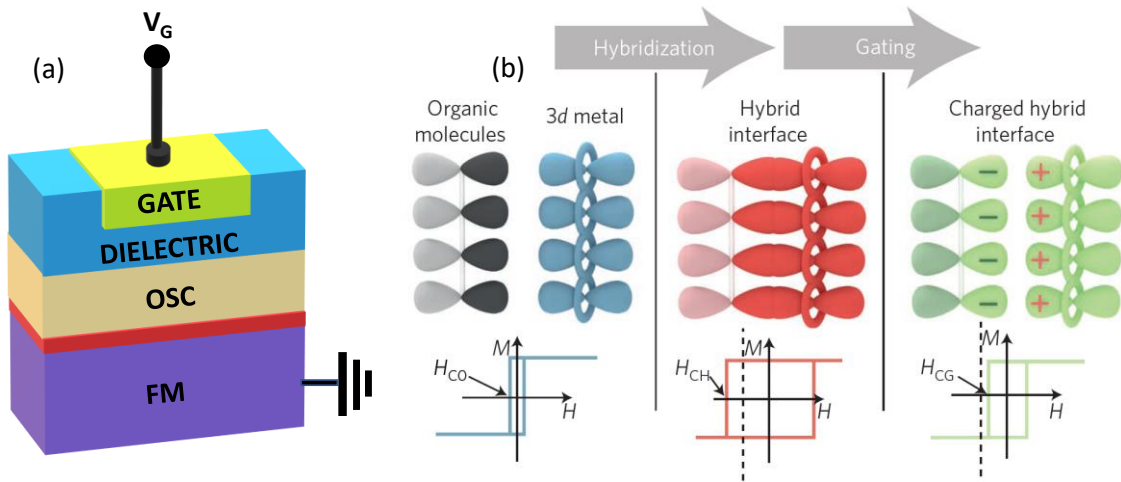


Figure 1. 14 (a) Sketch of the proposed device for voltage control of magnetism of a thin FM layer (dark blue)interfaced with a thin layer of OSC (ochre). A top gate electrode (yellow) deposited over an high-k dielectric (light blue) supplies a gating voltage that will induce a charge accumulation at the FM/Molecule interface (red). (b) The coercivity of the uncoupled FM layer (left) gets passively modified by the spinterface formation (middle). Charge accumulation/depletion at the interface will tune the value of H_C (right). (b) taken from[14].

Chapter 2

Magnetism in thin films

This Chapter is dedicated to a more detailed description of the concepts related to ferromagnetic properties introduced in the previous sections. This is felt as necessary for a better understanding of the roles of the molecular layer in modifying the magnetism of thin films. After describing how magnetic order may arise in a many-body system, all the other energy terms responsible for the hysteretic response of ferromagnets (i.e., anisotropy) will be described. Lastly a brief description of the concepts of superparamagnetism and antiferromagnetism is done.

2.1 Origin of magnetic order

Magnetic order in many body systems is a purely quantum mechanical effect. It stems from electronic correlation of the valence electrons of all the atoms bonded together to form the system. Considering a system of N electrons bound to M ions, one can calculate the energy level of the system using variational principles. Considering a static array of ions and a total electronic normalized wave function Ψ , there are three contributions to the energy of the system[46]:

$$\langle \Psi | H | \Psi \rangle = \langle H \rangle_{kin} + \langle H \rangle_{e-ion} + \langle H \rangle_{e-e} \quad (2.1)$$

here $\langle \mathcal{H} \rangle_{kin}$ is the electrons total kinetic energy, $\langle \mathcal{H} \rangle_{e-ion}$ represents the attractive interaction between the electrons and the (fixed) ions. $\langle \mathcal{H} \rangle_{e-e}$ takes into account the repulsive interaction between the electrons. The total electron wavefunction $|\Psi\rangle$ can be chosen as a Slater determinant of single-electron wave functions $|\varphi\rangle$ [46],[47] expressed in the coordinate representation

$$\Psi = (N!)^{-\frac{1}{2}} \det(\varphi_k) = (N!)^{-\frac{1}{2}} \begin{vmatrix} \varphi_1(\boldsymbol{\rho}_1) & \varphi_2(\boldsymbol{\rho}_1) & \dots & \varphi_N(\boldsymbol{\rho}_1) \\ \varphi_1(\boldsymbol{\rho}_2) & \varphi_2(\boldsymbol{\rho}_2) & & \vdots \\ \vdots & & \ddots & \vdots \\ \varphi_1(\boldsymbol{\rho}_N) & \dots & \dots & \varphi_N(\boldsymbol{\rho}_N) \end{vmatrix} \quad (2.2)$$

$\varphi_i(\boldsymbol{\rho}_j)$ is the wave function of the i -th electron when it is in the generalized coordinates $\boldsymbol{\rho}_j$, that are the position \mathbf{r}_j and the spin's z -component σ_j . One can assume the ansatz for each φ_i :

$$\varphi_i(\boldsymbol{\rho}_j) = \phi_i(\mathbf{r}_j) \eta_i(\sigma_j) \quad (2.3)$$

Here, ϕ_i is the spatial part of the wave function, and η_i is its spin part. To simplify calculation it is assumed that φ_k are orthonormal, so

$$\sum_{\sigma_k} \int d\mathbf{r}_k \phi_i^*(\mathbf{r}_k) \eta_i^*(\sigma_k) \phi_i(\mathbf{r}_k) \eta_i(\sigma_k) = \int d\boldsymbol{\rho}_k \varphi_i(\boldsymbol{\rho}_k) \varphi_j(\boldsymbol{\rho}_k) = \delta_{i,j} \quad (2.4)$$

In the second step the integral term also implies summation over the spin coordinates. One last assumption is considered: for each atom only the valence electrons are interacting with the ones of other atoms. Now, the electron-electron term of the Hamiltonian is a coulomb potential,

$$\hat{H}_{e-e} = \frac{1}{2} \sum_{i,j=1}^N H_{i,j} = \sum_{i,j=1}^N \frac{e^2}{|\mathbf{r}_i - \mathbf{r}_j|} \quad (2.5)$$

$\langle \mathcal{H} \rangle_{e-e}$ reads as

$$\langle H \rangle_{e-e} = \frac{1}{2} \sum_{i,j=1}^N \langle \Psi | H_{i,j} | \Psi \rangle = \frac{1}{2} \sum_{i,j=1}^N E_{ij} \quad (2.6)$$

where

$$E_{ij} = \frac{1}{N!} \int \det(\varphi_k^*) \frac{e^2}{|\mathbf{r}_i - \mathbf{r}_j|} \det(\varphi_{k'}) \prod_{l=1}^N d\boldsymbol{\rho}_l \quad (2.7)$$

It has to be noted that every integral involves *two* coordinates. The orthogonality requirement then implies that for each component of $\det(\varphi_k^*)$ only two of $\det(\varphi_{k'})$ will not give zero when integrated[46]. After some tedious calculation the following result is obtained:

$$\frac{1}{2} \sum_{i,j=1}^N E_{ij} = \frac{1}{2} \sum_{k,k'=1}^N \int d\boldsymbol{\rho}_i d\boldsymbol{\rho}_j |\varphi_k(\boldsymbol{\rho}_i)|^2 \frac{e^2}{|\mathbf{r}_i - \mathbf{r}_j|} |\varphi_{k'}(\boldsymbol{\rho}_j)|^2 + \quad (2.8)$$

$$-\frac{1}{2} \sum_{k,k'=1}^N \int d\rho_i d\rho_j \varphi_{k'}^*(\rho_i) \varphi_{k'}(\rho_j) \frac{e^2}{|\mathbf{r}_i - \mathbf{r}_j|} \varphi_k^*(\rho_i) \varphi_k(\rho_j)$$

The first summation of the Right-Hand Side (RHS) can be understood as the quantum mechanical equivalent of the “classical” coulomb electron-electron interaction. The second term does not have any classical analogy but can be understood as a quantification of the correlation between each pair of electrons. It is called the *exchange interaction*. Additionally, the first part is independent on the orientation of the electrons spin[46], while it is not the case for the exchange term. Expanding the term

$$\begin{aligned} \langle E \rangle_{\text{exc}} = & -\frac{1}{2} \sum_{k,k'=1}^N \sum_{\sigma_i, \sigma_j} \eta_{k'}^*(\sigma_j) \eta_{k'}(\sigma_i) \eta_k^*(\sigma_j) \eta_k(\sigma_i) \\ & \times \int d\mathbf{r}_i d\mathbf{r}_j \phi_{k'}^*(\mathbf{r}_i) \phi_{k'}(\mathbf{r}_j) \frac{e^2}{|\mathbf{r}_i - \mathbf{r}_j|} \phi_k^*(\mathbf{r}_i) \phi_k(\mathbf{r}_j) \end{aligned} \quad (2.9)$$

Due to the orthonormality of the spin eigenfunction, for a certain couple of states k k' the expectation value is zero except when σ_i and σ_j are parallel to each other. This energy term can be then understood as the difference in energy between a parallel and an antiparallel configuration of the spins. This energy term can be rewritten as[46], [48], [49]

$$\langle H_{\text{heis}} \rangle = - \sum_{i,j=1}^M J_{i,j} \mathbf{S}_i \cdot \mathbf{S}_j \quad (2.10)$$

where the summation has to be performed over all lattice sites. $\mathbf{S}_i, \mathbf{S}_j$ represent in this formula the *total* spin of the electrons bound to the atom, or ion, at i -th and j -th sites[46]. $J_{i,j}$ is the exchange integral between their total wavefunctions:

$$J_{i,j} = 2 \int d\mathbf{r}_1 d\mathbf{r}_2 \phi_i^*(\mathbf{r}_1) \phi_i(\mathbf{r}_2) \frac{e^2}{|\mathbf{r}_1 - \mathbf{r}_2|} \phi_j^*(\mathbf{r}_2) \phi_j(\mathbf{r}_1) \quad (2.11)$$

This integral depends on the overlap between two eigenfunctions for two different ionic position. If the electrons for the material tend to be localized around their atom, it is justified to extend the summation of (2.9) only to its nearest neighbors.

2.2 Band ferromagnetism

This model considers a gas of delocalized free electrons interacting with the background ions[46], [48]. In such a crystal the electronic bands are formed each of which can be divided

into spin up and spin down bands equally populated. To make the argument easily understandable the bands are considered as parabolic. If at the Fermi energy all the spin down electrons with energies between E_F and $E_F - \delta E$ are flipped to spin-up electrons they will be found in the other band in an energy interval between E_F and $E_F + \delta E$. If $g(E)$ is the electronic density of state (not spin-resolved) a total number of electrons $g(E_F)\delta E/2$ has been displaced, corresponding to an energy increase of [48]

$$\Delta E_E = \frac{1}{2} g(E_F) (\delta E)^2 \quad (2.12)$$

which seems unfavorable. However, now the number of spin-up electrons is

$$n_\uparrow = \frac{1}{2} (n + g(E_F)\delta E_F) \quad (2.13)$$

where $n/2$ is the number of electrons at Fermi energy for the unperturbed case. Conversely for the down electrons

$$n_\downarrow = \frac{1}{2} (n - g(E_F)\delta E_F) \quad (2.14)$$

This creates a net magnetization M

$$M = (n_\uparrow - n_\downarrow) \mu_B \quad (2.15)$$

since each electrons carries a magnetic moment of $1 \mu_B$. Adopting a molecular field approach developed by Weiss[46], [48], [50] it is possible to think that the exchange interaction causes each i -th spin to feel the same fictitious field

$$H_{MF} = \frac{1}{\mu_0 \mu_B} \sum_j J_{ij} S_j = \lambda M \quad (2.16)$$

where λ is a constant specifying the strength of the molecular field with respect to the systems magnetization. The total energy saved by the interaction of the magnetization with the molecular field is

$$\Delta E_{MF} = -\frac{1}{2} \mu_0 \lambda M^2 = -\frac{1}{2} \mu_0 \mu_B^2 \lambda (n_\uparrow - n_\downarrow)^2 \quad (2.17)$$

Since this effect is ultimately due to electrostatic interaction, this energy is rewritten as to explicitly insert a measure of the Coulomb energy [48], [51]

$$U = \mu_0 \mu_B^2 \lambda \quad (2.18)$$

so that

$$\Delta E_{MF} = -\frac{1}{2} U (g(E_F) \delta E)^2 \quad (2.19)$$

The condition to have ferromagnetism depends on whether the energy cost for promoting electrons from the spin down to the spin up band is less than the energy stored with the interaction with the molecular field

$$\Delta = \Delta E_K + \Delta E_{MF} = \frac{1}{2} g(E_F) \delta E^2 (1 - U g(E_F)) < 0 \quad (2.20)$$

this is known as the Stoner criterion which is expressed as follows

$$U g(E_F) \geq 1 \quad (2.21)$$

The value Δ , known as spin-splitting, then determines the amount of separation in energy between the two bands. This oversimplified model is useful to explain how exchange interaction can induce a splitting of the electronic bands. A more serious treatment (see [51] for a survey) shows that when exchange is taken into account for band calculation of $3d$ metals, some of the minority d and some of the s spin down electrons may be moved to higher energy spin-up states, guaranteeing a net saving of energy. This explains why experimentally all the $3d$ ferromagnets have a non-integer number of Bohr magnetons per atom.

It should be noted however that even today there is no clear consensus on what model best explains the overall magnetism of $3d$ transition elements, since each of them can explain some effect that the other can't [46]. Moreover the two theories seem to be complementary to some extent [51], [52], so ferromagnetism in $3d$ transition metals is regarded as partially due to localized d orbitals and partially due to an itinerant picture in which the more delocalized s electrons can mediate the interaction between d orbitals at different sites, as suggested by the observed distribution of magnetization in the unit cell of *fcc* iron [53].

2.3 Magnetic anisotropy

Both the localized and itinerant theory of ferromagnetism are focused on the energy gain those ferromagnetic materials acquire by having at least a non-negligible number of valence electrons spin aligned parallel to each other. Taking Eq. (2.10) it is clear that the exchange term is only dependent on the *mutual* orientation of the spins one to the other and nothing is said about any

particular preferential direction for this alignment. Were this the only energy term contributing to ferromagnetic phenomena, no such thing as hysteresis would appear. Taking a ferromagnetic particle of magnetic moment $\boldsymbol{\mu}$ inside an external applied field \mathbf{H} and φ the angle between the two vectors, the interaction energy is the Zeeman term $-\mu H \cos(\varphi)$. Then for an ensemble of particles it can be demonstrated[46] that the expectation value of the component of the normalized magnetization vector along a direction parallel to \mathbf{H} is

$$\langle \cos(\theta) \rangle = \frac{M_H}{M} = L\left(\frac{\mu H}{k_B T}\right) = 0 \text{ for } H = 0 \quad (2.22)$$

which is the Langevin function used to describe the magnetic response of paramagnets in the presence of an external field. Thus exchange alone cannot account for the empirical evidence of a stable magnetization possessed by magnetized magnets. This result instead stems out from the anisotropic character of all ferromagnetic materials, since other energy terms have to be taken into account. These are usually considerable as perturbations with respect to exchange energy but their dependence on some particular direction of the system results in a stable magnetization direction. In the next subsections I will describe the most important terms contributing to the magnetic anisotropy of a FM system, especially for the case of a thin film.

2.3.1 Shape anisotropy

It is perhaps the most intuitive form of anisotropy and is possessed by every ferromagnetic system. It originates entirely by the finiteness of any physical system. Taking the second Maxwell equation

$$\nabla \cdot \mathbf{B} = \mu_0 \nabla \cdot (\mathbf{H} + \mathbf{M}) = 0 \quad (2.23)$$

that is, the requirement of zero divergence of the magnetic field induction \mathbf{B} automatically translates to the requirement that, in presence of magnetization, a second field \mathbf{H} is generated the divergence of which is equal but opposite in sign to that of \mathbf{M}

$$\nabla \cdot \mathbf{M} = -\nabla \cdot \mathbf{H} \quad (2.24)$$

This field is called *demagnetizing field* (if inside the material) or *stray field* (if outside the material) and originates by the uncompensated “magnetic charges” that are generated at the boundary of the system when a non-zero mean value of \mathbf{M} is present. For a general shape it is shown[46], [48], [54] that this field can be written as

$$\mathbf{H} = -\hat{\mathbf{N}}\mathbf{M} \quad (2.25)$$

Where $\hat{\mathbf{N}}$ is a rank-2 tensor with unitary trace called *the demagnetizing tensor*. Only for particular shapes it can be diagonalized along the three cartesian axes. For the particular case of a sphere

$$N_{xx} = N_{yy} = N_{zz} = \frac{1}{3} \quad (2.26)$$

so for this particular shape no anisotropy is expected. For the case of a *prolate ellipsoid* (see **Figure 2. 1**) $N_{xx} = N_{yy} < N_{zz}$, for an *oblate ellipsoid* $N_{xx} = N_{yy} > N_{zz}$. In particular this latter case is used for the calculation of the shape anisotropy of thin and ultra-thin films by considering them as the limit case of the two major axis a (see **Figure 2. 1**) going to infinity and the minor axis c going to 0. In that case

$$N_{xx} = N_{yy} \rightarrow 0 \text{ and } N_{zz} \rightarrow 1 \quad (2.27)$$

These tensor components are useful to calculate the demagnetizing energy of the system, that can be written as

$$E_{MS} = -\frac{\mu_0}{2} \int_{\Omega} \mathbf{M}(\mathbf{r}) \cdot \mathbf{H}(\mathbf{r}) d\mathbf{r} \quad (2.28)$$

where Ω is the system volume. By using the usual approximation of a constant magnetization inside the ferromagnetic bodies this energy becomes

$$E_{MS} = \frac{\mu_0}{2} \mathbf{M} \cdot \hat{\mathbf{N}} \cdot \mathbf{M} \quad (2.29)$$

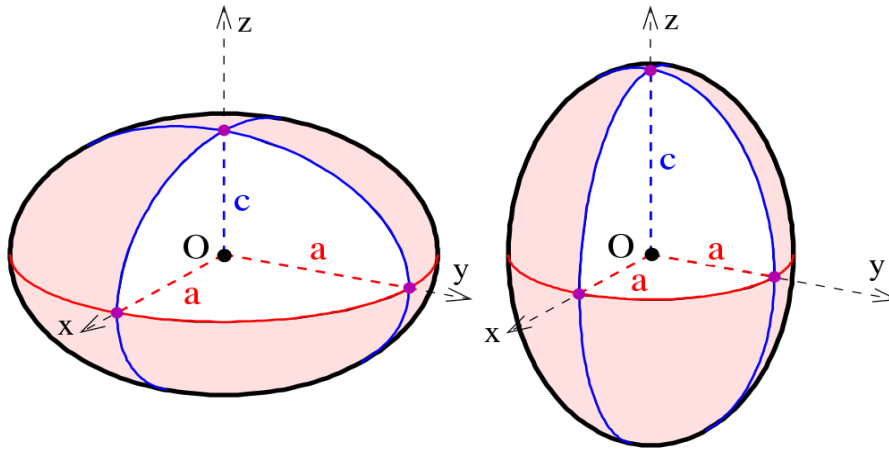


Figure 2. 1 Left: oblate ellipsoid. Right: prolate ellipsoid. Taken from [55].

For the case of interest of a thin film only the N_{zz} term is different from 0 so

$$E_{MS} = -\frac{\mu_0}{2} VM_z^2 = \frac{\mu_0}{2} VM^2 \cos^2(\theta) \quad (2.30)$$

where θ is the angle between \mathbf{M} and the film's normal. This kind of anisotropy is an example of *uniaxiality* since only one critical direction is involved. [55]

2.3.2 Magnetocrystalline anisotropy

This energy term arises from the spin-orbit coupling (SOC), a relativistic effect that couples the electrons spin with the magnetic field it creates while orbiting around the ions of the periodic lattice[56]. SOC can be written as

$$H_{SOC} = -\frac{e\hbar^2}{2m_e^2 c^2 r} \frac{\partial V}{\partial r} \mathbf{S} \cdot \mathbf{L} \quad (2.31)$$

where V is the spherically symmetric ionic potential and \mathbf{S}, \mathbf{L} are the spin and angular momentum vectors. This is typically treated phenomenologically[50], [56] as

$$H_{SOC} = \xi \mathbf{S} \cdot \mathbf{L} \quad (2.32)$$

where ξ is the spin-orbit coupling strength. For the case of a *3d* transition metal, the crystal field generated by the periodically arranged neighboring atoms breaks the spherical symmetry. Its energy of around 1 eV is large compared to the one of SOC (approximately 0.1 eV for Co[56]) and makes the orbital part of the wavefunction no more an eigenfunction of V . Rather this latter has to be taken as a linear combination of orbital wavefunctions that in turn produces an orbital quantum number $m_l \neq 0$ [48], [56]. The spin-orbit coupling however is able to lift partially this quenching making the gyromagnetic factor g of the *d* electrons ≈ 2.2 [56].

The SOC can be thought[56] as equivalent to an effective magnetic field that acts only on the orbital magnetic moment of the electrons

$$H_{SOC} = -\mu_B \mathbf{L} \cdot \mathbf{H}_{orb} = m_l \cdot \frac{\xi \mathbf{M}}{2\mu_B |\mathbf{M}|} \quad (2.33)$$

To lowest order in \mathbf{H}_{orb} this effect can be described by an orbital susceptibility $\hat{\chi}_{orb}$ that is a rank 2 tensor, so in this approximation the spin-orbit energy can be written as

$$E_{\text{soc}} = -\frac{1}{2} \mathbf{H}_{\text{orb}} \cdot \hat{\chi} \cdot \mathbf{H}_{\text{orb}} \quad (2.34)$$

This formula can be explicitly formulated for two cases of interest, relative to the most common arrangement of crystalline Co. For crystals in the *hexagonal close packed (hcp)* phase, the symmetry axis lies along the z direction and the energy term is given by (orb subscript is omitted)

$$E_{\text{soc}}(\text{hcp}) = -\frac{1}{2} \left(\frac{\xi}{2\mu_B} \right)^2 [\chi^{zz} + (\chi^{xx} - \chi^{zz}) \sin^2(\theta)] \quad (2.35)$$

again with θ the angular direction from the z axis. For crystals in the more symmetric *face centered cubic (fcc)* phase, the diagonal components are equal so no anisotropy is present at first order \mathbf{H}_{orb} . A nonlinear orbital susceptibility has to be considered and thus (orb subscript is omitted for χ and H)

$$E_{\text{soc}}(\text{fcc}) = -\frac{1}{2} \sum_{i,j} \chi_{i,j}^{0(2)} H_i H_j + \sum_{i,j,k,l} \chi_{i,j,k,l}^{0(4)} H_i H_j H_k H_l \quad (2.36)$$

Experimentally, it is customary to treat the Magnetocrystalline Anisotropy (MCA) phenomenologically, by doing a power series expansion of the direction cosines of the magnetization with respect to the crystallographic axis multiplied by constants K that are in general temperature dependent. Moreover, not directly the energy is considered but rather the *energy density* \mathcal{E} . For the *hcp* case only the c direction (parallel to the cartesian z direction) is important, so a uniaxial anisotropy is obtained

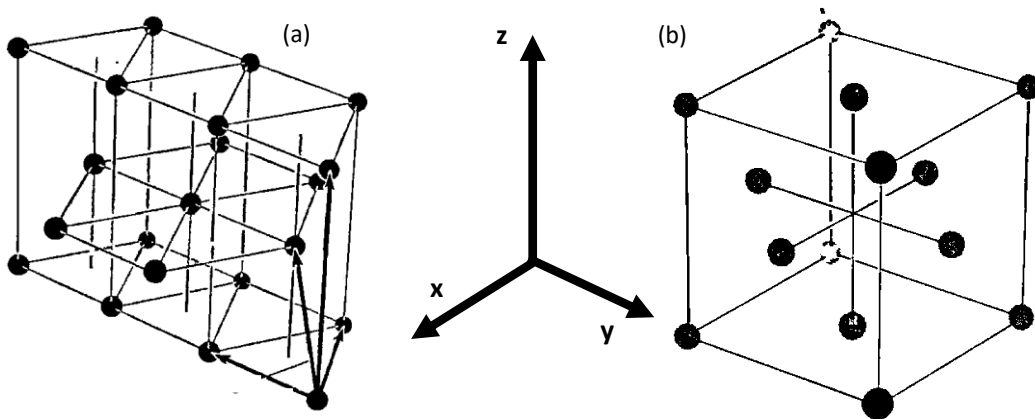


Figure 2. 2 Example of (a) *hcp* arrangement and (b) *fcc* arrangement. Taken from [47].

$$\frac{\varepsilon}{V} = \varepsilon_{MCA} = -K_1 \cos^2(\theta) + K_2 \cos^4(\theta) \approx -K_1 \cos^2(\theta) \quad (2.37)$$

here the convention adopted is that if K_1 is positive then the c-axis is an *easy direction* and the plane perpendicular to it an *hard plane*. For Co in *hcp* phase $K_1 \approx +4.5 \times 10^5 \frac{J}{m^3}$ [57]

For the *fcc* case, assuming a frame of reference oriented along the edges of the cube

$$\varepsilon_{MCA} = K_1 (m_x^2 m_y^2 + m_x^2 m_z^2 + m_y^2 m_z^2) + K_2 (m_x^2 m_y^2 m_z^2) \quad (2.38)$$

where the m_i are the components of the magnetization versor along the (100), (010) and (001) directions. For Co in *fcc* phase the value of K_1 is $6.8 \times 10^4 \text{ J/m}^3$, almost one order of magnitude lower than the *hcp* case.[47]

2.3.3 Surface and strain anisotropy

The MCA obtained for a given crystal symmetry can be distorted in magnitude and direction if some modification is induced to the crystal lattice. Two important cases will be briefly depicted, both discussed for the first time by Néel[58] that recognized the effect of a loss of crystal symmetries on the MCA for a ferromagnetic crystal. At the boundaries of the material (surfaces and edges), the outermost atoms have missing nearest neighbors, so the local symmetry is lowered. This results in a local modification of the MCA that is typically encoded in an energy (density) term K_S . It tells whether *locally* the magnetic moments prefer to be aligned along the crystalline direction normal to the film plane or not[46]. This term is sensitive to the surface plane[58] so in a theoretical point of view no general trend can be given unless a detailed calculation is performed. Moreover this term becomes important for very thin films where K_S may compensate the large demagnetizing energy that tends to keep the spins locked in plane.

The other mechanism that can induce a modification of the MCA is a mechanical deformation of the crystal lattice, that is stress or strain. In general, these deformations will modify the lattice parameters of the crystal structure effectively inducing extra terms that can even be forbidden for the unstrained case. For small deformations it is possible to do a power series expansion of the magnetoelastic energy density ε_{ME} for the strain tensor \hat{S} and the directions cosines of the magnetization m_α [56]

$$\varepsilon_{ME} = \sum_{i,j,k,l} B_{i,j,k,l} S_{i,j} m_k m_l + \dots \quad (2.39)$$

For a generic one-direction strain of modulus σ directed at an angle θ with respect to the magnetization direction, the anisotropy energy density can be modelled as[59]

$$\varepsilon_{ME} = -\frac{3}{2}\lambda_S\sigma\cos^2(\theta) = -K_{ME}\cos^2(\theta) \quad (2.40)$$

that is dependent on both the strain modulus and the magnetoelastic coupling λ

2.4 Domains and the Stoner-Wohlfarth model

Considering the magnetic anisotropy terms, in a real system the magnetic configuration is far from trivial and depends on the interplay between each energy term. As an intuitive example I will consider only the magnetostatic energy responsible for the shape anisotropy. Its minimization requires that the least amount of “magnetic charges” is produced (i.e. the least amount of stray field) favoring directions of the magnetization that are parallel to the system surface. For the simple case of a rectangle, a uniformly magnetized configuration will be oriented along longest side which is the easy direction. Nevertheless some uncompensated magnetic charges will be produced (see **Figure 2. 3**), increasing the energy of the system. This latter can try however to reduce this energy by creating two regions uniformly magnetized but with opposite direction, called *magnetic domains*. This comes at the cost of having an interface, called *domain wall*, in which the spins are aligned antiparallel to each other. Since this would increase the exchange energy term it seems an unfavorable scenario. The formation of domains can still be obtained if the spins are allowed to gradually rotate one to the other so as to minimize the extra energy produced by a non-parallel configuration. By requiring a small angle between two adjacent spins however comes at the cost of having them tilted away from the easy axis direction, so a trade-off must be reached. This is typically encoded in the *exchange length* which is defined as the typical length over which spins can be tilted to account for dipolar effects.

$$L_{ex} = \sqrt{\frac{A}{\mu_0 M_S^2}} \quad (2.41)$$

This length defines for example the critical dimension of a ferromagnetic system below which the energy cost of a domain wall formation is higher than the increase in magnetostatic energy. Such particles will always be found in a single domain state. For sufficiently large dimension the system is decomposed (magnetically) in domains of uniform magnetization (lowering the dipolar induced increase in energy) separated by domain walls. Two different kinds of domains are typically treated, that are Bloch and Néel walls. The former is a configuration in which spins

gradually rotate in a plane parallel to the wall, while for the latter they rotate in a plane perpendicular to the wall (see **Figure 2. 4**). From a theoretical point of view the Bloch walls are unlikely in thin films, for which M is in plane and so the spins would rotate out of the film plane creating large demagnetizing fields. On the contrary the latter would create uncompensated magnetic volume charges. For a thin film however these extra charges are less energy costly than the surface charges, so below a certain thickness they are the most likely[46], [50].

In a more realistic case in which also a uniaxial anisotropy term is present the energy balance is more complex. Interestingly it can be demonstrated [46] that the actual domain wall width, in the limit of either vanishing or infinite film thickness, can be expressed as[50], [54]

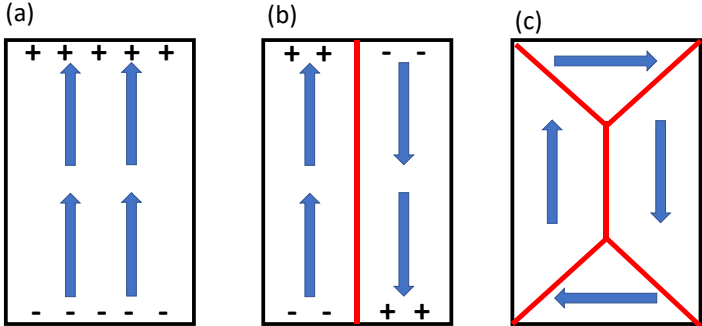


Figure 2. 3 A simple sketch depicting the way domain formation allows to reduce the demagnetizing energy. (a) uniform magnetization. (b) separation in two domains, still some surface charges are present. (c) closed loop configuration with zero magnetostatic energy. Red lines indicate domain walls in which the spins are rotated.

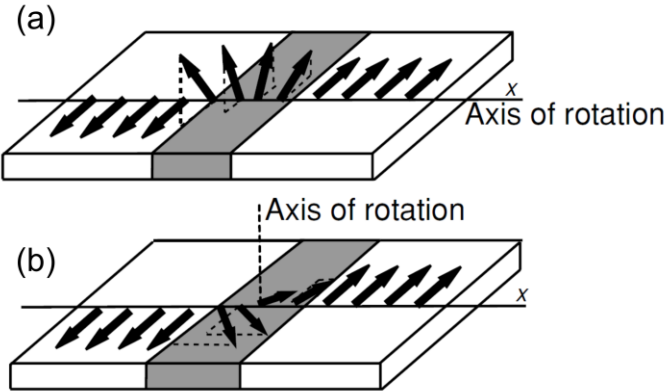


Figure 2. 4 Sketches of domain walls briefly discussed for the case of a thin film. For the Bloch wall (a) the spins rotate out of the film plane creating a demagnetizing field. For the Néel wall (b) the spins rotate inside the film plane, at the expense of creating internal volume magnetic charges. Taken from [50].

$$L_w \approx \sqrt{\frac{A}{K}} \quad (2.42)$$

regardless of the kind of wall. Finite thickness effect would complicate the picture but Eq. (2.42) is still useful for doing some estimations. For example, for *hcp* Co this value at RT is approximately 25 nm[50].

Such a complicated picture of the energy terms acting in a ferromagnet indicates clearly that the study of *magnetization reversals*, that is the study of how a magnetized material responds to an external applied field trying to magnetize it along an opposite direction, is also a highly nontrivial subject. The first model created to model magnetization reversal was proposed by Stoner and Wohlfarth, for the case of a uniformly magnetized, single-domain ellipsoid particle with uniaxial anisotropy. For an applied field \mathbf{H} along an angle θ from the easy axis the energy density is

$$\mathcal{E} = K_U \sin^2(\phi - \theta) - \mu_0 \mathbf{M} \mathbf{H} \cos(\phi) \quad (2.43)$$

Where ϕ is the angle between the magnetization and \mathbf{H} . For given values of H and ϕ , the direction of \mathbf{M} is determined by minimizing Eq. (2.43)

$$\frac{\partial \mathcal{E}}{\partial \theta} = 0; \quad \left(\frac{\partial \mathcal{E}}{\partial \theta} \right)_{\theta=\theta_0}^2 > 0 \quad (2.44)$$

yielding the following equations[46]:

$$\frac{1}{2} \sin(2(\phi - \theta)) + h \sin(\phi) = 0 \quad (2.45)$$

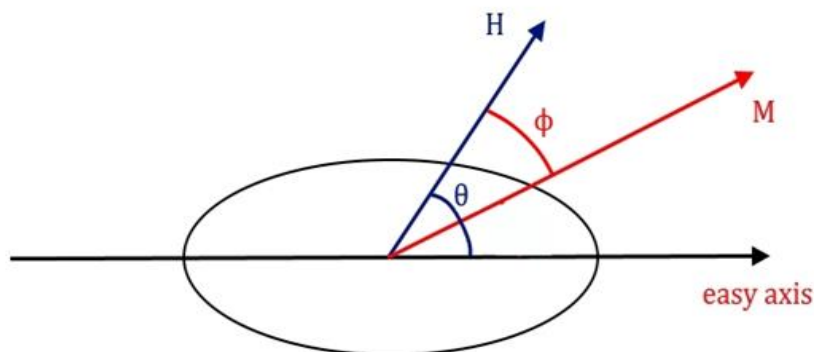


Figure 2. 5 Schematic representation of the configuration of \mathbf{H} , \mathbf{M} with respect to the easy axis of the particle.

$$\cos(2(\phi-\theta)) + h\cos(\phi) > 0 \quad (2.46)$$

with h a dimensionless quantity representing the ratio between the Zeeman and the anisotropy terms

$$h = \frac{\mu_0 M H}{K_U} \quad (2.47)$$

Analytical solutions exist only for the two special cases $\theta=0$ or $\theta=\pi$ which correspond to \mathbf{H} parallel and perpendicular to the easy axis respectively. For the first case the minimization yields

$$(h + \cos(\phi)) \sin(\phi) = 0 \quad \text{with} \quad 1 + h \cos(\phi) = 0 \quad (2.48)$$

Two solutions are possible:

- a maximum when $\cos(\phi) = -h$ that is valid in the interval $|h| < 1$
- a minimum when $\sin(\phi) = 0$ with $1 + h\cos(\theta) > 0$

The second solution implies that the angle ϕ between \mathbf{M} and \mathbf{H} is zero when $h > -1$ and is π when $h < -1$. In the intermediate region $-1 < h < 1$ both values of ϕ are valid. This is a clear manifestation of hysteretic behavior. If at the beginning a large positive field h is applied, only $\phi=0$ is a valid solution (\mathbf{M} parallel to \mathbf{H}). This configuration is stable until the ratio h is less than -1 . For such values of h the system abruptly goes to the other solution $\phi=\pi$. Translating to physical quantities the requirement for magnetization reversal is that the Zeeman energy term outweighs in magnitude the anisotropy energy term. For intermediate values ($-1 < h < 0$) the system finds itself in a maximum but the magnetization is forbidden to rotate to the minimum configuration since the anisotropy acts as an energy barrier, that is overcome when the applied field reaches a certain value. The same mechanism is found when starting with a large negative value $-h$. The magnetization reversal takes place for values of the applied field that are equal to the so-called *coercive field* H_C defined by

$$H = H_C = \frac{2K_U}{\mu_0 M} \quad (2.49)$$

The second case analytically treatable is when \mathbf{H} is applied perpendicularly to the easy axis. In this case no hysteresis is observed. Minimizing yields:

$$(h - \cos(\theta)) \sin(\phi) = 0 \quad \text{with} \quad -\cos(2\phi) + h \cos(\phi) = 0 \quad (2.50)$$

as in the previous case, with the difference that $\cos(\phi) = h$ is also a minimum. In the intermediate region $-1 < h < 1$ the system behaves as a paramagnet with a zero magnetization for $h=0$. For all the other direction of H with respect to the anisotropy axis the computation of the minimum and maximum of the energy have to be numerically resolved, but for all the cases (see **Figure 2. 6**): the system shows hysteresis. with values of coercive fields that are always lower than the one obtained along the easy direction. While this model may be an oversimplification of real systems it is widely used since it is one of the very few models for magnetization reversal that are relatively simple to use.

2.5 Magnetic anisotropy of thin films

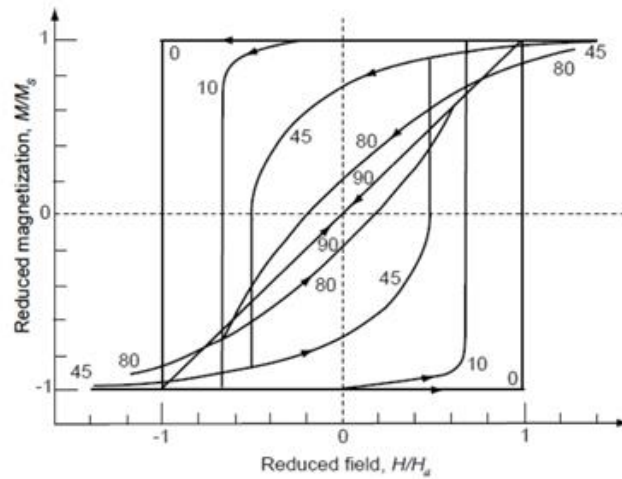


Figure 2. 6 Stoner-Wohlfarth model: hysteresis loops obtained for different values of the angle θ . For all the angular directions of the applied field but π the system presents an hysteretical response. Taken from [50].

The exchange interaction is not the only term that determines the properties of ferromagnetic materials. The microstructure and the shape of the FM system affect the magnetic behavior of the electrons resulting in *anisotropic* energy terms that are dependent on the orientation of the magnetization. I will now discuss how they affect the magnetic behavior a thin film of thickness t . In particular, I will limit the discussion to the specific case of polycrystalline thin films since they are the case system for my thesis. Note that their formulation is always given in term of energy density rather than the total energy.

The *shape anisotropy* is a term that originates from the minimization of the stray fields produced at the boundary of the FM. For a thin film with a perfectly flat surface it imposes the

magnetization to lie inside of the film plane due to the high demagnetizing fields that would be produced for a normal direction of M. Its value is

$$K_{sh} = \frac{1}{2} \mu_0 M_S^2 \cos^2(\theta) \quad (2.51)$$

where θ is the angle between the magnetization and the film's normal.

The *magnetocrystalline anisotropy* (MCA) originates from the coupling of the electrons spins with their orbit inside the crystal lattice. For this reason in polycrystalline systems it is usually taken as not influencing the overall anisotropy since for a random orientation of the grains it is expected that the total contribution averages out. However this assumption is not strictly valid. Consider an ensemble of exchange coupled ferromagnetic grains with a certain lateral size labelled D. In this case there is an interplay, for two adjacent particles, between the exchange forces trying to keep the spins parallel and the two randomly oriented uniaxial anisotropies, trying to take the spins aligned with the local easy direction. This competition can be quantified by the domain wall length

$$L_w = \sqrt{\frac{A}{K_1}} \quad (2.52)$$

where A is the exchange stiffness and K_1 is the anisotropy constant of the grains (assumed equal). L_w tells the strength between the exchange and the anisotropy. The higher A, the higher the energy cost of rotating two adjacent spins and the longer the domain wall is (to accommodate a large number of slightly rotated spins). This *random anisotropy model* developed by Herzer[60]–[62] considers this parameter and observes that if the lateral dimension of the domain is smaller than L_w the system is divided in magnetic domains that enclose a number N of grains (see **Figure 2. 7**) that is roughly given by

$$N = \left(\frac{L_w}{D}\right)^3 \quad (2.53)$$

For each domain the anisotropy constant averages out for N tending to infinity. For a finite value of N however, K does not average to zero but scales down as

$$K = K_1 \left(\frac{D}{L_w}\right)^6 \quad (2.54)$$

If one of the lateral dimension of the grains (i.e. the thickness) is approximately equal or less than L_w then $N = \left(\frac{L_w}{D}\right)^2$ and K_{eff} is reduced according to [62], [63]

$$K_{\text{eff}} = K \left(\frac{D}{L_w}\right)^2 \quad (2.55)$$

This shows that the grain sizes are an important parameter for the establishment of a MCA contribution to the system anisotropy. A more general case is taken also into account, considering a distribution of *structural phases*, that refers to all grains with equal anisotropy constant K_1 and same size D . Moreover it is added a second uniaxial anisotropy term, labelled K_U , that is considered uniform over distances far greater than the domain wall length L_w . In such case the general formula becomes

$$\langle K \rangle = \sqrt{K_U^2 + \sum_v K_{1,v}^2 x_v^2 \beta_v^2 \frac{D_v^3}{L_w^3}} \quad (2.56)$$

where v indexes the structural phases, x_v is the volume fraction of each phase in the volume defined by L_w , and β_v are constants of order unity. If a single kind of crystalline phase is present (as assumed in the beginning) then $K_{1,v}$ is independent on the index and thus the formula is a generalization for the realistic case of a distribution of grain sizes. Two limiting cases are

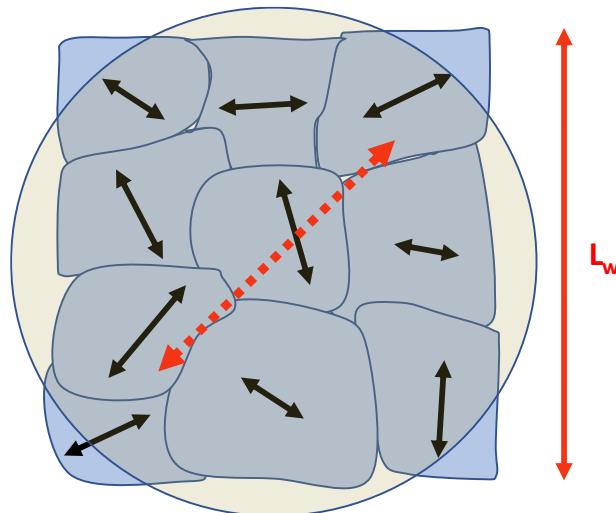


Figure 2. 7 A collection of grains randomly oriented with lateral dimension less than the domain wall length L_w . a large domain will be formed enclosing N grains and having a randomly oriented effective anisotropy (red dotted line).

envisioned. The first is when the uniform anisotropy constant dominates over the random one, that is

$$\frac{K_U}{K_1 N^{\frac{1}{2}}} \gg 1 \quad (2.57)$$

In this case the total anisotropy is principally determined by the uniform uniaxial anisotropy. If this one is vanishingly small,

$$\frac{K_U}{K_1 N^{\frac{1}{2}}} \ll 1 \quad (2.58)$$

then the total anisotropy is determined by the random term. Considering a thin film the uniform anisotropy can be the one produced by the shape. In this case it dominates over the random contributions and thus *along* the hard direction the random term is outweighed. However inside the plane this latter term can contribute to the hysteretic behavior of the magnetization reversal for an applied magnetic field parallel to the plane, regardless of the direction of \mathbf{H} .

Another way MCA can affect the overall anisotropy is given for the case of a preferential distribution of grains orientation, known as *texturing*. If the substrate surface promotes the growth of a certain phase with a preferential direction of the lattice parameters, then the angular distribution of easy and hard direction is not random so a preferential direction for the magnetization vector is produced. Importantly this may give rise to preferential directions even inside the film's plane.

Other known sources of magnetic anisotropy in thin films are caused by broken symmetry of the system that can be produced by strain and surfaces. Regarding the role of strain in thin film, it is best understood for epitaxial structures. In that case the lattice mismatch between the lattice parameters of the substrate surface and the ones of the FM crystalline phase will induce structural deformation in the first layers of the film. For a polycrystalline or amorphous films strain induced anisotropies are reported in literature[64], [65], and attributed to distortions of the crystal lattice at the grain boundaries[66]. Regarding the role of the surfaces, a treatment based on the concept of broken symmetry is not straightforwardly applicable to a polycrystalline thin film if a random distribution of grains is considered. It would follow that also the surfaces crystallographic directions are random. Nevertheless the role of the surface is known to be important for very thin films, since the magnetostatic energy term scales with the system thickness and becomes comparable to the other terms[46], [50]. In this case the *surface*

anisotropy term K_{sur} can be treated in a phenomenological sense and interpreted as a generic term that tells whether at the surface the spins prefer to be aligned normal to the surface or inside the film plane.

A last term that is to be addressed is the effect of the substrate shape. Apart for the case of strain already reported, if the substrate surface is stepped, then the FM surface is not flat. This has two implications. The first one is that the crystal symmetry is broken also at the interface between Co atoms and the substrate step edges[67]. This induces an anisotropy surface-like term called step anisotropy[67]. As for the other cases, for a polycrystalline material this term is important only if the step edges can promote a textured growth of the FM system. The second contribution is a dipolar term (i.e. a magnetostatic effect) that arises if the growth of the FM layer is such that it reproduces the surfaces features of the substrate. In that case a periodic modulation of the FM surface is obtained. If the systems is magnetized perpendicular to these modulations then in-plane stray fields will be produced due to uncompensated magnetic charges at the surface. A micromagnetic-based formula for the calculation of roughness induced uniaxial anisotropy was developed by *Schlömann*[68]. The demagnetizing factor for a periodic modulation of the surface, highly centered around a single wavelength λ is given by (assuming the modulation is directed along the x axis)

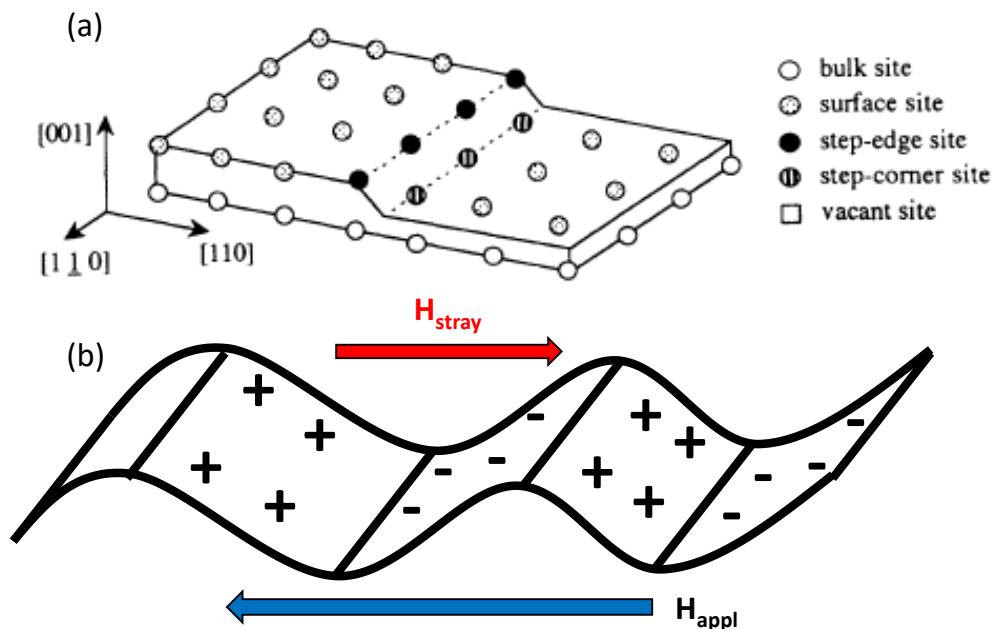


Figure 2. 8 (a) sketch of the surface FM atoms when grown over a stepped substrate (taken from [67]). (b) Applied field perpendicular to the ripples. The induced magnetization creates a stray field that is energetically unfavored.

$$N_{yy} = N \cong \frac{\pi \text{RMS}^2}{\lambda t} \quad (2.59)$$

where RMS is the mean standard deviation from the mean surface (i.e. the roughness) and t is the film's thickness. The dipolar energy term assumes the form

$$\mathcal{E} = -\frac{1}{2} N \mu_0 M_S^2 \quad (2.60)$$

In general $N \ll 1$ and this contribution is always orders of magnitude lower than the one for a direction along the film normal. Nevertheless it may become important for the establishment of an in-plane uniaxial anisotropy.

2.6 Superparamagnetism, antiferromagnetism and exchange anisotropy

From the discussion made in Subsection 2.3 it clearly emerges the role of anisotropy in making the system retain a nonzero net magnetization. At finite temperatures however the thermal fluctuations must be taken into account since statistically they can be able to make the system flip from one minimum energy configuration to the other. Consider again the case of a magnetic single domain particle with uniaxial anisotropy, fixed in place and not subject to any external fields. For a given temperature, the system will experience *on average* a spontaneous magnetization flip in a *relaxation time* τ defined by [46]

$$\frac{1}{\tau} = f_0 \exp\left(-\frac{KV}{k_B T}\right) \quad (2.61)$$

Where K is the anisotropy constant and k_B is the Boltzmann constant. f_0 is a constant that has the dimension of a frequency and in general is dependent on the ferromagnetic material analyzed. Some important conclusions can be drawn. The first is that the relaxation time exponentially depends on the system's volume, so that small variation of this parameter dramatically affects τ . The second one is that for a fixed relaxation time and particle volume, a *Blocking temperature* T_B may be defined as the one for which the system may be regarded as static [48]:

$$T_B = \frac{KV}{k_B} \ln(\alpha f_0 t) \quad (2.62)$$

where α is a dimensionless constant and t took the place of τ since it reflects a different concept explained in the following. The blocking temperature is not defined only by the anisotropy energy of the system but also by the timescales of the measurements with which one probes the magnetic behavior of the system. For example a particle that, at a fixed temperature T , has a relaxation time of 0.1 sec can be regarded as superparamagnetic if probed with magnetometry measurements such as VSM or SQUID, but appears static if probed with fast techniques such as Ferromagnetic Resonance. For this reason instead of τ in Eq. 2.52 I used the symbol t to indicate the measurement time, and α defines “how much longer” the measurement lasts with respect to the relaxation time.

The concept of blocking temperature is not limited to the case of a *ferromagnetic* system but can be easily extended to another other case of magnetic order, that is antiferromagnetism. Antiferromagnetic materials are characterized by a negative value of the exchange constant J , meaning adjacent spins are antiparallely coupled. The result is a net total magnetization for temperatures lower than the Néel temperature T_N , but differently to paramagnetic and diamagnetic materials the spins are in a ordered state. These systems can be thought of two compenetrating sublattices, labelled + and -, each of which with a nonzero value of the magnetization. Since the sum M^+ and M^- is zero, one of the order parameters that can be used to quantify the state is the *staggered magnetization* $M^+ - M^-$. All the discussion made in Section 2.3 and 2.4 is valid also for this class of systems, in particular the concept of magnetic anisotropy.

Antiferromagnetic (AFM) materials were intensively studied in the last decades due to their ability to stabilize the magnetization of a ferromagnetic system by the induction of an *exchange bias field* H_B . The first observation of this phenomenon was made by Meiklejohn and Bean 1956[69] who reported a horizontal shift of the hysteresis loops for a system of Co nanoparticles enclosed by a shell of CoO. Their proposed model assumes that a single domain rigid AFM layer (i.e. with infinite anisotropy constant) is exchange coupled to a single-domain FM layer. The interface is sharp and only one of the two sublattice of the AFM is present at the interface, i.e. it is totally uncompensated (see **Figure 2. 9**). They assumed a Stoner-Wohlfarth model for magnetization reversal in which a phenomenological second anisotropy term K_B is added that accounts for the observed shift

$$\mathcal{E} = \frac{1}{2} K_{FM} \sin^2(\phi - \theta) - \mu_0 M H \cos(\phi) - K_B \cos(\theta) \quad (2. 63)$$

then the minimization procedure yields similar results seen in Subsection 2.3. The role of K_B can be regarded as an additive field \mathbf{H}_B with fixed direction that is superimposed to the external applied field \mathbf{H}

$$\mathbf{H}' = \mathbf{H} - \frac{K_B}{\mu_0 M_S} \quad (2.64)$$

Considering that the only effect of the AFM is due to exchange coupling, \mathbf{H}_B can be redefined as

$$\mathbf{H}_B = \frac{J_{FM,AFM}}{\mu_0 M_S} \quad (2.65)$$

where $J_{FM,AFM}$ is the exchange coupling at the interface. This anisotropy energy term is called *exchange anisotropy*.

A generalization of the energy balance equation was done by Meiklejohn[70] focusing only on exchange anisotropy. He considered the effect of the AFM layer explicitly inserting its anisotropy constant K_{AFM}

$$\mathcal{E} = -\mu_0 M H \cos(\theta - \beta) + K_{AFM} \sin^2(\alpha) - J_{ex} \cos(\beta - \alpha) \quad (2.66)$$

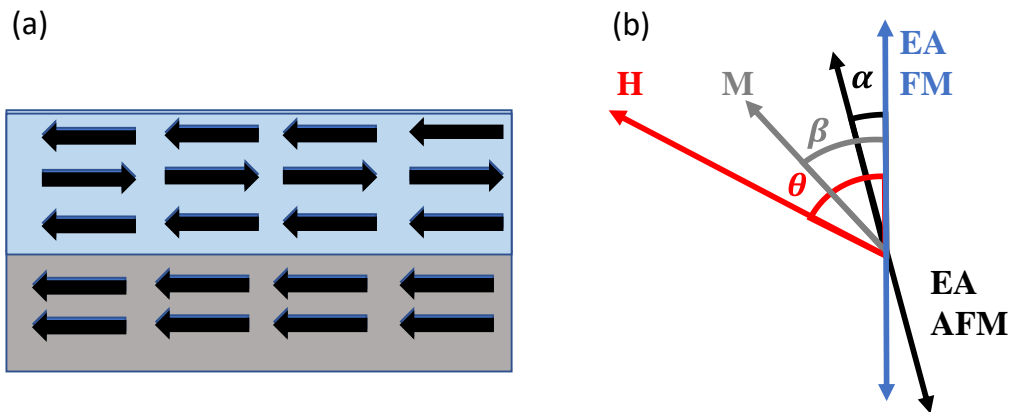


Figure 2. 9 (a) Sketch of the AFM/FM interface for the Meiklejohn and Bean model of exchange anisotropy. The spins of the top AFM layer are totally uncompensated at the interface and exchange coupled with the spins of the FM layer. (b) angular directions of the generalized energy equation of Meiklejohn. The uniaxial anisotropy of the FM layer enters the model only for definition of the angles.

where the angles are defined with respect to the easy direction of the FM layer. α , β and θ are the angular direction of the AFM easy axis (EA), magnetization vector and applied field respectively (see **Figure 2. 9**). J_{ex} is from now on the shorthand for $J_{\text{FM,AFM}}$.

Minimizing with respect to both the angles α and β

$$\sin(2\alpha) = \frac{J_{\text{ex}}}{K_{\text{AFM}}} \sin(\beta - \alpha) \quad (2. 67)$$

$$\sin(\beta - \alpha) = \frac{HM_{\text{S}}}{J_{\text{ex}}} \sin(\theta - \beta) \quad (2. 68)$$

In the limit of $K_{\text{AFM}} \gg J_{\text{ex}}$ α is a constant and the AFM layer does not follow the FM layer that is going through magnetization reversal, inducing an effective pinning field. For the opposite case $K_{\text{AFM}} \ll J_{\text{ex}}$ the AFM layer will follow the magnetization of the FM layer and does not contribute to any exchange bias. From the second limiting case it is qualitatively inferred that if the interfacial coupling is strong the magnetization reversal has anyway the additional pinning produced by the anisotropy of the AFM layer, contributing thus to the coercivity. This model while quite intuitive and didactical is oversimplified and gives estimate of the exchange fields that are orders of magnitude bigger than the measured ones[37]

Successive more realistic models were proposed for polycrystalline FM and AFM layer in which the dependence of the AFM magnetic state on the interplay between temperature and AFM mean size was considered[37], [71]–[75]. The basic common assumption is that an exchange interaction takes place at the interface between the surface spins of the FM and the ones of the AFM. Regardless of the way the exchange coupling at the interface modifies the magnetic configuration of the AFM (be it formation of domains parallel to the surface[72]–[74] or simply a rotation of the staggered magnetization[71], [76]), this latter influences the ferromagnetic layer in two ways. It is considered an antiferromagnetic system composed of randomly oriented grains with a statistical distribution of sizes and directions of the AFM easy axis (see **Figure 2. 10(a)**). For a given temperature at which a measurement is performed, $T_{\text{meas}} < T_{\text{N}}$, some of the grains (the bigger ones) will have a volume anisotropic energy sufficient to have a stable magnetic order, while others may be in an equivalent of the superparamagnetic state, depending on their blocking temperature. If a magnetic field is applied an additional Zeeman energy term is introduced.

For a sufficiently large applied field the FM layer will be magnetized along its direction. The AFM grains that can be thermally activated then will change the magnetization state according with the configuration of the FM, while the ones that are not thermally activated will retain their

magnetic state at the expense of an increased energy, that can be stored e.g. as partial domain walls inside the AFM[73]. The first kind of grains are responsible for the increase in coercivity, while the latter kind is responsible for the exchange bias field[37], [76]. From the point of view of the ferromagnetic layer, the presence of a random distribution of AFM grains means that regardless of the direction of the applied field, some of them will act locally as an additional energy barrier for FM magnetization reversal. This means that irreversible jumps of M will take place for any direction of the applied field, resulting in hysteretic behavior of the FM[73], [76]. A coupling between an AFM and a FM layer thus can increase both the coercivity and induce an exchange bias field. Interestingly an exchange-bias-like field can be obtained by coupling a soft ferromagnet (low anisotropy constant) to a strong ferromagnet (high anisotropy constant)[77], [78]. If the maximum applied field is strong enough to induce magnetization reversal in the weak FM but insufficient to fully reverse the hard layer, then this latter will act analogously to an AFM layer, producing an exchange bias field that sums to the external applied one.

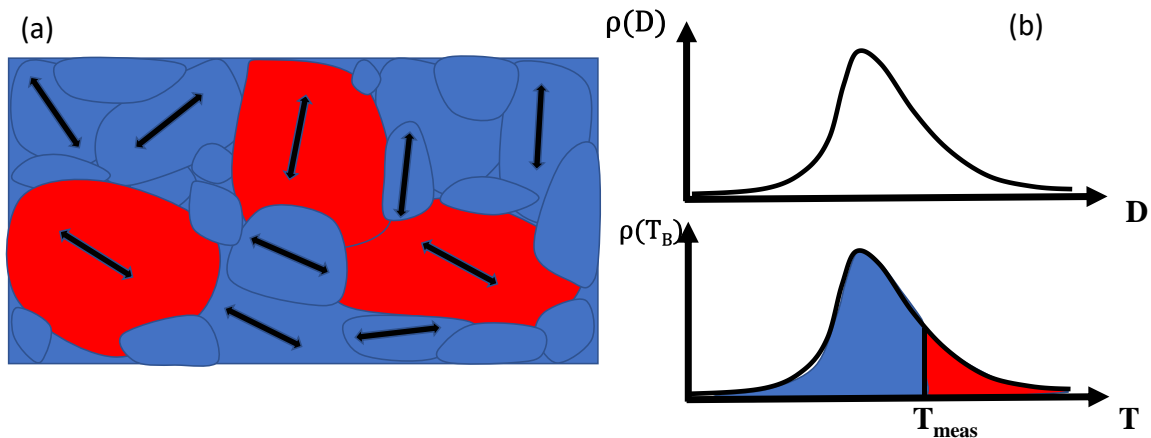


Figure 2. 10 (a) Sketch of the AFM layer, composed of a statistical distribution of grain sizes with a distribution of easy axes (black arrows). At a certain temperature T_{meas} only the grains with high anisotropy energy (colored in red) are thermally stable ($T_B > T_{meas}$) and will produce an exchange field to the FM layer. During magnetization reversal the smaller AFM grains, with $T_B < T_{meas}$ can jump from their initial configuration to the new minimum (i.e. they can follow the magnetization of the FM, aided by thermal effects, so they will act as pinning). (b) probability density distribution of grains with a certain lateral dimension D , corresponding to a distribution of grains with a certain blocking temperature (bottom). At the measurement temperature only a fraction of the total grains will be thermally stable.

Chapter 3

Fabrication techniques and characterization methods

This chapter is dedicated to the description of various setups and characterization techniques I used for investigating the spinterface formation in bilayers and devices. In Section 3.1 I will describe the UHV apparatus that I used for the growth of hybrid systems, along with a detailed description of the various procedures adopted for the samples fabrication. Section 3.2 is dedicated to the description of the techniques and setups used for the morphological and microstructural characterization of the systems, including Atomic Force Microscopy (AFM) and Transmission Electron Microscope (TEM). In Section 3.3 I will put focus on Magneto Optical Kerr Effect (MOKE) set-up used for magneto-optical characterization of the samples. The magnetic characterization has been carried out by Vibrating Sample Magnetometry (VSM) and Superconducting Quantum Interference Device (SQUID), described in Section 3.5. The description of the Nuclear Magnetic Resonance technique, with focus on the zero-field NMR technique will be presented in Section 3.5

3.1 UHV fabrication of hybrid systems

3.1.1 The growth chamber

The synthesis of multilayered structure of different materials involves different deposition systems, each best suited for the particular element or molecule that has to be deposited. Moreover, the choice of Cobalt, a *3d* metal ferromagnet, as the main constitutive ferromagnetic element in the hybrid system, requires high vacuum conditions for preserving its quality. The growth chamber is then a complex system composed of interconnected UHV chambers, each

devoted to different deposition techniques. The deposition system used for preparing the sample is schematized in **Figure 3. 1** and it consists of four different ultra-high-vacuum (UHV) steel chambers: the introduction chamber (INTRO), the effusion chamber (EFF), the metals chamber (MET) and the mask chamber (MAS). They are isolated from one another by gates (G). In every chamber UHV condition is granted by turbo pumps (TP), each with its own back scroll pump (SCR), with the only exception of MET for which a dedicated ionic pump (IP) is present. Pressure is measured by full range sensors, labeled by S in **Figure 3. 1** (Pirani + Cold Cathode). The sample can be displaced between the various chambers thanks to four fork-shaped arms (FA). The introduction chamber is dedicated to the insertion/extraction of samples. It is the only chamber exposed directly to the air during the sample loading, its base pressure is 5×10^{-8} mbar. This chamber is equipped with an evaporation cell for fast deposition of gold by Joule heating of Au microparticles. The chamber hosts also a gas inlet connected to an ultra-pure O₂ gas bottle, used for controlled oxidation of metals, and to a Nitrogen gas line for venting. The intro

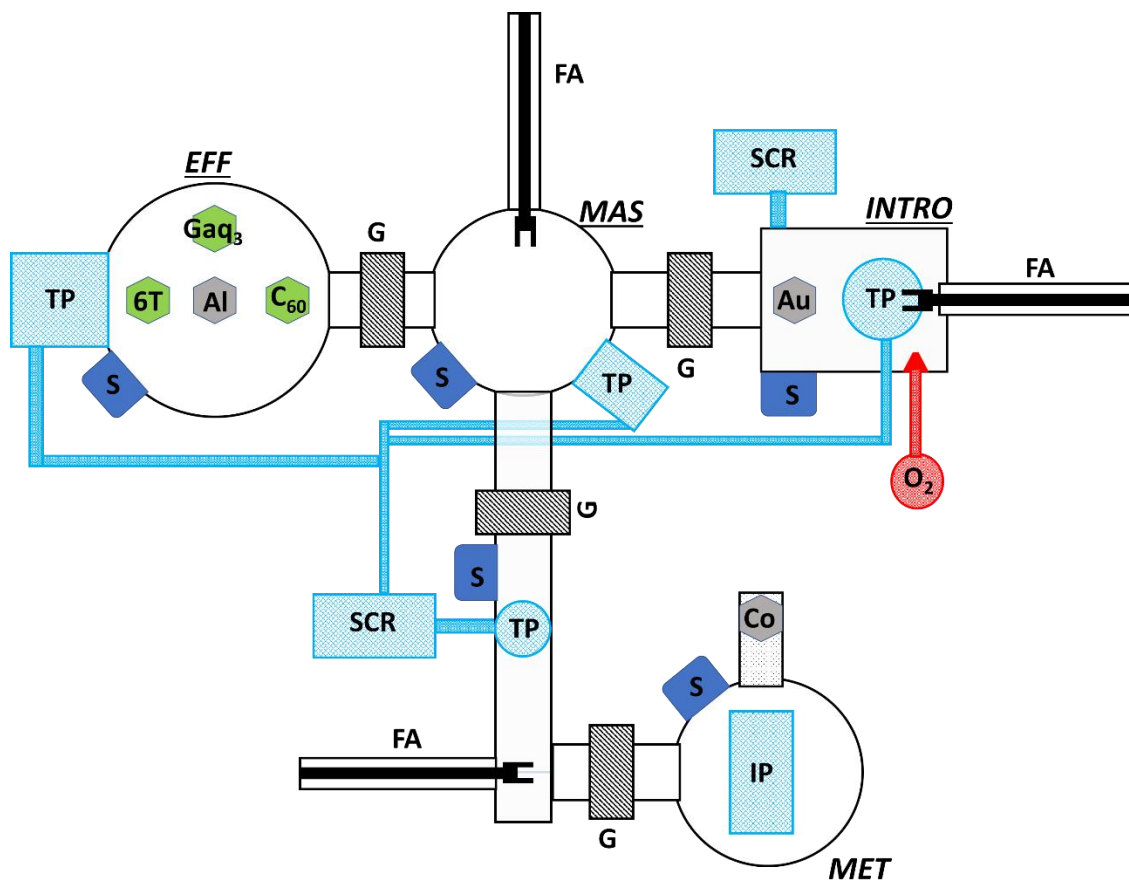


Figure 3. 1 Schematic of the growth chamber. Hexagons represent material sources (effusion cells, e-beam).

chamber is connected to the mask chamber from which the sample holder can be moved either into the effusion or the metal chamber. In this chamber it is possible to mount masks on top of the samples, kept in position by a mask holder with different patterns. The effusion chamber contains four effusion cells dedicated to the thermal evaporation of organic molecules (C₆₀, Gaq₃, T6) and Al. The metals chamber, reachable through a transfer line, is dedicated to the Co growth, performed by electron beam evaporation. Both chambers are also equipped with a Quartz microbalance for checking the deposition rate. The base pressure of MET and the transfer is 2.0x10⁻¹⁰mbar, whereas all the other chambers have base pressures of 9.0x10⁻⁸ mbar.

3.1.1.1 Cobalt deposition: electron beam evaporation

This evaporation technique is most suited for the sublimation of materials with high melting points. The process is by itself rather simple. The source of the material, that can be either a rod or a boat filled with the material, is heated by thermionic electrons that are emitted from a thin metallic wire and accelerated towards the source by the application of a high voltage. For sufficiently high currents flowing through the filament and voltage applied, the temperature of the source is high enough to allow the evaporation of the material. The schematic of the e-beam is reported in **Figure 3. 2**. the source is an ultra-pure (99.99%, Goodfellow) Co rod (2 mm diameter). The filament (0.125 mm diameter) is made of Tungsten doped with 1% Thorium which role is to lower its work function and facilitate the thermal emission. The filament is coil shaped for ensuring a uniform heating of the rod tip, that has to be placed in the most central position: this guarantees a uniform heating of the material. The evaporated material passes through a collimator that orients the flux of the material towards the substrates. A water-cooled copper shield surrounds the inner part of the electron gun for avoiding the systems overheating. The current passing through the filament and the voltage between the rod and the electron source is measured. In addition the evaporation is controlled also by the *emission current*, that is produced by the high energy electrons colliding on the tip of the rod. As the material evaporates as ions, the stripped electrons are flowing towards the ground and measured. The amount of evaporated material is controlled by a Quartz microbalance, described below. The emission flux can be adjusted by tuning three parameters: the filament current, the applied direct voltage between the filament and the source, and the z-position of the source. The current density of the thermionically emitted electrons reaching the rod tip is an exponential function,

$$j=AT^2\exp\left(-\frac{W}{K_B T}\right) \quad (3. 1)$$

where W is the metal work function, K_B is the Boltzmann constant, A is a parameter specific of the filament and T is the temperature. Since T is a function of the filament current, j (and consequently the evaporation rate) is extremely sensitive to small variations of this parameter. The applied High Voltage between the filament and the rod is a more accurate experimental parameter for control of the evaporation rate, since it varies linearly with the energy possessed by the thermionic electrons. A critical parameter is the relative distance between the source and the filament, especially if the source is a rod. An optimal evaporation is obtained if the source tip is in the plane that contains the coil. If it is lower than such plane the electrons available for the heating would be not enough and higher filament currents or applied voltages would be necessary. If it is higher the heating of the source will be less focused on the tip, with the risk of structural damage of the rod. The working pressure necessary to operate an electron gun needs to be at least 10^{-8} mbar. The principal reason is to avoid the ionization of air gas and contaminants due to the emitted electrons. A too high pressure can induce current arches between the filament and the rod harmful to the device. Moreover the evaporation material would be scattered by the air gases resulting in a poor quality of the deposition.

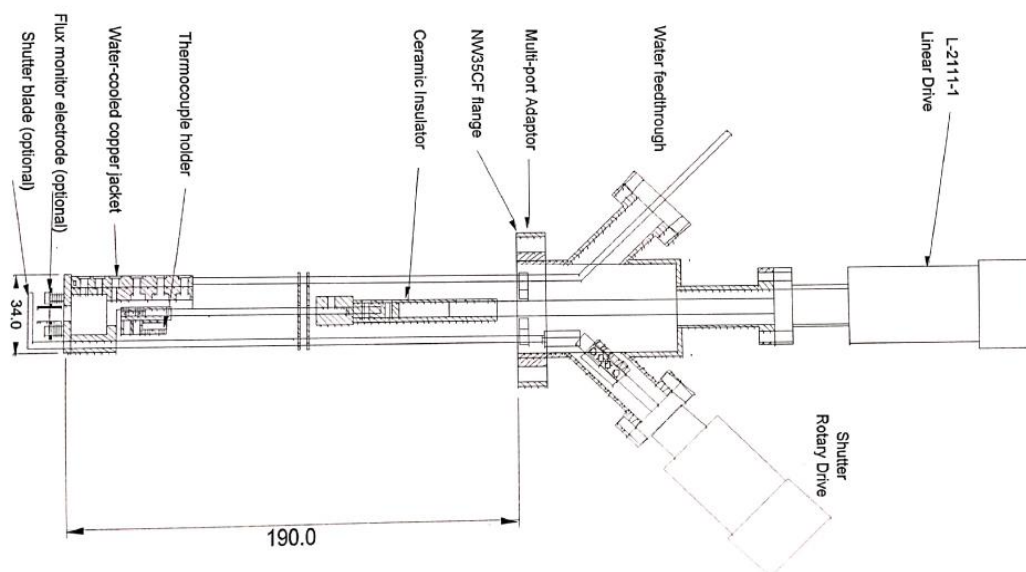


Figure 3. 2 Schematic of the e-beam evaporator used (taken from [79]).

3.1.1.2 Al and molecules deposition: thermal effusion cells

Thermal effusion cells are designed for soft and/or not stiff materials like organic molecules and Al. A schematic is reported in **Figure 3. 3**. A powder of the desired material to be evaporated is placed inside a crucible, that is heated by a resistive element. The thermal contact

between the two components is mediated by a nested system composed of a heat reservoir in contact with a high thermal conductor material that surrounds the crucible: this guarantees a uniform heating of the material during deposition. A water-cooled heat sink is responsible for heat dissipation. A thermocouple in close contact with the heat conductor is responsible for control of the cell's temperature. An orifice placed at the end of the crucible collimates the evaporating material. The working principle of the effusion cells requires them to sit in a vertical alignment, for avoiding material loss. Control of the evaporation process is obtained by an external power supply coupled with Proportional Integral Differential controller (PID). The only parameter to be controlled is the cell temperature, that is automatically regulated by a PID that governs the electrical power applied to the heater. For the deposition of Gaq₃ and T6, that are evaporated at 250° and 350°C respectively, the high thermal conductive material is a liquid metal. For the deposition temperatures of C₆₀ and Al, evaporated at 360°C and 1070°C respectively, thermal contact is done by a ceramic material.

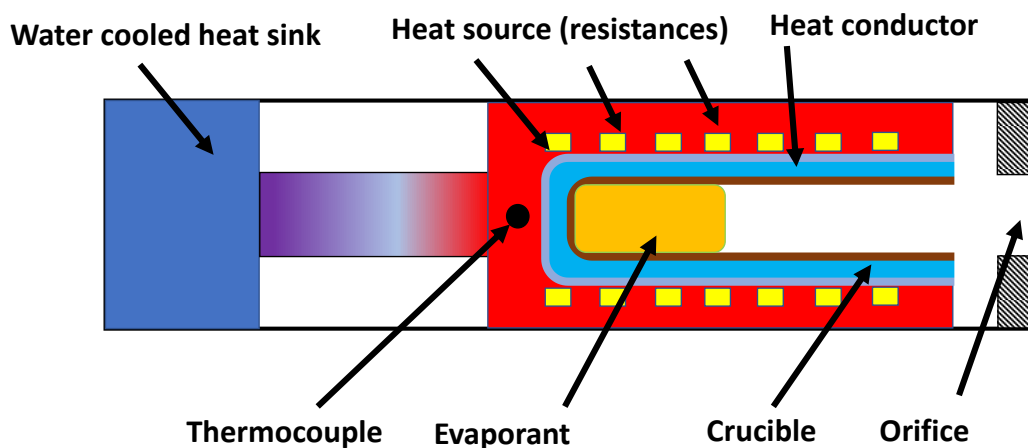


Figure 3. 3 Schematic of an effusion cell. The heat conductor may be a liquid metal or a ceramic material.

3.1.1.3 Control of the amount of evaporated material: Quartz microbalance

During the evaporation process, the deposition rate is checked by a Quartz microbalance (QMB). Its working principle is based on a resonantly oscillating Quartz piezoelectric microcrystal, that is driven into resonance oscillation by an external applied AC voltage. The change in frequency is critically related to the mass of the resonating system. When mass is added to the microcrystal by the evaporation process, its resonance frequency shifts by a measurable amount[79]

$$\frac{M_C - M_{\text{added}}}{M_C} = \frac{\Delta M_C}{M_C} = \frac{\Delta \omega_C(t)}{\omega_C} \quad (3.2)$$

where M_C and M_{added} are the masses of the piezoelectric crystal and the added mass by the deposited material, ω_C and $\Delta \omega_C$ are the resonance frequencies of the system and its variation by the deposited material.

3.1.2 Fabrication procedure

3.1.2.1 *Substrate cleaning procedure and preparation*

Before doing any deposition, all the substrates should have the surface as clean as possible. The presence of contaminants on the substrates is detrimental to the quality (microstructural, morphological, electrical, ...) of the future sample. For this reason, I perform a pre-cleaning procedure during the *ex-situ* substrate preparation followed by an *in-situ* heat treatment. The cleaning procedure consists in a three-steps ultrasonication at room temperature with respectively strong organic solvents, high purity (>99.8%) acetone and spectroscopic grade 2-propanol (>99.999%) for 15 minutes.

The substrates are then mounted on a sample holder system, necessary for the movement and the positioning of the samples inside the growth chamber. The sample holder has a 10x10 mm² slot for samples. The sample holder is equipped also with a mask holder, so it gives the possibility to deposit samples with a specific shape by shadow masking.

Once placed inside the intro chamber and after the vacuum has reached an acceptable value below 1.0x10⁻⁷ mbar, the sample holder is moved into the effusion chamber where it is put in contact with a heating element. Heat is generated by a resistance controlled by an external power supply. The process consists in a 20' heat ramp from room temperature to 250 °C and 30' at constant temperature of 250°C to desorb moisture and partially carbonates. After this latter step the substrates are cool down and ready for the subsequent deposition.

3.1.2.2 *Choice of the substrate*

All the produced samples are grown on top of Al₂O₃(0001) single crystal substrates. The choice of Al₂O₃ as a substrate was dictated by the high quality of its surface and by lattice parameters of its (0001) surface, having a lattice mismatch with the *hcp* Co(0001) and *fcc* Co(001) of 5.9% [80], [81]. MgO(001) was initially considered but were rapidly discarded due to its hygroscopicity [82], a not perfect quality of the substrate's surface.

3.1.2.3 Growth of bare cobalt thin films and Co/molecule bilayers

Most of the of Co/Molecule or Co/Al bilayers is grown with an *extended geometry*, i.e. both layers cover the whole $\text{Al}_2\text{O}_3(0001)$ without any shadow masking (see **Figure 3. 4**). The deposition procedure is the following. After the substrates are annealed, they are moved into the metals chamber for growing the Cobalt layer. The evaporation is performed by e-beam evaporation at base pressure of 2.0×10^{-10} mbar. The deposition rate is kept fixed for every deposition, with a value of $0.03 \text{ \AA}/\text{sec}$. Since the requirement is to have a polycrystalline Co thin film, all the substrates are kept at room temperature during the process. The rate is checked by a QMB (typical values of the parameters are reported in **Table 3. 1**) and controlled by keeping constant the emission current. For the bare Co substrates no additional layer is required, so samples are then extracted. For the case of Co/Molecule and Co/Al bilayers, the samples are

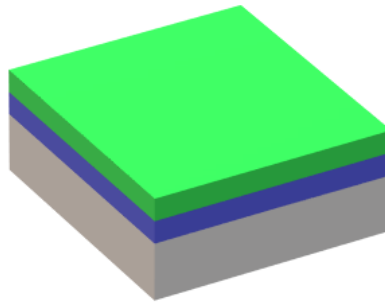


Figure 3. 4 Schematic of the samples grown. Co and Co/overlayer systems, extended geometry.

Table 3. 1 Deposition parameters for the used materials. P_0 is base pressure, T refers to the evaporation temperature of the materials.

Material	Co	Al	C_{60}	GaQ_3	T6
Evaporation	e-beam	Thermal	Thermal	Thermal	Thermal
Z ratio	0.343	1.080	3.4	1.000	8.800
Density (gr/cm ³)	8.71	2.73	1.65	1.49	1.4
P_0 (mbar)	2.0×10^{-10}	1.0×10^{-8}	1.0×10^{-8}	1.0×10^{-8}	1.0×10^{-8}
Rate ($\text{\AA}/\text{sec}$)	0.03	0.09	0.16	0.16	0.16
T ($^{\circ}\text{C}$)	X	1070	360	255	360
I_{fil} (A)	4.5	X	X	X	X
V (kV)	2.0	X	X	X	X
I_{emis} (mA)	5.0	X	X	X	X

moved back to the effusion chamber without breaking the vacuum where the deposition of the Al or molecular layer is performed. All the molecules (Gaq_3 , C_{60} , T6) and the Al are grown by thermal evaporation at base pressure of 1.0×10^{-8} mbar. More details on the deposition parameters are reported in **Table 3. 1**. Regardless of the materials deposited at this stage, the growth procedure is analogous. Deposition is performed at room temperature without any additional thermal treatment, while rate is checked by QMB: the deposition starts once the cell's temperature reaches the desired value and the rate is stable. To avoid inhomogeneities, the sample holder is constantly rotated during the process. In specific cases, to guarantee samples with the same Cobalt thickness, patterned masks are used to deposit multiple organic layer.

3.2 Microstructural characterization

3.2.1 Atomic Force Microscopy (AFM)

This microscopy technique is a powerful tool for imaging of surfaces. The resolution range of this instrument is wide as it goes from tens of micrometers down to tens of nanometers. It was invented in 1986 by Gerd Binnig and Calvin Quate[83] and it is part of the wide family of Scanning Probe Microscopy (SPM) techniques. Its major strength is that it can operate on a broad variety of surfaces, ranging from inorganic metals and insulators to organic molecules and even biological samples. Moreover it is capable of operating on different environmental conditions, from UHV to ambient pressure and even in liquid solutions.[84].

The working principle of AFM is rather intuitive. The probe is a flexible *cantilever* with a low curvature radius (<10 nm) tip. This latter is approached at a small distance from the surface to characterize (typical distance range from 10^2 to 10^{-1} nm). As the two systems are sufficiently close together, the electrostatic interactions result in a measurable bending of the cantilever, which is then measured and converted in a tip-surface distance value.

An AFM morphology image is taken by N linear translations (linescans) of the tip over the sample surface. For each linescan N equidistant points are probed, resulting in a $N \times N$ matrix of pixels each of which contains an height value, corresponding to the surface morphology.

3.2.1.1 *Tip-surfaces interactions*

In the following the discussion will be limited to the cases of interest for obtaining topographic information of the surface. The tip-surface interactions in this case are electrostatic in nature and are mainly Van der Waals and contact interaction.

The former is a weakly attractive interaction caused by electric dipoles present both in the tip and the surface, due to small unbalances of the charge distribution the outermost atoms. In general they can be either intrinsic of the system or induced by an external perturbation (induced dipoles). This force scales down as r^{-6} where r is the distance between the two systems interacting. For a typical AFM measurements this interaction is the main responsible for the cantilever bending for tip-surface distances of order 1-10 nm.[84].

Contact interactions on the other hand are strong repulsive forces that are due to Pauli exclusion principle. Since hundreds of atoms are involved at the same time, the typical approximation that is done is to treat this energy term as a classical mechanical contact interaction.

The general tip-surface interactions can be qualitatively summed up and understood by a Lennard-Jones potential (see also **Figure 3. 5**)

$$U(z) = U_0 \left[\left(\frac{z_0}{z} \right)^{12} - 2 \left(\frac{z_0}{z} \right)^6 \right] \quad (3. 3)$$

Here U_0 is the potential minimum, found at a distance z_0 from the surface. The z^{-12} term accounts for the highly repulsive contact forces, while the z^{-6} term incorporates a generic Van der Waals interaction. This very simplistic description allows to briefly discriminate from two classes of AFM measurement mode: contact and non-contact. In the former the tip is brought at sub-nm distances from the surface and the deflection is caused by the repulsive forces acting

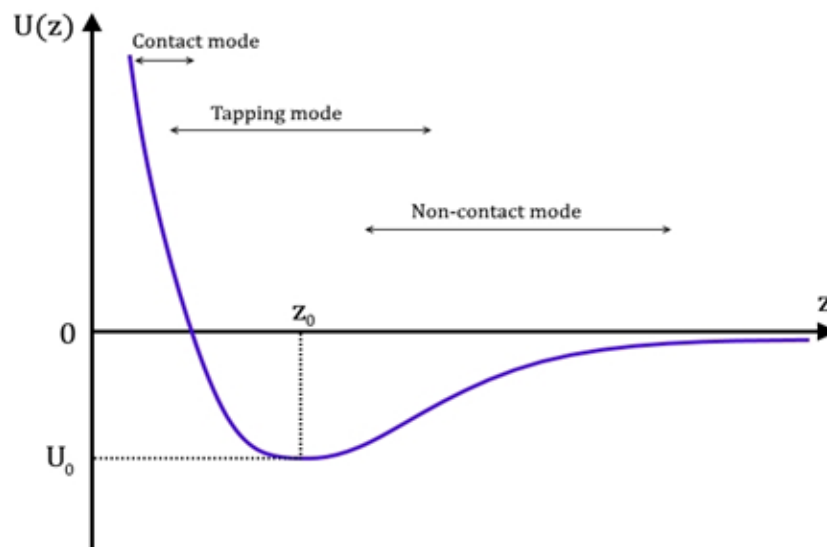


Figure 3. 5 Sketch of a Lennard-Jones potential. Arrows indicated the typical distance range for the possible tip-surface interaction

on the tip. In non-contact mode the deflection is caused by weak Van der Waals attraction and is best suited for mapping soft or damageable materials[84].

3.2.1.2 *Interaction models: point-mass model*

While conceptually intuitive, the actual theoretical treatment of the tip-surface interaction is highly complex, so much so that it is typically treated in the framework of classical mechanics. The case of interest is the amplitude modulation AFM (AM-AFM), in which the tip is driven into oscillation by an external retroaction system. In this case the equation governing the system is analogous to a driven harmonic oscillator with damping plus an additional term that contains information on the tip-surface interaction. [84] The tip-cantilever system is approximated by a point mass particle fixed at the end of a spring, connected to an external system that provides a sinusoidal forcing term. A damping element is also added to the system. The equation of motion is

$$m\ddot{z} = -kz - \frac{m\omega_0}{Q}\dot{z} + F_0 \cos(\omega t + \varphi) + F_{t,s}(d) \quad (3.4)$$

that is a nonlinear, second order differential equation. m is the tip mass, k is the cantilever elastic constant, z is the displacement from the equilibrium position ($=0$), ω_0 is the resonance frequency of the system, Q is a cantilever dependent parameter called quality factor, F_0 is the amplitude of the sinusoidal forced oscillation with frequency ω and $F_{t,s}(d)$ is a force representing the tip-surface interaction, dependent on the distance d . The damping term introduced considers the viscous friction with the air atmosphere. If the tip is placed far from the surface, then $F_{t,s}(d)=0$ and it can be shown[84] that the system, in the limit of high quality factor Q (vanishing damping), oscillates with amplitude

$$A(\omega) = \frac{\frac{F_0}{m}}{\sqrt{(\omega_0^2 - \omega^2)^2 + \left(\frac{\omega\omega_0}{Q}\right)^2}} \quad (3.5)$$

Which is a Lorentzian-like function peaked at maximum ω_0 with amplitude

$$A_0 = \frac{QF_0}{k} \quad (3.6)$$

Now if the tip is brought about the surface, the additional interaction term becomes non-negligible and results in a shift of the resonance frequency given by

$$A(\omega_0, z) = \frac{\frac{F_0}{m}}{\sqrt{\left(\frac{\dot{F}}{m}\right)^2 + \frac{\omega_0^4}{Q^2} - \frac{\omega_0^2 \dot{F}}{Q^2 m}}} \quad (3.7)$$

explicitly dependent on the gradient of the force produced by the tip-surface interaction.

3.2.1.3 Components of an AFM

An AFM can be divided in different components. The first one is the tip-cantilever system, that is the probe used for surface imaging. Typically (as is the case for the ones I used for this thesis) are made in silicon, with small (nm range) curvature radius of the tip. The back of the cantilever is translucent so it ensures optimal light reflection. This is important since the deflection of the probe is measured by shining a laser light on the top surface of the cantilever (see **Figure 3. 6**). The reflected beam is directed towards a matrix of photodiodes that measure its intensity and convert it into a photocurrent. Displacements of the cantilever then result in a modification of the measured photocurrent, that is converted into a tip-surface distance.

The tip-cantilever system is put into oscillation by a piezoelectric actuator, that is a device able to contract/expand upon application of a suitable voltage. The variation of lateral dimension can have a sub-Å accuracy. The movement of the tip with respect to the x-y plane defined by the surface is performed by the *scanner*, that is composed of a set of piezoelectric actuators that bend upon application of a voltage. In the instrument that I used for this work (NT-MDT Solver P47) instead, the cantilever is fixed in space and the sample to be measured is moved with respect to the tip.

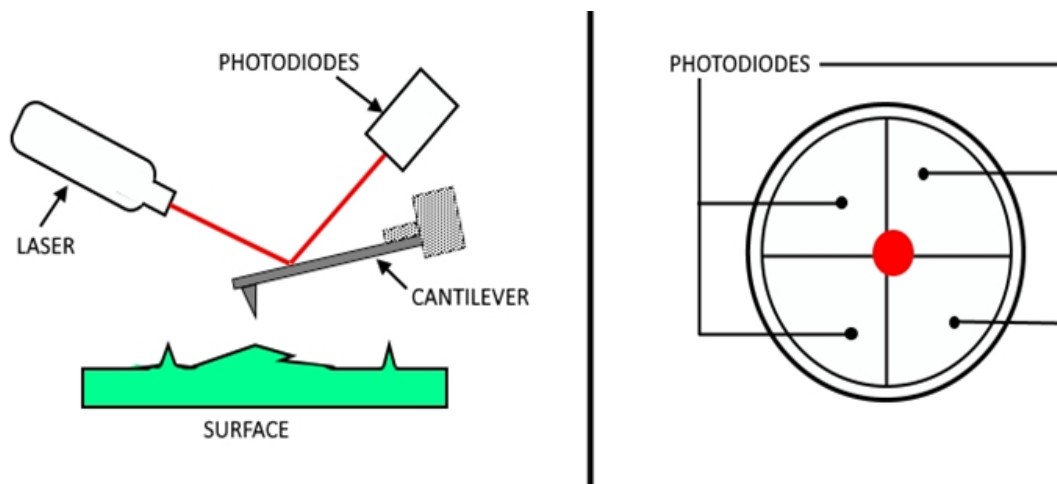


Figure 3. 6 Left: sketch of the deflection measurement. The laser reflected by the top plating of the cantilever hits a matrix of photodiodes (Right).

The vertical displacement of the tip is done by another piezoelectric actuator governed by the so-called *feedback system*. It is a set of electronic systems that are used for control of all the important parameters during scanning of the sample. For the case of AM-AFM, a lock-in amplifier is set to the oscillating frequency of the tip. The resulting signal is proportional to the amplitude oscillation, which is then compared to a particular reference value called *amplitude set-point* A_s . This value represents the desired oscillating amplitude of the cantilever when the tip is interacting with the surface and gives an indirect (and nontrivial) information on the tip-surface distance. The objective of the feedback system is thus to minimize the difference between A_s and the actual oscillation amplitude of the cantilever. It does this by outputting a voltage value that is sent to the piezoelectric actuator responsible for the vertical displacement of the sample.

3.2.2 AFM: Calculation of the surfaces characteristic length scales

3.2.2.1 Surface roughness

The roughness of the surface can be calculated in two different ways. The first and the most straightforward is to measure it as the Root Mean Square (RMS) of height distribution. For a set of N pixel containing the value z of the heights, the RMS is their standard deviation

$$\text{RMS} = \sqrt{\sum_{i=1}^N (z_i - Z)^2} \quad (3.8)$$

where Z is the average height. Although of easy implementation, its value can be easily modified by the presence of defects, intended in this context as any unwanted features of the image. A second method is to compute the height distribution function $\rho(z)$. For a random surface, it is expressed by a Gaussian function of the form

$$\rho(z) = A e^{-\frac{(z-Z)^2}{2\delta^2}} \quad (3.9)$$

where Z is the mean height and δ is standard deviation. If the number of unwanted pixels is much less than the ones of interest, or if we have two different well separated (in height) surfaces, then $\rho(z)$ is very well approximated by a Gaussian function in the heights range of interest. The roughness is then well associated to the value of δ . The value of RMS and δ coincide for random surfaces. As an example consider **Figure 3.7** in which a defective surface is presented. The calculation of RMS gives a value for the roughness of $(0.7 \pm 0.2 \text{ nm})$, while the fit of $\rho(z)$ with a Gaussian yield a value of $(0.3 \pm 0.1) \text{ nm}$.

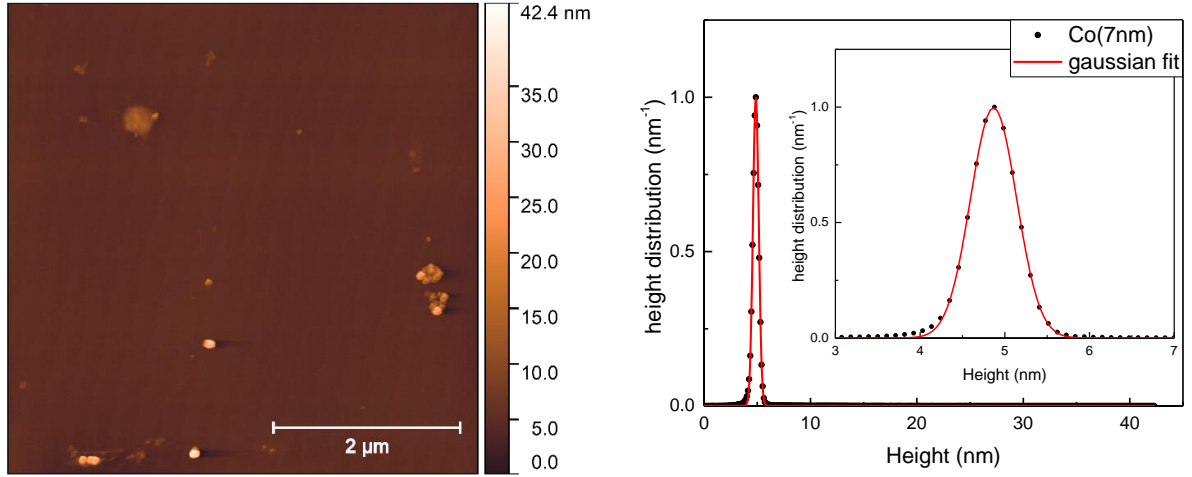


Figure 3. 7 Left: AFM image of a bare 7 nm Co surface, with presence of defects. Right: the height distribution of the images, showing a clear peak centered at 5 nm.

3.2.2.2 Mean Grain Size

It is determined by a procedure described in [85] and based on the work of *Rasigni et al.* [86]. The theoretical background is now presented. Given a generic surface, it is defined an autocorrelation function (ACF) $G(x)$ as the second-order moment of the function $H(x)$ describing the deviation in altitude from the mean height Z along a specific direction x (e.g. a line profile)

$$G(x) = \langle H(x)H(x') \rangle \quad (3. 10)$$

where $H(x)$ and x' is defined as

$$H(x) = z(x) - Z \quad (3. 11)$$

$$x' = x - \tau \quad (3. 12)$$

Z here is the mean height along that profile and τ a translation vector. The ACF can be expressed by a suitable function that takes for argument a scaled version of the position x

$$G(x) = \hat{G}\left(\frac{x}{\sigma}\right) \quad (3. 13)$$

The form of \hat{G} is typically a Gaussian or a Lorentzian [86]

$$\hat{G}_G(x) = \delta^2 \exp\left(-\frac{x^2}{\sigma^2}\right) \quad (3. 14)$$

$$\hat{G}_L(x) = \delta^2 \left(1 + \frac{x^2}{\sigma^2}\right)^{-1} \quad (3. 15)$$

Where $\delta = \sqrt{\widehat{G}(0)}$ is the roughness of the surface and σ is the autocovariance length (ACL). It is defined, for an arbitrary form of \widehat{G} , as the lateral distance after which the magnitude of the ACF is smaller than a certain value V , so it is interpreted as the average distance over which the structure is correlated. It is therefore straightforward to associate it with the medium grain size. Though there is no universally accepted value for V , in the case of a Lorentzian, σ is given by the following condition[86]:

$$|\widehat{G}_G(x)| < \frac{\delta^2}{2} \text{ for } x \geq \sigma \quad (3.16)$$

In general surfaces are not always random. There can be hidden periodicities along certain directions, so the surface is *pseudorandom*. In this case the ACF is not a monotonically decreasing function of the translation vector τ . It is then proven that the ACL extracted from initial portion of the ACF (small arguments) is still related to the small scale variations of the surface[86]. The evaluation of σ is then made by fitting the initial portion of the ACF, calculated along both the x and y scan directions, with either a Lorentzian or a Gaussian function (depending on the one that better reproduces the data) and extracting the values from the fit. The fitting functions are

$$\widehat{G}_G(x) = y_0 + a_G \exp\left(-\frac{(x-X)^2}{2b_G^2}\right) \quad (3.17)$$

$$\widehat{G}_L(x) = y_0 + a_L (b_L^2 + (x-x_0)^2)^{-1} \quad (3.18)$$

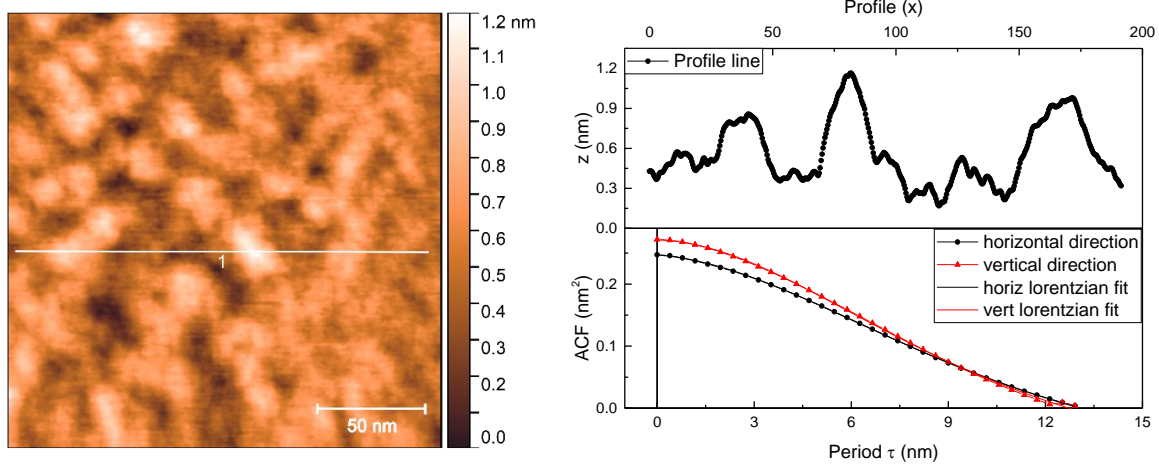


Figure 3. 8 Left: 200 nm lateral dimension Co(3nm) surface, clearly granular in nature. Right: line profile 1 and the ACF calculated along the horizontal and vertical linescan. Dots represent the calculated values from the data, lines the Lorentzian fit operated. The two curves are well-matching.

By a comparison with $\hat{G}_L(x)$ and $\hat{G}_G(x)$ the relation between b and σ are straightforward

$$\sigma = b_L \quad (3.19)$$

$$\sigma = b_L \quad (3.20)$$

Consider as an example **Figure 3. 8** in which is reported a $200 \times 200 \text{ nm}^2$ AFM image of a Co surface, 3 nm thick. The surface is granular and, as can be qualitatively understood by the profile, there are some repeating low scale features. It is difficult to properly understand the lateral dimension unless many profiles are taken, and the mean grain size is associated to the mean FWHM of the various bumps. The ACF calculated for low arguments is well in line with the performed fits, giving as value of the Mean Grain Size $(10 \pm 1) \text{ nm}$.

3.2.2.3 Surfaces periodicities

The presence of periodicities on the mapped surface can be extracted by both the ACF and the Power Spectrum Density function (PSDF). If employing the former function any periodicity will appear as secondary, evenly spaced maxima of the ACF. If employing the PSDF, that is the Fourier transform (FT) of the ACF, then the periodicity is highlighted by peaks centered above their wave vector. The second method is implemented for this work. Given that it is not known *a priori* if the periodicities will be parallel or perpendicular to the line scan, it is computed the radial PSDF. As an example consider **Figure 3. 9**, in which is reported an AFM image of an $\text{Al}_2\text{O}_3(0001)$ surface. A repeated pattern is clearly visible and highlighted by the profile line reported. The radial PSDF of the image shows a bump at a wave vector $k = 2.4 \times 10^7 \text{ m}^{-1}$ corresponding to a period of $260 \pm 15 \text{ nm}$.

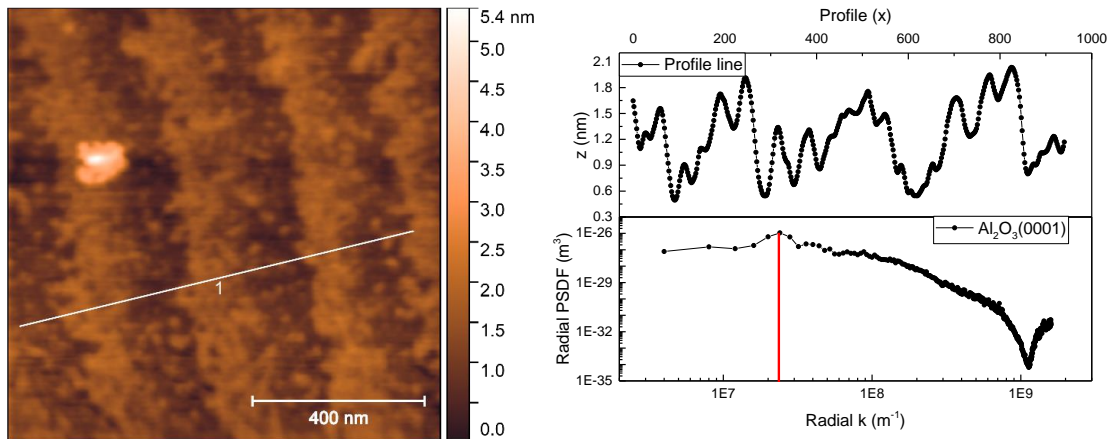


Figure 3. 9 Left: $\text{Al}_2\text{O}_3(0001)$ surface. A clear periodicity is evident. Right: line profile 1 highlighting a periodic pattern and the radial PSDF of the image, showing a bump at a wave vector corresponding to a period of $260 \pm 15 \text{ nm}$.

3.2.3 Transmission Electron Microscope

A Transmission Electron Microscope (TEM) is a microscopy instrument that exploits the wave-like nature of electrons for obtaining high resolution images of very thin samples. These microscopes work by accelerating and focusing a beam of electrons towards a sample to be imaged. Once inside the sample, the probe electrons are scattered (elastically or inelastically) by the coulomb potential generated by both the system nuclei and electrons. Once they are transmitted out of the sample, they are refocused and collected producing a detailed image of the system surface.

The advantage of using electrons as probes for imaging is the high resolution that can be achieved, since their de-Broglie wavelength (setting the diffraction resolution limit) is (considering relativistic effects)[87],[88]

$$\lambda = \frac{h}{\sqrt{2m_e eV \left(1 + \frac{eV}{2m_e c^2}\right)}} \quad (3.21)$$

where m_e is the rest mass of the electron, V the accelerating potential and h the Planck constant. For a 200 keV potential a wavelength value of 2.5 pm is obtained, so ideally structure smaller than an atom may be probed.

The main components of a TEM microscope are briefly discussed (see **Figure 3. 10**). The electrons are produced (as in the case of the JEOL JEM-2100F TEM used in this thesis) by a field emission gun, which is composed of a sharp tip (typically of Tungsten) with high curvature radius, biased by a positively charged anode[87]. This voltage lowers the tip's work function and allows electrons to exit the tip. A second anode accelerates the extracted electrons to the desired velocity. The electrons are then focused by electromagnetic lenses. These are electromagnets composed of a holed FM pole with axial symmetry, surrounded by copper coils. Electrons travelling through the electromagnet feel a Lorentz force proportional to their velocity component perpendicular to the generated B field induction. This creates a focusing effect correcting the trajectory of electrons entering with a direction of motion tilted with respect to B. Unavoidable inhomogeneities in the magnetic field of the lenses and slightly different focal points for electrons travelling closer to the optical axis (that is the desired direction of the electron beam) ultimately produce aberration that reduces the instrument resolution. They can be overcome by the use of apertures, that are metallic plates with a regulable hole of radius r . Electrons that are travelling at a radial distance from the optical axis higher than r are excluded.

After electrons exit from the sample they are refocused by a set of lenses and reach a screen, over which they reproduce the surface of the sample. For this thesis TEM was used to characterize the microstructure of the Cobalt layer. For doing so with a TEM, the sample needs to be sectioned in order to produce thin vertical slices, called *lamellae*. They are created by Focused Ion Beam (FIB). Its working principle is analogous to the TEM, but instead of electrons ions of a particular element, usually Gallium, are emitted from a suitable source and accelerated towards the sample. Electromagnetic lenses ensure highly focused beam. Ga ions impinging on the sample surface then sputter away the atoms of the system on a lateral range R ultimately determined by the degree of focusing of the Ga ions beam.

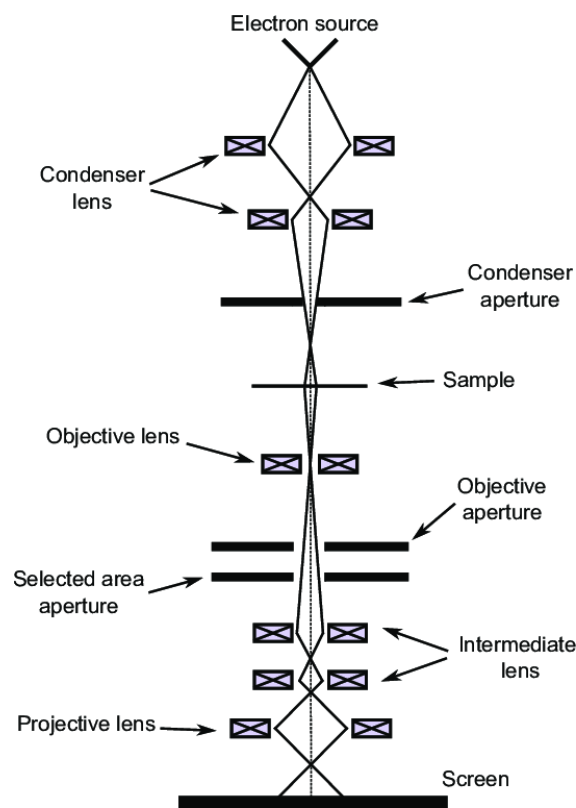


Figure 3. 10 Schematic of a TEM microscope. Taken from [88].

3.3 Magnetic characterization techniques

3.3.1 Magneto-Optic Kerr Effect (MOKE)

First discovered by Rev. John Kerr in 1877[89], the Magneto Optic Kerr Effect (MOKE) is essentially the modification of the polarization state of a light beam upon reflection from a magnetized material. This technique received massive consideration in the last decades, since

it allows the possibility to magnetically characterize in an easy and not too costly way the behavior of small-sized magnetic systems, such as ultra-thin films or low-dimensional magnets[90]. The technique is particularly suited for *in-situ* characterization of magnetic materials, since the probe is essentially a beam of light that gets reflected from the sample[48]. The technique proved to be effective also for fast and ultrafast high-density magneto-optical recording[91], [92]. The description of the magneto-optical interactions can be done either on a macroscopical or microscopical framework. The first uses a classic approach involving the modification of the dielectric tensor component by a phenomenological magneto-optic coupling, while the latter is developed in quantum theory framework, based on the effects of both exchange interaction and spin-orbit coupling on the absorption rates of left and right circularly polarized light [90], [93], [94].

3.3.1.1 *Theoretical background*

In the following I will give a brief description of the macroscopic and microscopic description of MOKE, a simple consideration will be done, based on the classical motion of electrons subject to electromagnetic fields. If a linearly polarized (LLP) light interacts with an electron, this latter will oscillate following the \mathbf{E} field. Moreover, LLP light can be considered as the sum of a left and a right circularly polarized (LCP and RCP) light beams in phase with each other and with the same amplitude E . Free electrons that interact with RCP or LCP will start to move in right and left circular motion respectively. Since both \mathbf{E}^\pm (+ and – indicate respectively RCP and LCP) are equal in amplitude and phase, the electron orbits will be equal and opposed, producing a LLP electromagnetic reflected wave equal to the incident one and no Kerr effect takes place. If an external magnetic field is applied parallel to the EM propagation direction, an additional Lorentz force will act on the electrons, modifying their orbits. Since the action of this \mathbf{B} field induces only clockwise circular orbits (given the \mathbf{H} direction chosen), the orbit radius caused by RCP light is increased while the other is decreased. This means that electrons motion under LLP + external \mathbf{B} is no more akin to an oscillating dipole but becomes elliptical, with the major axis rotated by an amount θ_K with respect to the incident light polarization axis. Thus the reflected EM wave is elliptically polarized, with a rotated major polarization axis. From this simple explanation it is already possible to define the two observable quantities in a MOKE experiment. The first is the Kerr angle θ_K , definable as the angle between the ellipse's major axis and the original polarization axis. The second is the ellipticity which is related to the ellipse principal axis by $\eta_K = \tan^{-1}(b/a)$ [94].

The macroscopic description of the MOKE effect is based on the modification induced by the magnetization on the dielectric tensor $\hat{\epsilon}$ of the magnetic system. This tensor can be separated into a symmetric and an antisymmetric term. Since the former is diagonalizable, it cannot give any Kerr effect[90]. The antisymmetric part can be written as

$$\hat{\epsilon} = \epsilon \begin{pmatrix} 0 & iQ_z & -iQ_y \\ -iQ_z & 0 & iQ_x \\ iQ_y & -iQ_x & 0 \end{pmatrix} \quad (3.22)$$

where $\mathbf{Q}=(Q_x, Q_y, Q_z)$ is the Voigt constant that encodes the strength of the magneto-optic coupling. The two modes of propagation of the light (i.e. RCP and LCP) inside a magnetic medium will acquire two different velocities and thus will gain a phase shift. This is what ultimately causes the Kerr rotation. Moreover, the two modes also have different absorption rates, effectively producing an elliptical polarization. It is then straightforward to associate to each mode a complex refraction indexes n_{\pm} given by

$$n_{\pm} = n \left(1 \pm \frac{1}{2} \mathbf{Q} \cdot \hat{\mathbf{k}} \right) \quad (3.23)$$

where $n = \sqrt{\epsilon}$ and $\hat{\mathbf{k}}$ is the light propagation direction. Then, both the Kerr rotation and the ellipticity can be encoded in a single complex-valued angle Φ_K , so that

$$\theta_K = \text{Re}(\Phi_K) = \text{Re} \left[\frac{\pi L}{\lambda} (n_+ - n_-) \right] \quad (3.24)$$

$$\eta_K = \text{Im}(\Phi_K) = \text{Im} \left[\frac{\pi L}{\lambda} (n_+ - n_-) \right] \quad (3.25)$$

where L is the thickness of the FM layer and λ is the wavelength of the light. It is assumed that $\lambda \ll L$ [90].

3.3.1.2 *Experimental setup*

Before describing the experimental setup, in the following I will describe the working principle on which it is based. The incident light is purely in the p-polarized state. Upon reflection by the magnetized sample, a small component of E along the s direction is induced. The ratio E_s/E_p is the Kerr angle[90]. In principle it would suffice to directly measure E_s by placing a polarizer aligned perpendicularly to the p direction. However, the measurement itself is done by a photodetector that measures the light intensity, that would be $I \propto |E_s|^2$ and thus insensitive to the directionality of the Kerr rotation. No hysteresis loop would be observed. Additionally the induced s component is small (typical values of θ_K range from 10 to 0.1 mdeg) and no

appreciable signal would be detected. This issue is circumvented by allowing a small component of E_p to cross the polarizer, by setting its polarization axis at an angle $90^\circ + \delta$ with δ small. The measured intensity is now

$$I = |E_p \sin \delta + E_s \cos \delta|^2 \approx |E_p \delta + E_s|^2 \quad (3.26)$$

that can be rewritten in terms of the Kerr angle E_s/E_p

$$I = |E_p|^2 \left| \frac{E_s}{E_p} + \delta \right|^2 = |E_p|^2 |\delta^2 + \phi' + i\phi''|^2 \quad (3.27)$$

and, to lowest order in the ϕ 's,

$$I \approx |E_p|^2 (\delta^2 + 2\delta\phi') = I_0 \left(1 + \frac{2\phi'}{\delta} \right) \quad (3.28)$$

where I_0 is the intensity measured when there is no Kerr rotation ($M=0$). Now the terms that are proportional to the magnetization are not squared so the measured intensity is also a function of the direction of the Kerr rotation and an hysteresis loops is obtainable. The maximum value of the Kerr rotation is then calculated as

$$\phi'_{\text{sat}} = \frac{\delta \Delta I}{4 I_0} \quad (3.29)$$

where ΔI is the difference between light intensity measured at the maximum applied field and the corresponding at the reversed value of H .

The homemade MOKE setup I used in this work is depicted in **Figure 3. 12**. Its configuration allows for measurement of hysteresis loops with magnetization parallel to the film's surface (L-MOKE configuration). The light source is a 5 mW He-Ne laser ($\lambda=632.8$ nm). A first polarizer

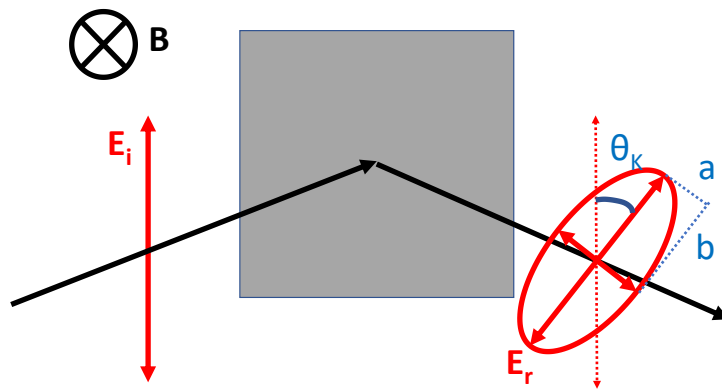


Figure 3. 11 MOKE effect: LLP light impinging on a magnetized sample by an external field \mathbf{H} will be reflected in an elliptical polarization state.

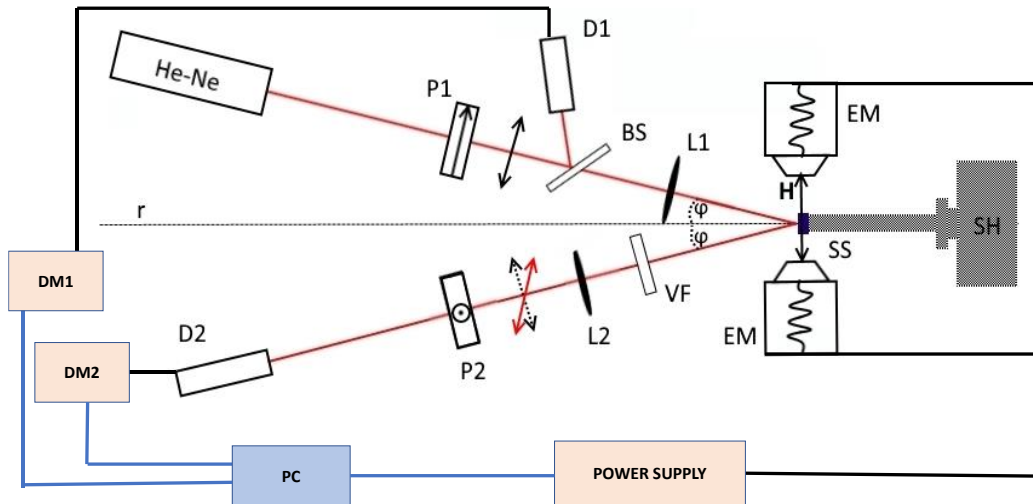


Figure 3. 12 Schematic of the MOKE setup.

(P1) sets the polarization state of the incident beam. For the measurements that I have performed a p-polarization was chosen. A beam splitter (BS) deflects part of the light to a reference photodiode (D1) that measures the initial light intensity. This value is used as a normalization constant to prevent intensity variations from affecting the measurement. A biconvex lens L1 focuses the laser beam over the sample, mounted on a rotatable sample holder (SH) and placed between the pole-caps of the electromagnets (EM – model GMW 3470) connected to a power supply (Kepco BOP 100-4D). SH allows rotation of the sample around the axis normal to the film plane. The reflected beam is refocused by a second lens (L2) and crosses a second polarizer (P2) with polarization axis oriented at $90^\circ + \delta$ with respect to P1. Light escaping P2 is collected by a second photodiode (D2). This latter is responsible for the actual Kerr rotation measurement. For measurement of the ellipticity, a $\lambda/4$ waveplate is placed before P2. The $\lambda/4$ role is to retard the EM wave phase by a quarter of wavelength. By looking at Eq. (3. 27) and (3. 28) the phase shift switches the real and imaginary part of the Kerr angle, so the actual measured quantity is η_K . The output voltage of the two photodiodes (proportional to the light intensity) is measured by two digital nano-multimeters (DM1 – HP 3457 A- and DM2 - Keithley 181). A PC connected to both the multimeters and the power supply controls the setup. The actual data acquisition is performed by a custom LabView program. For measurements in temperature, the sample holder is unmounted and replaced by a cryostat with Quartz window to allow for optical probing. Samples are then mounted over a cold finger that is manually inserted into the cryostat. This latter is connected to a turbo pump, ensuring UHV conditions. Control of the temperature is performed by an external control unit (Oxford Instruments MercuryITC).

3.3.2 Vibrating Sample Magnetometer (VSM)

The Vibrating Sample Magnetometer has become a standard tool for magnetic characterization of ferromagnetic samples. In a VSM setup (see **Figure 3. 13**), the sample is mounted over an actuator that puts it into vibration. An external static magnetic field H_A is applied for magnetizing the sample. The oscillating magnetic induction is measured by a set of pick-up coils. The change in magnetic flux induces an AC voltage inside the coils, with the same frequency of the vibration

$$V_{AC} = V_S \sin(\omega_s t - \phi_S) \quad (3. 30)$$

A reference system (e.g. a permanent magnet of known magnetic moment) is driven in synchronous oscillation with the sample in a set of reference pick-up coils. Both the sample and the reference voltages are sent to a lock-in amplifier. In this way the measured voltage, assured the condition $\omega_R = \omega_S + \delta\omega$ holds ($\delta\omega$ being the bandwidth of the band-pass filter), is

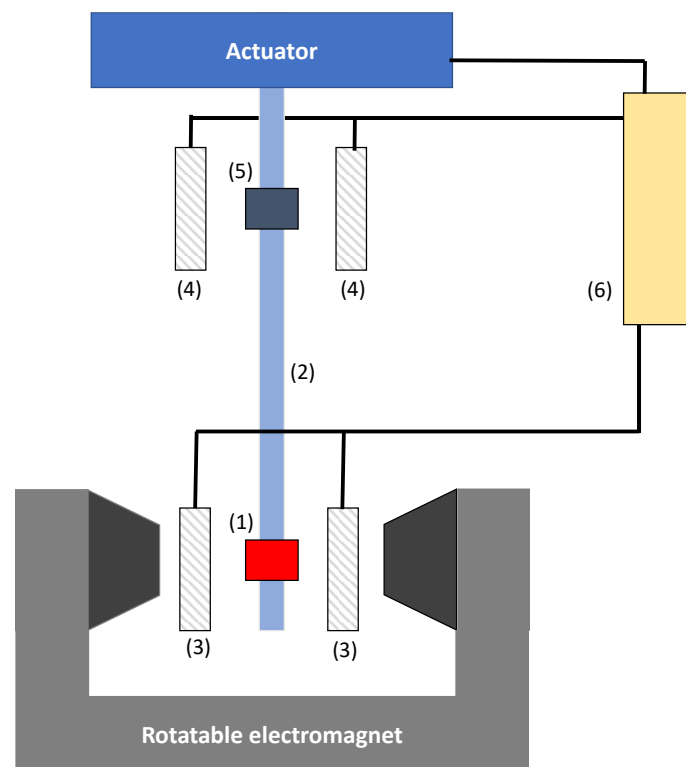


Figure 3. 13 Sketch of a VSM setup. The sample (1) is mounted on a sample holder (2) connected to a piezoelectric actuator. This latter puts the system into oscillation (perpendicularly to the applied field) producing a measurable AC signal detected by the pick-up coils (3) and sent to a Lock-in amplifier(6). This latter also measures the reference signal produced in another set of pick-up coils (4) by a reference ferromagnetic sample of known properties (5).

$$V = \frac{1}{2} V_R V_S \cos(\phi_S - \phi_R) \quad (3.31)$$

where V_R is the known voltage produced by the reference sample. By matching the two signal phases it is then possible to extract the value of the magnetic moment possessed by the sample for a given value of H_A . The setup used for this work is a MicroSense Model 10. It possesses four pair of pick-up coils, two of which are parallel to each other and connected, in order to measure the signal along one direction. The other two pairs are arranged in an equal fashion but are 90° rotated with respect to the others for collecting the signal produced in the orthogonal direction. This configuration allows to completely determine the value of the magnetization.

3.3.3 Superconducting Quantum Interference Device (SQUID)

This magnetometry technique takes advantage of the response of superconductors (SC) to external magnetic flux for probing magnetic fields. The SQUID sensor itself is a ring of superconducting material which contains two Josephson junctions[95] (see **Figure 3. 14(a)**), that are two SC layers separated by an insulator of thickness less than the SC coherence length ξ . The SQUID working principle is based on three main results. Firstly, in the presence of an external magnetic induction \mathbf{B} a superconducting current is generated. It is a consequence of the vector potential \mathbf{A} changing the phase ϕ of the wavefunction of the superconductor. Since this phase is quantized (i.e. $\Delta\phi = 2\pi m$ with m integer) it can be shown that the magnetic flux is given by

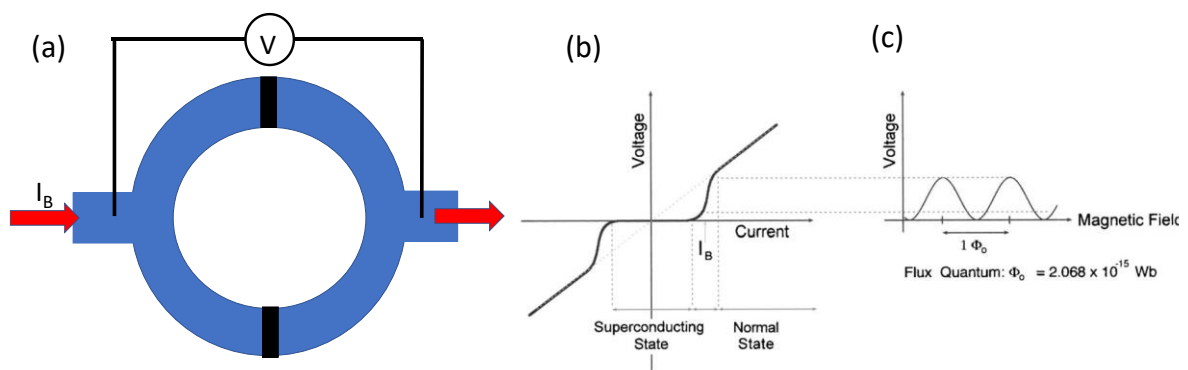


Figure 3. 14 (a) sketch of the SQUID device, composed of a SC ring (blue) separated by two Josephson junctions (black rectangles). (b) V-I curve of a Josephson junction, showing no voltage drop until a current higher than I_C is furnished. In the graph, I_B represents the typical setpoint of I_B for measurement of magnetic field. (c) periodicity of the voltage with the magnetic flux. Taken from [98].

$$\Phi = m \frac{h}{2e} = m \Phi_0 \quad (3.32)$$

which shows that the amount of flux inside the ring can take only discrete value i.e. is quantized[95]. The flux quantum Φ_0 amounts to 2.068×10^{-15} Wb. Secondly, if a superconductive current is induced in a Josephson junction, it will not show any resistive behavior since the insulating layer is thin enough to allow cooper pairs to quantum tunnel through the energy barrier. In this sense the junction is called *weak link*. This condition holds if the current is less intense than the *critical current* I_C of the junction, since it dictates the maximum amount sustainable before destroying the superconductive state. If $I > I_C$ then the junction has an ohmic behavior[95] (see **Figure 3. 14(b)**). Lastly, it can be shown that a magnetic-induced SC current flowing across a single Josephson junction is zero if the magnetic flux producing it is an integer number of Φ_0 .

A SQUID device operates as follows. A bias current I_B is applied to the extreme ends of the SC ring. Since the two branches (labelled 1 and 2) are equal, a current $I_B/2$ flows across each junction. If $I_B/2$ is set at a value very close to the critical current of the junction I_C , when an external magnetic field is applied to the device, the resulting flux will induce a screening current that sums up with $I_B/2$ in one branch ($I_1 = I_B/2 + I_{screen} > I_C$) while decreases the total current in the other ($I_2 = I_B/2 - I_{screen} < I_C$). This results in a measurable resistive response of the device. However, the junctions suppress currents if generated by a magnetic flux equal to an integer multiple of Φ_0 . The measured voltage is thus periodic in the applied flux, with period Φ_0 (**Figure 3. 14(c)**). By monitoring the change in voltage it is thus possible to determine the magnetic flux that is acting with the SQUID device[95]. By virtue of the dependence of the measured voltage on the

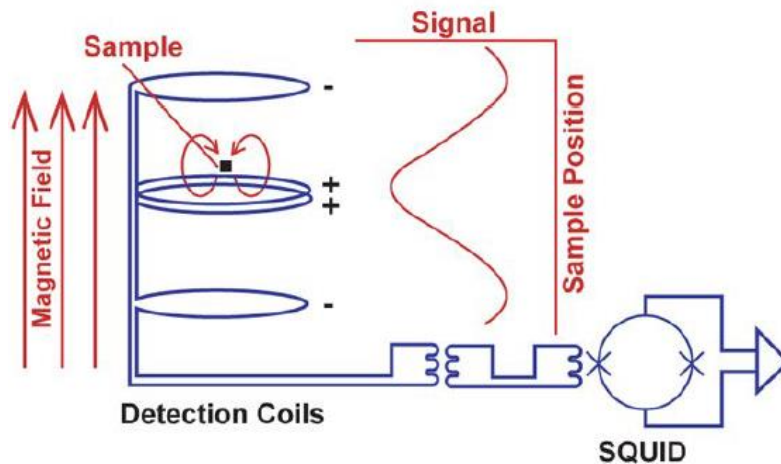


Figure 3. 15 Sketch of the SQUID detection apparatus (taken from [99]).

quanta of flux, this device can sense extremely low fields. Considering that $1 \text{ Wb}=1\text{T}/1\text{m}^2$, for a SQUID device of area 1cm^2 field inductions of $2.068\times 10^{-11} \text{ T}$ are theoretically measurable.

The squid experimental setup (Quantum Design MPMS-XL[96]) is briefly discussed in its basic components (see **Figure 3. 15**). The sample is mounted in a sample holder (*straw*) and positioned inside the detection region. A set of inductively coupled superconducting coils detects the magnetic flux produced by the sample as it moves back and forth perpendicularly to the coils. The current flowing through these latter is balanced by an electronic control mechanism in order to compensate the static applied field that magnetizes the sample. The coils are inductively coupled to the SQUID device, which is placed inside a superconducting shielded region, to avoid spurious signals coming from external magnetic fields. The SQUID then gives an output voltage which is proportional to the flux induced in the reference coils. A reference sample of known magnetic moment is used to calibrate the instrument.

3.4 Magnetic resonance characterization

3.4.1 Nuclear Magnetic Resonance

When an atomic nucleus with nonzero nuclear spin I and magnetic moment μ is subject to a magnetic field induction B_0 , it will start to rotate with Larmor frequency $\omega_L=\gamma B_0$ where γ is the nuclear gyromagnetic ratio. The energy of the interaction is then a Zeeman term

$$E=-\boldsymbol{\mu} \cdot \mathbf{B}_0=-g_N\mu_N m_I B_0 \quad (3. 33)$$

where $\mu_N=5.0508 \times 10^{-27} \text{ Am}^2$ is the nuclear magneton, g_I the nuclear g -factor and m_I is the projection of the nuclear spin along the quantization axis (parallel to B). This sets a ladder of $2I+1$ evenly spaced energy levels separated by an amount $g_N\mu_N B_0$. The allowed transitions are given by the selection rule $\Delta m_I=\pm 1$ [48]. If an external radiofrequency (*rf*) field H_{rf} is applied, then the nucleus is excited if the *rf* frequency ω is equal to

$$\omega=\frac{1}{\hbar} \Delta E=\frac{g_N\mu_N B_0}{\hbar}=\gamma B_0 \quad (3. 34)$$

A NMR measurement requires an external magnetic field to magnetize the nuclei of the system, and an inductive coil perpendicular to H_0 that serves as both generating the *rf* field H_{rf} and to probe the behavior of the nuclear magnetization \mathbf{M} in time. Here \mathbf{M} indicates the volume density of the nuclear magnetic moment. For a single isotope (as is the case of ^{59}Co) the equation of motion of \mathbf{M} subject to a static field H_0 and a *rf* field H_{rf} is described in a phenomenological manner by the Bloch equations[97], by treating the spins as classical objects. The main results

are reported in the following. When \mathbf{M} is driven out of equilibrium and tilted by an angle φ from the action of a pulsed *rf* field of duration τ , it would rotate for an indefinite amount of time about H_0 . However, nuclear spins are always coupled to their environment, i.e. to other nuclear spins and to the electronic system, called in jargon the *lattice*. This spin-lattice interaction takes the name of hyperfine interaction[48], [98]

$$H_{\text{HF}} = \mathbf{I} \cdot \hat{\mathbf{A}} \cdot \mathbf{J} \quad (3.35)$$

where \mathbf{J} is the total angular momentum of the ion and $\hat{\mathbf{A}}$ is a rank 2 tensor defining the coupling strength. This interaction allows nuclear spins to exchange energy with the lattice and thus to relax back to its equilibrium value $M_{z,\text{eq}}$ according to[97]

$$M_z(t) = M_{z,\text{eq}} \left(1 - \exp\left(-\frac{t}{T_1}\right) \right) \quad (3.36)$$

where T_1 is called the spin-lattice relaxation time. The interaction between nuclear spins, called spin-spin interaction, is a dissipative term. After the application of the *rf* pulse, \mathbf{M} acquires nonzero, oscillating components $M_x(t)$ and $M_y(t)$. Their oscillation amplitude, measured by the *rf* coil, decays to zero as the spin ensemble loses coherence, as

$$M_x(t) = M_{x,0} \exp\left(-\frac{t}{T_2^*}\right) \quad (3.37)$$

where T_2^* is the spin-spin relaxation time. This is not strictly correct however, since this decoherence is also due to field inhomogeneities, resulting in different precession frequencies. One way to overcome this issue is to apply a sequence of two pulses. One initial pulse of duration $\tau_{\pi/2}$ ($\pi/2$) rotates the nuclear magnetization at an angle $\pi/2$. The nuclear spins start to rotate in the *xy* plane meanwhile they are losing coherence. A second pulse of duration $\tau_{\pi} = 2\tau_{\pi/2}$ rotates the spins by an angle π , with the effect of rephasing the spin ensemble[48]. The *rf* coils will measure an oscillation amplitude that goes from 0 to a maximum value M_x and then decays again. The induced signal in the coils is called *spin echo* and contains information about the true spin-spin relaxation time T_2 . This signal is the one I used to gather information about the samples that I characterized. From now on all the term magnetization will be referred to the ferromagnetic one.

3.4.2 Ferromagnetic NMR

In a ferromagnetic sample, due to its spontaneous magnetization, the nuclear spins are always experiencing a magnetic field[99]. Focusing only on thin films of $3d$ transition metals, it can be shown[98] that the total field felt by the nuclei is (in absence of an external field H_{appl})

$$H_{\text{TOT}}=HF+H_{\text{DIP}} \quad (3.38)$$

where H_{DIP} is the dipolar field produced by all the other magnetic moments in the sample, and HF is the hyperfine field generated by the interactions between the nuclear spin and the magnetic moments of the electrons in the ion radius. The dipolar term in thin films is usually dominated by the demagnetizing factors, so it can be written as [100]

$$H_{\text{DIP}}=-\mu_0 M \cos(\theta) \quad (3.39)$$

where θ is the angle between \mathbf{M} (the magnetization of the electronic system) and the film's normal. For an in-plane magnetization $H_{\text{DIP}} \approx 0$. The hyperfine field instead can be decomposed in three main contributions[98]

$$HF=H_{\text{con}}+H_{\text{dip,at}}+H_{\text{orb}} \quad (3.40)$$

H_{con} is called the *contact field* and it arises from the Fermi contact interaction between the core electrons and the nucleus. As such, the main contribution to this term is *mainly* provided by s electrons of both core and valence levels[101]. Since their spin-polarization is due to intra-atomic exchange interaction with the $3d$ orbitals, H_{con} is aligned antiparallel to the sample's magnetization. $H_{\text{dip,at}}$ accounts for a dipole-dipole interaction between the nuclear magnetic moment and the spin density of the $3d$ shell. H_{orb} instead is related to the interaction between the nuclear magnetic moment and the unquenched part of $3d$ orbital momentum (due to SOC) [98], [102], [103]. This last term is thus proportional to the expectation value of the orbital momentum operator for a $3d$ orbital[99]

$$H_{\text{orb}} \propto \left\langle \frac{\hat{\mathbf{L}}}{r^3} \right\rangle \quad (3.41)$$

As such, for a cubic site symmetry this term is isotropic, while for hexagonal environments it acquires an angular dependence on the c axis[101], [104], making this contribution dependent on the direction of the magnetization.

In general the HF field is dependent on the symmetries of the environment: in this regard, in all the sites that present a loss of translational symmetry the nucleus will feel a different HF with respect to that of the bulk.

The crucial aspect of FNR is that the interaction between the nuclear spins and an applied *Radio Frequency (rf)* magnetic field H_{rf} is mediated by the electronic magnetic moments due to their coupling with the nuclear magnetic moments[98], [102]. The application of H_{rf} causes a small angular displacement $d\theta$ of the electrons' moment, that is reflected by a rotation $d\phi$ of HF (see **Figure 3. 16**). This means that the actual *rf* field felt by the nuclei is η times bigger than the applied one, η being called the *enhancement factor* and defined by

$$\eta = \frac{H_{rf,eff}}{H_{rf}} \quad (3. 42)$$

For *3d* ferromagnets typical values of η are in the range 10^2 - 10^4 . After the nuclear spins are driven out of equilibrium, they rotate back to their equilibrium position. In doing so, the nuclear magnetic moments exert a torque on the electronic magnetization (through HF) that is driven into oscillation. This latter acquires a transverse alternate component which is η times bigger than the nuclear component. As such, the *rf* signal probed by the coil is enhanced by a factor η [102]. As discussed in Chapter 2, in FM materials the electronic spins are aligned along preferential directions that are dictated by the anisotropy energy terms. The stronger the anisotropy, the more difficult it is to perturb the electronic moments. The enhancement factor is related to the local hardness of the system. This relationship is encoded in the so-called

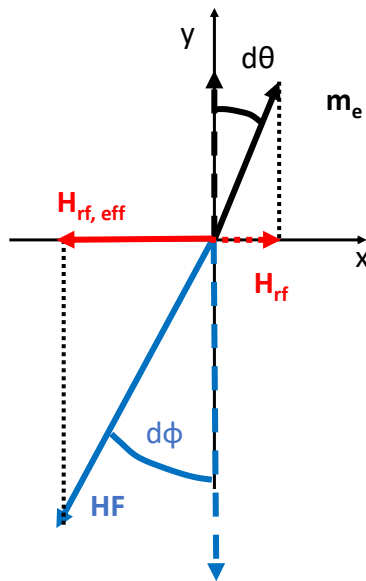


Figure 3. 16 The application of H_{rf} displaces the magnetic moments m_e by a small angle $d\theta$. In turn the HF is rotated by an angle $d\phi$, producing an enhanced *rf* field $H_{rf,eff}$ that acts on the nuclear spins.

restoring field H_r , that represent the torque exerted on the electronic magnetization after it is rotated by an angle $d\theta$. In absence of an external field it is due to the anisotropic energy terms. H_r can be expressed as

$$H_r = \frac{H_{rf}HF}{H_{rf,eff}} = \frac{HF}{\eta} \quad (3.43)$$

By recalling that HF is related to the nuclear Larmor precession frequency

$$\omega_L = \gamma HF \quad (3.44)$$

where γ is the nuclear gyromagnetic ratio (for ^{59}Co $\gamma = 6.3472 \frac{\text{rad}}{\text{Ts}}$). The restoring field can be also expressed as a function of the resonance frequency ω

$$H_r = \frac{\omega_L}{\gamma \eta} \quad (3.45)$$

From the above discussion one conclusion is drawn. The restoring fields is dependent on HF , and this latter is sensitive, for a given Co nucleus, to both the local structural and magnetic environment. It follows then that H_r depends on the actual environment probed by choosing a specific rf frequency, so it gives site-specific information on the local magnetic hardness. The frequency ranges implemented in a FNR characterization (GHz regime) are far from any electronic resonance frequencies, so the electronic magnetic moment follow the rf field adiabatically.

Regarding the signal measured by the rf coils as a function of both the applied field and the resonance frequency, it has the following form

$$S(\omega, H_{rf}) = I(\omega) \omega^2 \eta \exp\left(\frac{\log\left(\frac{H_{rf}}{H_{rf}^*}\right)^2}{2\sigma^2}\right) \quad (3.46)$$

here, $I(\omega)$ is the actual rf signal produced by the nuclei and H_{rf}^* is the applied field for which the maximum spin-echo signal is obtained. This field is expressed by the condition

$$\eta H_{rf}^* = H_{rf,eff}^* = \pi / (2\gamma\tau) \quad (3.47)$$

where τ is the duration of the probe pulse. From the above equation it is clear that the harder the magnetic material is, the more field intensity is needed to obtain a maximum of the spin-echo[105]. At fixed frequency the signal has a log-normal dependence on the H_{rf} intensity. Thus for obtaining the true signal coming from the ^{59}Co nuclei as a function of the resonance frequency, several spectra are taken by varying the applied rf field power P_{rf} . In this way it is possible to normalize the signal by its ω^2 dependence and the enhancement factor η .

3.4.3 Experimental setup

A schematic of the experimental setup is depicted in **Figure 3. 17**. The sample is placed inside a rectangular, four-turns *rf* untuned coil of copper and inserted in a cryostat filled with liquid nitrogen. The coil is connected to the spectrometer by a 50 Ω BNC cable. The spectrometer itself is the homemade broadband HyReSpect developed by *Allodi et Al.*[106]. Its main components are:

- an electronic hardware devoted to the production and transmission of pulsed *rf* fields to the sample (TX stage);
- a separate electronic hardware for reception of the spin-echo signal induced in the coils (RX stage);
- a data-acquisition system for Analog to Digital Conversion (ADC) of the *rf* signal measured;
- a set of digital electronics for control, timing and synchronization of the transmitter and receiver electronics.

The spectrometer is fully automatized once the desired parameters are set by a custom control software. The data acquisition for a single spin-echo signal at fixed value of transmitted *rf* power and variable frequency is now described. After an initial search of the setup parameters for an optimal FNR signal, a number N of spin-echo amplitude measurements are done. For each spin echo measurement, after a delay time *RixD* during which the spectrometer is inactive, the Transmission line is enabled and produces a pulse of duration *P1*. After a delay time *D* a second pulse of duration *P2* is produced (necessary for spin-echo measurement). After a waiting

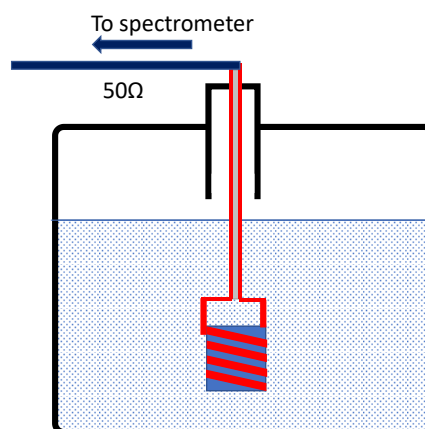


Figure 3. 17 Schematic of the experimental setup.

time RinH the receiver line is first enabled, followed by the ADC after another waiting time AcqD. Once the first acquisition is done, the spectrometer becomes inactive again for a time

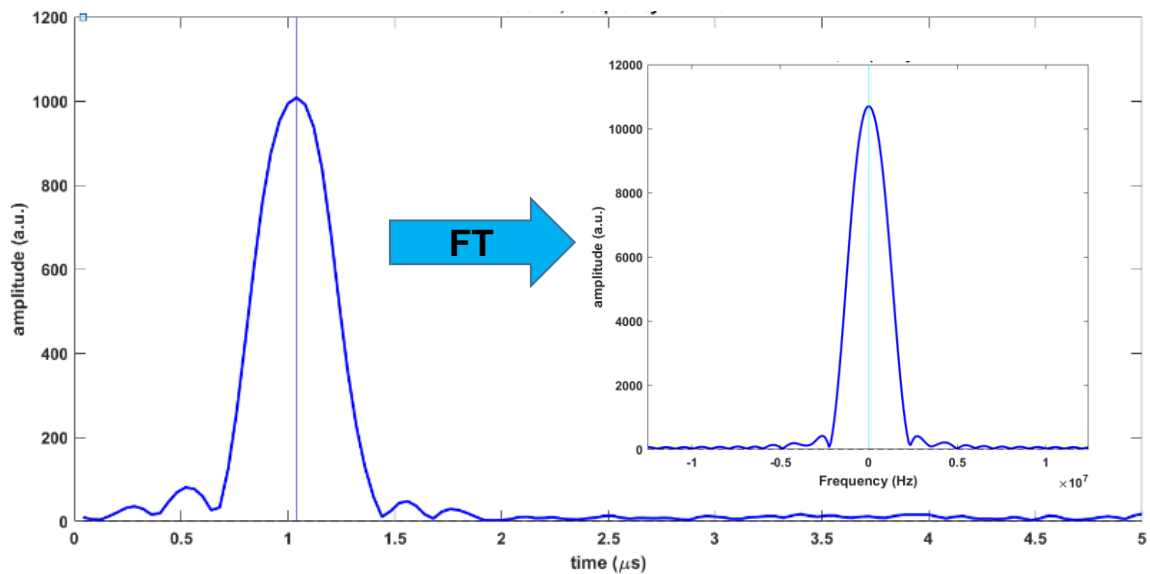


Figure 3. 18 Average spin-echo signal measured by the spectrometer. The maximum amplitude is normalized by the number N of acquisition. Inset: Fourier Transform of the spin echo signal. The amplitude at 0 MHz is the FNR signal.

RixD and the cycle starts again. This acquisition takes less than 1 ms. The waiting times are necessary to avoid any spurious signals due to transient phenomena. All the N spin-echo are summed up in real time, producing the final spin-echo amplitude (see **Figure 3. 18**). Then, the *rf* frequency is automatically changed and the procedure described starts again, until all the frequencies to be probed are obtained. For having a 2D map, a second series of FNR measurements is done for the same set of frequencies but with different values of the transmitted *rf* power. The actual FNR signal used for obtaining the spectra is the peak value of the spin-echo Fourier Transform.

Chapter 4

Morphology and microstructure of hybrid systems

This chapter is dedicated to the morphological and structural characterization of investigated samples. In this chapter I will present the results of the structural characterization of the systems investigated in this thesis. First the surface of the $\text{Al}_2\text{O}_3(0001)$ is discussed, followed by an analysis of the Co thin films as a function of their thickness. Then the morphologies of the various molecular layer will be presented along with the one of the Al capping used for Co reference thin films. Finally, the TEM characterization of the Co microstructure is discussed.

4.1 AFM Characterization of the surfaces

All the measurements were performed *ex-situ*, in air, with a NT-MDT Solver P. (Si tips resonance frequencies 260 KHz, Q factor of 500) are used. Data analysis is performed with *Gwyddion* software. For a detail on how the various extracted parameters are calculated see Chapter 3.2.2. The error associated to the measured quantities are quantified based on a conservative approach to the measurements performed, more than the actual error extracted from the fits. The error associated to height-related quantities (e.g. the roughness) is always not less than 1 Å. The errors associated with the mean grain size or the mean lateral dimensions are no less than the resolution of the image taken: for a 1-micron lateral scale, with 512 pixels per linescan, the lateral resolution and thus the lowest possible error value is $\frac{1000}{512} \approx 2 \text{ nm}$. For the calculation of the mean period of a surface periodic feature, the error associated to it is half the lateral step between two consecutive wave vectors.

4.1.1 Al₂O₃(0001) substrates and Cobalt thin films

In **Figure 4. 1** are reported two AFM images of the Al₂O₃(0001) substrate with different lateral scales. The surface is atomically flat, with an RMS roughness of 0.2 ± 0.1 nm. Grain-like features are evident. The profile lines better show that they are 1-4 Å in height. To better look at their lateral dimensions, the AutoCorrelation Function (ACF) of the small-scale images is

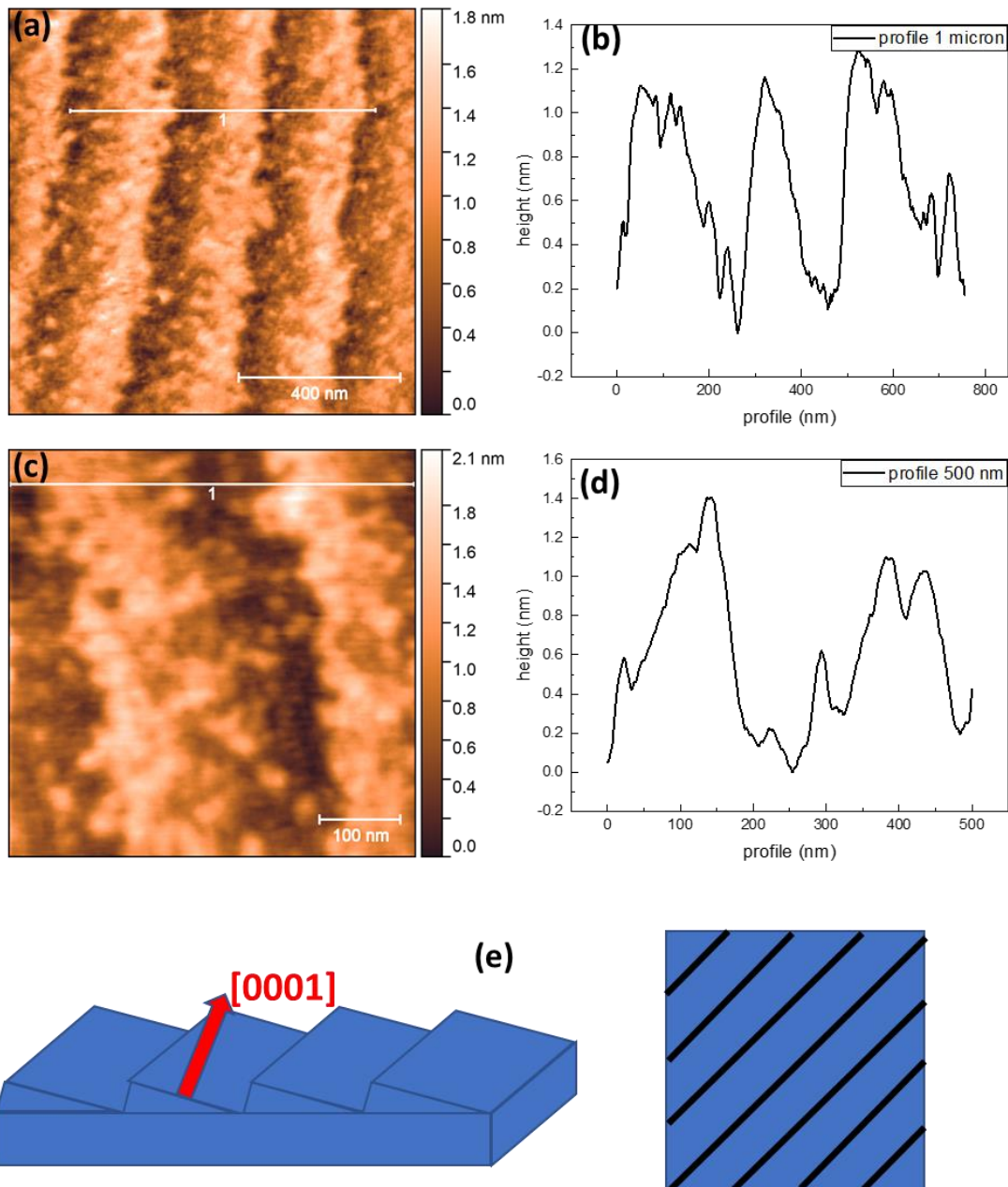


Figure 4. 1 AFM images of a bare Al₂O₃(0001) substrate, 1 micron (a) and 500 nm (c) lateral scale. A profile line is taken for each image (b,d) to help the visualization and to highlight the sawtooth-like periodicity. (e) sketch of the terraces over the substrate.

taken and, by the procedure reported in Chapter 3.2.2, a mean lateral dimension of (24 ± 1) nm is calculated. From **Figure 4. 1(a),(c)** a spatial sawtooth-like periodicity is evident: the value of the wavelength of this linear feature is obtained by the radial Power Spectrum Density Function (PSDF), reported in **Figure 4. 2(e)**, where a peak is found for a wave vector $k=2.5 \times 10^7$ m^{-1} yielding a value of (250 ± 15) nm. From the profile lines, the peak-to-peak height is (0.8 ± 0.2) nm. The origin of this periodicity can be attributed to the polishing procedure (performed by the manufacturing company) as reported also in literature[107]–[109]. The polishing induces a small miscut angle of the (0001) surface that results in terraces and atomic step edges and that is then slightly tilted from the substrate normal. From these studies the terraces correspond to step-edges oriented along the [11-20] crystal direction. The heights of the jumps are related to the different crystalline surfaces of the two adjacent terraces, for example Al-Al or O-O edges. From this it is concluded that even the small-scale grain-like features (10 nm region) are in fact terraces surrounded by atomic step edges. By manually adjusting the substrate with respect to the scanline, the direction of the terraces with respect to the substrate edge is estimated as $(45 \pm 15)^\circ$. Having assessed the substrate morphology, now are presented the results of the Co-on- Al_2O_3 surfaces. For this study, Cobalt thin films of thickness 3, 5, 7 and 10 nm are grown on sapphire following the procedure reported in Chapter 3.1.2. Due to the exposure to air, a layer of Cobalt oxide, mainly CoO, is formed. Its thickness is not known a priori, but different studies reveal that depending on the Co thickness, it can range from 1 to 2.5 nm[110], [111]. The surfaces of the Co thin films are reported in **Figure 4. 2(a)-(d)**. The Co surface appears granular in composition, though atomically flat. The value of the roughness is independent on the Co thickness, with a value of (0.3 ± 0.1) nm. From the images it appears that the morphology still presents some long scale periodicity presented by the $\text{Al}_2\text{O}_3(0001)$ surface. To quantify it, the radial PSDF from these images is taken and reported in **Figure 4. 2(e)** along with the one obtained from the AFM image reported **Figure 4. 1**. A common peak is present in all the PSDF curves, corresponding to a spatial periodicity of (250 ± 15) nm, compatible with the lateral dimension of the bare sapphire long-scale terraces. The value obtained for the 10 nm thick Co thin film is (220 ± 15) nm, not statistically different from all the others. To better study the low scale behavior, 500 nm scale images are taken to improve the lateral resolution. They are reported, along with a representative profile, in **Figure 4. 3**. The estimated mean grain sizes are independent on the films thickness (see **Table 4. 1**) with a value of (10 ± 1) nm, except for the 10 nm Co for which a value of (7 ± 1) nm is calculated. This discrepancy can be attributed to the scarce quality of the image for the 10 nm thick Co film. On the overall the grain dimensions

are quite similar to each other but less than the value found for the sapphire surface. This is also in accordance with the profile linescans, more variable with respect to the ones drawn from

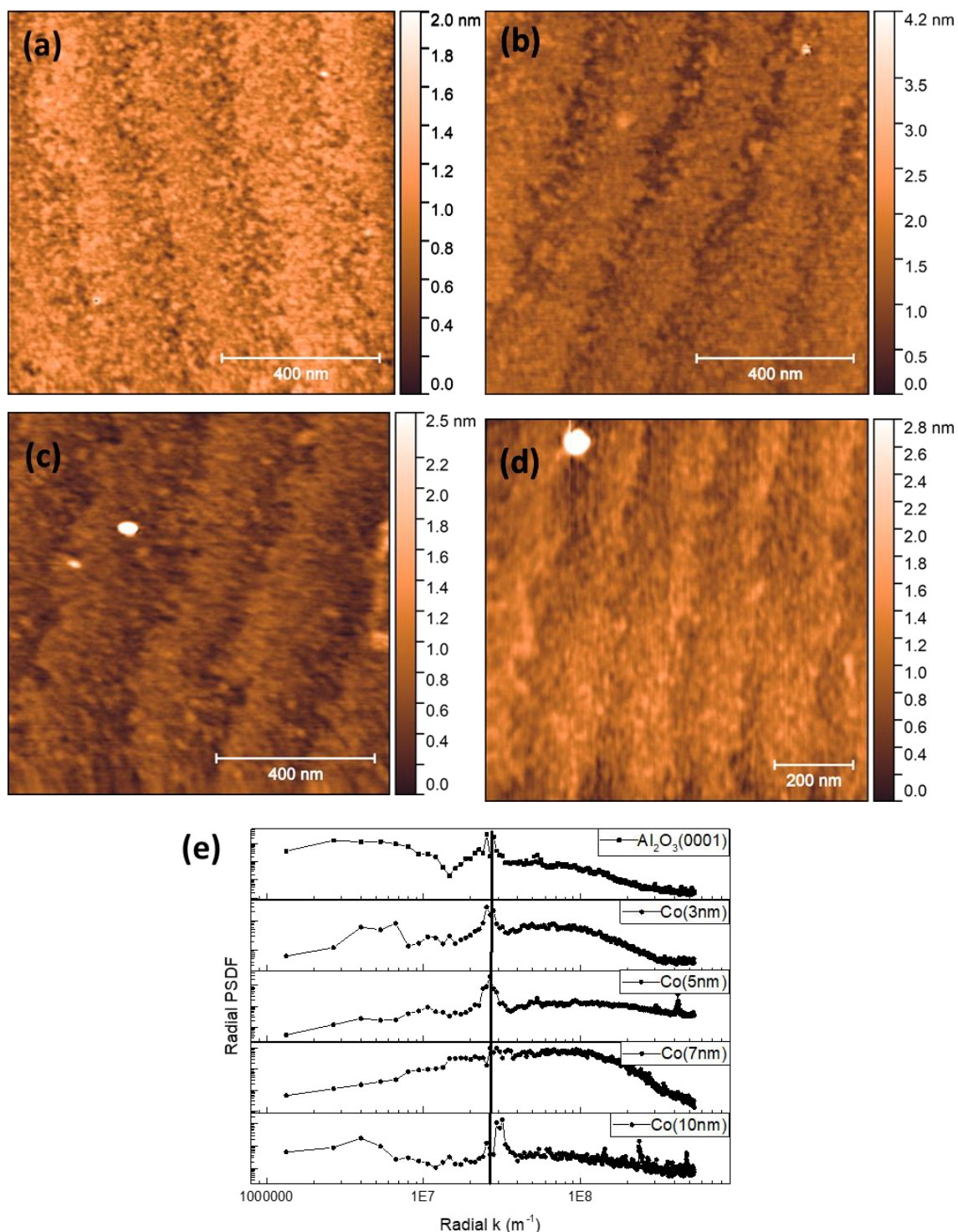


Figure 4. 2 1-micron lateral resolution AFM images of 3 nm (a), 5 nm (b), 7 nm (c) and 10 nm (d) thick Co thin films grown on Al₂O₃(0001) substrates. From each image the radial PSDF is calculated and reported in (e), along with the one extracted from the sapphire substrate (Figure 3. 1 (a)).The black line represents the peak position for the substrate.

the sapphire surface. The Co growth well reproduces the surface features of the $\text{Al}_2\text{O}_3(0001)$ on a large scale, while for the small scale (10 nm regime) the Co granularity is evident. This seems to suggest that Co grown at RT has a low mobility and thus forms small aggregates that eventually coalesce one with the other.

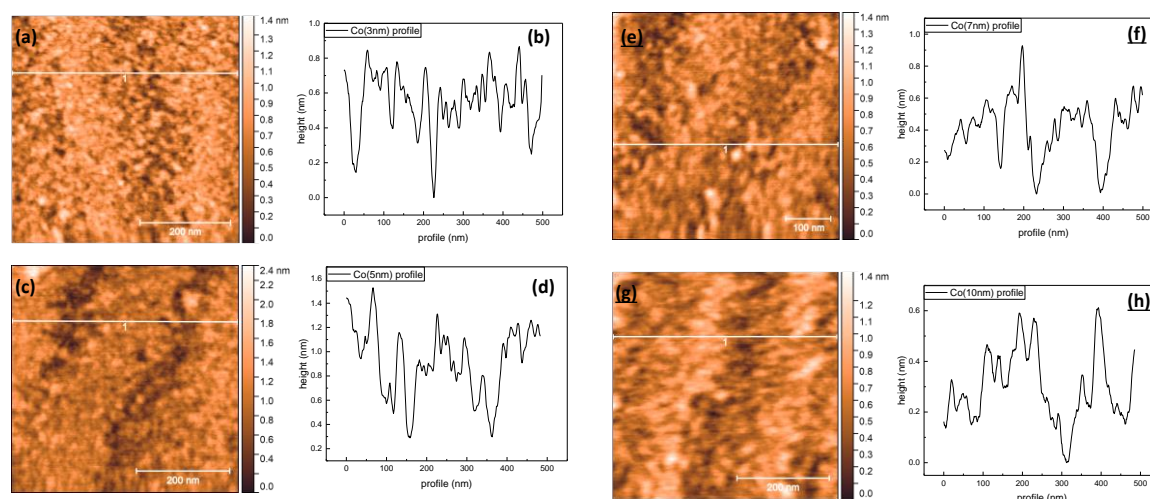


Figure 4.3 500 nm lateral resolution AFM images of 3 nm (a), 5 nm (c), 7 nm (e) and 10 nm (g) thick Co thin films grown on $\text{Al}_2\text{O}_3(0001)$ substrates. (b),(d),(f),(h) profile line scans of the Co surfaces.

Table 4.1 Parameters extracted from the AFM images of the Co surface.

Co thickness	3 nm	5 nm	7 nm	10 nm
Roughness	0.2 ± 0.1	0.3 ± 0.1	0.3 ± 0.1	0.3 ± 0.1
Periodicity	250 ± 15	250 ± 15	250 ± 15	220 ± 15
Mean Grain Size	9 ± 1	11 ± 1	11 ± 1	7 ± 3

4.1.2 The Al capping layer

Now the morphology of Co films capped with 3 nm Al is discussed. Since the Co layer morphology proved to be rather thickness independent, for the study of the Al surface only $\text{Al}_2\text{O}_3(0001)//\text{Co}(5\text{nm})/\text{Al}(3\text{nm})$ samples are considered. Such low value of the capping is a tradeoff between a uniform coverage and the possibility to perform magneto-optical measurements. It is known from literature that even a thin layer of 2 nm of Al on top of Co is

enough to prevent oxidation of the underlying layer for days[112]. The samples are grown with the procedure reported in Chapter 3.1.2, with a deposition rate of $0.09 \text{ \AA}/\text{sec}$ and without heating the samples during the deposition. In **Figure 4. 4(a)** is shown the Al surface. It is evident the granular nature of the film, though the layer is rather flat, with a roughness of $(0.2 \pm 0.1) \text{ nm}$. Interestingly, as suggested by the radial PSDF **Figure 4. 4(c)**, the peak found for all the Co samples is disappeared. In fact no trace of terraces is visible. The mean grain size estimated by the ACF yields a value of $(16 \pm 2) \text{ nm}$, slightly bigger than values found for Co. All these results suggest that the underlying Co structure is well covered by the deposition of Al.

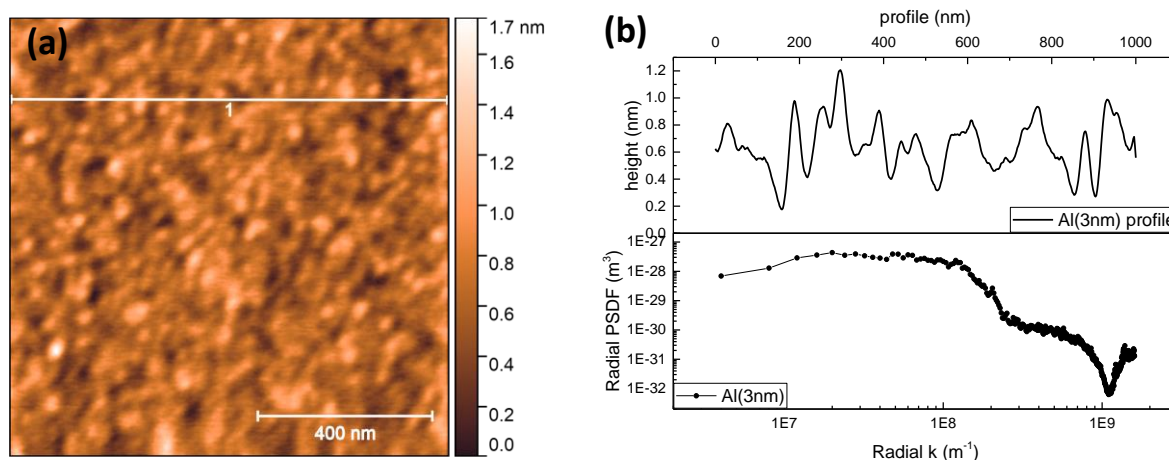


Figure 4. 4 (a) 1- μm wide AFM image of the Al surface deposited on $\text{Al}_2\text{O}_3(0001)//\text{Co}(5\text{nm})$. Profile taken along line 1 is reported in **(b)**. The radial PSDF of the image **(c)** does not present any peak related to the step terraces, suggesting a more disordered growth.

4.1.3 The molecular layers

Now the molecule-on-Co surfaces are discussed. As in the case of the Al layer, since the morphology of the Co layer is rather thickness independent, the morphology of the molecular layers is investigated only for $\text{Al}_2\text{O}_3(0001)//\text{Co}(5\text{nm})/\text{Molecule}$ sample, by the procedure reported in Chapter 3.1.2. The deposition rate was kept fixed at $0.17 \text{ \AA}/\text{sec}$ for each molecule and no heating of the substrate is performed, to avoid any modification of the Co structure. For the Co/Molecule bilayers a thick layer of 25 nm is always deposited, to guarantee a complete coverage of the Co layer and better protect its surface from oxidation. The first organic layer analyzed is C_{60} . Different studies showed that the growth of C_{60} on epitaxial Co surfaces is

ordered and well-oriented[113], [114] but due to the Fullerene low mobility over this metal at RT[115] tends to grow in a disordered manner on randomly oriented Co crystalline structure.

Figure 4. 5(a) reports the AFM image of the 25 nm thick Fullerene layer grown on

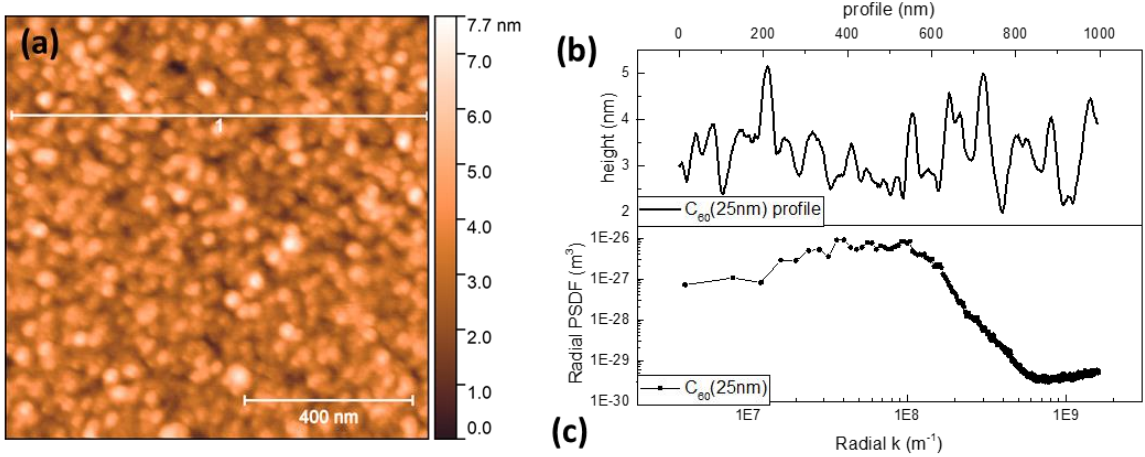


Figure 4. 5 (a) 1-micron wide AFM image of the C₆₀ surface deposited on Al₂O₃(0001)//Co(5nm). Profile taken along line 1 is reported in **(b)**. The radial PSDF of the image **(c)** does not present any peak related to the step terraces, suggesting a loss of conformity.

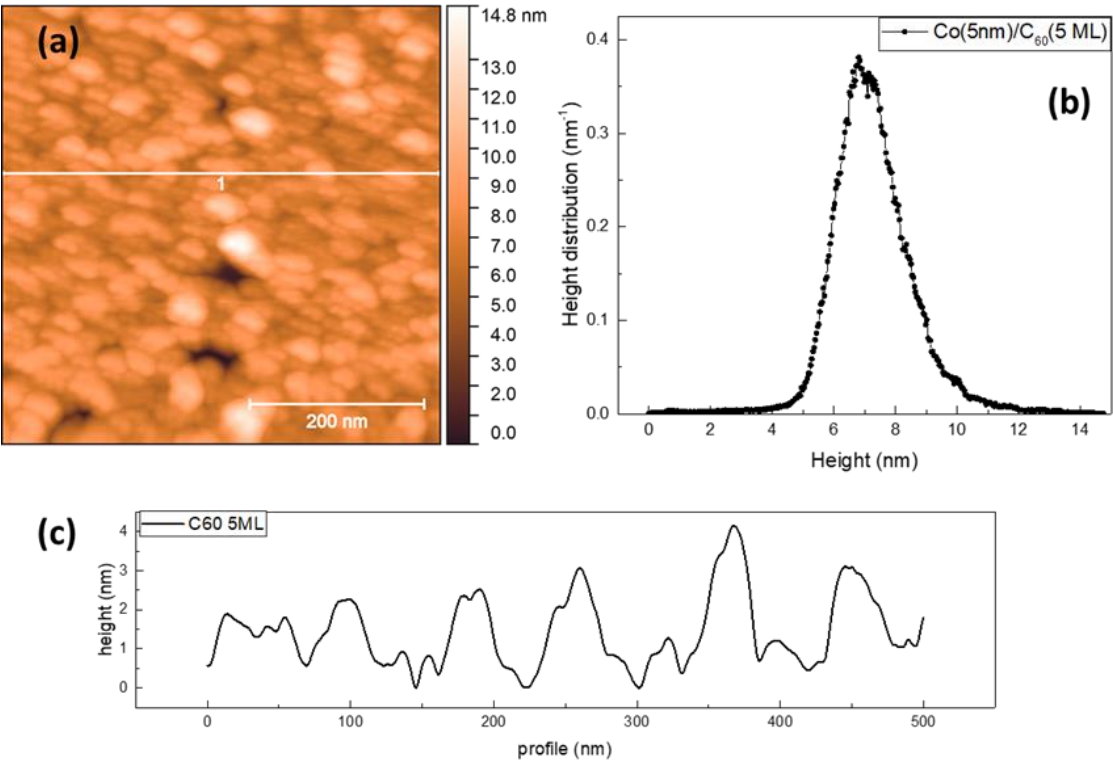


Figure 4. 6 (a) 500 nm, wide AFM image of the 5ML thick C₆₀ surface deposited on Al₂O₃(0001)//Co(5nm). Profile taken along line 1 is reported in **(c)**. **(b)** The height distribution shows that the majority of the heights is concentrated on a narrow interval.

Al₂O₃(0001)//Co(5nm). The surface is not uniform, showing round shaped cluster of Fullerenes of mean lateral dimension (13 ± 1) nm. Thus, it is reasonable to deduce that the C₆₀ films deposited are disordered on a long scale but an oriented growth dependent on the surface of each Co grain cannot be excluded. The roughness measured is of (1.2 ± 0.2) nm, five times bigger than the bare Co layer. Moreover, the profile reported in **Figure 4. 5(b)** does not show a high variation of the heights. All these findings indicate that the C₆₀ well covers the Co surface. For observing the initial growth process, a 5 ML thick (approximately 5 nm) C₆₀ layer was grown on top of a Al₂O₃(0001)//Co(5nm). Its surface (see **Figure 4. 6(a)**) is very similar to the 25 nm thick case. The RMS roughness is of 1 nm, which is compatible with the molecule size. Cluster-like features are evident, suggesting that growth proceeds by C₆₀ aggregates instead of a layer-by-layer growth. By looking at the height distribution (**Figure 4. 6(b)**), they are concentrated in a narrow region around 7 nm. The amount of area corresponding to the total number of pixels of height <5nm, is 1.5% of the total. From this characterization it is concluded that a 5 ML thick C₆₀ film covers almost uniformly the Co surface.

The next molecular layer to be discussed is a 25 nm thick Gaq₃ deposited on Al₂O₃(0001)//Co(5nm). Again, no other Co thickness is considered since the similarity of the surfaces. Room temperature growth of Metal-Quinoline (Alq₃, Gaq₃) is highly disordered if the substrate is either an oxide or a metal[116]–[118]. Additionally, over a Co ordered surface the first layer that chemisorbs on it gets heavily distorted by the formation of bonds with the surface Co atoms[20], [22]. The AFM characterization (see **Figure 4. 7**) shows that the Gaq₃ surface is

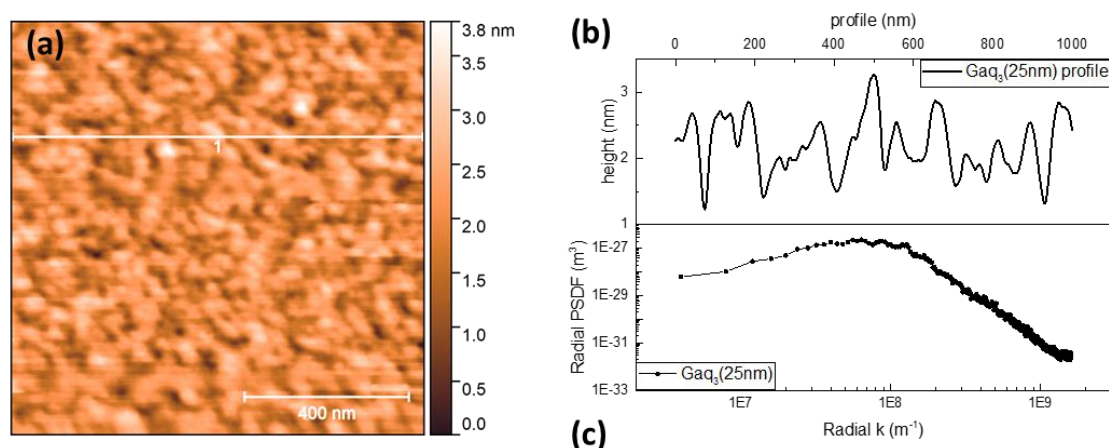


Figure 4. 7 (a) 1-micron wide AFM image of the surface of 25 nm Gaq₃ deposited on Al₂O₃(0001)//Co(5nm). Profile taken along line 1 is reported in (b). The radial PSDF of the image (c) does not present any peak related to the step terraces, suggesting a loss of the underlying surface features.

rather flat, with a roughness of (0.4 ± 0.1) nm, less than the C_{60} layer. Similarly to the latter, Gaq_3 seems to grow in aggregates, as can be seen from the image. Nevertheless the low roughness and the small differences in height (range from 0 to 4.4 nm) suggests a uniform growth and a complete coverage of the Co surface. Moreover the absence of the peak at $2.5 \times 10^7 \text{ m}^{-1}$ in the radial PSDF indicates that the long scale periodicity is not reproduced. The mean lateral dimension of the small-scale features is (14 ± 1) nm, not too far from the values calculated for the Co surface.

Finally, the T6 layer is discussed. The growth of this molecule over different substrates is known to be well-ordered. Over epitaxial oxides[24], [119] the growth starts layer-by-layer, in each of which the molecule disposes itself with its major axis tilted with respect to the surface normal. When deposited on noble or transition metals[28], [29], [120] the first layer of T6 in contact with the substrates is known to grow with the major axis lying parallel to the film surface, forming a so-called *wetting layer*[28]. The subsequent layers can be either parallel or almost perpendicular to the film normal. This proved to be the case also for a polycrystalline

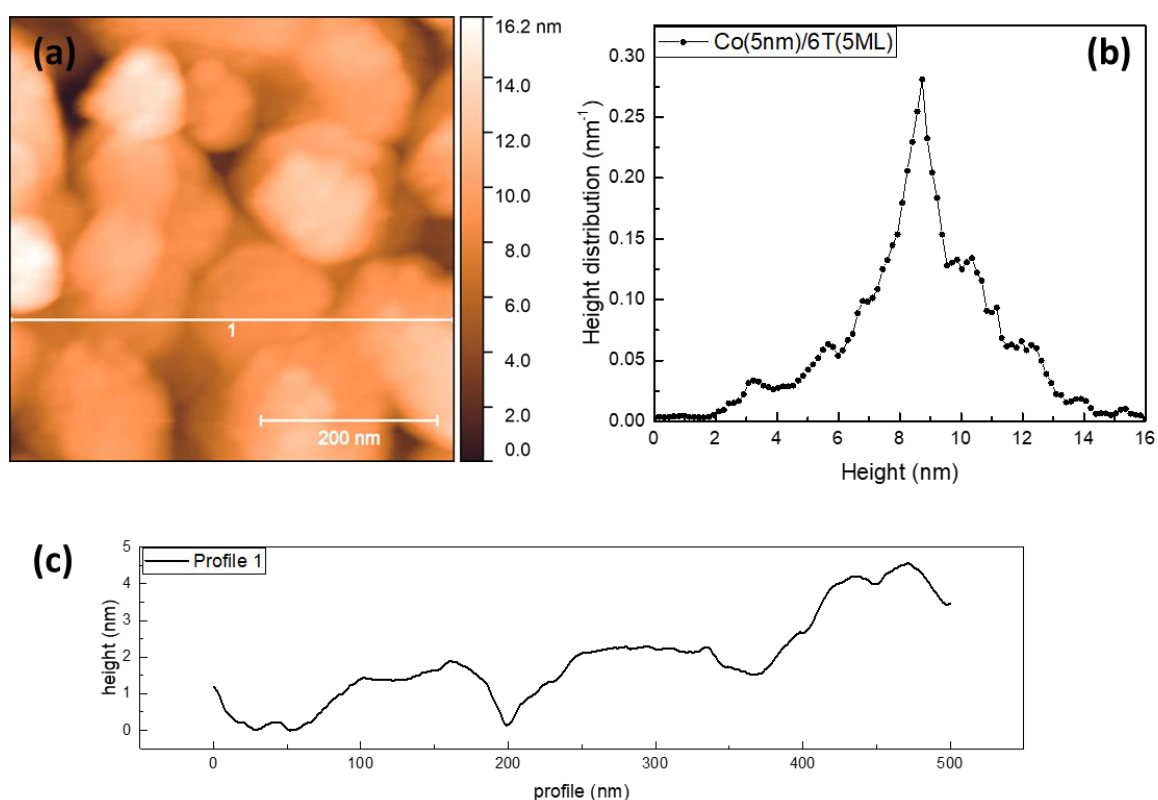


Figure 4. 8 (a), (b) AFM images of a 5 ML thick T6 layer on $Al_2O_3(0001)//Co(5nm)$. The molecules are aggregated in islands, suggesting an ordered growth. (c), (d) profile lines along the (a), (b) images respectively. For the surface reported in (b) the height distribution is calculated (e) and fitted with a 3 gaussian for the calculation of the roughness of each single T6 layer.

Co surface, where the first layer of T6 produces a wetting layer that is capable of avoiding the formation of Cobalt oxides[121]. In order to verify this process, a 5ML thick T6 film was grown on top of Al₂O₃(0001)//Co(5nm) at room temperature by the procedure reported in Chapter 3.1.2. In **Figure 4. 8** is reported the AFM images of the T6 surface. A well-ordered growth of the T6 molecules is visible, with well-defined islands, highlighted in the height profile taken along a linescan. The terrace-like features appear to be smoothed, and sub-nm modulation is visible. The mean height can be estimated as (2.0 ± 0.3) nm, compatible with a tilted major axis, its length being 2.6 nm[122]. This suggests a 2D-3D growth, where single initial layers are formed acting as nucleation centers for the subsequent layers inhibiting the completion of the underneath layers. However the amount of pixels below 3nm is only 2% of the total area suggesting an almost complete coverage of the Co surface. By looking at the height distribution reported in **Figure 4. 8(b)**, heights are concentrated in different intervals, compatible with a 3D growth. Several peaks are present but rather smoothed. The measured RMS is of (2.2 ± 0,3) nm. These results suggest that while 5 ML may be not enough for a complete Co coverage, it is expected that by increasing the amount of deposited material will be enough for preventing oxidation of the Cobalt.

Table 4. 2 Roughness and mean lateral dimension of the Co overlayers.

Material	Al	C ₆₀	Gaq ₃	T6
RMS Roughness (nm)	0.2 ± 0.1	1.2 ± 0.2	0.5 ± 0.1	0.7 ± 0.1
Roughness st.dev (nm)	0.2 ± 0.1	1.2 ± 0.1	0.4 ± 0.1	2.2 ± 0.4
Mean lateral dimension (nm)	16 ± 2	13 ± 1	14 ± 1	X

4.2 Cross-Section TEM analysis of Co thin films

Having assessed the morphological properties of the various layers, now the Co microstructure is discussed. For this study Al₂O₃(0001)//Co/C₆₀(25nm) systems were fabricated with the procedure discussed in Chapter 3.1.2. Co thin films of nominal thicknesses of 3, 5 and 10 nm were considered, and are labelled Co3, Co5 and Co10. Given that this kind of characterization requires a capping layer which is effective in oxidation prevention and at the same time is not interfering with the Co microstructure, for these systems a C₆₀ coverage was considered. The analysis and characterization of the Co/C₆₀ systems was conducted at the Department of

Materials Science and Engineering, National Chung Hsing University of Taiwan under the supervision of Professor Ko-Wei Lin, by using a JEOL (JEM-2100F) field emission TEM (FETEM) operating at 200 kV. The samples were cutted using a JEOL (JIB-4601F) focused ion beam (FIB) system. A thin Pt layer is deposited over the C₆₀ layer to protect the samples from the Ga⁺ ions used for the preparation procedure.

The images obtained are reported in **Figure 4. 9**. From them, it is possible to see the Pt coating forms a few-nm thick diffuse region with the C₆₀ layer. The Fullerene layer does not present any particular structure, suggesting an amorphous layer. The resolution of the images (see also **Figure 4. 10**) is not enough to address the question of the structure of the first molecular layer on top of the ferromagnet. Regarding the Co layer, some differences related to the thickness are evident. The measured thicknesses (see also **Figure 4. 10**) are slightly different from the nominal ones. The actual values are $(3.7 \pm 0.2)\text{\AA}$, $(4.4 \pm 0.2)\text{\AA}$ and $(9.9 \pm 0.2)\text{\AA}$ for the Co3, Co5 and Co10 samples respectively. For Co3 and Co5, the contrast of the Cobalt is not uniform along the whole layer, suggesting non-crystalline and disordered portions of the film. For the Co10 samples the Cobalt layer appears more uniform, but with columnar-like structures evidenced by the Co contrast. Individual particles are then examined using electron microscopy, to obtain crystalline phase and orientation with the calculation of electron diffraction patterns. They are reported in **Figure 4. 10**. All samples present Co in the *hcp* phase, but only the Co10 sample presents also grains in *fcc* phase. Different orientations of the grains are found, suggesting that no preferential direction is induced by the sapphire substrate. Moreover, regions

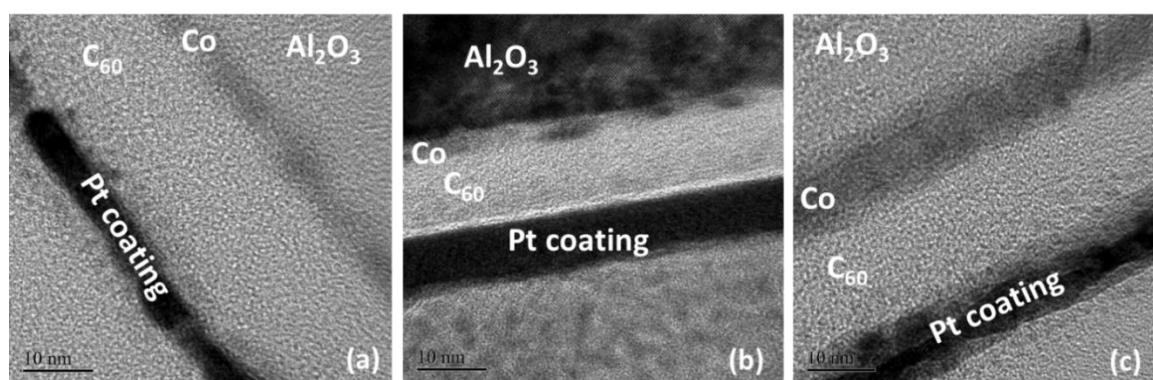


Figure 4. 9 Cross Section TEM images with equal lateral resolution of the Al₂O₃(0001)//Co/C₆₀(25nm) systems for Co3 (a), Co5 (b) and Co10 (c). The C₆₀ does not present any particular texture, suggesting an amorphous growth. For Co3 and Co5 area of low contrast are present, suggesting a loss of crystallinity. Columnar-like regions are visible for Co10, suggesting an increase in crystalline order.

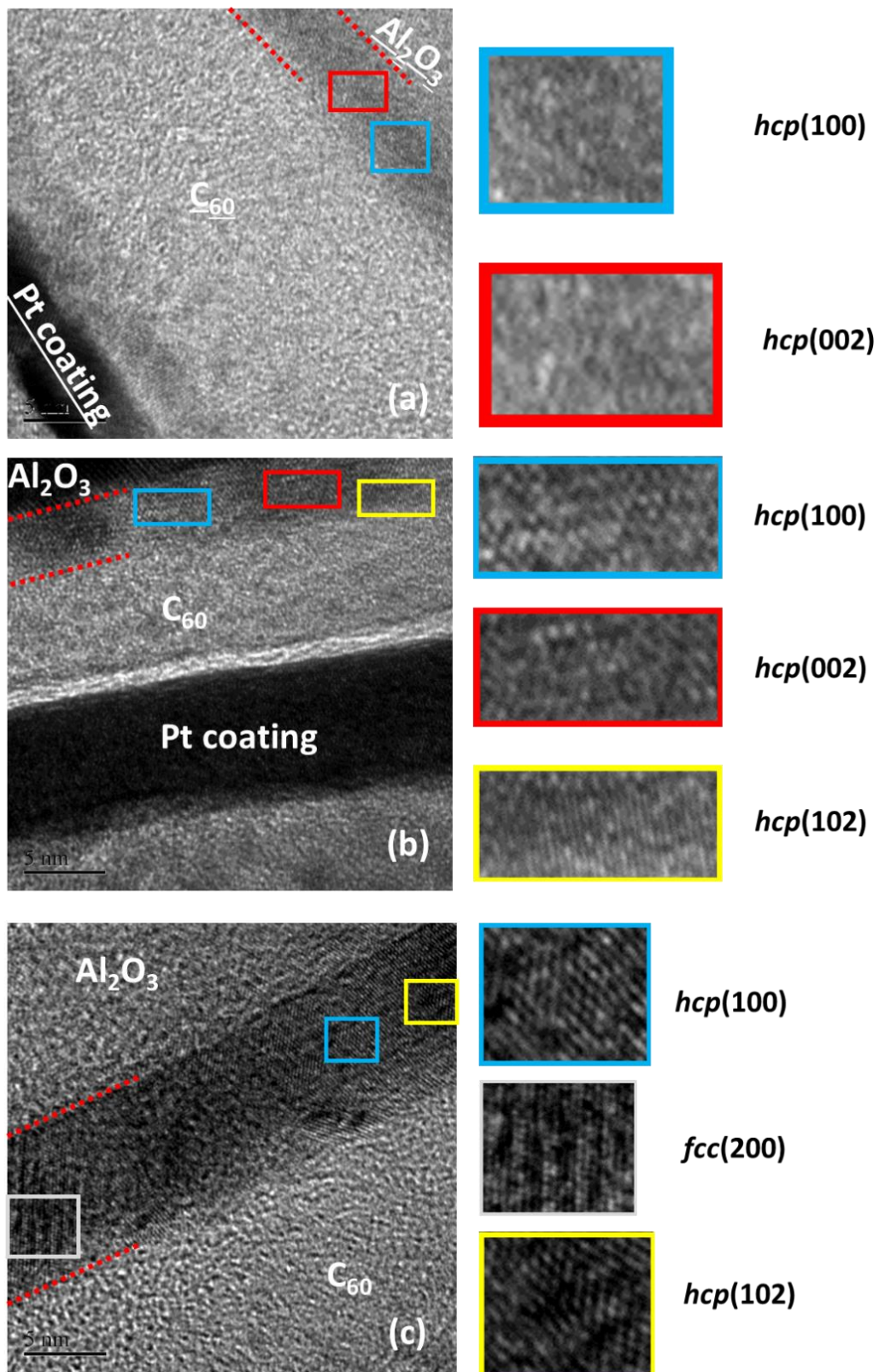


Figure 4. 10 Cross Section TEM images of Co3 (a), Co5 (b) and Co10 (c). Colored rectangles mark areas of clear crystal structure, enlarged and reported to the right of each image. Lateral scale bar: 5 nm. Dotted lines are put to highlight the Co layer.

with same contrast are found with different orientations. Some of the crystalline areas are highlighted by colored rectangles and enlarged for better comprehension. For the Co3 and Co5 samples, the crystalline structure of the low contrast areas (better visible in **Figure 4. 9(a,b)**) is not straightforward. While the result of AFM characterization excludes a discontinuous Co layer, the apparent absence of crystalline order can be explained by the presence of region of amorphous Cobalt in between regions with well-defined crystallinity. These finding hints toward a microstructural rearrangement for a thick enough layer of Cobalt, allowing the more disordered areas to relax and reorganize into small crystal grains.

4.3 Conclusions

In conclusion, AFM morphology characterization showed that the Al₂O₃(0001) substrates have an atomically flat surface, though atomic step edges are present due to the polishing procedure performed by the manufacturing company. The Co layers, regardless of the thickness, well reproduce the substrate features, maintaining a very low roughness of (0.3 ± 0.1) nm. The surface is granular, as expected by a polycrystalline layer, and with very few defects. The grain sizes are found to be approximately (10 ± 1) nm in lateral dimension. The Al capping layer, used for the growth of reference samples, grows uniformly over the Co surface with a low roughness, (0.2 ± 0.1) nm, suggesting a good protection against oxidation of the ferromagnetic layer. Also, all the molecules used in this work proved to cover completely the Cobalt, at least for a 25 nm thickness, but with different growth processes. For C₆₀ the growth is disordered on large scales but locally it forms separated clusters of molecules with boundaries with one another. The same behavior is observed also for Gaq₃ while T6 grows layer by layer forming islands of ordered molecules directed with the major axis approximately parallel to the surface. The Cross-Section TEM images show a different Cobalt microstructure depending on the thickness. While all Co layers are polycrystalline in nature, the thinner ones (3 and 5 nm nominal thickness) have regions of *hcp* crystallinity separated by regions of not defined crystallinity, tentatively attributed to amorphous Cobalt. For the 10 nm thick Co layer columnar-like structure are found, with Co grains in either *hcp* or *fcc* phase, suggesting a microstructural transition takes place for a thick enough layer.

Chapter 5

Coercivity and anisotropy of Co/Molecule hybrid systems

As discussed in Chapter 1 the establishment of a hybrid interface between a FM and a molecular layer affects the magnetic properties of the ferromagnet. In particular, it was observed the increase in coercivity for a Co thin film upon adsorption of different molecules[1]–[4] and the possibility to tailor the magnetic anisotropy (MA) both in terms of its strength (different values of K) and its orientation[5]. Among the many magnetic properties, anisotropy is one of most relevance for the exploitation of FM thin films for information storage and processing applications [6].

This chapter is thus dedicated to the study of the coercivity and of the magnetic anisotropy of Co/Molecule hybrid interface systems by various characterization techniques. The first section is dedicated to the room temperature (RT) study of MA by means of L-MOKE and VSM magnetometry, motivated by the device relevant operation environment. It will be shown that Co/Molecule systems noticeably increase the coercivity and even modify qualitatively the anisotropy of the reference Co films. The second part completes the characterization by studying the temperature dependence the coercivity and of the anisotropy by L-MOKE and SQUID characterization, demonstrating that the trend in temperature is qualitatively different from that of the reference Co samples and that the coercivity in Co/Molecule systems is enormously enhanced by lowering the temperature.

5.1 RT anisotropy of hybrid systems

In this section I will analyse the in-plane anisotropy of thin Co films of different thicknesses and with different overlayers. Considering possible exploitation of molecule-induced effects for device ideation, the focus is put here to the RT behavior. Samples have been fabricated, following the procedure reported in Chapter 3.1.2. For Co, nominal thicknesses of 3, 5, 10 nm

were considered. I will mainly focus on the C₆₀ molecule but results for Gaq₃ and T6 will be also shown. For comparison of data, Co/Al(3nm) bilayers were considered as a reference system. Note that Al thin layers are widely used for protecting ferromagnetic metals surfaces from oxidation[112]. Different studies proved that when deposited over Co there is relative low interdiffusion at the interface, estimated as ranging from 0 to 8 Å[112], [123], [124]. As already discussed in Chapter 4.1, the Al capping layer is fixed at 3 nm and the molecular layers at 25 nm, the selected thicknesses ensure a complete coverage (as shown in Chapter 4.1) while allowing for magneto-optical probing of the underneath Co layer. To characterize the RT anisotropy of these systems, *ex-situ* room temperature L-MOKE magnetometry was performed. Hysteresis loops at room temperature were collected for different in-plane direction of the applied field. From such loops the values of the coercive field H_C and the normalized remanent magnetization, sometimes referred as squareness S, are extracted. The former is defined as the value of the applied field for which the net magnetization goes to zero,

$$M(H_C)=0 \quad (5.1)$$

while the latter is defined as the value of the magneto-optic signal magnetization when there is no applied field, that is

$$S = \frac{\theta_K(H=0)}{\theta_K(H_{Max})} = \frac{M(H=0)}{M_S} \quad (5.2)$$

All the hysteresis loops measured have typically distorted shapes due to the presence of components quadratic in the magnetization vector. To deal with these effects all the loops reported in this work have been symmetrized by the procedure reported in Appendix 4A, where a detailed explanation on how the actual calculation of the coercivity and the normalized remanent magnetization is shown. The anisotropy is discussed by showing polar plots of the normalized remanent magnetization as a function of the in-plane angular direction φ of the applied field. For each sample, the $\varphi=0^\circ$ direction is defined as the one for which the external field H is applied along one of the sample edges, with an error of $\pm 10^\circ$.

5.2 Uniaxial anisotropy of Co/Al reference samples

First I will present the results of investigation of the reference Co(x=3,5,10nm)/Al(3nm) systems. For sake of simplicity I define the samples as Co3Al, Co5Al, Co10Al. The in-plane values of S as a function of the in-plane angular direction are reported in **Figure 5. 1(a),(c),(e)**. For each thickness of the Cobalt layer, a twofold symmetry of the squareness with φ is a clear indication of in-plane uniaxial anisotropy (UMA). The hysteresis loops of the samples

measured along the easy direction are reported in **Figure 5. 1(b),(d),(f)** presents a rather squared loop, even if a small distortion, likely to be derived by a small mixing of s and p polarization state of the light impinging on the sample, is visible. The coercivity values for the three samples are summarized in **Table 5. 1**: they show a slight increase with decreasing the Cobalt thickness, as expected for ferromagnetic ultra-thin films[125].

The easy axis (EA) of magnetization is always found at angles that are either 45° or 135°. As reported in Chapter 4.1, morphological characterization showed that the Co surfaces possess a spatial sawtooth-like periodicity that is induced by the terraces found on the substrate (a sketch is reported in **Figure 5. 2**). The dimension of these ripples for all the Co films are (250 ± 15) nm for the periodicity, (0.8 ± 0.2) nm for the peak-to-peak values of the ripples and (0.3 ± 0.1) nm for the surface roughness. Since the direction of the terraces is estimated as being along one of the diagonals of the samples, the in-plane easy axis seems correlated to the films terraces suggesting they play a role in the establishment of the in-plane anisotropy. As reported in Chapter 4.1, the presence of periodicities over the FM can induce an anisotropy due to magnetostatic energy minimization. If the system is magnetized perpendicularly to the ripples direction demagnetizing fields are produced inside the film. The demagnetizing factor was shown to be given by

$$N \cong \frac{\pi \text{RMS}^2}{\lambda t} \quad (5. 3)$$

where RMS is the mean standard deviation from the mean surface (i.e. the roughness) and t is the films thickness. Taking the values of the periodicity and the RMS found from the surface characterization (see Chapter 4) and using the nominal thicknesses (3 to 10 nm), N ranges between (1-4)x10⁻⁴. Now, this value of N is calculated for a single surface. Since the modulation of the surface is caused by the substrate, also the Al₂O₃/Co interface has to be considered. Then the calculated value of N has to be multiplied by 2. Taking a value of μ₀M_S for bulk Co[50] of 1.81 T, the resulting demagnetizing field inductions responsible for coercivities can be calculated as

$$\mu_0 H_C = \mu_0 H_{\text{dem}} = -\mu_0 N M \quad (5. 4)$$

The calculated values range from (1.4 ± 0.5) mT for a 3nm Co thickness to (0.5 ± 0.2) mT for a Co thickness of 10 nm. The coercivities extracted by the loops, reported in **Table 5. 1**, are systematically higher than the ones calculated by the Schlömann's formula. Moreover the choice of bulk values for M_S may be debatable especially for the thinner Co/Al sample. If the

values of M_S for the measured systems is lower, then the calculated values of $\mu_0 H_{dem}$ are an overestimation.

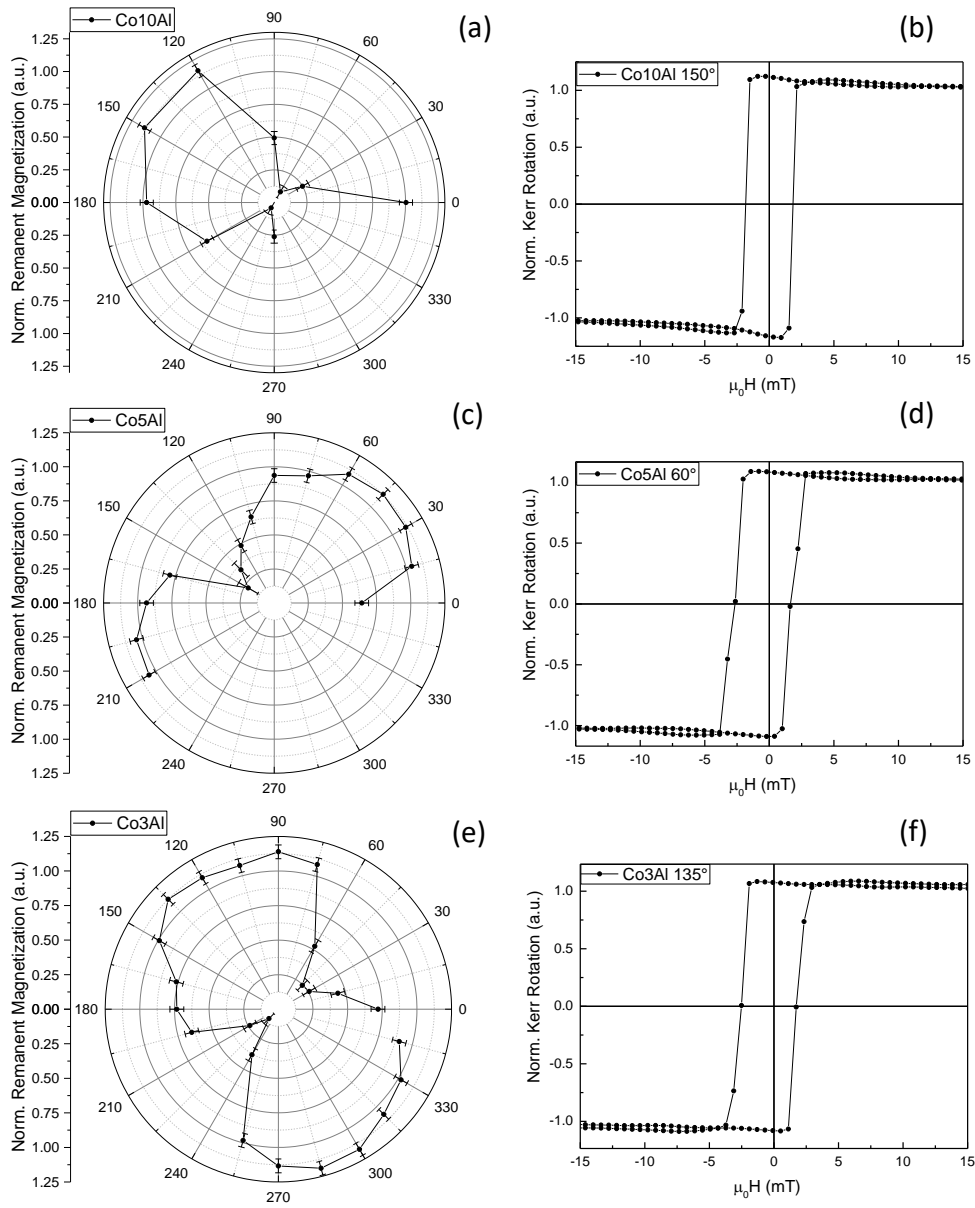


Figure 5. 1 Polar plots of the squareness for Co10Al (a), Co5Al (c) and Co3Al (e). They all exhibit a twofold symmetry that is proper of a uniaxial anisotropy. For each sample the corresponding hysteresis loop of the EA are reported in (b),(d),(f).

Table 5. 1 Co/Al samples: values of coercivity and normalized remanent magnetization extracted from the loops taken along the easy direction.

	Co10Al	Co5Al	Co3Al
EA $\mu_0 H_C$ (mT)	1.8 ± 0.3	2.3 ± 0.3	2.4 ± 0.3
EA M_S/M_R (a.u.)	1.09 ± 0.06	1.05 ± 0.04	0.95 ± 0.07

Other sources of magnetic anisotropy for thin films discussed in Chapter 2.5 shall be considered. The polycrystalline nature of our films should rule out a direct effect of the magnetocrystalline anisotropy (MCA). Considering the Random Anisotropy Model (see Chapter 2.5) a residual anisotropy can still be present. Recalling that the effective anisotropy K_{eff} of the system will be reduced according to

$$K_{\text{eff}} = K \left(\frac{D}{L_w} \right)^6 \quad (5.5)$$

Grain sizes of the Co layers analyzed in this work are estimated as (10 ± 1) nm. A gross estimation of the value of K_{eff} , considering only a uniaxial MAE value of 411 kJ/m^3 [50] for *hcp* Co at RT and a domain wall length of 25 nm [50] yields a value of approximately 65 kJ/m^3 , resulting in coercivities (taking again bulk values of M_s) of approximately 50 mT, one order of magnitude higher than the ones measured over these samples. This estimation however does not consider that the grains are likely to have a distribution of sizes that, according to the TEM analysis, may be well below the estimated values from Atomic Force Microscopy. A value of

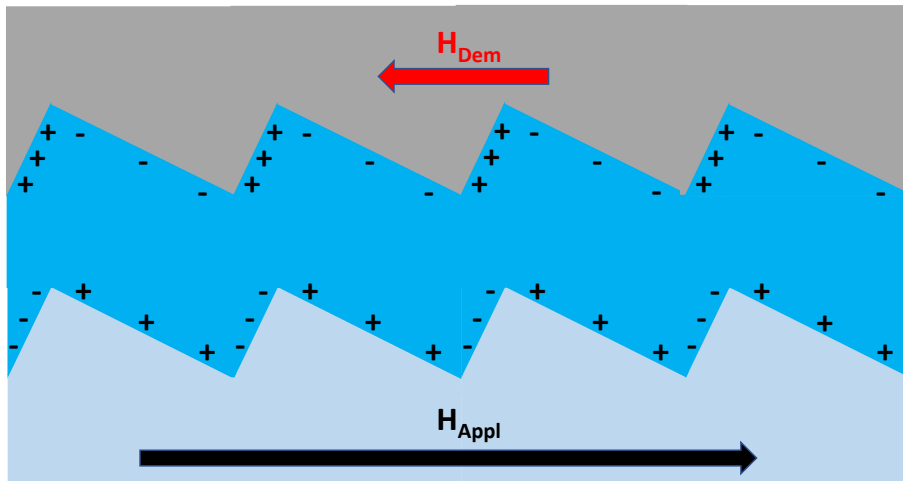


Figure 5. 2 Sketch of the demagnetizing fields produced by uncompensated magnetic charges when the sample is magnetized perpendicular to the ripples direction.

Table 5. 2 Calculated values of the demagnetizing factor and the corresponding demagnetizing fields by the Schlomann's formula, using bulk values of Co M_s , and measured values of the coercivity for Co/Al system.

	$N(\times 10^{-4})$	$\mu_0 H_{\text{dem}}$ (mT)	$\mu_0 H_C$ (mT)
Co3Al	8 ± 3	1.4 ± 0.5	2.4 ± 0.3
Co5Al	5 ± 2	0.8 ± 0.3	2.3 ± 0.3
Co10Al	3 ± 1	0.5 ± 0.2	1.8 ± 0.3

K_{eff} due to small, residual effective anisotropy is compatible with the measured coercivities, but it would add a nonvanishing contribution along every direction, which is excluded given the strong drop of the squareness along the hard axis (HA).

Another possible term that can contribute to the in-plane UMA is residual strain originating from the merging of the Co islands during film growth[64], [65]. These works however consider this contribution as increasing with the film thickness due to competition of the Co islands. Since the coercivities measured are decreasing with increasing the Co thickness this contribution is ruled out. Moreover the actual mechanism with which a uniaxial, stress-induced anisotropy would emerge from an inherently disordered and random system are not yet been proven.

The effect of a stepped substrate surface on the surface anisotropy term for Co atoms at reduced symmetry sites are of interest, on a qualitative level. Step-induced anisotropies for thin ferromagnetic layers deposited on terraced surfaces have been reported[67], [126], [127] but the FM layer needs to be epitaxial. While the Co films studied are disordered in nature, a random distribution of easy direction, on a scale larger than the domain wall lengths, implies that an effective continuous rotational symmetry may be assumed. Thus the presence of step edges is effectively breaking the translational symmetry of Co film[128], [129], promoting an uniaxial easy direction. Additionally, it cannot be disregarded a possible step or substrate-induced texturing, promoting a non-random distribution of easy directions.

Finally, since UMA is a property possessed by all the Co/Al systems, regardless of the Co thickness, it implies that it is independent of the Co microstructure. This is an additional indication of the role of ripples in the establishment of the uniaxiality, either by magnetostatic terms and symmetry-breaking terms.

5.2.1 UMA reduction and magnetic hardening of Co/C₆₀ systems

Having discussed the Co/Al systems, now the Co/C₆₀ samples are presented. The notation follows the previous one, so samples Al₂O₃(0001)//Co(t=3,5,10 nm)/C₆₀(25 nm) are labelled Co3C₆₀, Co5C₆₀, Co10C₆₀. **Figure 5. 3(a),(c),(e)** reports for each thickness the polar plot of the normalized remanent magnetization as a function of the in-plane angular direction of the applied field. While the twofold symmetry of $S(\varphi)$ reveals the presence of a uniaxial anisotropy, the remanent state of the system along any direction is always characterized by a non-zero value of the magnetization. This behavior is present independently of the Co layer thickness. Co10C₆₀ exhibits the highest degree of anisotropy, with a minimum measured value of S of

(0.30 ± 0.06) A.U. The partial “lifting” of the magnetic anisotropy is clear also by looking at the hysteresis loops for the direction of most reduced normalized remanent magnetization reported in **Figure 5. 3(b),(d),(f)**, where the hysteretical behavior is evident. The hysteresis loops along the easy direction are characterized by an almost square-like shape, with values of the coercivity

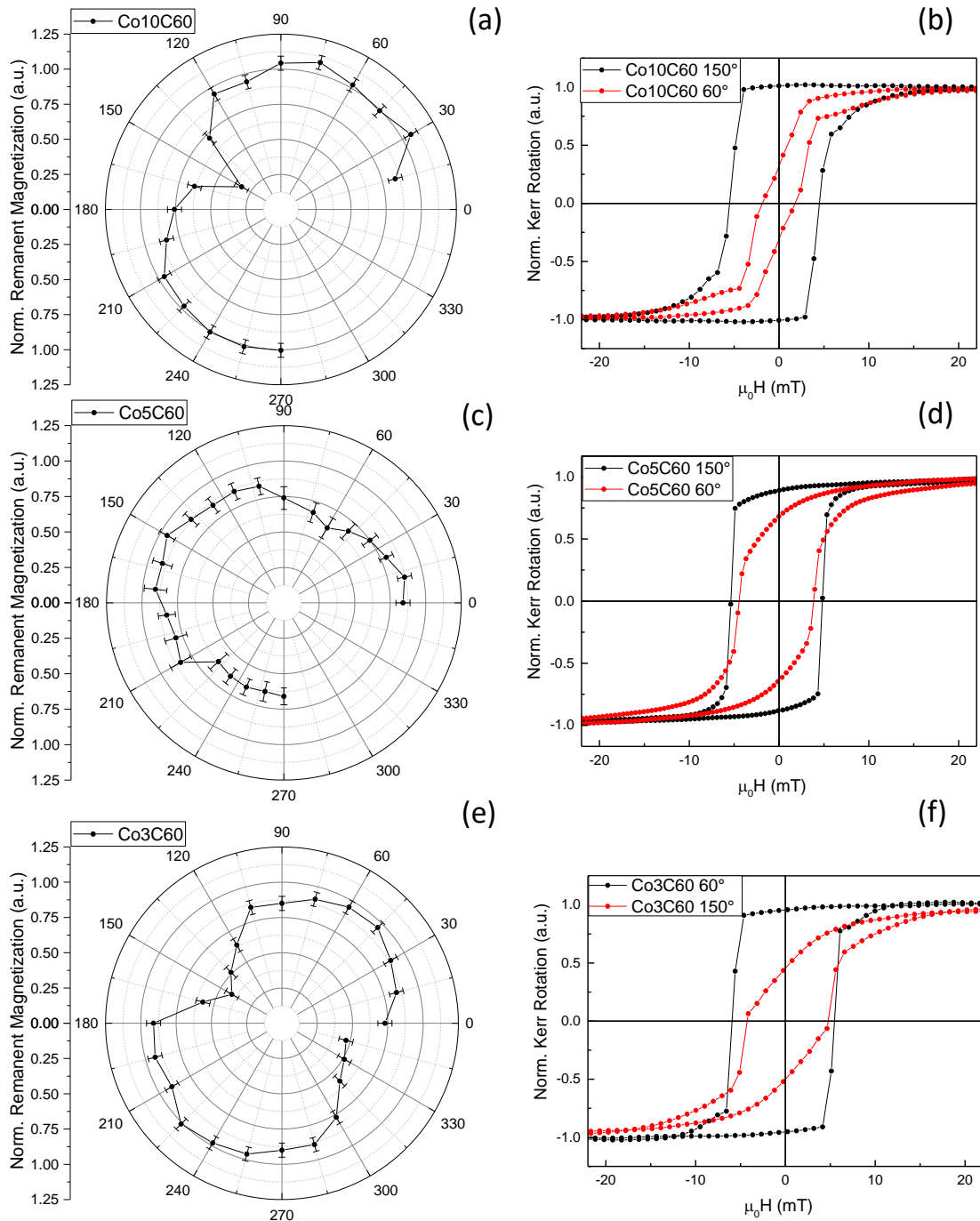


Figure 5. 3 Polar plots of the squareness for Co10C60 (a), Co5C60 (c) and Co3C60 (e). They all exhibit a twofold symmetry that is proper of a uniaxial anisotropy. For each sample the corresponding hysteresis loop of the EA and HA are reported in (b),(d),(f).

(reported in **Table 5. 3**) slightly increasing with decreasing Co thickness. Remarkably these values are double the ones measured on the Co/Al reference samples (see **Figure 5. 4**). This clearly indicates that the deposition of a thin layer of C₆₀ results in a considerable increase of the coercivity, accompanied by a partial suppression of the in-plane UMA.

Other works already reported this hardening effect on similar Co/C₆₀ systems[21], [30], [33]. However, it is the first time that it is showed for polycrystalline samples over a thickness range from 3 to 10 nm, with values that are double the ones of the reference. Moreover, so far there is no work showing the reported partial suppression of the in-plane uniaxiality. All the previous works on Co/C₆₀ bilayers attribute the molecule-induced hardening of Co as a consequence of hybridization of the surface *d* orbitals of Co atoms bonded with the π orbitals of the C₆₀ molecule. The work of *Bairagi et al*[33] focuses on the modified contribution to the MCA of the bonded Co atoms (see Chapter 1.2.2). Their calculation assumes an epitaxial FM layer; however in a second article they suggested that the local modifications of both the anisotropy and the exchange constants of the Co atoms near the interface act as local sources of magnetic inhomogeneities[34]. Such defects (from the point of view of the FM layer) would act as pinning centers for domain wall propagation, a magnetization reversal mode typical for thin films[130], [131].

The proposed model of enhanced magnetic anisotropy may be a possible straightforward explanation of the coercivity increase. While proposed for an epitaxial thin film, it may be generalized to a polycrystalline system by considering that it possessed a random distribution of local easy directions and surface orientations. Then if the formation of an interface between the molecules and each of the Co grains enhances their local magnetic anisotropy, it consequently modifies the value of K_{eff} , since L_w is dependent on the anisotropy constant K (see Eq. (2. 52)). If the values of K are increased, then the number of grains that will be correlated one to the other decreases and consequently K_{eff} increases in magnitude with little angular dependence. Moreover this would determine lower domains sizes. Considering instead the interfacial Co/Molecule layer as a source of pinning centers, then the disordered and random nature of the FM film suggests that the interfacial layer should be disordered as well. Here “disordered” is used to indicate that the pinning sites will not induce any preferential direction for the propagation of domain walls. Regardless of the origin of the coercivity enhancement, a simple phenomenological model can be proposed, which basically adds to the term responsible for uniaxiality, K_{UMA} , an isotropic contribution K_{ISO}

$$K_{TOT} = K_{UMA} \sin^2(\varphi - \varphi_0) + K_{ISO} \quad (5.6)$$

where φ_0 is the direction parallel to the substrate-induced terraces. Its independence with respect to the in-plane angular direction guarantees the hysteretic behavior observed in the Co/C₆₀ systems.

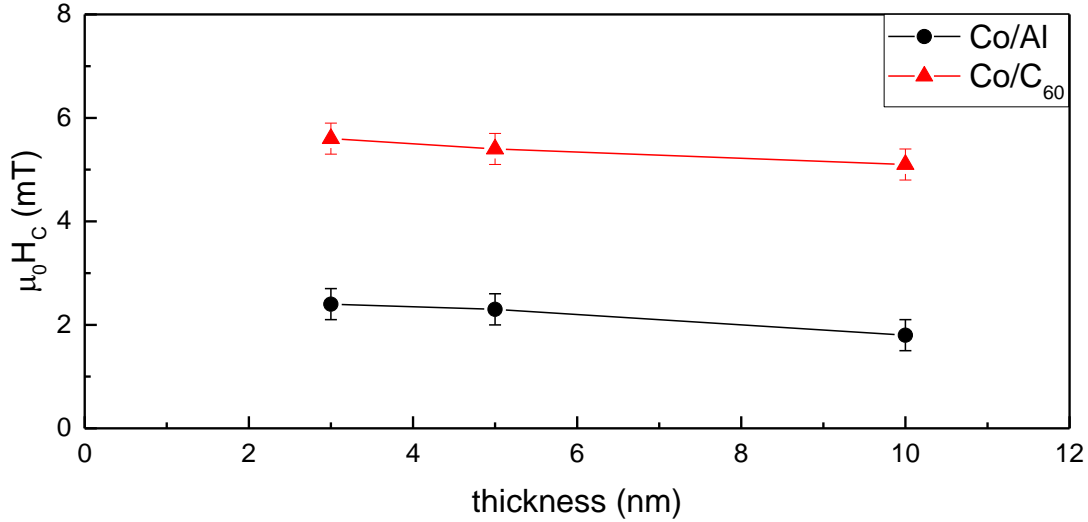


Figure 5. 4 Coercivity as a function of Co thickness for Co/Al (black dots) and Co/₆₀ bilayers (red triangles).

Table 5. 3 Co/C₆₀ samples: values of coercivity and normalized remanent magnetization extracted from the loops taken along the easy direction.

	Co10C60	Co5C60	Co3C60
EA $\mu_0 H_c$ (mT)	5.1 ± 0.3	5.4 ± 0.3	5.6 ± 0.3
EA M_S/M_R (a.u.)	0.99 ± 0.05	0.95 ± 0.05	0.95 ± 0.06

5.2.2 Loss of UMA and magnetic hardening of Co/Gaq₃ and Co/T₆ hybrid systems

The hardening effect and the partial suppression of UMA are not a peculiarity of the Co/C₆₀ systems but is also observed for both Co/Gaq₃ and Co/T₆ systems. Here I report the results obtained for a 5 nm thick Co layer covered with either T₆ or Gaq₃. The notation follows the previous one, so samples Al₂O₃(0001)//Co(5nm)/Gaq₃(25nm) and Al₂O₃(0001)//Co(5nm)/T₆(25nm) are labelled Co5Gaq₃ and Co5T₆ respectively. As can be

seen from the polar plots and the hysteresis loops reported in **Figure 5. 5**, both samples do not show uniaxiality apart for a very small modulation of the squareness. With respect to the reference Co/Al systems, the coercivity is increased (along the easy axis) by a factor of 2 for Co5T6 and a factor of 3/2 for Co5Gaq3 (see also **Table 5. 4**). The hardening effect is thus confirmed also for these two molecules. Additionally they have proven to practically suppress the uniaxiality of the Co layer. This result is of primary importance since it is the first time that the effect is observed for a Co/Gaq3 and a Co/T6 system and especially for a polycrystalline Co layer.

While the increase in coercivity resulted a common property of the Co/Molecule system characterized, the almost total suppression of UMA is not observed for a C₆₀ molecule. That Metal-Quinolines can modify the magnetic anisotropy of Co thin film was demonstrated experimentally in the work of *Bairagi et al.*[34], in which they observed the same in-plane to out-of-plane easy axis reorientation induced by C₆₀[1]. In this regard they suggest that the same *p-d* hybridization mechanism inducing a modification of the MCA for the Co/C₆₀ should also apply for Alq₃, since also this latter molecule (and importantly Gaq₃) forms hybrid *p-d* bonds when deposited over Co[20], [22]. A similar argument can also be invoked for the T6 molecule since, as already discussed in Chapter 1, the first molecular layer of T6 chemisorbs on transition metals by forming *p-d* bonds with the surface Co atoms. While the magnetic hardening may be qualitatively explained by the common model of hybridization-induced modification of the MCA, the less pronounced suppression of UMA for C₆₀ suggests that some differences should be present.

Surely the three molecules that have been used are different in symmetry and adsorption geometry. C₆₀ structure may be slightly deformed upon adsorption on Co but this is highly dependent on the FM surface symmetry[23]. Moreover, it tends to form ordered structures over well-oriented surfaces. Even if the Co layer is polycrystalline, the estimated mean grain size (approximately 10 nm) suggests that on this length scales C₆₀ can grow in a regular arrangement. On larger scales the different surfaces orientations results in a loss of order for the molecular layer. On the other hand, Gaq₃ molecules over Co surfaces instead become heavily distorted or even fragmented[22], [132]. This suggests a highly disordered growth even at the nm scale, as also the morphology study (see Chapter 4) suggests. The nature of the adsorption configuration, where two of the Quinoline monomers lie almost flat to the Co surface[22], makes possible the formation of more FM-Molecule bonds per molecule with respect to the C₆₀ case. Additionally Co atoms hybridizes not only with C atoms but also with

N and O[133], this latter known for its role in the modification of magnetic anisotropy for FM/Oxides systems[134]. From the calculation of Thiophenes on Co, their symmetry is modified due to the different interaction between C-Co and S-Co. Additionally, as discussed in Chapter 4, T6 is known to chemisorb with the major axis parallel to the substrate surface [28].

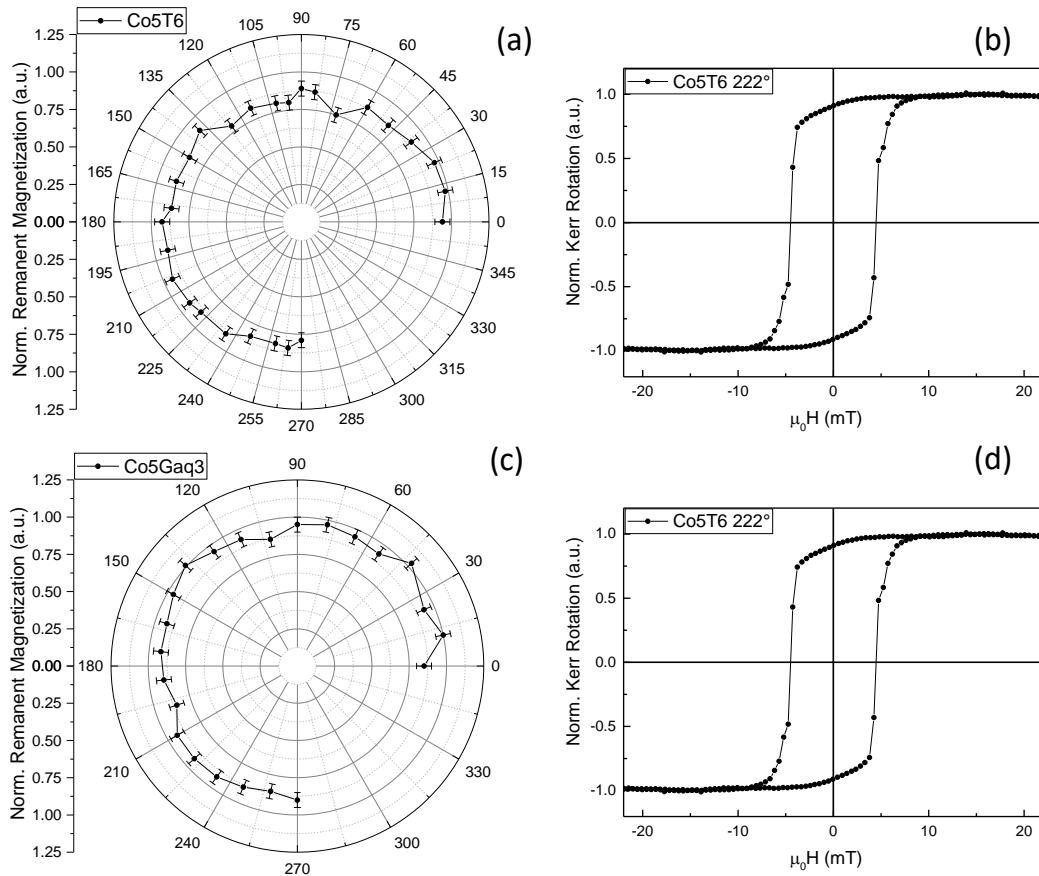


Figure 5.5 Polar plot of the normalized remanent magnetization as a function of the in-plane angular direction of the applied field and hysteresis loops for the easy and the hard directions for Co5T6 sample (a)(b) and Co5GaQ3 sample (c)(d). These samples show only a weak modulation of the uniaxiality, and the coercivity is slightly increase when the remanent normalized magnetization is lower.

Table 5.4 Values of coercivity and normalized remanent magnetization extracted from the loops taken along the easy (EA) and hard (HA) directions for Co5T6 and Co5GaQ3. The values found for Co5Al are reported for easier comparison.

	Co5Al	Co5T6	Co5GaQ3
EA $\mu_0 H_C$ (mT)	2.3 ± 0.3	4.5 ± 0.3	3.4 ± 0.3
EA M_S/M_R (a.u.)	1.09 ± 0.06	0.91 ± 0.05	1.01 ± 0.05

Thus an increased number of hybrid bonds per molecule are expected for both Gaq₃ and T6 with respect to C₆₀. In Author's opinion the reduction in symmetry and the increased number of hybrid bonds per molecule suggests that a more disordered Co/Molecule surface can result in a isotropic magnetic behavior of the hybrid system.

The complete suppression of UMA for these former molecules is an important achievement, suggesting the tunability of the anisotropy symmetry by molecular tailoring, and further studies are required to obtain a clear explanation of this effect.

5.3 The Co/C₆₀ case: evaluation of the anisotropy constant

For having a more complete comprehension of the variation of the magnetic anisotropy of the Co/C₆₀ systems, a vectorial VSM characterization was performed on Co/C₆₀ systems with different nominal thickness of Co layer and analogous Co/Al samples taken as a reference. As before the notation is based on the Co thickness and the molecule deposited. Samples Al₂O₃(0001)//Co(t=5,10nm)/Al(3nm) are labeled Co5Al and Co10Al, while Al₂O₃(0001)//Co(t=5,10nm)/C₆₀(25nm) are labeled Co5C60 and Co10C60.

Originally also a 3 nm Co nominal thickness was considered but the signal measured for the sample was too faint to be properly detected and analyzed. The magnetic characterization was performed with a Model 10 MicroSense VSM magnetometer at the CNR-ISM in Rome Montelibretti under the supervision of Dr. Gaspare Varvaro. Hysteresis loops were taken along the easy in-plane angular direction and the normal to the film plane. The cycles were corrected by the procedure reported in Appendix 4B. As can be seen in **Figure 5. 6** for both Co/Al and Co/C₆₀ systems no hysteretic behavior is seen when applying a field normal to the plane, confirming it as an hard axis. The coercivity values are reported in **Table 5. 5**. From the hysteresis loops along the easy direction the values of the saturation magnetization were obtained by normalizing the values of the magnetic moment at saturation, $m_s=|\mathbf{m}_s|$, considering the samples volume. For the calculation of the volume a 10% error was considered for both the area and the thickness. The values of the sample magnetic moment at saturation were obtained by averaging the values of \mathbf{m} obtained for applied magnetic field inductions higher than 1 T. Their associated error is the standard deviation. The values of M_s and μ_0H_C are reported in **Table 5. 5**. At any given thickness, even if a slight increase of the saturation magnetization is

detectable for the Co/C₆₀ system, the superposition of the error bars implies that M_S at most does not appreciably change by the presence of the organic molecule.

The effective out-of-plane magnetic anisotropy K is obtained by the procedure reported in [135], [136] by calculating the area enclosed between the in-plane (INP) and out-of-plane

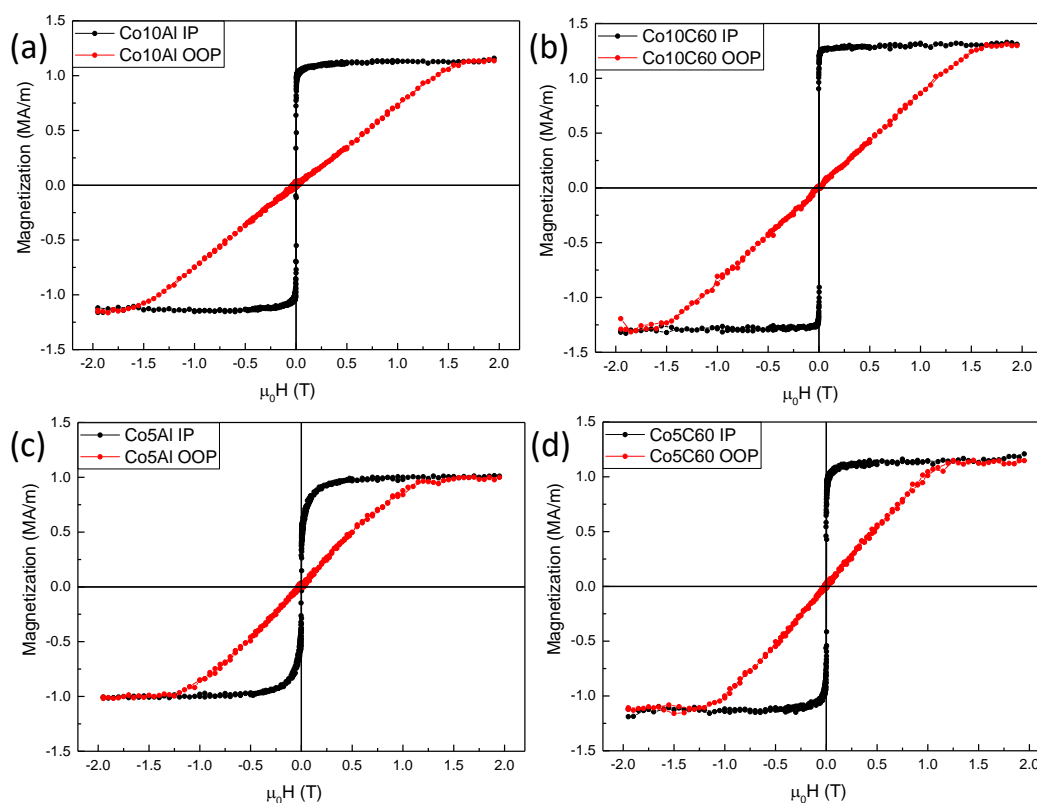


Figure 5. 6 Hysteresis loops taken along the in-plane easy direction (IP) and the film normal (OOP) for Co10Al (a), Co10C60 (b), Co5Al (c) and Co5C60 (d). All the cycles taken along the film normal are typical of an hard axis. A comparison of the cycles taken along the easy axis for a 5 nm (e) and 10 nm (f) Co thickness shows that Co/Al systems have a reduced remanent state. An increase in coercivity is still observed for the Co/C₆₀ systems.

Table 5. 5 Values of saturation magnetic moment (m_s), saturation magnetization (M_S) and coercivity (μ₀H_c) obtained by the VSM hysteresis loops reported in **Figure 5. 6**.

	thickness (nm)	area (mm ²)	m _s (nAm ²)	M _S (MA/m)
Co10Al	10 ± 1	1.8 ± 0.2	102 ± 1	1.1 ± 0.1
Co10C60	5.0 ± 0.5	1.8 ± 0.2	117 ± 2	1.3 ± 0.2
Co5Al	10 ± 1	1.8 ± 0.2	90 ± 1	1.0 ± 0.1
Co5C60	5.0 ± 0.5	1.8 ± 0.2	102 ± 2	1.1 ± 0.1

(OOP) half-branch from 0 to $+H_M$ of the anhysteretic curves (see **Figure 5. 7**). The anisotropy energy density is calculated as

$$K = \int_0^{H_M} M_{OOP}(H) - M_{IP}(H) dH \quad (5. 7)$$

it is adopted the convention that *a negative value of the anisotropy constant is corresponding to the film's normal being an hard magnetic direction*. The detailed procedure for the calculation of K is reported in Appendix 4B. For extracting the surface contribution to the OOP magnetic anisotropy it is used the well-known empirical formula[137] that decomposes K as the sum of a bulk contribution, labelled K_V , and a surface contribution K_S . The former contains typically the MCA and the shape anisotropy, while the latter is related to the interaction of the ferromagnetic atoms at the interface with both the substrate and the overlayer (this latter either Al or C_{60}):

$$K(t) = K_V + \frac{K_{S \text{ sub,Co}} + K_{S \text{ Co,overlayer}}}{t} \quad (5. 8)$$

In this characterization, due to the polycrystalline nature of the films, K_V is expected to be dominated by the shape anisotropy term. The surfaces contributions are interpreted in a phenomenological sense, meaning that

- the case $K_S > 0$ corresponds to the surface normal as an easy direction
- the case $K_S < 0$ corresponds to the surface normal as a hard direction

The resulting values of K are then multiplied by the thickness

$$Kt = K_{vol}t + K_{S \text{ sub,Co}} + K_{S \text{ Co,overlayer}} \quad (5. 9)$$

and for each thickness the values of Kt are subtracted. The corresponding quantity is

$$\Delta(Kt) = (Kt)_{Co,Al} - (Kt)_{Co,C60} \approx K_{S \text{ Co,Al}} - K_{S \text{ Co,C60}} \quad (5. 10)$$

assumes that the volume contribution to the OOP anisotropy is equal for both films. For polycrystalline samples the largest contribution comes from the large demagnetizing fields, produced when the film is magnetized perpendicular to the film plane. The magnetization values for the Co/ C_{60} system are always slightly bigger with respect to the corresponding of the reference. The associated error however allows to assume as a first approximation that the values of the shape anisotropy are the same for each system. This procedure allows to calculate the difference between the surface anisotropy energy of the Co/ C_{60} system with respect to the reference Co/Al. For a Co thickness of 5 nm a reliable value of $(-0.8 \pm 0.4) \text{ mJ/m}^2$ is obtained.

A similar result is obtained for the 10 nm thick Co systems. However, the associated error of each of the K_t suggests that for such thickness the surface terms is either negligible or quantitatively different. This latter possibility cannot be discarded due to the thickness dependent microstructure of the FM layer.

Focusing on the 5 nm Co systems, the findings from the VSM characterization requires to be discussed in more detail. First of all the increased in-plane anisotropy is not in contradiction with the results obtained by *Bairagi et al.*[33], [34] since the Co films characterized in this work are different from theirs in both thickness and composition. From their results for epitaxial Fe(001) they showed that the enhancement of the anisotropy may promote an in-plane easy direction as well[33]. Two possibly concurring causes can be pinpointed for the explanation of the increase in the in-plane anisotropy. The first one is that the surface anisotropy term due to the Co/C₆₀ is lower in magnitude with respect to the Co/Al reference. It has to be stressed at this point that for the Al thickness deposited over the Cobalt it is possible that the whole Aluminum is fully oxydized. While the interaction of Co with AlO_x is able to increase the PMA of the ferromagnetic layer, it has to be highlighted that this is the case when epitaxial Co is deposited

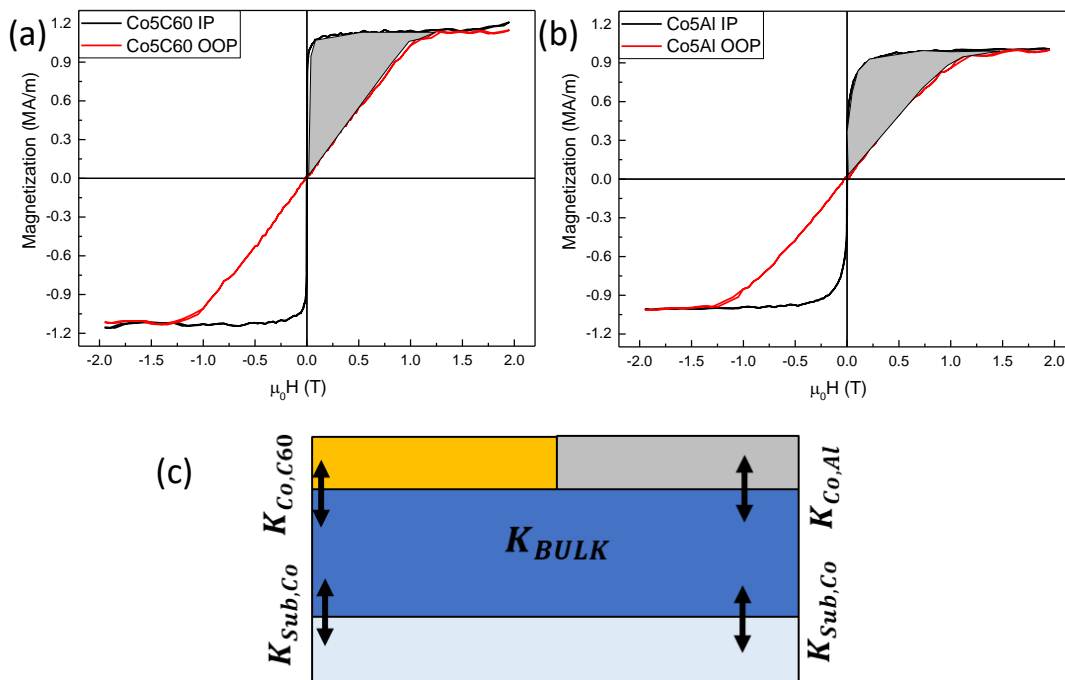


Figure 5. 7 Calculation of the effective anisotropy constant of sample Co5C60 (a) and Co5Al (b). The grey area is equal to the quantity calculated in Eq. (5.7). (c) Sketch of the anisotropies terms affecting the value of the effective anisotropy constant of the samples. Light blue Al_2O_3 substrate, blue Co, gray Al, orange C_{60} . The surface term corresponding to the $Al_2O_3(0001)/Co$ is common for both Co/Al and Co/ C_{60} systems.

over high SOC material such as Pt[134], [138], [139]. A possible effect of the oxidation of the Al layer cannot be excluded. C_{60} however is expected to modify the surface anisotropy term by the same $p-d$ hybridization mechanism of AlO_x , but increases the in-plane anisotropy. A second possibility is the increase of the shape anisotropy term by the increase in the magnetization of the sample. If the values of M_S are increased for the Co/ C_{60} system, then the energy difference in Eq. (5. 10) also contains a term proportional to the shape of the sample

$$\Delta(Kt) = (K_{sh\ Co,Al} - K_{sh\ Co,C60})t + K_{S\ Co,Al} - K_{S\ Co,C60} \quad (5. 11)$$

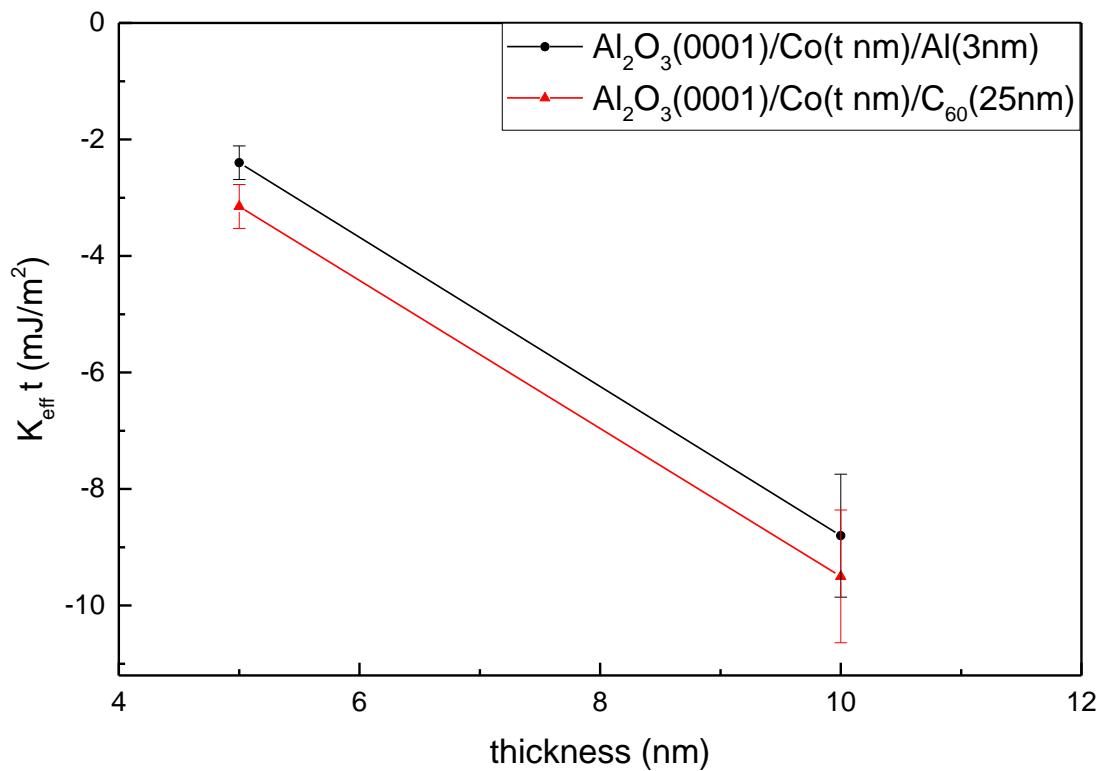


Figure 5. 8 effective anisotropy constant multiplied by t as a function of t .

Table 5. 6 Values of the effective anisotropy constant K and Kt calculated for each sample. The negative values mean that the normal to the film plane is an hard axis. In third column the difference in Kt between Co/ C_{60} and Co/Al are reported for each thickness.

	K (MJ/m ³)	Kt (mJ/m ²)
Co10Al	-0.88 ± 0.12	-9 ± 1
Co10C60	-0.95 ± 0.15	-10 ± 1
Co5Al	-0.48 ± 0.06	-2.4 ± 0.3
Co5C60	-0.64 ± 0.09	-3.2 ± 0.3

While the uncertainty in the calculated values of M_S forces to consider this quantity independent on the Co overlayer, the work done by *Moorsom et al.*[21] goes in the opposite direction showing a gradual decrease in the magnetization for a 5 nm thick Co film covered with an increasing thickness of C_{60} . For a 20 nm molecular thickness the loss of magnetization corresponds approximately to 0.2 MA/m. A direct comparison with their system is not strictly viable since they used a different substrate (a Ta seed layer) for stabilizing the microstructure of Co and the reference sample is a 2 nm Cu(001) layer decoupling the C_{60} layer. The combination of the results coming from the L-MOKE and VSM sheds more light on the magnetic anisotropy of the Co thin films interfaced with C_{60} . While only a comparative value of the surface anisotropy for Co/ C_{60} is obtained, the evidence of the loss of the in-plane UMA suggests the possibility of an absolute *negative* value of K_s , which means that this anisotropy constant favors an *easy plane* for the Co film.

5.4 The temperature dependence of molecular induced hardening effects

The RT characterization of the Co/Molecule bilayers highlighted the hardening effects of all the molecular species on the coercivity and the also the modification of the anisotropy of the Co layers. To get a deeper insight on this result and see how it evolves at low thermal energies, a temperature dependent characterization is performed by means of both L-MOKE and SQUID magnetometry. Firstly the magneto optical investigation is discussed.

Since the magnetic hardening proved to be rather thickness independent, a nominal Co thickness of 5 nm is chosen as a tradeoff between highlighting the interface-induced modification and at the same time guaranteeing an optimal S/N ratio. In order to discuss any possible role of Cobalt oxide, both a bare Co thin film and an Al-covered Co/ C_{60} bilayers were considered. The samples list is the following:

- $Al_2O_3(0001)//Co(5nm)$, named Co5Bare;
- $Al_2O_3(0001)//Co(5nm)/Al(3nm)$ named Co5Al;
- $Al_2O_3(0001)//Co(5nm)/C_{60}(25nm)$ named Co5C60;
- $Al_2O_3(0001)//Co(5nm)/C_{60}(25nm)/Al(4nm)$ named Co5C60Al;
- $Al_2O_3(0001)//Co(5nm)/Ga_2O_3(25nm)$, named Co5Ga3.

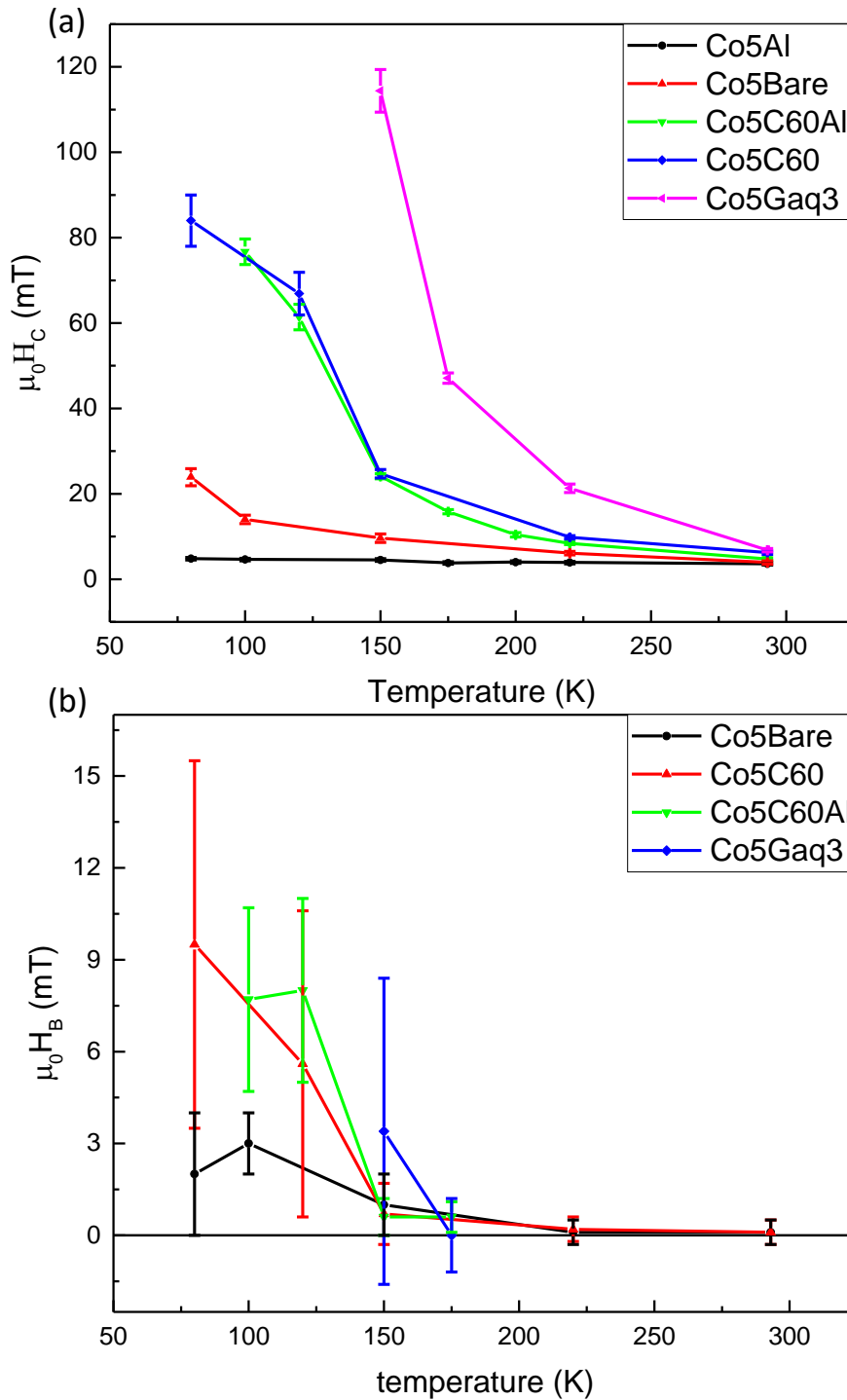


Figure 5. 9 (a) Values of coercivity as a function of temperature. A distinct increase in coercivity is visible for the Co/Molecule systems. CoGaQ3 and CoC60Al have lower coercivities after the temperature is decrease below 120 K and 80 K respectively. (b) Bias fields as a function of temperature. A slight bias field is visible for CoBare below 100 K, while CoC60 and CoC60Al present it below 120 K.

The applied field is parallel to the easy axis direction of the systems. All the samples were mounted on a copper cold finger and inserted in a cryostat with Quartz windows to allow for optical probing.

All the cycles are symmetrized by the procedure reported in Appendix 5B. The coercivity as a function of the temperature is reported in **Figure 5. 9(a)**. The Co5Al sample has an almost linear increase in hardness with decreasing the temperature, while for Co5Bare a change of slope is visible for temperatures below 100 K. A significant enhancement of the coercivity is visible for Co5C60, Co5C60Al and Co5Gaq3, with respect to both Co5Bare and the reference Co5Al. The μ_0H_C trend in temperature is clearly nonlinear for the Co/Molecule systems. At 150 K, for example, Co5Gaq3 held a value for μ_0H_C of (114 ± 5) mT, Co5C60 (25 ± 1) mT, Co5C60Al (24.1 ± 0.6) mT against a value of (4.5 ± 0.3) mT for the reference Co5Al sample and (10 ± 1) mT for Co5Bare. As can be seen from **Figure 5. 9(b)**, for low enough temperatures a horizontal offset was observed for hysteresis loops of the samples except Co5Al. This offset is observed below 100 K for Co5Bare and below 150 K for Co5C60 and Co5C60Al. While CoGaq3 too presented evidence of a field offset, the spacing between two adjacent measurements of the Kerr rotation was too coarse to determine it with certainty.

The first remarkable result is that the molecule-induced hardening effect observed at RT is greatly enhanced by decreasing the temperature. Moreover this colossal enhancement of coercive fields (CEHc) is molecule dependent. Already at 150 K the Co/Molecule systems have a one order of magnitude increase of coercivity if related to the reference Co/Al. Moreover, the qualitatively different trends of μ_0H_C in temperature suggest a more profound impact of the molecular layer on the magnetic behavior of the Co layer. Importantly, the very similar behavior of Co5C60 and Co5C60Al suggest that the Fullerene layer successfully prevents Co oxidation at the surface. The observation of horizontal offsets of the hysteresis loops are a fingerprint of a magnetic coupling between two different magnetically ordered phases, typically when a FM layer is exchange coupled to an AFM layer[37], [50], [73], [140]. As discussed in Chapter 2, this latter acts as an additional energy barrier for magnetization reversal of the ferromagnet and it is modelled as an additional, unidirectional field that is superimposed to the external applied field: $\mathbf{H}_{\text{eff}}=\mathbf{H}_{\text{appl}}+\mathbf{H}_{\text{exc}}$, inducing a horizontal shift of the hysteresis loops. The onset of this effect is found for temperatures below the so-called blocking temperature, that is the temperature at which the AFM layer becomes thermally stable and retains its magnetic state for sufficiently long times with respect to the measurement times[46], [50]. For Co5Bare sample the reported offset can be straightforwardly attributed to the formation of a CoOx layer at the

top surface[110]. For the Co/C₆₀ systems the origin of the field offset is not clear-cut. One possibility is that, as suggested by the work of Boukari et al.[36], the exchange bias field in Co/Molecule systems is related to a coupling between the FM layer and the magnetically ordered first molecular layers (see Chapter 1). A second possibility is that, before the deposition of the molecular layer, some portion of the Co layer becomes slightly oxidized. This eventuality conduces to interesting prospects. Surely the eventual amount of Cobalt oxide (CoOx) at the Co/Molecule interface is lower with respect to that of a Co surface exposed to atmosphere. In turn, its blocking temperature, hence the onset of exchange bias, would be found at a lower temperature than the one of the oxidized Co samples, given the lower amount of the AFM. The fact that Co/C₆₀ possesses an exchange bias at 150 K instead of 100 K or less indicates that either the amount of CoOx is negligible or that the Fullerene is able to affect the AFM CoOx magnetic properties. While this latter eventuality cannot be excluded at the moment, its eventual confirmation would be of paramount interest for tailoring of AFM properties for applications in FM/AFM systems.

5.4.1 Decoupling the interface:Co/CoOx/Molecule systems

In order to probe the robustness of the interaction between the Co and the molecular layer, in this subsection I will briefly present a recent comparative study of a set of Co/Molecule systems where their constituents are separated by a thin layer of Cobalt oxide. The growing procedure is the same of the other FM/Molecules bilayers studied, but after the growth of the Co layer the samples are moved back to the intro chamber where they were oxidized in a controlled O₂ atmosphere. Co layer has a 7 nm Co original nominal thickness and was subjected to an oxidation dose of 10⁴ L. For this latter a CoO layer of 2 nm is expected[141]. The sample are named based on (substrate is implied) Co(7 nm)/Ox/overlayer, so Co(7nm)/CoOx is Co7Ox, Co(7nm)/CoOx/Gaq₃ is Co7OxGaq₃ and Co(7nm)/CoOx/C₆₀ is Co7OxC60.

Hysteresis loops were collected at three different values of T=70,150,293 K. The coercivities as function of temperature are reported in **Figure 5. 10**. The trend for Co7OxC60 and Co7OxGaq₃ is equal to the one of Co7Ox without any detectable variation of the μ_0H_C values. This indicates that a thick Cobalt oxide layer effectively decouples the molecules from the Co film. This is also in favor of the hypothesis that the observed hardening effect reported for the non-oxidized Co/Gaq₃ and Co/C₆₀ systems is effectively originating by the FM/Molecule interface.

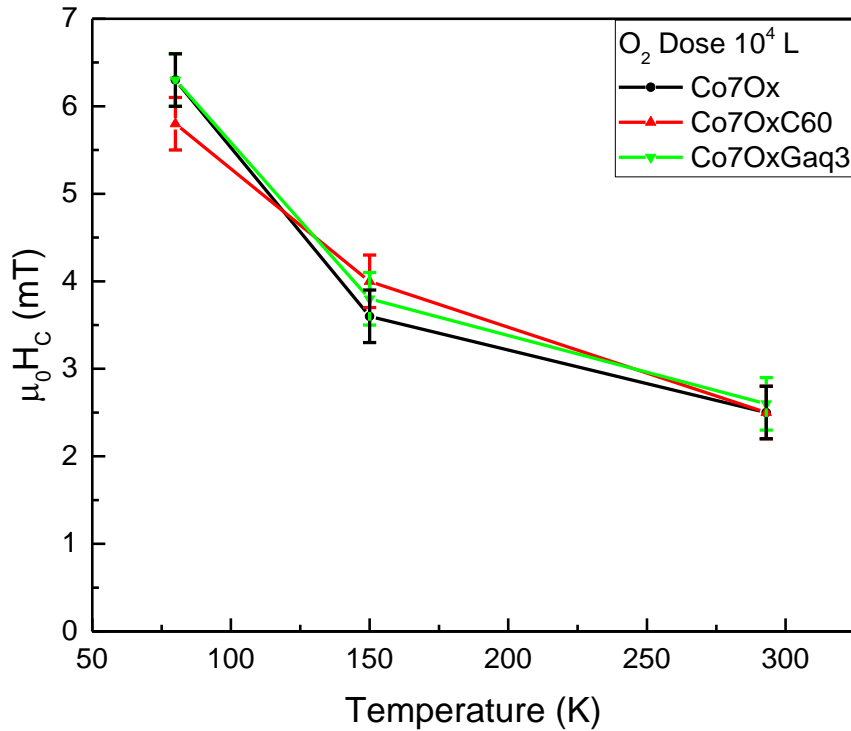


Figure 5. 10 Coercivity vs temperature for the Co/CoOx systems. The measured values are superimposable indicating a decoupled Co/Molecule interface.

5.5 Co/C₆₀: low temperature behavior

SQUID magnetometry was performed on a set of two samples of Co/C₆₀ systems with a Cobalt thickness of 5 and 10 nm respectively. The measurements were performed at the University of Manitoba under the supervision of Prof. J.V. Lierop, using a Quantum Design MPMS-XL SQUID magnetometer. These measurements allowed for a better definition of the samples magnetization values. Additionally the possibility to cool down the samples to 5 K permitted to obtain the values of coercivity and exchange bias field down to 5 K. The samples are named as in the previous sections by adding an S to indicate the nature of the characterization. Al₂O₃(0001)//Co(5nm)/C₆₀(25 nm) is sample Co5C60S and Al₂O₃(0001)//Co(10nm)/C₆₀(25 nm) sample Co10C60S. Importantly, these two samples were produced in parallel with the Co/C₆₀ systems used for the TEM microstructural characterization in Chapter 4.2. This means that the Co layer is the same and thus the thickness of these samples is well defined. So

- Co5C60S has an estimated thickness of (4.4 ± 0.2) nm
- Co10C60S has an estimated thickness of (9.9 ± 0.2) nm

A set of hysteresis loops as a function of temperature in the range 5-300 K were taken. Since the field step size was too coarse for well defining the coercivity from loops taken at temperatures of 100 K and higher, they are not reported. In **Figure 5. 11(a),(b)** are displayed the hysteresis loops of both samples for temperatures below 50 K, plus the RT measurement. All the measurements were performed by starting with a large positive applied field H_A^+ . For each sample the saturation magnetization is constant with the temperature, indicating that RT is far from the Curie temperature of the system. The calculated values of M_S are $(1.12 \pm 0.06)\text{MA/m}$ for Co10C60S and $(1.10 \pm 0.08)\text{MA/m}$ for Co5C60S, showing that the magnetization is not dependent on the Co thickness.

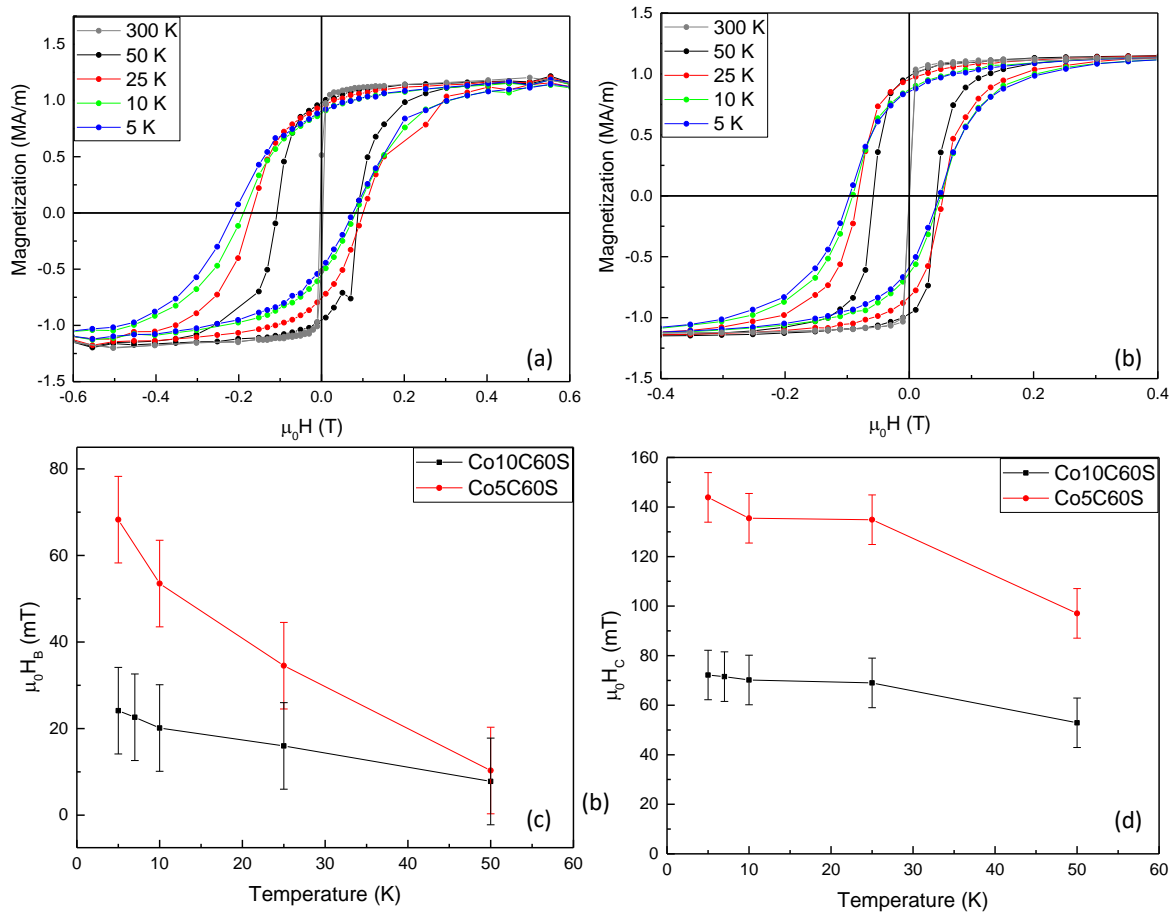


Figure 5. 11 Hysteresis loops of sample Co5C60S (a) (range reported ± 0.6 T) and Co10C60S (b) (range reported ± 0.4 T), showing a symmetric shape but with negative offset with respect to the origin, indicating the presence of a bias field. Their values are reported in (c) where a linear dependence with temperature is observed. Coercivities are reported in (d), also showing a linear dependence with T.

Both the coercivities and the exchange bias field instead are rather dependent on it. Since the TEM characterization (see Chapter 3.2) revealed an increased disorder for the 5 nm Co, it is likely to be the cause of the increase in coercivity as suggested by other works in literature[66], [142], [143]. All the cycles present a negative offset indicating the presence of an exchange bias field, as expected from the T dependent MOKE characterization results. Their values are shown in **Figure 5. 11(c)**, where a linear increase with decreasing temperature is visible for both samples. Higher values are found for Co5C60S sample, as expected due to its thickness. The extracted values of the coercivity reported in **Figure 5. 11(d)** shows that this quantity linearly increases with decreasing the temperatures in the temperature range 5-50 K, differently from the nonlinear trend exhibited for Co(5nm)/C₆₀ samples in the range 80-293 K.

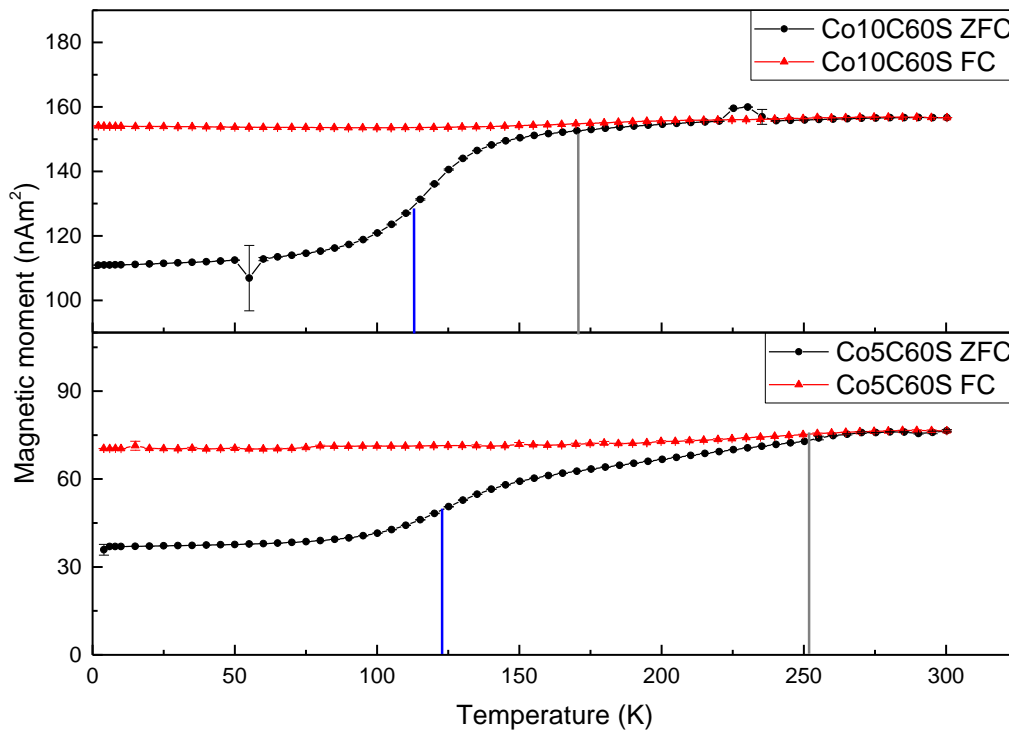


Figure 5. 12 FC (red triangles) and ZFC (black dots) curves for Co10C60S (up panel) and Co5C60S (down panel) for an applied magnetic induction of 10 mT. For a Co thickness of 5 nm a more gradual increase of m is observed with respect to the steeper trend of Co10C60.

Table 5. 7 Resume of the values of saturation magnetization M_S , blocking temperature T_B and irreversibility temperature T_I and r ratio for Co5C60S and Co10C60S.

	t (nm)	M_S (MA/m)	T_B (K)	T_I (K)	r (%)
Co5C60S	4.4 ± 0.2	1.10 ± 0.08	123 ± 5	252 ± 5	70 ± 2
Co10C60S	9.9 ± 0.2	1.12 ± 0.06	118 ± 5	170 ± 5	55 ± 2

For understanding the role of a different Co microstructure and looking for possible correlations with the hardening effect, Field Cooled (FC) and Zero-Field Cooled (ZFC) measurements performed. The ZFC curves were obtained by cooling down the sample to 5 K, followed by the application of a constant applied field induction of 10 mT and subsequent acquisition of the magnetic moment m values as a function of T up to 300 K. The FC curves instead are performed by cooling the samples in a constant applied field induction of 10 mT and by recording the values of m from 300 K to 5 K.

The obtained curves are plotted in **Figure 5. 12**. For each sample the FC curves are almost constant in temperature indicating that their Curie temperature is well above RT as also suggested by the magnetization values of the hysteresis loops reported. From the ZFC plots it emerges that at low temperatures (approximately < 25 K for Co5C60S and 50 K for Co10C0S) the applied field is not able to fully magnetize the sample, indicating that some magnetic moments are locked along their local preferential direction. Increasing the temperature allows these moments to “unfreeze” and freely align to the applied field, increasing the measured values of the m component parallel to the applied field. This recovery of magnetic moment is not sudden but rather diluted in a broad range of temperatures. After a certain temperature the ZFC curves is almost superimposed to the FC, indicating that a complete magnetization of the sample is obtained. Two temperatures are calculated for describing the behavior of the Zero-Field Cooled measurement. The first is the so-called irreversibility temperature T_I that is defined as the temperature below which the difference of the two curves is greater than 5% of the FC value. The second one is the blocking temperature T_B that is calculated as the temperature at which the derivative of the ZFC reaches its maximum, i.e. the inflection point of the curve[144]. While for the two samples the blocking temperature is approximately the same (see **Table 5. 7** for the values), T_I of Co5C60S is approximately 80 K higher than the one of Co10C60S, and reflects the broadening of the recovery of magnetization. Moreover the ratio $r = \frac{m_{ZFC}}{m_{FC}}$ between the magnetic moment of the ZFC and the one of FC at 3 K is (see also **Table 5. 7**) $(70 \pm 2)\%$ for Co10C60S and $(55 \pm 2)\%$ for Co5C60S. As showed in Chapter 4.2, the only difference between the two samples is the microstructure. While for the 10 nm thick Co layer the crystallinity was well-defined, the 4.4 nm thick Co layer exhibited areas of low contrast with unclear crystalline phase. An increase in disorder can be accompanied by a wider distribution of Co grains, explaining the broadening of the ZFC curve for Co5C60S. At the same time the more disordered structure may result in less correlated grains, increasing the amount of Co that, lowering the temperature, is free to locally align the magnetic moment along their preferential

direction. It is worthy at this point to look at the trend in coercivity of the Co/C₆₀ systems in the whole available range of temperatures, reported in **Figure 5. 13**. The double-log scale helps to highlight the two different trends of coercivity increase for a temperature threshold value of approximately 100 K. Below that temperature the coercivity increases at a slower rate. Interestingly, a similar behavior is observed in the ZFC curve of the Co(5nm)/C₆₀ system, with a nonlinear decrease of the magnetic moment followed by a stabilization at around the same value. This seems to suggest a correlation with the microstructural disorder of the Co layer. At the same time, however, the Co/Al reference system behaves linearly between 80 and 293 K. In principle one cannot exclude a qualitative different trend for temperatures below 80 K. However, the observed differences between the H_C(T) curves of Co/Al and of Co/C₆₀ systems in the same temperature range (80-293 K) indicates that the microstructure of the Co layer cannot account alone for both the ZFC trend and the increase in coercivity for the Co/C₆₀ systems.

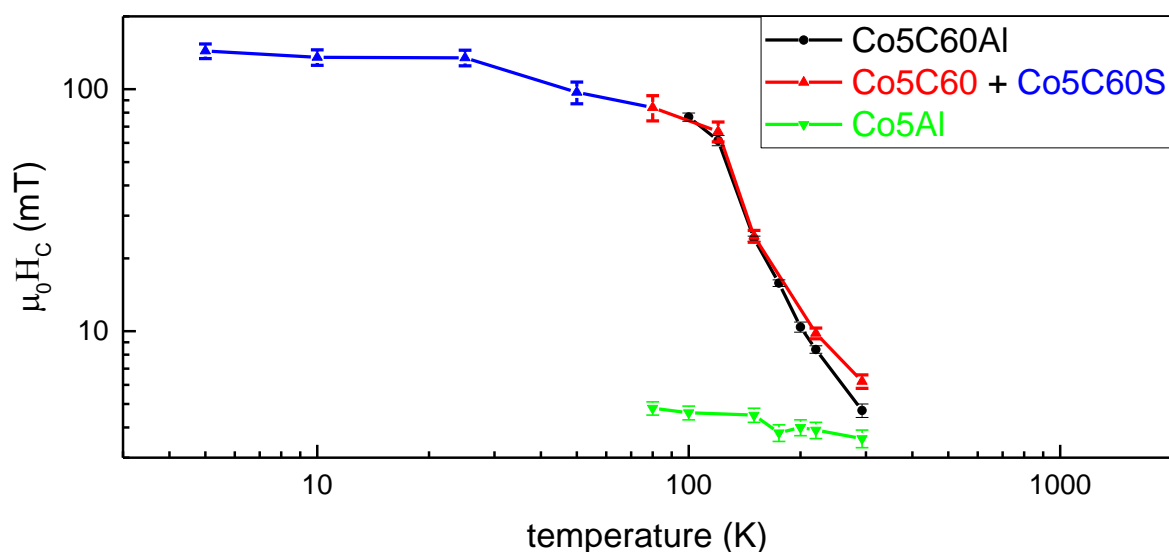


Figure 5. 13 Coercivity vs T plot for the Co/C₆₀ systems in the whole available temperature range, in double log scale. Also Co5Al system is displayed for comparison. Two different temperature regimes are observed for Co/C₆₀ systems.

5.6 Conclusions

All the results showed in the previous subsections clearly indicate that the polycrystalline Cobalt layer has the magnetic anisotropy substantially altered if interfaced with either Fullerene, Gallium-Quinoline or Sexithiophene.

Compared to the reference Cobalt layers, all the Co/Molecule system presented systematically a substantial enhancement of the coercivity at room temperature, which is important for device design and fabrication, accompanied by a reduction of uniaxiality, i.e. hysteretic behavior for every in-plane angular direction of the applied field. This latter effect is strongly molecule dependent, resulting in nearly isotropic in plane dependence for Cobalt interface with Gallium Quinoline or Sexithiophene, while with Fullerene a residual uniaxiality was detected. This result is a first suggestion for the role of disorder in the observed molecule-induced effects.

Detailed investigation on Co/C₆₀ showed that while the saturation magnetization is not appreciably modified by the molecular layer, its interfacial contribution is higher than the one of the reference Co layers. This result is almost complementary to the loss of UMA, suggesting that at least for this system an additional anisotropy term, independent on the in-plane angular direction, is superimposed to the uniaxial one possessed by the reference Co film.

At low temperatures, All Co/Molecules systems showed a colossal enhancement of the coercive fields. The most remarkable increase is observed by the Co interfaced with Gaq₃ which possesses a coercivity that is 30 times higher than the reference Co/Al at 150 K. A lower but significative enhancement of a factor 7 is showed by Cobalt interfaced with Fullerene. At the same temperature the bare Co thin film oxidized in air showed only a twofold increase in coercivity. The temperature characterization of oxidized Co/CoOx/C₆₀ and Co/CoOxGaq₃ systems showed that an oxide layer effectively decouples the FM layer from either C₆₀ or Gaq₃, highlighting the role of the molecules in the establishment of the hardening effect.

The hardening effect is accompanied at sufficiently low temperatures by the onset of an exchange bias field. For the Co/C₆₀ is observed at temperatures lower than 150 K, differently from the bare Co thin film for which it appeared only at 100K. The origin of this exchange bias is under further analysis. Additionally, the absence of an exchange bias for the Co/Al systems highlights the role of Al as Oxygen getter and suggests that O₂ tends to not diffuse from Al to Co and form a CoOx layer.

Finally, the similarities between the trend of coercivity in temperature and the ZFC for the Co(5nm)/C₆₀ system is a further suggestion of the presence of disordered magnetism tentatively attributable to the Co/Molecule interfaces.

Appendix 5A MOKE hysteresis loops treatment

In the following it is reported the procedures for the MOKE data corrections and the extrapolation of the values of interest. All the loops were taken by starting from a large negative value of the applied field H_{Max}^- to the opposite positive value H_{Max}^+ and back ($H_{\text{Max}}^- \rightarrow H_{\text{Max}}^+ \rightarrow H_{\text{Max}}^-$).

Normalization procedure, coercivity, bias field and squareness calculation.

The normalization of the loops is performed by dividing all the points for the value of the Kerr rotation measured at the maximum applied field. For each branch the value of the coercive field is obtained by searching for its point of interception with the x-axis (=0). To better visualize see also **Figure 5A.1**. To find it, the straight line that connects the last point in the negative y half plane (labelled A) to the first point in the positive y half-plane (labelled B) is determined. The coordinates ($\mu_0 H$, M/M_s) of the two points are used for the calculation of the angular coefficient m and the intercept q by geometry arguments, the value of the coercive field for a single branch is given by

$$\mu_0 H_C = - \left(\frac{\frac{M(A)}{M_s}}{m} - \mu_0 H(A) \right) \quad (5A. 1)$$

The coercivity is the mean value of the values measured along each branch

$$\langle \mu_0 H_C \rangle = 0.5 \mu_0 (|H_C^-| + |H_C^+|) \quad (5A. 2)$$

Where the superscript -, + refer to the start and return branch respectively. The bias field is calculated as

$$\mu_0 H_B = -\mu_0 H_{\text{offset}} = -0.5 \mu_0 (|H_C^+| - |H_C^-|) \quad (5A. 3)$$

If the hysteresis loop is heavily distorted however, the calculation of the coercivity is performed by a direct inspection of the loop. The error associated to the measurements is, for being conservative, chosen as half the value of the field resolution, i.e.

$$\delta(\mu_0 H) = 0.5 |H(i) - H(i+1)| \quad (5A. 4)$$

For each branch, the calculation of the value of the squareness S , i.e. the normalized remanent magnetization, is more straightforward. It is taken as the average y coordinate of the last point

in the negative x half plane (labelled C) to the first point in the positive x half-plane (labelled D):

$$S = \frac{M_R}{M_S} = 0.5 \left(\frac{M(C)}{M_S} + \frac{M(D)}{M_S} \right) \quad (5A.5)$$

This procedure is less precise, but it is the best thing in practice since for noisy loops any finer procedure would be useless. For this reason, the error associated to the measurement is always not less than 5% of the measured value.

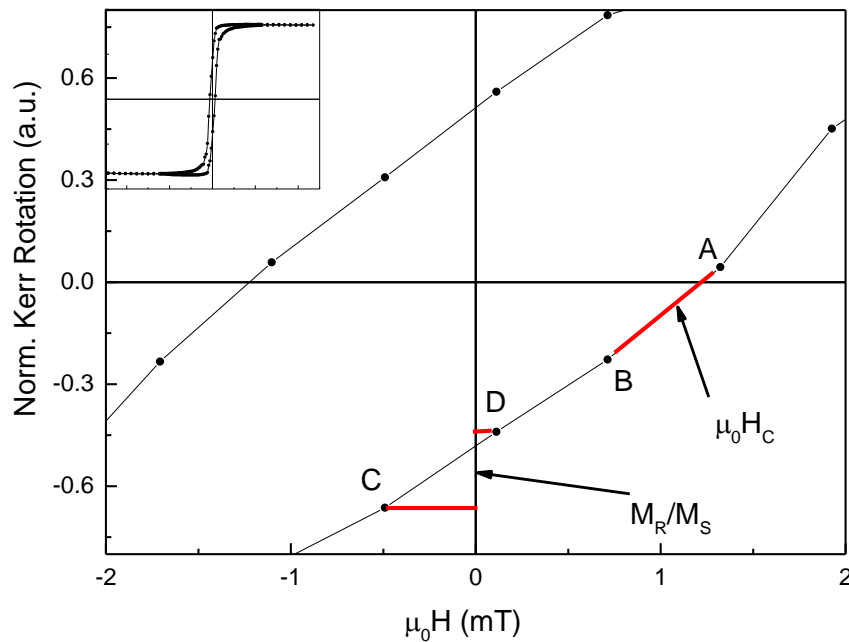


Figure 5A.1 Example of the determination of the coercivity and the squareness.

Loop adjustments: quadratic contributions removal

The raw L-MOKE loops measured on a given sample often are different from the typical shape that the theory predicts. Different additional contributions can be superimposed to the ordinary ferromagnetic signal, the one of interest. In the following I will present the extra terms that can be encountered and how to correct the signal. The first to be addressed is a second-order contribution to the magneto-optical response of the sample, called quadratic MOKE (QMOKE)[145]. It was first discovered by *Osgood et al.*[146] and *Postava et al.*[147] for epitaxial ferromagnetic thin film with in-plane magnetization. This effect arises by a magneto-optical coupling that is second order in the magnetization vector, containing the mixed terms $M_L M_T$ and $M_L^2 - M_T^2$. This effect sums up to the term linear in M_L (in the case of longitudinal

MOKE configuration) and presents an even parity. The two components can be easily separated by applying a symmetrization procedure on the hysteresis loop[145], [148]. A general method is developed for the treatment of epitaxial thin films[148]. The even (quadratic) and odd (linear) components of an hysteresis loop taken along a certain direction of the applied field φ are obtained by summing (subtracting) the Kerr rotation values θ_k with the ones obtained from the hysteresis loop taken at the direction $\varphi+180^\circ$:

$$\theta_{K,Asym}(\varphi) = \frac{1}{2} (\theta_K(\varphi) + \theta_K(\varphi+180^\circ)) \quad (5A. 6)$$

$$\theta_{K,Sym}(H) = \frac{1}{2} (\theta_K(\varphi) - \theta_K(\varphi+180^\circ)) \quad (5A. 7)$$

In this thesis the procedure followed is the one developed by *Hamrle et al.*[145]. Given an hysteresis loop, its even (quadratic) and odd (linear) components are calculated by summing (subtracting) the values of θ_k in the first branch of the loop (for example from $-H_{Max}$ to $+H_{Max}$), denoted *inc*, with the corresponding values of the second branch ($+H_{Max}$ to $-H_{Max}$), denoted *dec*.

$$\theta_{K,A}(H) = \frac{1}{2} (\theta_{K,inc}(-H) + \theta_{K,dec}(+H)) \quad (5A. 8)$$

$$\theta_{K,S}(H) = \frac{1}{2} (\theta_{K,inc}(-H) - \theta_{K,dec}(+H)) \quad (5A. 9)$$

Experimentally this procedure has to be performed over a discrete dataset of N datapoints on the form $(\mu_0 H, \theta_K)$, $N/2$ belonging to the first branch and $N/2$ belonging to the second branch. To symmetrize the loops, the first branch is (anti)symmetrized point to point. For the i -th point, ranging from 1 to $N/2$ included,

$$\theta_{K,A}(i) = \frac{1}{2} \left(\theta_K(i) + \theta_K\left(i + \frac{N}{2} - 1\right) \right) \quad (5A. 10)$$

$$\theta_{K,S}(i) = \frac{1}{2} \left(\theta_K(i) - \theta_K\left(i + \frac{N}{2} - 1\right) \right) \quad (5A. 11)$$

where the second term in the right-hand side is the corresponding value of the Kerr rotation in the second branch. For the return branch the procedure is the same

$$\theta_{K,A}(i) = \frac{1}{2} \left(\theta_K\left(i + \frac{N}{2} - 1\right) + \theta_K(i) \right) \quad (5A. 12)$$

$$\theta_{K,S}(i) = \frac{1}{2} \left(\theta_K\left(i + \frac{N}{2} - 1\right) - \theta_K(i) \right) \quad (5A. 13)$$

The issue that is encountered in this procedure is the presence of loop shifts, induced by the presence of either an exchange bias or (more common) the presence of a trapped field due to the ferromagnetic polecaps of the electromagnets. This additional field shifts the value of the actual field felt by the sample of a certain value H_s , that can result in an index mismatch between the two branches. It is detrimental in the correct symmetrization especially in the vicinity of the coercive field. In order to be systematic and avoid any error induced by the symmetrization procedure, the values of H_C and H_s are calculated *before* the symmetrization procedure.

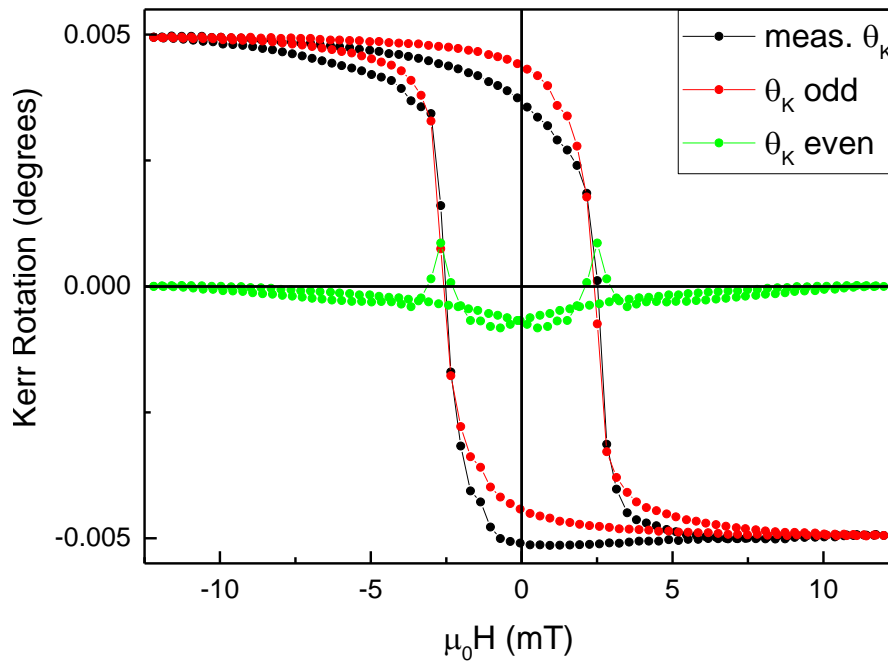


Figure 5A.2 Symmetrization procedure of the hysteresis loop. Black dots represent the measured values of the Kerr Rotation, red dots are the symmetric component ($\theta_{K,S}$) and green dots are the antisymmetric component ($\theta_{K,A}$).

Appendix 5B VSM and SQUID loops treatment

Removal of the background signal

All the $m(H)$ hysteresis loops obtained by either VSM or SQUID contains additional spurious signals that can be related either to the sample holder or to a paramagnetic/diamagnetic contribution of the studied samples. In particular a diamagnetic contribution due to the $Al_2O_3(0001)$ substrate is always encountered. For the VSM measurements the correction was done by subtracting point-by-point the signals of both the sample holder and the bare substrate, that were measured separately. In the case of SQUID measurement, the procedure was done by taking a linear fit

of the saturated region of the hysteresis loops, for both positive and negative values. The diamagnetic contribution is then removed by subtracting a straight line with the mean slope obtained by the fitting procedure.

Calculation of the anisotropy constant

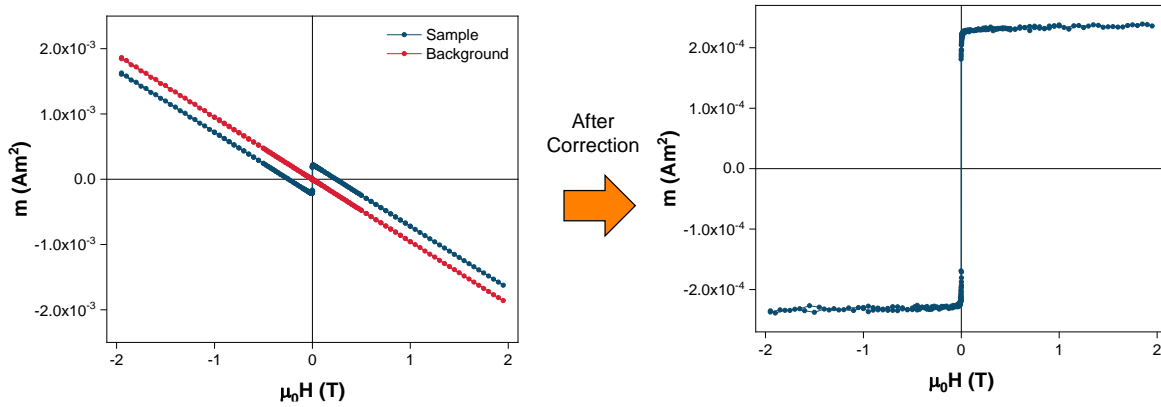


Figure 5B. 1 Example of background signal removal for a VSM raw loop, by subtracting point by point the contribution of the sample holder + substrate, taken separately.

The calculation of the anisotropy constant is done based on equation

$$K = \int_0^{H_M} M_{OOP}(H) - M_{IP}(H) dH \quad (5B. 1)$$

For each sample, the actual steps for the calculation of K are the following. First both the IP and OOP loops are averaged with its reversed order copy (so that the return branch is mediated with the start branch), obtaining thus the loop $m(B)$. Each of these cycles are numerically integrated by the trapezoid method, with absolute areas. Note that no conversion from the magnetic moment (raw data) to the magnetization is performed. The result is in J. The calculated area is 4 times the area of interest (see **Figure 5B. 2**), and is thought as, if divided by 4, the average area under the curve. The K value (in J/m^3) is then

$$K = \frac{(I_{OOP} - I_{INP})}{4At} \quad (5B. 2)$$

where A and t are the sample area and thickness respectively. Since the values of m are never transformed, the calculation of Kt is directly

$$Kt = \frac{(I_{OOP} - I_{INP})}{4A} \quad (5B. 3)$$

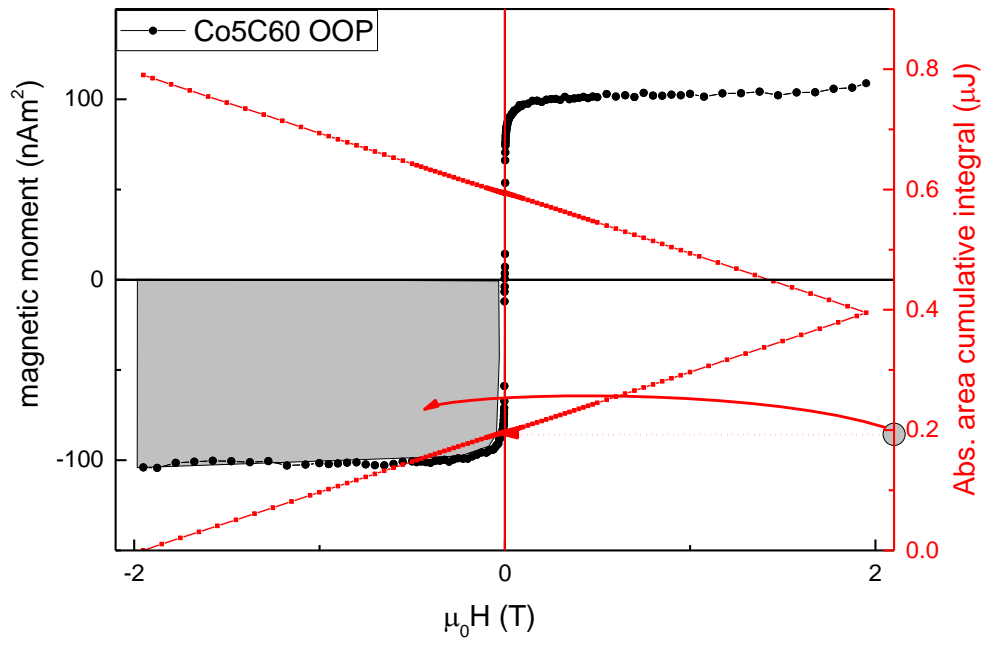


Figure 5B. 2 Example of the calculation of the area under the anhyseretic curve. Black dots represent the anhyseretic curve, red dots represent the value of its cumulative absolute integral, which is 4 times the integral I.

Chapter 6

Probing the depth of the spinterface

As discussed in Chapter 1, the OSC-induced modifications of the magnetic properties are considered as localized at the very boundary between the FM and the molecular layers. The magnetic hardening effect reported in Chapter 5 proved to be substantial for Co thicknesses up to 10 nm. The natural question that arises is thus whether this effect is localized near the interface or is extended to a significant portion of the ferromagnet. In this perspective Nuclear Magnetic Resonance (NMR) is a perfect experimental technique for probing the magnetic responses on interatomic length scales. In particular, NMR characterization on ferromagnetic samples can be performed, even at room temperature[149], without the need of an external applied field[104]. In FM systems the nuclear spins are aligned to the magnetization through the hyperfine field HF generated by the spin-polarized electrons[98], [104], [150]. This technique is usually called zero-field NMR or Ferromagnetic NMR (FNR) and has proven to be important for characterization of magnetic multilayers[151], [152] and alloys[153], due to its sensitivity to the Co environment and the system magnetic arrangement.

This chapter is thus dedicated to the ^{59}Co FNR characterization of Co/C₆₀ and Co/Ga₃ films. In the first section I will present the results related to the local magnetic hardness of the Co films interfaced with the OSC, discussing how much of the Cobalt layer is effectively modified by the molecular layer. The last section is dedicated to the contribution of the interface to the ^{59}Co FNR spectra by comparing the results with a reference Co system.

6.1 Bulk modification of the magnetic hardness

The samples characterized by ^{59}Co FNR are Co(7nm)/Ga₃(25 nm) and Co(7nm)/C₆₀(25 nm) bilayers, named Co7Ga₃ and Co7C₆₀ respectively. A reference Co(7nm)/Al(8nm) bilayer was considered (named Co7Al). These samples were grown using the procedure reported in Chapter 3.1.2. Importantly, in order to perform a comparative study, all the samples were fabricated in a single deposition, ensuring an equal Co thickness.

^{59}Co FNR was performed at the Department of Physics of the University of Parma under the supervision of Prof. Giuseppe Allodi, using the HyReSpect NMR setup[106] described in Chapter 3.4. Temperature was fixed at 77 K, the spin-echo signal was obtained by a T-T pulse sequence (pulse duration 0.405 μs , delay between pulses 500 μs) in zero external applied field. For avoiding shifts of the resonance frequency due to demagnetizing fields, the rf field was applied inside the film plane, along the same direction for each sample. In order to obtain information about the samples magnetic hardness and reconstruct the ^{59}Co spectra, I took several NMR spectra in the range 192-232 MHz for different values of the applied RF power P_{rf} [154]. The ^{59}Co FNR signal as function of both the resonance frequency and P_{rf} (in dBm) are reported in **Figure 6. 1(a)** as 2D contour colormaps. Their shape is typical of Co polycrystalline samples[102], [105] as expected. Most of the signal is obtained at resonance frequencies attributed to bulk Co (210-230 MHz)[104], [151], [152], [155]. The maximum global spin-echo response of each sample is found at different positions in both ω and P_{rf} . Both Co7Al and Co7C60 are peaked at around 222 MHz while Co7Gaq3 at 217 MHz. More interestingly the optimum value of P_{rf} is found at 20 dBm for Co7Al, 27 dBm for Co7C60 and 33 dBm for Co7Gaq3. In general for each frequency the center of mass of the spin echo signal is translated towards high values of applied field power for the Co/Molecule system, suggesting a global hardening of the whole film. Indeed, the optimal power for the excitation of Co7Al does not produce measurable spin-echo amplitudes (thus, rotations of the electronic magnetic moment) in both Co7C60 and Co7Gaq3.

For verifying this result, I calculated, in the range 210-228 MHz, the enhancement factor for each sample. For each frequency, η is found by fitting the FNR signal as function of P_{rf} (in dBm) with a single Gaussian[102]. The value corresponding to the maximum spin-echo peak is then converted into a η value by a calibration procedure. Since the focus is to evaluate how the magnetic hardness is affected by the deposition of the organic molecule, I calculated for each frequency the ratio R between the enhancement factor of Co7Al and the corresponding one of both Co7C60 and Co7Gaq3. This corresponds to the ratio between the restoring fields, because

$$R = \frac{\eta(\text{Co7Al})}{\eta(\text{Co7OSC})} = \frac{\left(\frac{HF}{H_r}\right)_{\text{Co7Al}}}{\left(\frac{HF}{H_r}\right)_{\text{Co7OSC}}} = \frac{H_r(\text{Co7OSC})}{H_r(\text{Co7Al})} \quad (6. 1)$$

where OSC=C₆₀ or Gaq₃. The results are plotted in **Figure 6. 1(b)**. As can be seen, the values of R are always significantly bigger than 1, regardless of the frequency. Additionally the ratio

for Co7Ga₃ is systematically higher than the corresponding of Co7C₆₀. The slight modulation of R is attributed to a non-uniform response of the RF coil. This is a clear evidence that even inside the bulk the Co thin films interfaced with either C₆₀ or Gaq₃ become magnetically harder, the latter molecule being the more effective. This hardening is also confirmed by L-MOKE

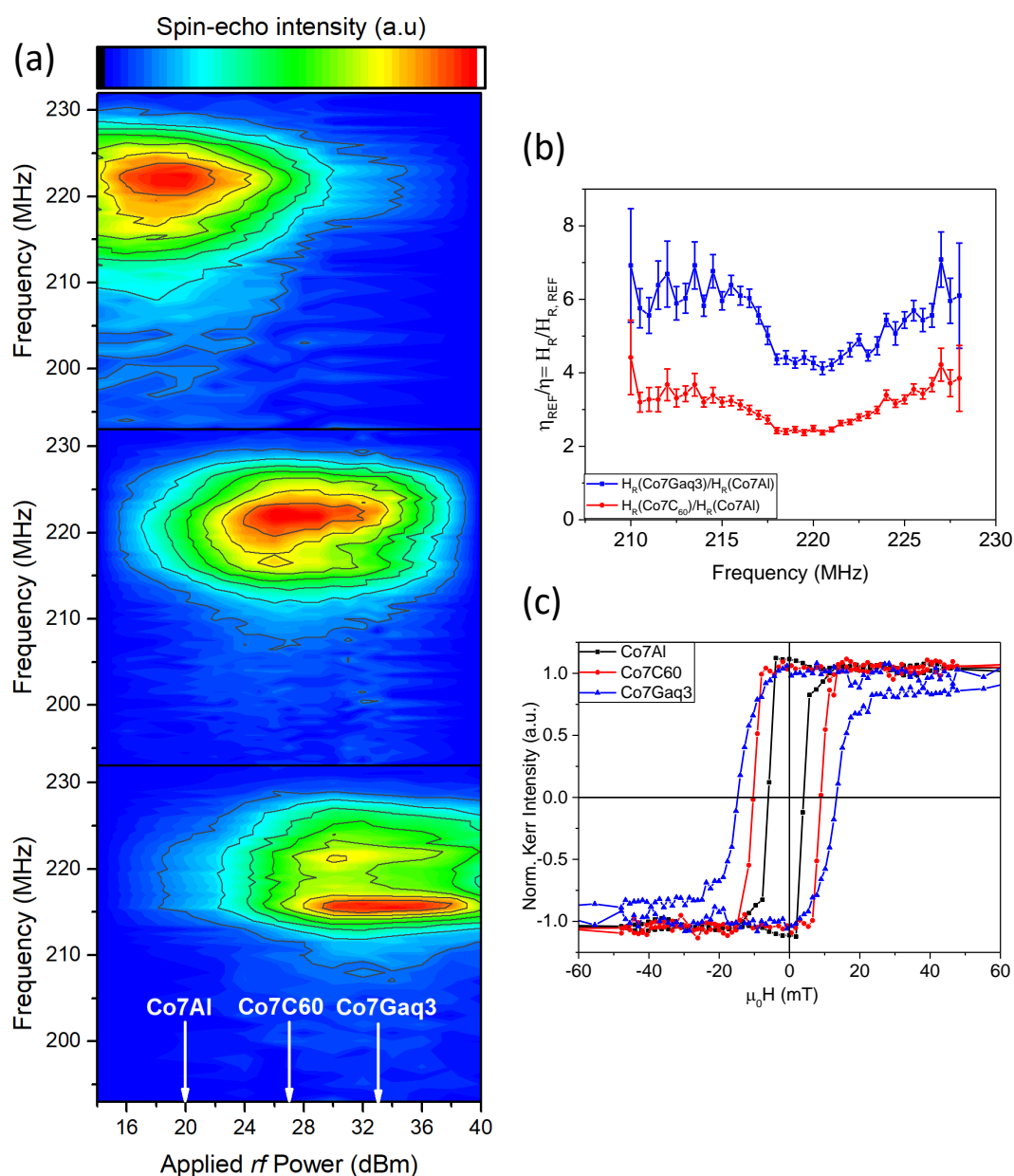


Figure 6. 1 (a) 2D contour heatmaps of the spin-echo signal at 77 K. The P_{rf} value of the global maximum is highlighted by white arrows. A general shift of the towards high values of P_{rf} is evident for Co7C60 and Co7Ga₃. (b) Ratio R for Co7C60 and Co7Ga₃ in the frequency range corresponding to the bulk. The Co/Molecule system becomes magnetically harder even several nm from the interface. (c) L-MOKE hysteresis loops at 77 K confirms this effect showing a coercivity increase for Co7C60 and Co7Ga₃.

hysteresis loops taken at 77 K, reported in **Figure 6. 1 (c)**. The external field was applied along the same direction of the *rf* field in the NMR measurement. Co7Al system has the lowest coercivity, (5.0 ± 0.3) mT, which is half the one of Co7C60, (9.6 ± 0.4) mT and roughly 1/3 the one of Co7Gaq3, (14.1 ± 0.4) mT. This hardening effect is an additional confirmation of the results reported in Chapter 5. In addition to this, however, the observation of the increase in restoring fields for frequencies proper of bulk Co is a strong evidence that this molecule-induced effect manifests itself even at several nanometers from the Co/Molecule interface.

6.2 Interfacial contribution to the FNR spectra

In the previous section it is showed that the interface-induced effects are extended to a considerable portion of the Cobalt layer. In this section, I focus on how this last is affected at the interface with the molecules. From the 2D analysis the ^{59}Co spectra (reported in **Figure 6. 2**) are reconstructed by normalizing, for each sample, the spectra with the highest FNR signal by the average enhancement factor and subsequently by the total spectral area. The spectra are in agreement with those associated to polycrystalline Cobalt samples, with a non-zero contribution coming from the low-frequency range (frequency less than 210 MHz). The correct attribution of peaks is debated in literature, and often related to the crystalline structure of the sample[98], [151], [152], [154], [156]. Three main peaks (labelled I, II, III in **Figure 6. 2**) can be associated respectively to *fcc* phase (215-217 MHz), stacking faults (of both *fcc* and *hcp*) and *hcp1* (220-224 MHz), *hcp2* (224-228 MHz); *hcp1* and *hcp2* account for different responses of the relative direction of the magnetization vector and the crystal c-axis. The fourth broad component (IV in **Figure 6. 2**) incorporates all the contributions of the Co nuclei that are not ascribed to the above phases. This includes Co nuclei that are in a ferromagnetic environment different with respect to that the bulk, like for example grain boundaries[151], interfaces with non-magnetic species like Copper or Aluminum[103], [152], [153], [157].

The four components are clearly visible in **Figure 6. 2**, represented by four Gaussian contributions of the spectra. The numerical results of the fitting procedure are reported in **Table 6. 1**. The spectral weight of each peak is proportional to the percentage of the Co nuclei resonating at that frequency. Co7Al and Co7C60 have similar spectral shapes, with a 1:2 ratio between peak I and II, and their total weights account for the 50% of the overall spectrum. The center of peak IV for Co7Al is found at a lower frequency than for Co7C60. Noteworthy, in Co7Gaq3 the spectral shape is different, featuring a 1:1 ratio between peaks I and II, while their total weights still account for the 50% of the overall spectrum. The position of the peak IV is

nevertheless very close to the one of Co7C60. The relative intensity of peak III does not vary significantly from sample to sample.

Now I will analyze the possible contribution of the interface to peak IV. To do this the cumulative integral of each spectrum is calculated and normalized to the total spectral area (see

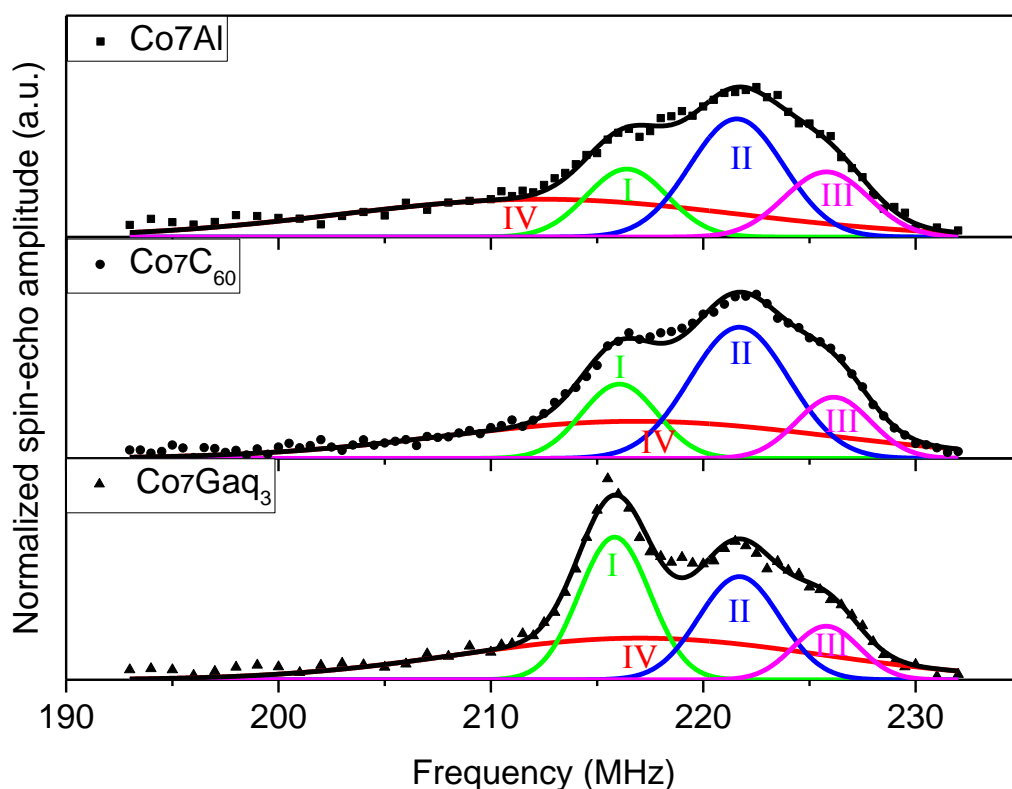


Figure 6. 2 Normalized corrected FNR spectra (points) fitted with four Gaussians (colored lines).

Table 6. 1 Results of the fitting procedure (peak position and area under the peak) of the FMR spectra of Co7Al (2nd and 3rd row), Co7C60 (4th and 5th row) and Co7 Gaq₃ (6th and 7th row). ω_P : resonance frequency peak. S.W.: Spectral Weight.

PEAK	I	II	III	IV
ω_P (MHz)	216.0 ± 0.2	221.7 ± 0.3	226.2 ± 0.2	212 ± 2
S.W (%)	15 ± 5	30 ± 8	15 ± 4	40 ± 8
ω_P (MHz)	216.0 ± 0.2	221.7 ± 0.3	226.2 ± 0.2	217.0 ± 0.6
S.W. (%)	15 ± 3	37 ± 4	11 ± 3	37 ± 3
ω_P (MHz)	215.7 ± 0.3	221.5 ± 0.4	225.9 ± 0.5	216 ± 1
S. W. (%)	24 ± 2	25 ± 5	8 ± 5	40 ± 5

Figure 6. 3 (b)). The spectral region below 210 MHz is typically associated to Co nuclei at the interface with non-magnetic atoms[152]. The Co7Al sample has a significant contribution in this frequency interval, estimated as $(17 \pm 2)\%$. This low frequency component of the spectra is ascribed to the interfacing of the surface Co atoms with the nonmagnetic Al layer much higher than both Co7C60 and Co7Ga_q3 samples, $(10 \pm 1)\%$ and $(12 \pm 1)\%$ respectively. Remarkably, this spectral component is strongly decreased in Co7Ga_q3 and Co7C60, being moved to higher frequencies. The signal below 210 MHz nevertheless is not reduced to zero for both Co/Molecule systems, and this can be tentatively attributed to Co atoms in grain boundaries[105], likely present in polycrystalline samples.

To emphasize this effect, I subtracted the normalized spectrum of the Co7Al from those of Co7Ga_q3 and Co7C60 (see **Figure 6. 3 (a)** for the spectra and **Figure 6. 3 (c)** for the subtraction result). For this latter the subtracted spectrum shows that the loss of low frequency contribution below 210 MHz is balanced by the rise of a broad contribution in the bulk-related frequencies above 210 MHz. For the Co7Ga_q3 subtracted spectrum the low frequency part is moved to a sharp positive peak centered at 215.5 MHz, while it has a negative contribution below 210 MHz and above 218 MHz. The subtraction procedure emphasizes thus the spectral differences, in specific the spectral weights of peak I and II between the three samples reported in **Figure 6. 2** and **Table 6. 1**.

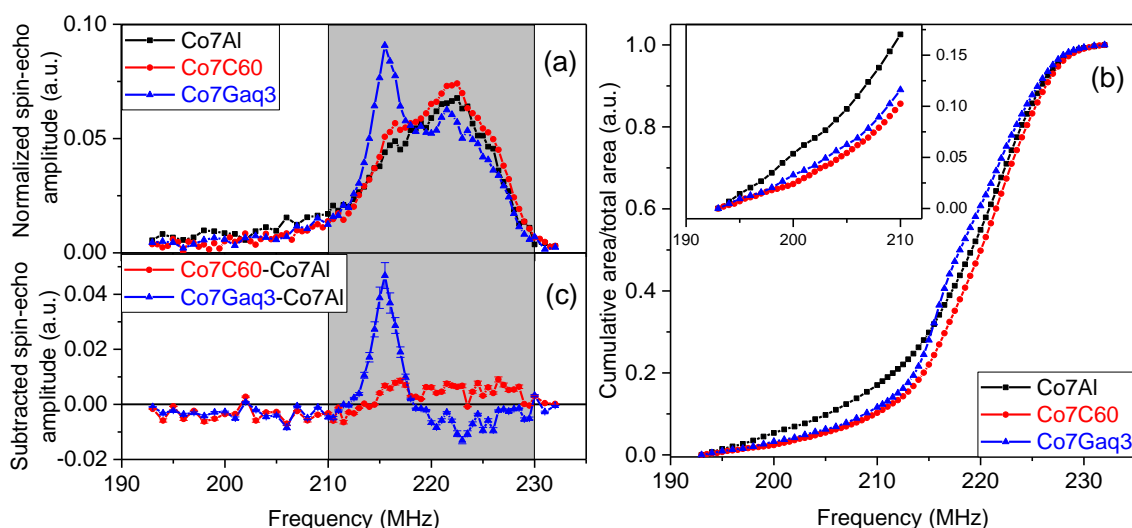


Figure 6. 3 (a) Normalized spectra of each sample. **(b)** Normalized cumulative spectral area of each sample. Inset: normalized cumulative spectral area in the region of interest, frequency <210 MHz. and **(c)** the normalized spectra of Co7C60 (red) and Co7Ga_q3 (blue) subtracted by that of Co7Al, showing a negative contribution in the low frequency and a sample dependent positive contribution in the central region. Estimated error for each point: 10% of the subtracted value.

The differences in spectral weights from Co7Al and Co7Gaq3 or Co7C60 for the low frequency part accounts approximately for 5% of the total resonating nuclei. The differences in spectral weights from Co7Gaq3 and Co7Al or from Co7C60 and Co7Al (in peak I and II) accounts for approximately 10% of the Co nuclei (see **Table 6. 1**), corresponding to a 7 Å length. This indicates that a different interfacial contribution may be compatible with the observed differences in the FNR spectra between Co7Gaq3 and Co7C60 with respect to Co7Al. Concerning about the difference in the peak I,II ratio, it is excluded that it can be a result of different microstructures (i.e. different mixture of *hcp* and *fcc* phases), since all the Cobalt layers were grown during the same deposition cycle on identical substrates, ensuring the same thickness, morphology and crystalline composition. The spectral differences between Co7Al and molecular-based samples can be partly due to the diffusion of aluminum in cobalt, producing up to 0.8 nm intermixed Co/Al interfacial layers[158]–[160], inducing additional defectiveness at the Co surface with respect to an ideal Co surface environment. Nevertheless, the above consideration alone does not explain the strong molecule-dependent differences in the peak I,II ratio and in the spectral shapes of Cobalt layers, as especially emphasized in the representation in (c). The redistribution of the spectral weight for samples interfaced with molecules suggests that the Cobalt nuclei at the interface with the OSC experience a more intense ferromagnetic environment (i.e., higher hyperfine fields) than the ones interfaced with Al. This is a strong indication that a specific magnetic reconstruction of the cobalt surface takes place.

6.3 Conclusions

The application of FNR technique to the investigation of Co/Molecule interfaces (spinterfaces) allowed to unravel previously unknown properties and sheds new light on already debated problems.

The first main finding is that both FNR and MOKE characterizations consistently show a magnetic hardening effect on the Cobalt layer if interfaced with C₆₀ or Gaq₃, even stronger for this latter. Moreover, the observation of this modification by FNR adds additional valuable information since it allows to obtain the local (atomic scale) magnetic hardness. The fact that even at frequencies proper of bulk Cobalt the restoring fields are higher for Co/Molecule systems clearly indicates that this magnetic hardening effect is not confined to the Co/molecule interface but propagates to several nanometers into the ferromagnetic layer. This is an indication that the role of the interface is far more prominent than just modifying the local magnetic properties of the surface Co atoms. In this respect, a still open question is any possible role of

the delocalized electrons in mediating the interfacial modification into the bulk, since for a $3d$ ferromagnet the energy band of the d electrons are superimposed, and to some extent hybridized, to the $4s$ bands even at the Fermi level[51].

The second finding is the reduction of the low-frequency (<210 MHz) contribution to the overall ^{59}Co FNR spectrum for the Co thin films interfaced with either Gaq₃ or C₆₀. As already discussed, interfaces between Co atoms and nonmagnetic elements such as Cu or Al are characterized by a reduction of the overall magnetization. In fact, at these interfaces the FM atoms are lacking a certain number of magnetic nearest neighbors (NN) that are substituted by nonmagnetic atoms[103], [157]. This results in an overall decrease of the HF felt by the Co nuclei, and thus on a shift of the resonance frequency. The reduced spectral weight of the low-frequency region for both Co/C₆₀ and Co/Gaq₃ may be qualitatively explained by the following argument. As discussed in Chapter 1, the spinterface formation upon adsorption of molecular entities over FM surfaces proved to induce novel and intricate magnetic phenomena at the interface, that are ultimately related to the formation of hybrid $p-d$ bonds. Recalling the contributions to the hyperfine field,

$$\text{HF} = H_{\text{con}} + H_{\text{dip,at}} + H_{\text{orb}} \quad (6.2)$$

all these terms for a $3d$ ferromagnet are related in one way or the other to the effects of the spin-polarized d electrons on both the valence and core s electrons and directly on HF through H_{orb} . In this perspective one possibility is that the reduction(increase) of the overall spectral weight of the low(high) frequency ranges (the boundary set at 210 MHz) results to a more intense HF field felt from Co nuclei at the boundary with the OSC layer. This may be interpreted as either to an enhanced spin-polarization of the interfacial layer, as also verified experimentally for a Co/Gaq₃ system[22]. Another factor that could be considered is the lower density of the OSC with respect to Al. All the theoretical calculations of the adsorption of C₆₀ over Co show that at most 7 Co atoms bond to a molecule, that occupies approximately 1 nm^2 . This results in a lower amount of nonmagnetic NN for Co atoms at the interface with respect to Al. A still open question that will be addressed in the future is the origin of the different spectral contribution in the high frequency region for Co/C₆₀ and Co/Gaq₃.

Chapter 7

Major results and final conclusions

The research work pursued in this thesis was both innovative and challenging. The driving idea of the enhancement of the magnetic anisotropy in thin Cobalt films via their hybridization with molecular layers was already reported in literature and partly investigated. Nevertheless, the main results of that research were based on epitaxial films, interesting and versatile for laboratory research, while hardly applicable and transferable in device-related technologies. I explored here interface-induced effects in polycrystalline *3d*-metal films, widely employed in various magnetic devices for memory, sensing and other applications, and performed a thorough and very detailed investigation, employing several molecules and studying various thickness cases. This study was also performed by using several complementary magnetic and structural characterization techniques, revealing an entire set of reliable data describing such interface effects in much more detail than in previously available sources.

The main achievements of this thesis are:

- The observation of a Colossal Enhancement of the in-plane coercive fields (CEHc) of Cobalt thin films hybridized with C₆₀ and Gaq₃. Already at a temperature of 150K the enhancement effect reaches the factor of 30 for Co/ Gaq₃ and 7 for Co/ C₆₀. The effect remains strong and clearly device relevant also at room temperature, where a 100% enhancement is routinely detected.
- The enhancement of the coercive fields, also called hardening effect, is accompanied by a strong reduction of the uniaxial anisotropy characteristic of the reference Co films. The reduction is partial for Co/C₆₀ and nearly total for Co/Gaq₃ e Co/T6. This suggests that the enhancement mechanism is isotropic in its nature, giving important hints for the development of the physical models for the observed CEHc.

- The effect of the enhancement of the coercive field was independently detected by a number of different methods, including MOKE, SQUID, VSM and NMR, as well as by AMR (work in progress, not reported in this thesis)
- Another key result is the propagation of the interface-induced effects deep in the bulk of the Cobalt films. The magnetic resonance studies (FNR) revealed the modification of magnetic parameters in the whole volume of the 7 nm thick Cobalt film, including the magnetic hardening. This observation stimulates discussions and puts questions to the role of localized and delocalized electrons in the *3d* metal and the interaction of these two sub-systems with the interface. These discussions are additionally supported by the magnetic modifications of the surface Co atoms as detected by FNR.
- The structural investigations indicated a significant variation of the bulk nano-crystallinity for films of 3, 5 and 10 nm thicknesses (TEM), while a quite similar granularity was detected by surface investigations with AFM. On the basis of the performed magnetic characterizations, the observed hardening effect seems to be independent of Co nano-crystallinity, while it cannot be neither confirmed or ruled out its dependence on the granular structure.
- A clearly measurable exchange bias was detected in Co/CoOx, Co/C₆₀ and Co/Gaq₃ at low temperatures: below 100 K in Co/CoOx, and below 150 for molecular based systems. While we cannot exclude that the induced bias is caused in all the samples by the presence of antiferromagnetic Cobalt-oxide layer or inclusions, the differences between detected temperature advances the hypothesis of the possible AFM effects induced at metal-molecular interfaces.
- Considering the polycrystalline structure of the starting Co films, their surface was nearly atomically flat, allowing to fabricate well defined hybrid interfaces. Moreover, the observation of these colossal effects in polycrystalline samples and also at room temperature, is of great importance for technological applications.

The results give some indication about the nature of the interface that, interacting with a *3d* ferromagnet, modifies its magnetic properties. The models reported in literature based only on

the modifications of the anisotropy constant do not account for the CEHc reported at low temperatures. The model of *Callsen et al.*[31] shows a linear increase of H_C by lowering the temperature for highly ordered magnetic layer. As suggested by *Bairagi et al.*[34] the increase in coercivity can be related to the increased density of pinning centers induced by the interfacial layer composed of Co atoms bonded to the molecule. In this perspective the suppression of the in-plane uniaxiality observed for the Co thin films interfaced with OSC hybrid systems is an indication that the magnetic behavior is governed by the establishment of a disordered spin configuration, induced on at least the uppermost layer of Co atoms by the hybrid bonds shared with the molecular layer. An indication that increased magnetic disorder should play a relevant role is also given by the qualitatively different trend in temperature, manifested by both Co/C₆₀ and Co/Ga₃ systems with respect to the reference Co films. For the Co/C₆₀ bilayers, the temperature dependence of the coercivity shows the same trend of the ZFC curves, with a strong change in the behavior at the blocking temperature. Remarkably such H_C trend is strongly different, at least in the commonly measured temperature range, for the reference Co films, whose microstructure is equivalent to that of all the other ferromagnetic layers. Thus, the CEHc is associated to an interface-induced disordered magnetic structure and not to a microstructural effect. The phenomenological description of this CEHc is currently ongoing in collaboration with the A.F.Ioffe institute, St. Petersburg and Josef Stefan Institute, Ljubljana in the framework of a European project FET OPEN.

The other major achievement, that is the induced magnetic hardening down to the bulk of the Cobalt layer indicates that the current picture of spinterface effects as due only to local variations of the superficial Co atoms magnetic parameters (magnetic moment, anisotropy constant, ...). These models are all based on the modifications of the surface $3d$ orbitals, that are usually considered as localized. Regardless of the theoretical approach to band calculation for $3d$ metals, the total DOS always shows a superposition of narrow $3d$ bands with broad $4s$ bands. Whether $s-d$ hybridization is taken into account, at Fermi level it should be always expected a non-negligible contribution of s electrons, as discussed in detail in a review by *Mott*[51]. Moreover it is argued that $3d$ electrons should be considered as localized, while s electrons itinerant[52]. Such arguments should be taken into account for a more complete understanding of the spinterface effects on the magnetic properties of $3d$ metals thin films, as the nature of the DOS is fundamental for the formation of a spinterface[12], [17]. In this perspective the contribution of the more delocalized electrons, whether s -like or d -like in nature may be responsible for the observed propagation of the spinterface-induced *global*

modifications. In this view, the role of delocalized electrons in the local interfacial hybridization is under theoretical investigation in collaboration with the Computational Spintronics Group (Trinity College, Dublin).

It is worth noting that the changes of H_c and anisotropy of the Co films is caused, in principle, by molecules bounded with an adsorption energy of approximately 1 eV [22], [23]. Then, even slight modifications of the hybridization strength (of few hundreds meV) would induce detectable variations of the coercivity. This is a promising hint on the practicability of proof-of-concept devices exploiting the application of a gating voltage for modifying the interfacial hybridization and, in turn, the magnetic parameters (as the coercivity) of the ferromagnet.

Bibliography

- [1] K. Bairagi *et al.*, ‘Tuning the Magnetic Anisotropy at a Molecule-Metal Interface’, *Phys. Rev. Lett.*, vol. 114, no. 24, p. 247203, Jun. 2015, doi: 10.1103/PhysRevLett.114.247203.
- [2] F. Al Ma’Mari *et al.*, ‘Beating the Stoner criterion using molecular interfaces’, *Nature*, vol. 524, no. 7563, Art. no. 7563, Aug. 2015, doi: 10.1038/nature14621.
- [3] M. Ziese and M. J. Thornton, *Spin electronics*, vol. 569. Springer, 2007.
- [4] C. Rinaldi *et al.*, ‘Determination of the spin diffusion length in germanium by spin optical orientation and electrical spin injection’, *J. Phys. D: Appl. Phys.*, vol. 49, no. 42, p. 425104, Sep. 2016, doi: 10.1088/0022-3727/49/42/425104.
- [5] R. H. Friend *et al.*, ‘Electroluminescence in conjugated polymers’, *Nature*, vol. 397, no. 6715, pp. 121–128, Jan. 1999, doi: 10.1038/16393.
- [6] V. Dediu, M. Murgia, F. C. Maticotta, C. Taliani, and S. Barbanera, ‘Room temperature spin polarized injection in organic semiconductor’, *Solid State Commun.*, vol. 122, no. 3–4, Art. no. 3–4, 2002, doi: 10.1016/s0038-1098(02)00090-x.
- [7] V. Dediu *et al.*, ‘Room-temperature spintronic effects in Alq_3 -based hybrid devices’, *Phys. Rev. B*, vol. 78, no. 11, p. 115203, Sep. 2008, doi: 10.1103/PhysRevB.78.115203.
- [8] I. Bergenti, V. Dediu, M. Prezioso, and A. Riminucci, ‘Organic spintronics’, *Philos. Trans. R. Soc. A-Math. Phys. Eng. Sci.*, vol. 369, no. 1948, Art. no. 1948, Aug. 2011, doi: 10.1098/rsta.2011.0155.
- [9] V. A. Dediu, L. E. Hueso, I. Bergenti, and C. Taliani, ‘Spin routes in organic semiconductors’, *Nature Mater*, vol. 8, no. 9, pp. 707–716, Sep. 2009, doi: 10.1038/nmat2510.

- [10] ‘15.3: Pi Molecular Orbitals of Benzene’, *Chemistry LibreTexts*, May 27, 2015. [https://chem.libretexts.org/Bookshelves/Organic_Chemistry/Map%3A_Organic_Chemistry_\(Vollhardt_and_Schore\)/15%3A_Benzene_and_Aromaticity%3A_Electrophilic_Aromatic_Substitution/15.03%3A_Pi_Molecular__Orbitals__of_Benzene](https://chem.libretexts.org/Bookshelves/Organic_Chemistry/Map%3A_Organic_Chemistry_(Vollhardt_and_Schore)/15%3A_Benzene_and_Aromaticity%3A_Electrophilic_Aromatic_Substitution/15.03%3A_Pi_Molecular__Orbitals__of_Benzene) (accessed Jan. 22, 2022).
- [11] I. Bergenti and V. Dediu, ‘Spinterface: A new platform for spintronics’, *Nano Materials Science*, vol. 1, no. 3, pp. 149–155, Sep. 2019, doi: 10.1016/j.nanoms.2019.05.002.
- [12] C. Barraud *et al.*, ‘Unravelling the role of the interface for spin injection into organic semiconductors’, *Nat. Phys.*, vol. 6, no. 8, Art. no. 8, Aug. 2010, doi: 10.1038/nphys1688.
- [13] M. Prezioso *et al.*, ‘A Single-Device Universal Logic Gate Based on a Magnetically Enhanced Memristor’, *Advanced Materials*, vol. 25, no. 4, pp. 534–538, 2013, doi: 10.1002/adma.201202031.
- [14] M. Cinchetti, V. A. Dediu, and L. E. Hueso, ‘Activating the molecular spinterface’, *Nat. Mater.*, vol. 16, no. 5, Art. no. 5, May 2017, doi: 10.1038/nmat4902.
- [15] S. Sanvito, ‘The rise of spinterface science’, *Nature Physics*, vol. 6, no. 8, Art. no. 8, Aug. 2010, doi: 10.1038/nphys1714.
- [16] J. P. Muscat and D. M. Newns, ‘Chemisorption on metals’, *Progress in Surface Science*, vol. 9, no. 1, pp. 1–43, Jan. 1978, doi: 10.1016/0079-6816(78)90005-9.
- [17] M. Galbiati *et al.*, ‘Spinterface: Crafting spintronics at the molecular scale’, *MRS Bulletin*, vol. 39, no. 7, pp. 602–607, Jul. 2014, doi: 10.1557/mrs.2014.131.
- [18] S. Delprat *et al.*, ‘Molecular spintronics: the role of spin-dependent hybridization’, *J. Phys. D: Appl. Phys.*, vol. 51, no. 47, Art. no. 47, Sep. 2018, doi: 10.1088/1361-6463/aad9dc.
- [19] H. Vázquez, Y. J. Dappe, J. Ortega, and F. Flores, ‘Energy level alignment at metal/organic semiconductor interfaces: “Pillow” effect, induced density of interface states, and charge neutrality level’, *J. Chem. Phys.*, vol. 126, no. 14, p. 144703, Apr. 2007, doi: 10.1063/1.2717165.

- [20] A. Droghetti *et al.*, ‘Dynamic spin filtering at the Co/Alq(3) interface mediated by weakly coupled second layer molecules’, *Nat. Commun.*, vol. 7, p. 9, Aug. 2016, doi: 10.1038/ncomms12668.
- [21] T. Moorsom *et al.*, ‘Spin-polarized electron transfer in ferromagnet/C-60 interfaces’, *Phys. Rev. B*, vol. 90, no. 12, Art. no. 12, Sep. 2014, doi: 10.1103/PhysRevB.90.125311.
- [22] A. Droghetti *et al.*, ‘Electronic and magnetic properties of the interface between metal-quinoline molecules and cobalt’, *Phys. Rev. B*, vol. 89, no. 9, Art. no. 9, Mar. 2014, doi: 10.1103/PhysRevB.89.094412.
- [23] D. Li *et al.*, ‘Symmetry-selected spin-split hybrid states in C 60 / ferromagnetic interfaces’, *Phys. Rev. B*, vol. 93, no. 8, Art. no. 8, Feb. 2016, doi: 10.1103/PhysRevB.93.085425.
- [24] I. Bergenti *et al.*, ‘Spinterface Formation at α -Sexithiophene/Ferromagnetic Conducting Oxide’, *J. Phys. Chem. C*, vol. 125, no. 11, Art. no. 11, Mar. 2021, doi: 10.1021/acs.jpcc.0c09713.
- [25] L. Cai, Y. Tian, X. Yuan, G. Hu, and J. Ren, ‘Electronic structures of spinterface for thiophene molecule adsorbed at Co, Fe, and Ni electrode: First principles calculations’, *Applied Surface Science*, vol. 389, pp. 916–920, Dec. 2016, doi: 10.1016/j.apsusc.2016.08.022.
- [26] X. Wang, Z. Zhu, A. Manchon, and U. Schwingenschlögl, ‘Peculiarities of spin polarization inversion at a thiophene/cobalt interface’, *Appl. Phys. Lett.*, vol. 102, no. 11, p. 111604, Mar. 2013, doi: 10.1063/1.4798255.
- [27] M. Oehzelt, S. Berkebile, G. Koller, J. Ivanco, S. Surnev, and M. G. Ramsey, ‘ α -Sexithiophene on Cu(110) and Cu(110)-(2 \times 1)O: An STM and NEXAFS study’, *Surface Science*, vol. 603, no. 2, pp. 412–418, Jan. 2009, doi: 10.1016/j.susc.2008.12.005.
- [28] T. Wagner, D. R. Fritz, and P. Zeppenfeld, ‘ α -6T on Ag(110): The formation of the wetting layer’, *Synthetic Metals*, vol. 161, no. 17, pp. 2006–2010, Sep. 2011, doi: 10.1016/j.synthmet.2011.07.014.

- [29] T. Wagner, D. R. Fritz, and P. Zeppenfeld, ‘Standing and flat lying α -6T molecules probed by imaging photoelectron spectroscopy’, *Organic Electronics*, vol. 12, no. 3, pp. 442–446, Mar. 2011, doi: 10.1016/j.orgel.2010.12.011.
- [30] K. V. Raman *et al.*, ‘Interface-engineered templates for molecular spin memory devices’, *Nature*, vol. 493, no. 7433, pp. 509–513, Jan. 2013, doi: 10.1038/nature11719.
- [31] M. Callsen, V. Caciuc, N. Kiselev, N. Atodiresei, and S. Blügel, ‘Magnetic Hardening Induced by Nonmagnetic Organic Molecules’, *Phys. Rev. Lett.*, vol. 111, no. 10, Art. no. 10, Sep. 2013, doi: 10.1103/PhysRevLett.111.106805.
- [32] R. Friedrich, V. Caciuc, N. S. Kiselev, N. Atodiresei, and S. Blugel, ‘Chemically functionalized magnetic exchange interactions of hybrid organic-ferromagnetic metal interfaces’, *Phys. Rev. B*, vol. 91, no. 11, Art. no. 11, Mar. 2015, doi: 10.1103/PhysRevB.91.115432.
- [33] K. Bairagi *et al.*, ‘see supplementary information. Tuning the Magnetic Anisotropy at a Molecule-Metal Interface’, *Phys. Rev. Lett.*, vol. 114, no. 24, Art. no. 24, Jun. 2015, doi: 10.1103/PhysRevLett.114.247203.
- [34] K. Bairagi *et al.*, *Experimental and theoretical investigations of magnetic anisotropy and magnetic hardening at molecule/ferromagnet interfaces*, vol. 98. 2018. doi: 10.1103/PhysRevB.98.085432.
- [35] M. Gruber *et al.*, ‘Exchange bias and room-temperature magnetic order in molecular layers’, *Nature Mater*, vol. 14, no. 10, pp. 981–984, Oct. 2015, doi: 10.1038/nmat4361.
- [36] S. Boukari *et al.*, ‘Disentangling Magnetic Hardening and Molecular Spin Chain Contributions to Exchange Bias in Ferromagnet/Molecule Bilayers’, *Nano Lett.*, vol. 18, no. 8, pp. 4659–4663, Aug. 2018, doi: 10.1021/acs.nanolett.8b00570.
- [37] K. O’Grady, L. E. Fernandez-Outon, and G. Vallejo-Fernandez, ‘A new paradigm for exchange bias in polycrystalline thin films’, *Journal of Magnetism and Magnetic Materials*, vol. 322, no. 8, pp. 883–899, Apr. 2010, doi: 10.1016/j.jmmm.2009.12.011.

- [38] T. Moorsom *et al.*, ‘ π -anisotropy: A nanocarbon route to hard magnetism’, *Phys. Rev. B*, vol. 101, no. 6, p. 060408, Feb. 2020, doi: 10.1103/PhysRevB.101.060408.
- [39] F. Matsukura, Y. Tokura, and H. Ohno, ‘Control of magnetism by electric fields’, *Nature Nanotech*, vol. 10, no. 3, pp. 209–220, Mar. 2015, doi: 10.1038/nnano.2015.22.
- [40] M. Weisheit, S. Fähler, A. Marty, Y. Souche, C. Poinsignon, and D. Givord, ‘Electric Field-Induced Modification of Magnetism in Thin-Film Ferromagnets’, *Science*, Jan. 2007, doi: 10.1126/science.1136629.
- [41] T. Maruyama *et al.*, ‘Large voltage-induced magnetic anisotropy change in a few atomic layers of iron’, *Nature Nanotech*, vol. 4, no. 3, pp. 158–161, Mar. 2009, doi: 10.1038/nnano.2008.406.
- [42] M. Endo, S. Kanai, S. Ikeda, F. Matsukura, and H. Ohno, ‘Electric-field effects on thickness dependent magnetic anisotropy of sputtered MgO/Co₄₀Fe₄₀B₂₀/Ta structures’, *Appl. Phys. Lett.*, vol. 96, no. 21, p. 212503, May 2010, doi: 10.1063/1.3429592.
- [43] K. Nakamura, R. Shimabukuro, Y. Fujiwara, T. Akiyama, T. Ito, and A. J. Freeman, ‘Giant Modification of the Magnetocrystalline Anisotropy in Transition-Metal Monolayers by an External Electric Field’, *Phys. Rev. Lett.*, vol. 102, no. 18, p. 187201, May 2009, doi: 10.1103/PhysRevLett.102.187201.
- [44] D. Chiba, S. Fukami, K. Shimamura, N. Ishiwata, K. Kobayashi, and T. Ono, ‘Electrical control of the ferromagnetic phase transition in cobalt at room temperature’, *Nature Mater*, vol. 10, no. 11, pp. 853–856, Nov. 2011, doi: 10.1038/nmat3130.
- [45] W.-G. Wang, M. Li, S. Hageman, and C. L. Chien, ‘Electric-field-assisted switching in magnetic tunnel junctions’, *Nature Mater*, vol. 11, no. 1, pp. 64–68, Jan. 2012, doi: 10.1038/nmat3171.
- [46] A. Aharoni, *Introduction to the Theory of Ferromagnetism*, vol. 109. Clarendon Press, 2000.
- [47] Neil W. Ashcroft and N. D. Mermin, *Solid State Physics*. 1976.
- [48] S. Blundell, ‘Magnetism in condensed matter’, 2003.

- [49] G. T. Rado and H. Suhl, *Magnetism Vol. IIB*. 1966.
- [50] J. M. D. Coey, *Magnetism and Magnetic Materials*. Cambridge: Cambridge University Press, 2010. doi: 10.1017/CBO9780511845000.
- [51] N. F. Mott, ‘Electrons in transition metals’, *Advances in Physics*, vol. 13, no. 51, pp. 325–422, Jul. 1964, doi: 10.1080/00018736400101041.
- [52] C. Herring, ‘The State of d Electrons in Transition Metals’, *Journal of Applied Physics*, vol. 31, no. 5, pp. S3–S11, May 1960, doi: 10.1063/1.1984588.
- [53] C. G. Shull and H. A. Mook, ‘Distribution of Internal Magnetization in Iron’, *Phys. Rev. Lett.*, vol. 16, no. 5, pp. 184–186, Jan. 1966, doi: 10.1103/PhysRevLett.16.184.
- [54] G. Bertotti, ‘Chapter 6 - Micromagnetics’, in *Hysteresis in Magnetism*, G. Bertotti, Ed. San Diego: Academic Press, 1998, pp. 163–187. doi: 10.1016/B978-012093270-2/50055-6.
- [55] Ag2gaeh, ‘Spheroid with coordinate axes’. [Online]. Available: <https://upload.wikimedia.org/wikipedia/commons/5/53/Ellipsoid-rot-ax.svg>
- [56] P. Bruno, ‘Physical origins and theoretical models of magnetic anisotropy’, *Magnetismus von Festkörpern und Grenzflächen*, vol. 24, pp. 1–28.
- [57] D. M. Paige, B. Szpunar, and B. K. Tanner, ‘The magnetocrystalline anisotropy of cobalt’, *Journal of Magnetism and Magnetic Materials*, vol. 44, no. 3, pp. 239–248, Oct. 1984, doi: 10.1016/0304-8853(84)90248-8.
- [58] L. Néel, ‘Anisotropie magnétique superficielle et surstructures d’orientation’, *J. Phys. Radium*, vol. 15, no. 4, Art. no. 4, 1954, doi: 10.1051/jphysrad:01954001504022500.
- [59] A. Seeger, ‘THE EFFECT OF DISLOCATIONS ON THE MAGNETIZATION CURVES OF FERROMAGNETIC CRYSTALS’, *J. Phys. Colloques*, vol. 27, no. C3, pp. C3-77, Jul. 1966, doi: 10.1051/jphyscol:1966308.

- [60] G. Herzer, 'GRAIN-STRUCTURE AND MAGNETISM OF NANOCRYSTALLINE FERROMAGNETS', *IEEE Trans. Magn.*, vol. 25, no. 5, Art. no. 5, Sep. 1989, doi: 10.1109/20.42292.
- [61] G. Herzer, 'The Random Anisotropy Model', in *Properties and Applications of Nanocrystalline Alloys from Amorphous Precursors*, Dordrecht, 2005, pp. 15–34.
- [62] G. Herzer, 'Magnetization process in nanocrystalline ferromagnets', *Materials Science and Engineering: A*, vol. 133, pp. 1–5, Mar. 1991, doi: 10.1016/0921-5093(91)90003-6.
- [63] S. Thomas *et al.*, 'Microstructure and random magnetic anisotropy in Fe–Ni based nanocrystalline thin films', *J. Phys. D: Appl. Phys.*, vol. 41, no. 15, p. 155009, Jul. 2008, doi: 10.1088/0022-3727/41/15/155009.
- [64] A. S. Dev, D. Kumar, P. Gupta, P. Vishwakarma, and A. Gupta, 'Development of residual stress and uniaxial magnetic anisotropy during growth of polycrystalline Co film', *Materials Research Bulletin*, vol. 121, p. 110616, Jan. 2020, doi: 10.1016/j.materresbull.2019.110616.
- [65] R. Dubey, A. Gupta, P. Sharma, N. Darowski, and G. Schumacher, 'Tailoring of magnetic anisotropy in amorphous and nanocrystalline soft magnetic alloys using swift heavy ions', *Journal of Magnetism and Magnetic Materials*, vol. 310, no. 2, Part 3, pp. 2491–2493, Mar. 2007, doi: 10.1016/j.jmmm.2006.11.091.
- [66] J. D. Agudelo-Giraldo, E. Restrepo-Parra, and J. Restrepo, 'Grain boundary anisotropy on nano-polycrystalline magnetic thin films', *Scientific Reports*, vol. 10, no. 1, Art. no. 1, Mar. 2020, doi: 10.1038/s41598-020-61979-z.
- [67] D. S. Chuang, C. A. Ballentine, and R. C. O'Handley, 'Surface and step magnetic anisotropy', *Phys. Rev. B*, vol. 49, no. 21, pp. 15084–15095, Jun. 1994, doi: 10.1103/PhysRevB.49.15084.
- [68] E. Schlömann, 'Demagnetizing Fields in Thin Magnetic Films Due to Surface Roughness', *Journal of Applied Physics*, vol. 41, no. 4, pp. 1617–1622, Mar. 1970, doi: 10.1063/1.1659081.

- [69] W. H. Meiklejohn and C. P. Bean, ‘New Magnetic Anisotropy’, *Phys. Rev.*, vol. 102, no. 5, pp. 1413–1414, Jun. 1956, doi: 10.1103/PhysRev.102.1413.
- [70] W. H. Meiklejohn, ‘Exchange Anisotropy—A Review’, *Journal of Applied Physics*, vol. 33, no. 3, pp. 1328–1335, Mar. 1962, doi: 10.1063/1.1728716.
- [71] E. Fulcomer and S. H. Charap, ‘Thermal fluctuation aftereffect model for some systems with ferromagnetic-antiferromagnetic coupling’, *Journal of Applied Physics*, vol. 43, no. 10, pp. 4190–4199, Oct. 1972, doi: 10.1063/1.1660894.
- [72] A. P. Malozemoff, ‘Random-field model of exchange anisotropy at rough ferromagnetic-antiferromagnetic interfaces’, *Phys. Rev. B*, vol. 35, no. 7, pp. 3679–3682, Mar. 1987, doi: 10.1103/PhysRevB.35.3679.
- [73] M. D. Stiles and R. D. McMichael, ‘Coercivity in exchange-bias bilayers’, *Phys. Rev. B*, vol. 63, no. 6, p. 064405, Jan. 2001, doi: 10.1103/PhysRevB.63.064405.
- [74] M. D. Stiles and R. D. McMichael, ‘Model for exchange bias in polycrystalline ferromagnet-antiferromagnet bilayers’, *Phys. Rev. B*, vol. 59, no. 5, pp. 3722–3733, Feb. 1999, doi: 10.1103/PhysRevB.59.3722.
- [75] D. Mauri, H. C. Siegmann, P. S. Bagus, and E. Kay, ‘Simple model for thin ferromagnetic films exchange coupled to an antiferromagnetic substrate’, *Journal of Applied Physics*, vol. 62, no. 7, pp. 3047–3049, Oct. 1987, doi: 10.1063/1.339367.
- [76] M. Grimsditch, A. Hoffmann, P. Vavassori, H. Shi, and D. Lederman, ‘Exchange-Induced Anisotropies at Ferromagnetic-Antiferromagnetic Interfaces above and below the Néel Temperature’, *Phys. Rev. Lett.*, vol. 90, no. 25, p. 257201, Jun. 2003, doi: 10.1103/PhysRevLett.90.257201.
- [77] A. Berger, D. T. Margulies, and H. Do, ‘Magnetic hysteresis loop tuning in antiferromagnetically coupled bilayer structures’, *Appl. Phys. Lett.*, vol. 85, no. 9, pp. 1571–1573, Aug. 2004, doi: 10.1063/1.1787161.
- [78] Ch. Binek, S. Polisetty, X. He, and A. Berger, ‘Exchange Bias Training Effect in Coupled All Ferromagnetic Bilayer Structures’, *Phys. Rev. Lett.*, vol. 96, no. 6, p. 067201, Feb. 2006, doi: 10.1103/PhysRevLett.96.067201.

- [79] ‘Inficon STM-2 operating manual’. 2016. [Online]. Available: <https://www.inficon.com/v1/attachment/ce6a66fe-d8c9-42bb-b92d-608e59429802>
- [80] M. Ohtake, O. Yabuhara, J. Higuchi, and M. Futamoto, ‘Preparation and characterization of Co single-crystal thin films with hcp, fcc and bcc structures’, *Journal of Applied Physics*, vol. 109, no. 7, Art. no. 7, 2011, doi: 10.1063/1.3537817.
- [81] M. Ohtake, O. Yabuhara, Y. Nukaga, and M. Futamoto, ‘Preparation of Co(0001)hcp and (111)fcc Films on Single-Crystal Oxide Substrates’, *J. Phys.: Conf. Ser.*, vol. 303, p. 012016, Jul. 2011, doi: 10.1088/1742-6596/303/1/012016.
- [82] ‘Magnesium oxide CAS#: 1309-48-4’. https://www.chemicalbook.com/ProductChemicalPropertiesCB8853024_EN.htm (accessed Jan. 06, 2022).
- [83] G. Binnig, C. F. Quate, and Ch. Gerber, ‘Atomic Force Microscope’, *Phys. Rev. Lett.*, vol. 56, no. 9, pp. 930–933, Mar. 1986, doi: 10.1103/PhysRevLett.56.930.
- [84] G. Haugstad, *Atomic Force Microscopy*. Wiley, 2012.
- [85] G. Portale *et al.*, ‘Influence of metal–support interaction on the surface structure of gold nanoclusters deposited on native SiO_x/Si substrates’, *Phys. Chem. Chem. Phys.*, vol. 16, no. 14, pp. 6649–6656, Mar. 2014, doi: 10.1039/C3CP54847C.
- [86] G. Rasigni, M. Rasigni, J. Palmari, C. Dussert, F. Varnier, and A. Llebaria, ‘STATISTICAL PARAMETERS FOR RANDOM AND PSEUDORANDOM ROUGH SURFACES’, *J. Opt. Soc. Am. A-Opt. Image Sci. Vis.*, vol. 5, no. 1, Art. no. 1, Jan. 1988, doi: 10.1364/josaa.5.000099.
- [87] D. B. Williams and C. B. Carter, *Transmission Electron Microscopy A Textbook for Materials Science*, 2nd edition. Springer, 2009.
- [88] N. Marturi, ‘Vision and visual servoing for nanomanipulation and nanocharacterization in scanning electron microscope’, PH. D. thesis, 2013.
- [89] J. Kerr, ‘XLIII. On rotation of the plane of polarization by reflection from the pole of a magnet’, *The London, Edinburgh, and Dublin Philosophical Magazine and*

Journal of Science, vol. 3, no. 19, pp. 321–343, May 1877, doi: 10.1080/14786447708639245.

[90] Z. Q. Qiu and S. D. Bader, ‘Surface magneto-optic Kerr effect’, *Rev. Sci. Instrum.*, vol. 71, no. 3, Art. no. 3, Mar. 2000, doi: 10.1063/1.1150496.

[91] S. Klahn, P. Hansen, and F. J. A. M. Greidanus, ‘Recent advances in thin films for magneto-optic recording’, *Vacuum*, vol. 41, no. 4, pp. 1160–1165, Jan. 1990, doi: 10.1016/0042-207X(90)93898-S.

[92] A. Kirilyuk, A. V. Kimel, and T. Rasing, ‘Ultrafast optical manipulation of magnetic order’, *Reviews of Modern Physics*, vol. 82, no. 3, Art. no. 3, 9, doi: 10.1103/RevModPhys.82.2731.

[93] P. Bruno, Y. Suzuki, and C. Chappert, ‘Magneto-optical Kerr effect in a paramagnetic overlayer on a ferromagnetic substrate: A spin-polarized quantum size effect’, *Phys. Rev. B*, vol. 53, no. 14, pp. 9214–9220, Apr. 1996, doi: 10.1103/PhysRevB.53.9214.

[94] J. Hamrle, ‘Magneto-optical determination of the in-depth magnetization profile in magnetic multilayers’, phdthesis, Université Paris Sud - Paris XI, 2003. Accessed: Jan. 26, 2022. [Online]. Available: <https://tel.archives-ouvertes.fr/tel-00002948>

[95] R. L. Fagaly, ‘Superconducting quantum interference device instruments and applications’, *Review of Scientific Instruments*, vol. 77, no. 10, p. 101101, Oct. 2006, doi: 10.1063/1.2354545.

[96] ‘Magnetic Property Measurement System® Quantum Design MPMS 3 User’s Manual’. [Online]. Available: https://www.mrl.ucsb.edu/sites/default/files/mrl_docs/instruments/1500-100%20Rev.%20F1%20MPMS%203%20Users%20Manual.pdf

[97] C. Kittel, P. McEuen, and P. McEuen, *Introduction to solid state physics*, vol. 8. Wiley New York, 1996.

[98] H. A. M. de Gronckel, ‘The nanostructure of multilayered films : a NMR study’, Technische Universiteit Eindhoven, 1993.

- [99] H. Akai, 'Hyperfine field calculation for various alloy systems', *Hyperfine Interactions*, vol. 68, no. 1, Art. no. 1, Apr. 1992, doi: 10.1007/BF02396447.
- [100] H. Wieldraaijer, 'Co films for magnetoresistive devices: an NMR study', *Technische Universiteit Eindhoven*, 2006, doi: 10.6100/IR609109.
- [101] H. A. M. de Gronckel, 'The nanostructure of multilayered films: a NMR study', Technische Universiteit Eindhoven, 1993.
- [102] C. Meny and P. Panissod, 'Chapter Two - Nuclear magnetic resonance in ferromagnets: Ferromagnetic nuclear resonance; a very broadband approach', in *Annual Reports on NMR Spectroscopy*, vol. 103, G. A. Webb, Ed. Academic Press, 2021, pp. 47–96. doi: 10.1016/bs.arnmr.2021.02.001.
- [103] C. Meny, E. Jedryka, and P. Panissod, 'SATELLITE STRUCTURE OF CO-59 NMR-SPECTRA IN SOME CO ALLOYS', *J. Phys.-Condes. Matter*, vol. 5, no. 10, pp. 1547–1556, Mar. 1993, doi: 10.1088/0953-8984/5/10/012.
- [104] P. Panissod, *Structural and magnetic investigations of ferromagnets by NMR. Application to magnetic metallic multilayers*, vol. 49. Dordrecht: Springer, 1998. [Online]. Available: [://WOS:000076311900010](https://www.worldscientific.com/doi/10.1007/978-1-4020-0000-1_49)
- [105] P. Panissod and C. Mény, 'Nuclear magnetic resonance investigations of the structure and magnetic properties of metallic multilayers and nanocomposites', *Appl. Magn. Reson.*, vol. 19, no. 3, pp. 447–460, Jul. 2000, doi: 10.1007/BF03162388.
- [106] G. Allodi, A. Banderini, R. De Renzi, and C. Vignali, 'HyReSpect: A broadband fast-averaging spectrometer for nuclear magnetic resonance of magnetic materials', *Rev. Sci. Instrum.*, vol. 76, no. 8, Art. no. 8, Aug. 2005, doi: 10.1063/1.2009868.
- [107] R. Wang, D. Guo, G. Xie, and G. Pan, 'Atomic Step Formation on Sapphire Surface in Ultra-precision Manufacturing', *Sci Rep*, vol. 6, no. 1, p. 29964, Jul. 2016, doi: 10.1038/srep29964.
- [108] X. Shi, L. Xu, Y. Zhou, C. Zou, R. Wang, and G. Pan, 'An in situ study of chemical-mechanical polishing behaviours on sapphire (0001) via simulating the chemical product-removal process by AFM-tapping mode in both liquid and air

environments’, *Nanoscale*, vol. 10, no. 42, pp. 19692–19700, Nov. 2018, doi: 10.1039/C8NR04645J.

[109] G. Atiya, D. Chatain, V. Mikhelashvili, G. Eisenstein, and W. D. Kaplan, ‘The role of abnormal grain growth on solid-state dewetting kinetics’, *Acta Materialia*, vol. 81, pp. 304–314, Dec. 2014, doi: 10.1016/j.actamat.2014.08.038.

[110] L. Smardz, U. Kobler, and W. Zinn, ‘OXIDATION-KINETICS OF THIN AND ULTRATHIN COBALT FILMS’, *J. Appl. Phys.*, vol. 71, no. 10, Art. no. 10, May 1992, doi: 10.1063/1.351378.

[111] W. F. Egelhoff *et al.*, ‘Oxygen as a surfactant in the growth of giant magnetoresistance spin valves’, *Journal of Applied Physics*, vol. 82, no. 12, pp. 6142–6151, Dec. 1997, doi: 10.1063/1.365620.

[112] L. Gan, R. Gomez, C. Powell, R. McMichael, P. Chen, and W. Egelhoff Jr, ‘Thin Al, Au, Cu, Ni, Fe, and Ta films as oxidation barriers for Co in air’, *Journal of applied physics*, vol. 93, no. 10, pp. 8731–8733, 2003.

[113] C. Fourmental *et al.*, ‘Evidence of a C₆₀/Co interface reconstruction and its influence on magnetic properties’, *Physical Review B*, vol. 104, no. 23, p. 235413, 2021.

[114] J. Kollamana *et al.*, ‘Scanning Tunneling Microscopy Study of Ordered C₆₀ Submonolayer Films on Co/Au(111)’, *J. Phys. Chem. C*, vol. 120, no. 14, pp. 7568–7574, Apr. 2016, doi: 10.1021/acs.jpcc.5b12365.

[115] M. Cummings, S. Gliga, B. Lukanov, E. I. Altman, M. Bode, and E. V. Barrera, ‘Surface interactions of molecular C₆₀ and impact on Ni(100) and Co(0001) film growth: A scanning tunneling microscopy study’, *Surface Science*, vol. 605, no. 1, pp. 72–80, Jan. 2011, doi: 10.1016/j.susc.2010.10.002.

[116] Z. Wang, A. Pronschinske, and D. B. Dougherty, ‘Scanning tunneling microscopy of a disordered Alq₃–metal interface’, *Organic Electronics*, vol. 12, no. 11, pp. 1920–1926, Nov. 2011, doi: 10.1016/j.orgel.2011.07.020.

[117] Z.-A. Jian *et al.*, ‘Effects of isomeric transformation on characteristics of Alq₃ amorphous layers prepared by vacuum deposition at various substrate temperatures’,

Journal of Applied Physics, vol. 101, no. 12, p. 123708, Jun. 2007, doi: 10.1063/1.2749209.

[118] F. F. Muhammadsharif, S. Hashim, K. Sulaiman, and G. Baldacchini, ‘A new insight into the temperature induced molecular aggregations in tris(8-hydroxyquinoline) metals’, *Journal of Materials Research and Technology*, vol. 9, no. 3, pp. 4558–4565, May 2020, doi: 10.1016/j.jmrt.2020.02.084.

[119] G. Hlawacek and C. Teichert, ‘Nucleation and growth of thin films of rod-like conjugated molecules’, *J. Phys.: Condens. Matter*, vol. 25, no. 14, p. 143202, Mar. 2013, doi: 10.1088/0953-8984/25/14/143202.

[120] L. K. Scarbath-Evers, R. Hammer, D. Golze, M. Brehm, D. Sebastiani, and W. Widdra, ‘From flat to tilted: gradual interfaces in organic thin film growth’, *Nanoscale*, vol. 12, no. 6, pp. 3834–3845, Feb. 2020, doi: 10.1039/C9NR06592J.

[121] Soncini, Cristian, ‘Modulazione delle proprietà chimico-fisiche dell’interfaccia ferromagnete/organico’, University of Bologna.

[122] J. Ivanco, T. Haber, J. R. Krenn, F. P. Netzer, R. Resel, and M. G. Ramsey, ‘Sexithiophene films on ordered and disordered TiO₂(110) surfaces: Electronic, structural and morphological properties’, *Surface Science*, vol. 601, no. 1, pp. 178–187, Jan. 2007, doi: 10.1016/j.susc.2006.09.020.

[123] H. M. Hwang *et al.*, ‘Asymmetric intermixing in a Co–Al thin film system: An investigation using coaxial impact collision ion scattering spectroscopy’, *Journal of Applied Physics*, vol. 101, no. 9, Art. no. 9, May 2007, doi: 10.1063/1.2730562.

[124] J. D. R. Buchanan *et al.*, ‘Intermixing of aluminum-magnetic transition-metal bilayers’, *Journal of Applied Physics*, vol. 93, no. 10, Art. no. 10, May 2003, doi: 10.1063/1.1544094.

[125] J. Camarero, J. J. de Miguel, R. Miranda, and A. Hernando, ‘Thickness-dependent coercivity of ultrathin Co films grown on Cu(111)’, *J. Phys.: Condens. Matter*, vol. 12, no. 35, pp. 7713–7719, Aug. 2000, doi: 10.1088/0953-8984/12/35/306.

[126] R. K. Kawakami, M. O. Bowen, H. J. Choi, E. J. Escorcía-Aparicio, and Z. Q. Qiu, ‘Effect of atomic steps on the magnetic anisotropy in vicinal Co/Cu(001)’, *Phys.*

Rev. B, vol. 58, no. 10, pp. R5924–R5927, Sep. 1998, doi: 10.1103/PhysRevB.58.R5924.

[127] D. Zhao, F. Liu, D. L. Huber, and M. G. Lagally, ‘Step-induced magnetic-hysteresis anisotropy in ferromagnetic thin films’, *Journal of Applied Physics*, vol. 91, no. 5, pp. 3150–3153, Mar. 2002, doi: 10.1063/1.1433179.

[128] R. A. Hyman, A. Zangwill, and M. D. Stiles, ‘Magnetic reversal on vicinal surfaces’, *Phys. Rev. B*, vol. 58, no. 14, pp. 9276–9286, Oct. 1998, doi: 10.1103/PhysRevB.58.9276.

[129] R. A. Hyman, M. D. Stiles, L.-H. Tang, and A. Zangwill, ‘Coercivity of ultrathin films with in-plane magnetization’, *Journal of Applied Physics*, vol. 81, no. 8, pp. 3911–3913, Apr. 1997, doi: 10.1063/1.365068.

[130] A. S. Arrott, ‘Micromagnetics of ultrathin films and surfaces’, *Journal of Applied Physics*, vol. 69, no. 8, pp. 5212–5214, Apr. 1991, doi: 10.1063/1.348078.

[131] P. Bruno *et al.*, ‘Hysteresis properties of ultrathin ferromagnetic films’, *Journal of Applied Physics*, vol. 68, no. 11, pp. 5759–5766, Dec. 1990, doi: 10.1063/1.346944.

[132] A. N. Caruso, D. L. Schulz, and P. A. Dowben, ‘Metal hybridization and electronic structure of Tris(8-hydroxyquinolato)aluminum (Alq₃)’, *Chemical Physics Letters*, vol. 413, no. 4, pp. 321–325, Sep. 2005, doi: 10.1016/j.cplett.2005.07.098.

[133] Y.-P. Wang, X.-F. Han, Y.-N. Wu, and H.-P. Cheng, ‘Adsorption of tris(8-hydroxyquinoline)aluminum molecules on cobalt surfaces’, *Phys. Rev. B*, vol. 85, no. 14, p. 144430, Apr. 2012, doi: 10.1103/PhysRevB.85.144430.

[134] H. X. Yang, M. Chshiev, B. Dieny, J. H. Lee, A. Manchon, and K. H. Shin, ‘First-principles investigation of the very large perpendicular magnetic anisotropy at Fe/\$MgO and Co/\$MgO interfaces’, *Phys. Rev. B*, vol. 84, no. 5, p. 054401, Aug. 2011, doi: 10.1103/PhysRevB.84.054401.

[135] K. Inoue, H. Shima, A. Fujita, K. Ishida, K. Oikawa, and K. Fukamichi, ‘Temperature dependence of magnetocrystalline anisotropy constants in the single variant state of L10-type FePt bulk single crystal’, *Appl. Phys. Lett.*, vol. 88, no. 10, p. 102503, Mar. 2006, doi: 10.1063/1.2177355.

- [136] G. Varvaro, A. M. Testa, E. Agostinelli, D. Peddis, and S. Laureti, ‘Magnetic Characterization of Perpendicular Recording Media’, in *Ultra-High-Density Magnetic Recording*, Jenny Stanford Publishing, 2016.
- [137] M. T. Johnson, P. J. H. Bloemen, F. J. A. den Broeder, and J. J. de Vries, ‘Magnetic anisotropy in metallic multilayers’, *Rep. Prog. Phys.*, vol. 59, no. 11, pp. 1409–1458, Nov. 1996, doi: 10.1088/0034-4885/59/11/002.
- [138] A. Manchon *et al.*, ‘Analysis of oxygen induced anisotropy crossover in Pt/Co/MOx trilayers’, *Journal of Applied Physics*, vol. 104, no. 4, p. 043914, Aug. 2008, doi: 10.1063/1.2969711.
- [139] N.-H. Kim *et al.*, ‘Role of top and bottom interfaces of a Pt/Co/AlOx system in Dzyaloshinskii-Moriya interaction, interface perpendicular magnetic anisotropy, and magneto-optical Kerr effect’, *AIP Advances*, vol. 7, no. 3, p. 035213, Mar. 2017, doi: 10.1063/1.4978867.
- [140] L. Smardz, U. Kobler, and W. Zinn, ‘TEMPERATURE AND THICKNESS DEPENDENCE OF UNIDIRECTIONAL MAGNETIC-ANISOTROPY EFFECTS IN CO/COO THIN-FILMS’, *Vacuum*, vol. 42, no. 4, Art. no. 4, 1991, doi: 10.1016/0042-207x(91)90038-k.
- [141] M. Gruyters and D. Riegel, ‘Optimized exchange biasing by controlled in situ oxidation’, *Journal of Applied Physics*, vol. 88, no. 11, pp. 6610–6613, Dec. 2000, doi: 10.1063/1.1321782.
- [142] D. Sander, ‘The correlation between mechanical stress and magnetic anisotropy in ultrathin films’, *Reports on Progress in Physics (Online)*, vol. 62, no. 5, pp. 809–858, 1999.
- [143] J. D. Agudelo-Giraldo, F. N. Jiménez-García, and E. Restrepo-Parra, ‘The Influence of Thickness on the Magnetic Properties of Nanocrystalline Thin Films: A Computational Approach’, *Computation*, vol. 9, no. 4, Art. no. 4, Apr. 2021, doi: 10.3390/computation9040045.
- [144] I. J. Bruvera, P. Mendoza Zélis, M. Pilar Calatayud, G. F. Goya, and F. H. Sánchez, ‘Determination of the blocking temperature of magnetic nanoparticles: The

good, the bad, and the ugly’, *Journal of Applied Physics*, vol. 118, no. 18, p. 184304, Nov. 2015, doi: 10.1063/1.4935484.

[145] J. Hamrle *et al.*, ‘Huge quadratic magneto-optical Kerr effect and magnetization reversal in the Co₂FeSi Heusler compound’, *J. Phys. D-Appl. Phys.*, vol. 40, no. 6, Art. no. 6, Mar. 2007, doi: 10.1088/0022-3727/40/6/s09.

[146] R. M. Osgood III, S. D. Bader, B. M. Clemens, R. L. White, and H. Matsuyama, ‘Second-order magneto-optic effects in anisotropic thin films’, *Journal of Magnetism and Magnetic Materials*, vol. 182, no. 3, pp. 297–323, Mar. 1998, doi: 10.1016/S0304-8853(97)01045-7.

[147] K. Postava, H. Jaffres, A. Schuhl, F. Nguyen Van Dau, M. Goiran, and A. R. Fert, ‘Linear and quadratic magneto-optical measurements of the spin reorientation in epitaxial Fe films on MgO’, *Journal of Magnetism and Magnetic Materials*, vol. 172, no. 3, pp. 199–208, Aug. 1997, doi: 10.1016/S0304-8853(97)00098-X.

[148] T. Mewes, H. Nembach, M. Rickart, and B. Hillebrands, ‘Separation of the first- and second-order contributions in magneto-optic Kerr effect magnetometry of epitaxial FeMn/NiFe bilayers’, *Journal of Applied Physics*, vol. 95, no. 10, pp. 5324–5329, May 2004, doi: 10.1063/1.1697640.

[149] A. C. Gossard and A. M. Portis, ‘Observation of Nuclear Resonance in a Ferromagnet’, *Physical Review Letters*, vol. 3, no. 4, pp. 164–166, 8, doi: 10.1103/PhysRevLett.3.164.

[150] T. P. Das, ‘Calculation of Magnetic and Electric Hyperfine Fields in Metals’, *Physica Scripta*, vol. 11, no. 3–4, pp. 121–132, Mar. 1975, doi: 10.1088/0031-8949/11/3-4/003.

[151] P. Panissod, J. P. Jay, C. Meny, M. Wojcik, and E. Jedryka, ‘NMR analysis of buried metallic interfaces’, *Hyperfine Interact.*, vol. 97–8, no. 1–4, pp. 75–98, 1996, doi: 10.1007/bf02150169.

[152] J. Lu, P. L. Kuhns, M. J. R. Hoch, W. G. Moulton, and A. P. Reyes, ‘Magnetic field distribution in ferromagnetic metal/normal metal multilayers using NMR’, *Phys. Rev. B*, vol. 72, no. 5, p. 054401, Aug. 2005, doi: 10.1103/PhysRevB.72.054401.

- [153] M. Malinowska *et al.*, ‘Identification of magnetic phases in granular Co₁₀Cu₉₀ alloy using Co-59 NMR method’, *J. Magn. Magn. Mater.*, vol. 198–99, pp. 599–601, Jun. 1999, doi: 10.1016/s0304-8853(98)01222-0.
- [154] G. Avedissian, J. Arabski, J. A. Wytko, J. Weiss, and C. Meny, ‘Revealing the morphology and the magnetic properties of single buried cobalt-ZnTPP hybrid interfaces by ferromagnetic nuclear resonance spectroscopy’, *Phys. Rev. B*, vol. 102, no. 18, p. 6, Nov. 2020, doi: 10.1103/PhysRevB.102.184114.
- [155] J.-P. JAY, ‘ETUDE PAR RESONANCE MAGNETIQUE NUCLEAIRE DE L’ORDRE A COURTE DISTANCE DANS LE SYSTEME COBALT/FER :DE L’ALLIAGE MASSIF A LA MULTICOUCHE’, PH. D. thesis, Universite Louis Pasteur - Strasbourg I, 1995.
- [156] P. C. Riedi, ‘MAGNETIC STUDIES WITH ZERO-FIELD NMR’, *Hyperfine Interact.*, vol. 49, no. 1–4, pp. 335–355, Jun. 1989, doi: 10.1007/bf02405148.
- [157] G. Avedissian, J. Arabski, J. A. Wytko, J. Weiss, and C. Meny, ‘Probing the Growth of Organic Molecular Films Embedded between Cobalt and Iron Electrodes: Ferromagnetic Nuclear Resonance Approach’, *Adv. Funct. Mater.*, vol. 30, no. 46, p. 6, Nov. 2020, doi: 10.1002/adfm.202005605.
- [158] J. D. R. Buchanan *et al.*, ‘Intermixing of aluminum-magnetic transition-metal bilayers’, *Journal of Applied Physics*, vol. 93, no. 10, pp. 8044–8046, May 2003, doi: 10.1063/1.1544094.
- [159] H. M. Hwang *et al.*, ‘Asymmetric intermixing in a Co–Al thin film system: An investigation using coaxial impact collision ion scattering spectroscopy’, *Journal of Applied Physics*, vol. 101, no. 9, p. 093525, May 2007, doi: 10.1063/1.2730562.
- [160] W. F. Egelhoff *et al.*, ‘Surface oxidation as a diffusion barrier for Al deposited on ferromagnetic metals’, *Journal of Applied Physics*, vol. 89, no. 9, Art. no. 9, May 2001, doi: 10.1063/1.1359151.